An Experimental Investigation of Adsorption and Desorption Characteristics of Coal and Rock

Maram Almolliyeh

Geoenvironmental Research Centre

Cardiff School of Engineering

Cardiff University

Thesis submitted in candidature for the degree of Doctor of Philosophy at Cardiff University

May 2022

Acknowledgements

I would like to thank NRN-LCEE and Cardiff University for funding this project and my PhD.

I would also like to thank my main supervisors Professor Tripathy, whose support, feedback and critique gave me guidance along the way and helped shape my research. May appreciation also goes to my second supervisor Professor Thomas.

Big thank you to all the technicians in engineering; not just for their help in the lab and machine set-up, that made the experiments done for this research possible; but also, for all the moments, laughter, and great conversations we shared together while we worked in the lab over the past few years. Harry, Malcolm, Amanda, Steve, Harvey, Gary, Richard, Ian, Paul, Carl and Tony and Duncan from Earth Sciences, you have made the famously solitary research journey less lonesome, and your presence has made the long hours spent in the lab brighter and more tenantable.

My gratitude also extends to Davide and Gareth, from the British Geological Surveyors and to Aberystwyth University and their wonderful staff, Professor Andrew, Dr. Sarah, Dr Arwyn and Dr. André for their brilliant work on this project.

I cannot speak of companionships without thanking all the current and former peers in the Geo-Environmental Research Centre; Sanjana, Shakil, Renato, Alex, Min, Wu, Lee, Anni, Manju, James, Jack, Irfan, Lee your commitment and our shared interest in the field has been a great source of inspiration for me in this work.

I would also like to thank all the staff of the Cardiff University Engineering Research Office specially Aderyn and Jeanette for accommodating the difficult circumstances that have hit the progress of this project at times during the past few years.

Also, thanks to all Cardiff PhD students that I have met during the past years who I have shared laugh and cry moments with them.

I'm extremely grateful to my colleague Siva along with his wife and two children; Anita, Sivani and Sivasumedhar, for giving me a second family here in Cardiff.

Last but not least, I would like to thank my family of my mother, sisters, niece and nephew along with my friends for their unconditional support, love and patience over the past four years despite all the missed calls, birthdays and occasions while I worked away in the lab.

Finally, I would like to dedicate this research to the loving memory of my brother and my father. Their intellectual presence was the first source of inspiration for my curious and inquisitive nature, and it continues to be with me to this day.

Summary

The adsorption characteristics of coal and the associated caprock system are the key aspects of carbon sequestration in un-mineable coal seams. The effects of injection pressure, fabric, presence of water, biogeological conditions of coal, and compositions of caprock systems tend to affect the CO_2 adsorption-desorption behaviour.

Adsorption-desorption behaviour of an anthracite coal (Aberpergwm) and a bituminous coal (Big Pit) from South Wales Coalfield, a sedimentary rock from East Irish Sea, a sand and two clays (Speswhite kaolin and MX80 bentonite) were studied at sub-critical (up to 6.1 MPa) and near-critical (6.1 MPa and 6.4 MPa) injection pressures at a temperature of 298.15 K. A state-of-the-art manometric gas adsorption experimental apparatus was used for this purpose. The water retention characteristic curves of the coals were established using the chilled-mirror dew-point technique for a large range of suctions.

For the coals studied, both powdered and intact samples were tested at various water contents. The rock samples tested were from two different depths and had different chemical compositions. The sand was tested under dry, wet and *Bacillus mojavensis* (bacteria) loaded conditions. The clays were tested in powder form. Existing Langmuir and Brunauer-Emmett-Teller (BET) adsorption isotherm models, pseudo-first-order (PFO), pseudo-second order (PSO), and Bangham pore diffusion kinetic models, and characteristic curves based on potential theory of adsorption and adsorbed phase density were used to evaluate the experimental data.

At the subcritical pressure region, the adsorption characteristics of powdered coal samples differed from those of intact coal samples, highlighting the significance of the fabric and structure of the sample in relation to the coal rank. Similarly, at near-critical pressure ranges, the CO_2 adsorption isotherm pattern of intact coal was significantly different from that of a powdered sample of the same coal rank (anthracite). The CO_2 adsorption capacities of wet intact coal samples were found to be higher than those of dry samples for anthracite coal. Wet powdered coal samples, on the other hand, had a lower adsorption capacity than dry samples. The CO_2 adsorption-desorption hysteresis of a wet powdered anthracite coal sample demonstrated that CO_2 molecules interact with coal differently than those of dry samples. The findings show that at lower injection pressures (<2 MPa), CO_2 molecules must compete with water molecules, but at higher pressures, CO_2 molecules can replace the water present in the pores and occupy the water-activated sites.

The findings from the water retention behaviour and pH buffering capacity of coal supported the need to investigate the CO_2 adsorption capacity of wet coal. *Bacillus mojavensis* bacteria was found to grow well on coal samples, implying that CO_2 biomineralization should be taken into account and emphasised the importance of examining intact samples with site conditions.

CO_2 adsorption experimental data were better fitted with the Langmuir model (monolayer) at lower pressures (<6.1 MPa) for both intact and powdered samples. At near critical pressures (6.1 to 6.4 MPa), the BET model (multilayer) was fitted well for the intact samples, indicating different mechanisms of adsorption occur. The kinetic model fitting (PFO, PSO and Bangham pore diffusion kinetic models) showed that surface interaction and pore diffusion mechanisms are the rate-determining mechanisms of CO_2-coal adsorption processes. The experimental data for CO_2 adsorption on coal were well fitted with characteristic curves based on surface potential and adsorbed phase density.

Rock samples with higher calcium and iron contents absorbed more CO_2, emphasizing the significance of caprock chemical composition in CO_2 adsorption. Wet and Bacillus mojavensis-loaded sand samples had higher CO_2 adsorption capacities than dry sand, indicating the possibility of a chemical reaction (bio-mineralization). At equilibrium pressures of 3.6 MPa, MX80 bentonite exhibited a greater CO_2 adsorption capacity than Speswhite kaolin, and both dry and wet sand samples. Experiments on CO_2 adsorption and modelling of kinetics showed that physical adsorption occurs with dry sand and clays, while mineralization and surface interactions occur when sand is mixed with biofilm or water.

Nomenclature

A	Binding site for adsorbent**,** defined in equation (2.1)
A_0	Vacant adsorption sites on adsorbents (Defined in section 2.4.1)
A_1	Monolayer Occupancy, defined in equation (2.1) and equation (2.10)
A_s	Specific surface area (m^2/kg)
A_i	Multi-layer occupancy, defined in equation (2.11) and equation (2.12)
A_{i-1}	i^{th} layer occupancy, defined in equation (2.12)
A'	Dimensionless Peng-Robinson equation of state parameter
A	Dimensionless Peng-Robinson equation of state parameter
a_1	Frequency factor (BET), Defined in equation (2.12)
a_i	Frequency factor (BET), Defined in equation (2.12)
a_s	Effective surface area covered by 1 mol of CO_2 (m^2/mol)
B	Dimensionless Peng-Robinson equation of state parameter
b'	Dimensionless Peng-Robinson equation of state parameter
b	Langmuir constant (Pa^{-1})
b_0	Exponential factor (Pa^{-1}), Defined in equation (2.7)
ΔH_{ad}	The energy of adsorption (J/mole)
ΔG_{ad}^0	Gibbs free energy of adsorption (J/mole)
c	Dimensionless parameter related to the heat of adsorption (BET)
C_p	Constant related to van der Waals forces (Jm^3/mol)
D_o	The effective radius of the molecule (m)
k	First-order rate constant defined in equation (3.17) (h^{-1})
k_{a1}	First-order rate constant (h^{-1})
k_{a2}	Second-order rate constant (kg g^{-1} h^{-1})
k_{d1}	First-order rate constant for desorption (h^{-1})
k_{d2}	Second-order rate constant for desorption (kg g^{-1} h^{-1})
k_{ad}	Adsorption rate constant
k_{ad}^1	Adsorption rate constant for 1st layer adsorption (BET)
k_{de}	Desorption rate constant
K_0	The equilibrium constant for adsorption at the surface (BET)
K_1	The equilibrium constant for the physical adsorption of the overlaying layers (BET)
M	Molecular mass of CO_2 (0.04401 kg/mol)
m	Fitting parameter for van Genuchten equation
m_s	Mass of adsorbent (kg)
m_{eq}	Amount of CO_2 adsorbed at given equilibrium pressure (mol/kg or g/kg)
m_∞	Langmuir maximum adsorption capacity (mol/kg or g/kg)
n	Constant for Bangham model
n	Fitting parameter for van Genuchten equation
k_b	Constant for Bangham model (h^{-1})
n_{He}	The number of moles of He (mol)
n_{mon}	Number of moles required for monolayer coverage (BET)

$n_e^{CO_2}$	Amount of CO_2 at adsorbed at equilibrium, (mol/kg)
$n_{equ,ad}^{CO_2}$	Amount of CO_2 adsorbed over a known mass of adsorbent at equilibrium, defined in in equation (3.4) (mol/kg)
$n_{equ,de}^{CO_2}$	Amount of CO_2 desorbed from a known mass of adsorbent at equilibrium, defined in in equation (3.5) (mol/kg)
n_L	Number of moles of liquid CO_2 (mol)
N_m	Number of molecules adsorbed (mol/kg)
$n_t^{CO_2}$	Total number moles injected in RC, Defined in in equation (2.16) (mol)
n_v	Molar volumes of vapour CO_2 (m^3/mol)
P	Pressure (Pa)
t	Time (h)
V	Volume (m^3)
Pc	The critical pressure (Pa)
p_{cc}	Pressure in calibration cell (Pa)
p_{rc}	Pressure in reference cell (Pa)
P_{eq}	Equilibrium gas phase pressure (Pa)
$p_{eq}^{CO_2}$	Equilibrium pressure of CO_2 (Pa)
P_{He}	The pressure of He (Pa)
P_0	Saturation pressure of the gas (Pa)
q_e	Mass of CO_2 adsorbed per mass of adsorbent at time equilibrium (g/kg)
Q_1	Heat of adsorption on the bare surface (BET) (J/mol)
$Q2$	Heat of adsorption for physisorption of the overlaying layers (heat of condensation) (BET) (J/mol)
q_t	Mass adsorbed per mass of adsorbent at time t (g/kg)
R	Universal gas constant (8.314 Pa.m^3/K.mole)
r_a	Rate of adsorption, Defined in equation (2.1)
r_{ad}^1	Rate of adsorption in first layer, Defined in equation (2.9)
r_d	Rate of desorption, Defined in equation (2.2)
r_{de}^i	Rate of adsorption in i^{th} layer, Defined in equation (2.11)
t	Time (h)
T	Temperature (K)
Tc	Critical temperature (K)
V_{cc}	The void volume of the calibration cell (m^3)
v_d	The void volume available for gas in the adsorption cell (m^3)
v^F	Volume fraction of CO_2 vapour phase (m^3)
V_{rc}	The void volume of the reference cell (m^3)
V_{sc}	The void volume of the empty sample cell (m^3)
V_{scv}	The void volume of the sample cell with sample loaded (m^3)
V_m^L	Molar volume of liquid CO_2 (m^3/mol)
p_{svc}	The pressure of loaded sample cell (Pa)

V_{sv}	The sample solid volume (m^3)
w	Water content (%)
x	Thickness of the liquid like adsorbed layer related to density and effective surface area by adsorbents (m)
x_L	Volume fractions of liquid
x_v	Volume fractions of vapour
Z	Compressibility factor
Z_L	Compressibility factor of liquid CO_2
Z_g	Compressibility factor of gas CO_2
Z_{He}	Compressibility factor of He
α	Peng-Robinson equation of state parameter
σ_A	Cross sectional area covered by one CO_2 molecule (m^2)
$\varkappa$	Parameter for Peng-Robinson equation of state
μ_v	Partial pressure of pore-water vapour (Pa)
μ_{v0}	Saturation pressure of water vapour over a flat surface of pure water at the same temperature (Pa)
ρ	Gas density (mol/m^3)
ρ_w	Density of water (kg/m^3)
τ_0	The residence time of CO_2 molecule, defined in equation (2.7) and (3.11) (s^{-1})
ψ	Soil suction (Pa)
Γ	Moles adsorbed over the specific surface area (mol/m^2)
ω	Parameter for Peng-Robinson equation of state
ω_v	Molecular mass of water vapor (18.016 kg/kmol)
α	Parameter for Peng-Robinson equation of state
θ_n	Volumetric water content (%)
a_{vg}	Fitting parameter for van Genuchten equation, air entry value (MPa^{-1})
w	Gravimetric water content (%)
w_r	Residual gravimetric water content (%)
w_s	Saturated gravimetric water content (%)

Table of Contents

Chapter 1

Introduction

1.1 Background

Since the middle of the last century, the global average temperature has risen by more than 1.5°C (Marcott et al. 2013; IPCC 2014; 2018 and NOAA 2022). These climatic changes are related to increasing atmospheric concentrations of greenhouse gases caused by anthropogenic activities (UNEP 2019). Anthropogenic emissions of carbon dioxide (CO_2) (63.6%), methane (CH_4) (19.2%), nitrous oxide (N_2O) 5.7%, and chlorofluorocarbons (CFCs) (11.5%) are the largest contributors (Prusty 2008; Mavor et al. 2002). According to the Paris Climate Agreement (UNFCCC 2015), the global temperature increase must be kept to <1.5 °C in order to avoid serious damage. However, comparing the emission level and temperature increase of the preindustrial reference period with current data, global warming has already reached 1°C above the preindustrial reference period (Figure 1.1). The cumulative CO_2 emissions from 1870 to 2015 were estimated to be 2035 ± 205 Gt of CO_2 (Le Quéré et al. 2015) and increasing at a rate of 40 $GtCO_2$/yr in 2015, with annual emission rate expected to exceed 120 $GtCO_2$/yr by 2100. Global warming is very likely to exceed 1.5°C and 2°C during the twenty-first century unless critical steps are taken in the coming decades to control CO_2 and other greenhouse gas emissions (IPCC Special Report 2022; Figure 1.1 a).

Current atmospheric CO_2 concentrations now exceed 430 ppm, the highest level in 800,000 years (NOAA 2022) and have been increasing at about 20 ppm per decade since 2000. This increase is estimated to be ten times faster than any other sustained increase over the past 800,000 years (Lüthi et al. 2008; Bereiter et al. 2015). Over 36 billion tons of CO_2 are currently emitted per year, and the trend is rising, leading to

significant fluctuations in air temperature and precipitation (Figure 1.1 b) (ONeal et al. 2005; MET office 2019; Ritchie and Roser 2020; NOAA 2022).

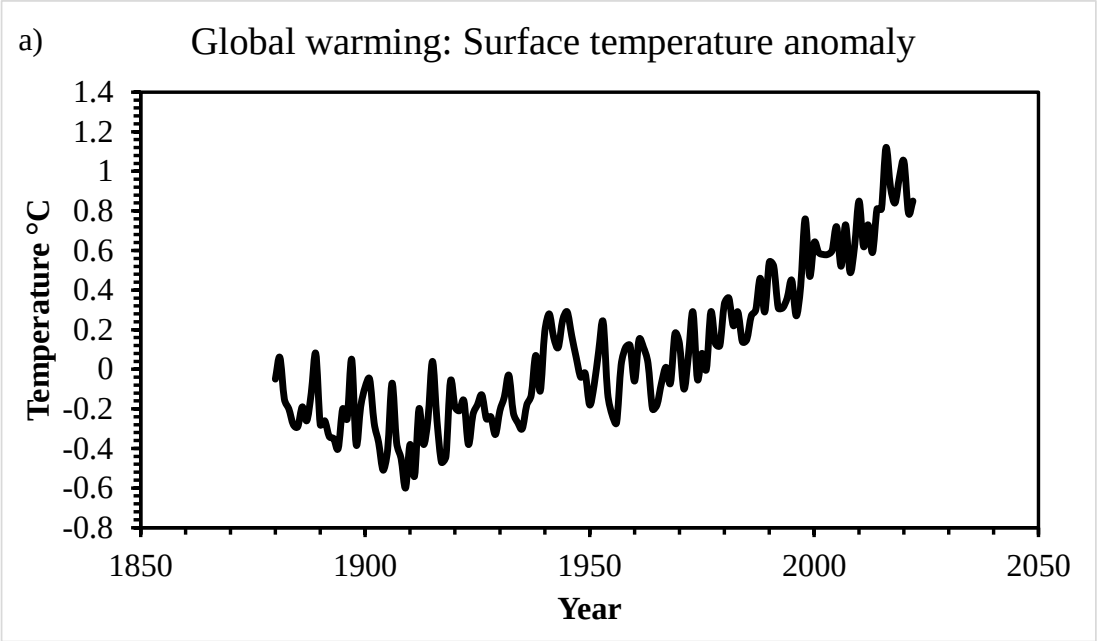

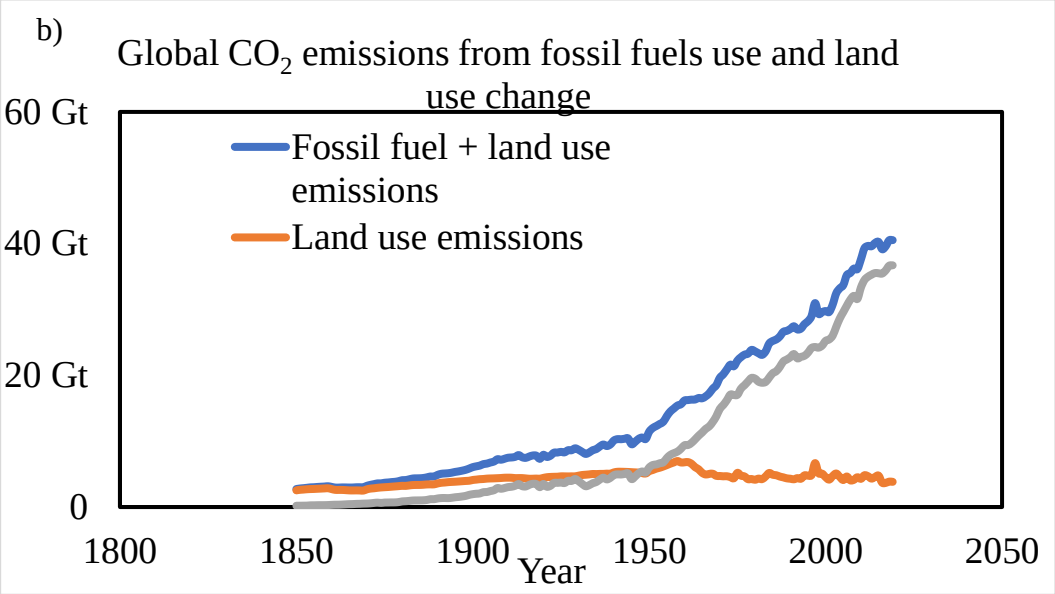

Figure 1.1: (a) CO_2 emission and global warming temperature rise (NOAA, 2022) and (b) cumulative emission in giga tonnes (Gt) from preindustrial era (from the Data compiled by One World Data (Ritchie and Roser 2020).

Sustained CO_2 emissions at current or higher levels will result in extreme temperature rises, droughts, low water availability in some areas, extreme precipitation, impacts on biodiversity, impacts on oceans, and human impacts; thus, adaptation and mitigation strategies are required to reduce and manage the risk of climate change (IPCC 2018). The Paris Agreement aimed to limit average global warming to no more than 2°C above pre-industrial levels by the end of the century, with hopes of reducing this to 1.5°C by the end of the century (Fleurbaey et al. 2014; Kolstad et al. 2014; Global CCS Institute 2016; COP21 2015). To achieve this goal, the IPCC (2018) and UNEP (2019) reports proposed that net anthropogenic global CO_2 emissions must decrease by approximately 35% from 2018 levels by 2030 and reach "net zero" by 2050. The United Kingdom aims to achieve the goals established at COP26 to limit global warming to 1.5°C by focusing on the highest priority areas, such as the coal phase-out. (Great Britain. Department for Business, Energy & Industrial Strategy 2021; COP26 2021).

Several initiatives are being considered to reduce CO_2 emissions, including the phase-out of fossil fuels, increased electricity efficiency, conversion to renewable energy, carbon capture and geological storage (CCS), CO_2 utilisation, and nuclear energy use (StatoilHydro 2009; IEA 2015). Carbon sequestration is a natural or artificial process that removes CO_2 from the atmosphere or captures it from its source and stores it in solid or liquid form. CCS is viewed as a potential mitigation method for reducing CO_2 emissions to meet climate change targets (Gu 2009; Bui et al. 2018). According to the IPCC (2005), a power plant equipped with CCS could reduce CO_2 emissions to the atmosphere by approximately 80–90% compared to a plant without CCS. CO_2 sequestration in geological formations is a storage process that involves capturing CO_2 directly from anthropogenic sources and storing in porous rocks or disposal of it deep into the ground for geologically significant periods (Orr 2009 and Bachu 2010).

Various geologic storage options have been considered for the captured CO_2, including ocean sequestration, geological reservoirs such as oil and gas fields, deep saline aquifers, deep coal seams (enhanced coal-bed methane recovery), and caverns

and mines. (Figure 1.2) (Wildenborg and Lokhorst 2005; Benson and Orr 2008; IEA 2013; WCA 2017).

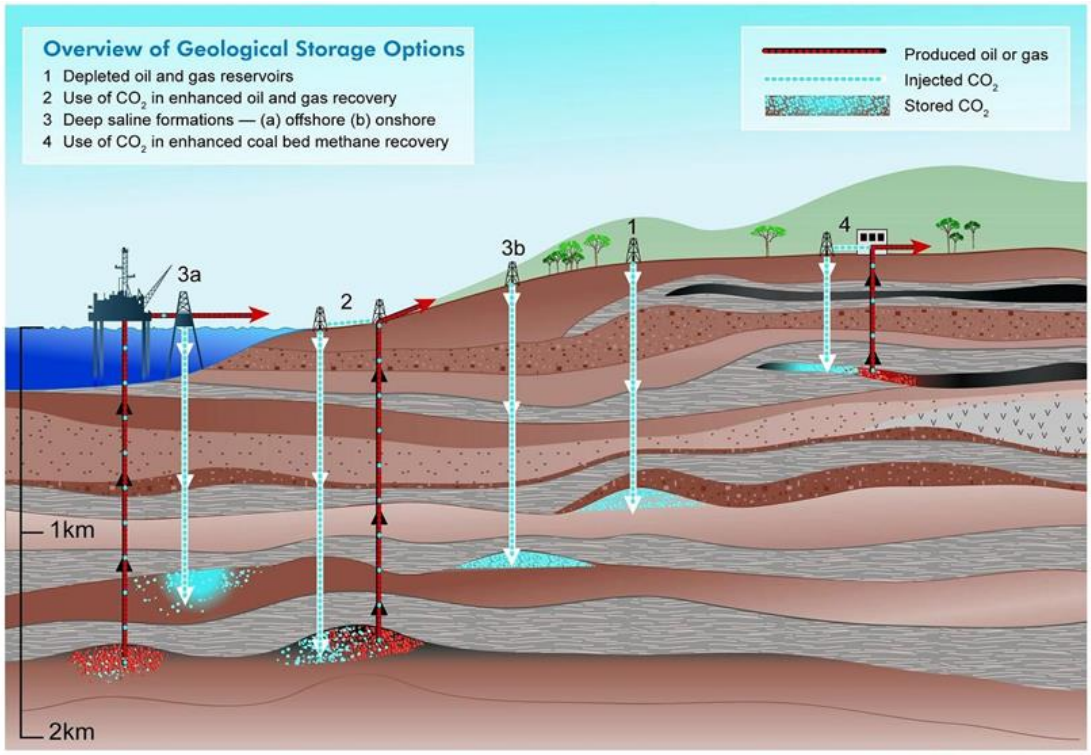

Figure 1.2: Options for geological storage of carbon dioxide (IPCC 2005).

1.2 Carbon sequestration in un-minable coal seams

CO_2 sequestration in deep un-mineable coal seams is a long-term solution for storing CO_2 from anthropogenic sources for a geologically long period of time with or without a natural gas recovery, such as enhanced methane recovery. Un-mineable coals are either too thin, too deep, or too dangerous to mine and historically mined coal seams may also be excessively high in sulphur or mineral matter, or excessively low in British thermal unit (BTU) value, to be economically profitable (Byrer and Guthrie 1998 and White et al. 2005). These coal seams are termed as un-mineable or uneconomical coal seams. Un-mineable coal seams are often found near the high-carbon-emitting industries. Countries are being urged to accelerate the phase-out of

coal to achieve global net-zero emissions by mid-century and meet the 1.5°C goals (COP26 2021). The effective use of the un-mineable coal seams as a potential storage reservoir for CO_2 would be a viable option. Coal seams have the potential to store 300-964 Gt CO_2 globally (Kuuskraa et al. 1992; White et al. 2005).

Due to the different geological nature of coal seams, the CO_2 trapping mechanism varies with coal seams and should have specific screening and selection requirements. The selection criteria for un-mineable coal seams are based on storage capacity, permeability, injectivity, swelling characteristics of the coal, confinement, water content, and depth (White et al. 2005; Vangkilde-Pedersen et al. 2009; Masoudian 2016; Chen et al. 2020). The gas phase adsorption properties of CO_2 on coal are another important factor in determining the storage capacity of coal seams. Gas adsorption is a surface phenomenon in which gas molecules (adsorbates) are retained on a solid surface (adsorbents) by the van der Waals force of attraction (physical adsorption) or chemical reactions (chemical adsorption) (Atkins and Paula 2017).

Coal is classified as lignite, sub-bituminous, bituminous and anthracite (ranked low to high, respectively) based on the physical/ chemical properties and formation mechanism (Speight 2005; White et al. 2005; Thomas 2013). Coal is a dual-porosity rock that has a porous matrix as well as a natural fracture system (cleats) with high surface area (Puri et al. 1991; Clarkson and Bustin 1999; Li et al. 2012; Mitra et al. 2012; Ramandi et al. 2016; Pirzada et al. 2018).The gas in the coal seam is adsorbed on the internal surface of the porous matrix, while the remaining gas can be found in the fracture system (Laubach et al. 1998; White et al. 2005). CO_2 is preferentially adsorbed on the coal than the CH_4 gas which predominately found in coal seams (Strąpoć et al. 2005; Jones et al. 2008; Majewska et al. 2010; Zhang et al. 2011)

The storage capacity of coal seams can be determined using CO_2 adsorption capacity and kinetics. The adsorption capacity and kinetics of CO_2 adsorption on coal samples were found to be significantly related to coal rank, moisture content, swelling characteristics, porosity, temperature, and operating pressures (White et al. 2005; Vangkilde-Pedersen et al. 2009; Masoudian 2016; Qin et al. 2021).

In general, as pressure increases, so does the CO_2 adsorption capacity of coal. However, at pressures near and above the critical pressure (7.38 MPa at 304.1 K), the adsorption capacity decreases (Krooss et al. 2002; Fitzgerald et al. 2005; Siemons and Busch 2007; Lee et al. 2013; Zagorščak 2019). The adsorption capacity increased with decreasing temperature (Busch et al. 2003), and the majority of current literature reported the adsorption isotherms obtained at higher temperatures above critical point (308.15 K, 318.15 K, 328.15 K, and 377.15 K) (Li et al. 2010; Siemens and Busch 2007), with very limited data available at lower temperatures that expected at shallow level coal seams (298.15 K and 290.15 K) (Day et al. 2008a and Mastalerz et al. 2004).

Most of the literature focused on supercritical injection in coal seams at depths of 1000 m to achieve high density, high adsorption capacity, and lower environmental risk. However, creating a laboratory-like controlled environment in the field is uncertain to keep the CO_2 in supercritical condition, and species such as CO_2 escapes to different temperature-pressure zones. Moreover, the high confining pressure may have an influence on the CO_2 injectivity at a depth of 1000 m. Because CO_2 adsorption is a gas/liquid phase adsorption at coal seam depths where the temperature and pressure values are less than the critical parameters of CO_2 (304.15 K and 7.38 MP), the subcritical temperature/pressure adsorption behaviour of CO_2 is needed to be studied which is currently less understood (Saghafi et al. 2007; Bachu 2010). The density of CO_2 is extremely sensitive near the critical point (van der Waals loop region) where the coexistence of the liquid and vapour phases would influence the way CO_2 is adsorbed in general (Eliot and Lira 2012; De Silva and Ranjith 2014). Studying subcritical (liquid/gas) adsorption would be beneficial to the current European initiatives of injecting CO_2 in shallow level coal seams and horizontal injection in underground coal mines at subcritical conditions (ROCCS 2020). These interesting aspects of the temperature/pressure effect on CO_2 adsorption on coal can be explored by conducting isothermal adsorption experiments using manometric adsorption apparatus at 298.15 K and at pressure range of 0.5 MPa to 6.4 MPa (the temperature and pressure range expected in shallow level coal seams).

Adsorption capacity and kinetics data on intact coal samples is limited (Pone et al. 2009; Espinoza et al. 2014; Zagorščak 2017) due to the experimental difficulties, time needed to achieve adsorption equilibrium, permeability, and pore

diffusion/condensation (Espinoza et al. 2014). The adsorption-desorption hysteresis patterns previously studied showed a positive deviation, which was attributed to the sorbent/sorbate system being in a meta stable state and the adsorbate gas not readily released at corresponding thermodynamic equilibrium values of the adsorption process (Busch et al. 2003). The pore structure varies with the coal rank and reflected on the adsorption-desorption hysteresis pattern observed. The pore trapping mechanisms such as pore blockage, gas cavitation, adsorption induced deformation and pore network effect (ink bottle effect) affect the adsorption-desorption hysteresis pattern and correlates with the coal rank (Ren et al. 2022). The reversibility of CO_2 trapped in the pores is critical for understanding coal's ability to retain CO_2. Pulverizing coal samples can alter or lose its physical nature, which affects its CO_2 adsorption properties (Xu et al. 2015; Tan et al. 2018; Lu et al. 2020). Consequently, it stands to reason that comparing the CO_2 adsorption capacity of intact and powdered samples of various coal ranks would reveal the effect of the sample's physical nature.

Most coal seams are wet and studying the adsorption capacity of wet coal is important to replicate the impact of field conditions on the adsorption capacity. The adsorption capacity was suppressed in the presence of moisture for low-rank brown coals, and the experimental results showed that CO_2 prefers the H_2O sites (competing with water), especially in bituminous coal (Day et al. 2008b; Ozdemir and Schroeder 2009; Pone et al. 2009). There is a scarcity of data on the adsorption of CO_2 on wet intact coal samples apart from the studies conducted on constructed coal samples (Zhang et al. 2019). Most previous studies conducted the adsorption experiments with moisture equilibrated powdered samples using ASTM: D1412 which does not represent the field conditions (Gao et al. 2015; Wang et al. 2017). However, the effect of water presence on CO_2 adsorption on coal can be comprehended by establishing different water saturation method for intact coal samples.

The water holding capacity of bituminous coal is higher than that of anthracite coal (Kaji 1986), which would reflect on the CO_2 adsorption capacity. The amount of water in coal is linked to the magnitude of suction. Therefore, it is beneficial to study the water retention behaviour of coal by measuring suction using dew-point chilled-mirror potentiometer (WP4C) for samples with a range of water content (Ferrari et al. 2014). The CO_2-H_2O-coal interaction would raise the carbonic acid content and

dissolve alkaline (Ca, Na, K, and Mg-containing) minerals from the coal, and induce CO_2 mineralisation as $CaCO_3$ (Massarato et al. 2010). Further investigating this physical-chemical interaction between coal and water would improve our understanding of the influence of water on the CO_2 sequestration in coal.

The kinetics of CO_2 adsorption are extremely crucial for transferring laboratory data to the field. Previous laboratory experiments on the desorption kinetics revealed that bituminous coal samples have CO_2 pore trapping capabilities. A significant amount of CO_2 gas molecules remained in the coal structure due to pore entrapment (Majewska et al. 2009). Desorption kinetics can also be used to investigate the reversibility of pore-trapped CO_2 as well as evidence of pore diffusion and condensation. Further detailed kinetic studies would provide insights on the implication of shallow level CO_2 sequestration (≈ 500 m) (Mukherjee et al. 2021).

Pseudo-first-order (PFO) and pseudo-second-order (PSO) kinetic models have been widely used to predict the physical adsorption of CO_2 on coal (Alvarez-Gutierrez 2017). Among the two dominant models, the PSO model agreed well with the experimental results obtained using a manometric adsorption experimental set up for an intact (Shi et al. 2020) and powdered bituminous coal samples (Hou et al. 2020) implying that CO_2 adsorption kinetics and hysteresis was determined by pore diffusion/condensation. In general limited number of studies modelled the desorption kinetics. Njikam and Schiewer (2012) modified the commenly used adsorption kinetic models (PFO and PSO) to adopt the desorption process. These models have not been explored for gas desorption so far, especially for CO_2 adsorption-desorption. The rate determining steps for the adsorption-desorption process can be predicted by fitting the adsorption-desorption kinetics experimental data in Bangham pore diffusion model (Swan and Urquhart 1927) and modified PFO and PSO equations (Njikam and Schiewer 2012).

A review of the literature suggests that the Langmuir monolayer and the Brunauer–Emmett–Teller (BET) isotherm models have been widely used for evaluation of the CO_2 adsorption of coals (Harpalani et al. 2006; Kelemen et al. 2009; Yang 2012; Lafortune et al. 2014; Baran et al. 2016; Abunowara et al. 2016 and Mukherjee et al. 2018). The models have been used in case of test results of powdered

coal samples. It has been recognized that evaluating the experimental data obtained for the intact coal samples against the isotherm models are important to explain the adsorption process by an appropriate theory (monolayer/multilayer). The predicted Longmuir half loading pressure and maximum adsorption capacity are important economic parameters for field scale implementation of CO_2 injection in coal seams (Harpalani et al. 2006). To ascertain the practical application of these model parameters, it is necessary to compare the experimental data with the isotherm models for the intact and powder coal samples. Additionally, taking into account theories other than Langmuir and BET, such as the potential theory of adsorption (Butt et al. 2003) and the theory based on the varying adsorbed phase density (Brunauer et al. 1940), would enhance the fundamental understanding of CO_2 adsorption behaviour of coal.

1.3 CO_2 adsorption on caprocks

The rock strata above the coal seam serve as a caprock system for the CO_2 reservoir in the coal seam. CO_2 can be captured through a variety of mechanisms, including structural trapping, residual trapping, solubility trapping, mineral trapping, and adsorption on the caprock. Sandstone and mudstone formations dominate the rock strata above the coal seams. Sandstone is primarily composed of quartz, with trace amounts of clays (e.g., kaolinite and bentonite). In consequence, studying the CO_2 adsorption capacity of sand and clays would advance our understanding of CO_2 sequestration in un-minable coal seams (Wang et al. 2003; Yang and Yang 2011; Botan et al. 2010).

CO_2 adsorption experiments on montmorillonite were carried out at higher temperatures and pressures (318 K, 328 K; up to 12 MPa) (Jeon et al. 2014). The kaolinite experiments were carried out at 298.15 K with a very low-pressure range (0.1 MPa) (Chen and Lu 2015). It was necessary to investigate the effect of temperature (298.15 K) and subcritical pressure range expected at the caprock system to the coal seams on CO_2 adsorption.

Quartz, the primary mineral in sandstone, is hydrophilic in nature and affects CO_2 adsorption on rock (McGrail et al. 2009; Kwak et al. 2011; Loring et al. 2011; Shao et al. 2011; Tokunaga and wan 2013). The effect of dry or wet condition of sand on CO_2 adsorption capacity has not been clearly supported by available experimental research studies (Wensink et al. 2000; Rahaman et al. 2008; Malani and Ayappa 2009; Kerisit et al. 2012).

Microbial activities have also been reported in rock strata and influence the fate and transport mechanism of CO_2 at potential geological carbon sequestration (GCS) sites (Morozova et al. 2010; Lavalleur and Colwell 2013; Peet et al. 2015). Supercritical nature of CO_2 can serve as a disinfectant against microorganisms. Microbes such as *Bacillus mojavensis*, on the other hand, resilient to supercritical CO_2 (Mitchell et al. 2008). *Bacillus mojavensis* is a native microorganism found in coalfield sandstones (Mitchell et al. 2009) that thrives under high pressure conditions (Kanihira et al. 1987; Enomoto et al. 1997; Zhang et al. 2006). This important finding emphasises the need for further experimental research on *Bacillus mojavensis*-loaded sand samples at various pressure ranges to understand the influence of the biofilm on the CO_2 adsorption characteristics of sand.

1.4 Aim and objectives of the thesis

A comprehensive literature review was conducted to formulate the aim and objectives of the thesis. The review of the literature suggested that there are limited data on subcritical and near critical pressure range of CO_2 adsorption on intact coal samples at 298.15 K. Therefore, the purpose of the present study is to answer the following research questions.

(1) How do the CO_2 adsorption capacity and kinetics of intact anthracite and bituminous coal samples compare to the powdered samples?

(2) What are the effects of subcritical, near critical injection pressure range at 298.15 K (expected conditions at shallow level coal seams, 500 m deep) on CO_2 adsorption on powdered and intact coal samples?

(3) How does the water influence the adsorption capacity of powdered and intact samples of anthracite coal?

(4) How does the adsorption-desorption isotherm hysteresis differ for the powder and intact samples in terms of the physical structure of coal? and

(5) How do the biogeological conditions and chemical composition of the constituents of the rock strata influence the CO_2 adsorption behaviour?

To address the research gaps identified, experimental investigations are an effective way of studying the complex physical and chemical mechanisms involved in CO_2 adsorption on coal.

The main objectives of the experimental study are:

1. To conduct manometric CO_2 adsorption-desorption experiments on coal to determine the adsorption capacity of intact and powdered samples of low rank (bituminous) and high rank (anthracite) coals under isothermal conditions (298.15 K) and at varying pressures (< 6.1 MPa and near-critical pressure range (6.1 MPa to 6.5 MPa)).
2. To conduct adsorption-desorption experiments on water-saturated intact and powdered samples of coal to gain a better understanding of how moisture affects adsorption capacity. To study the effect of the coexistence of liquid and vapour CO_2 on the adsorption characteristics of coal in the near critical pressure region (6.1 MPa to 6.4 MPa).
3. To evaluate the adsorption-desorption processes by fitting CO_2 adsorption experimental data to existing adsorption isotherm models (Langmuir and the Brunauer-Emmett-Teller (BET) isotherm models). Explore the theories other than Langmuir and BET by fitting experimental data to CO_2 adsorption characteristics curves based on the potential theory of adsorption and the molar volume/density of the adsorbed phase of CO_2. Collect experimental data of adsorption and desorption kinetics to gain a better understanding of the CO_2 adsorption-desorption process. To predict the rate-determining step and obtain kinetic parameters, fit the experimental kinetic data with existing adsorption

kinetics models (pseudo-first order (PFO), pseudo-second order (PSO) kinetic and Bangham pore diffusion models). Fit the desorption kinetics experimental data of coal in to modified PFO and PSO model.

4. To conduct adsorption experiments with rock and clay minerals. Investigate the adsorption characteristics of dry, wet and obtain first-hand information on biofilm (*Bacillus mojavensis*) loaded sand samples to understand the impact of bio-geological conditions on the CO_2 adsorption capacity of the mineral constitutions of the caprock.

1.5 Overview of the thesis

A brief description of each chapter is presented below.

CHAPTER 1 provides a general introduction to carbon sequestration in un-mineable coal seams and rocks, the research gaps, need for the additional research as well as the aims and objectives of this research and the thesis outline.

CHAPTER 2 summarises the current state of knowledge regarding CO_2 gas adsorption on coal, rock, sand, and clay minerals. The fundamentals of gas adsorption are discussed in this chapter, as well as existing theoretical models of gas adsorption related to CO_2 adsorption. The chapter provides background information on the experimental method of manometric gas adsorption and desorption as well as the gas thermodynamic basis for the calculation methods. The chapter discusses the importance of additional research and identifies gaps in current understanding of the research topic.

CHAPTER 3 presents information about the physical and chemical properties of the materials used in the study. The chapter describes the methods for preparing dry and wet, powder and intact coal samples, wet and bacteria-loaded adsorbents (coal and sand) to replicate the field and biogeological conditions. This chapter illustrates the manometric gas adsorption experimental apparatus, adsorption-desorption experimental procedures, and calculation methods including theoretical methods in detail. The experimental methods used to obtain information about coal-water-CO_2

interactions, specifically the water retention properties of the coal sample, are described in this chapter.

CHAPTER 4 presents the adsorption and desorption experimental results obtained for the two coal ranks used. The adsorption isotherm patterns obtained for powdered and intact bituminous and anthracite coal samples are compared in this chapter. The adsorption-desorption isotherm patterns are interpreted to determine pore condensation/diffusion and CO_2 entrapment. The effect of conducting CO_2 adsorption experiments at near critical pressure ranges (6.1 MPa to 6.4 MPa) at 298.15 K is discussed in this chapter. The chapter also includes experimental observations (pressure versus time) curves to provide a general overview of adsorption and desorption kinetics.

CHAPTER 5 presents the impact of presence of water in coal seams on the CO_2 adsorption properties of coal. The water retention characteristics of the two coal samples, as well as the pH buffering capacity of coal, were interpreted to better understand of the CO_2-water-coal interaction. This chapter also provides evidence for the presence of a CO_2-resistant bacterium, *Bacillus mojavensis*, on coal samples. This chapter presented the experimental CO_2 adsorption-desorption isotherm results obtained from wet powdered and wet intact anthracite coal samples. The results of the adsorption experiments on wet coal samples were compared to the results on dry samples.

CHAPTER 6 evaluates CO_2 adsorption experimental data using existing theoretical adsorption isotherm models (Langmuir and BET) and kinetic models (PFO, PSO and Bangham pore diffusion models). The experimental results were fitted to the Langmuir and BET models to obtain the model parameters. In this chapter, the maximum adsorption capacity of Langmuir, the half-load pressures, the energy of monolayer adsorption, the energy of condensation of CO_2 in multilayer adsorption and the available surface area for CO_2 in coal samples are presented. Together with existing isotherm models, the experimental data is fitted into characteristic curves to interpret the CO_2 adsorption using other theories based on physical attractive forces (Van der Waals attractive forces) and the molar volume of the adsorbed phase. To predict the rate determining step in the CO_2 adsorption process, the adsorption-

desorption kinetics data were fitted into pseudo-first order, pseudo-second order and Bangham pore diffusion models.

CHAPTER 7 presents an insight into the CO_2 adsorption behaviour of the caprock adjacent to un-mineable coal seams. This chapter discusses the adsorption experiments conducted on rocks and clay minerals. This chapter also presents the results of adsorption-desorption experiments conducted on sands under different biogeochemical conditions (dry, wet and *Bacillus mojavensis*-loaded sand samples). The isotherm and kinetics models were used to interpret the results.

CHAPTER 8 presents the main conclusions drawn based on the results of this study, along with suggestions for future work.

Chapter 2

Literature Review

2.1 Introduction

CO_2 and other greenhouse gases are known to contribute to global warming. Researchers are looking into the possibility of storing CO_2 in un-mineable coal seams to help tackle climate change. Adsorption of CO_2 on coal is one of the main mechanisms for retaining CO_2 in un-mineable or uneconomic coal seams. A quantification of adsorption capacity of coal samples under various conditions is required for exploring the potential CO_2 sequestration sites. CO_2 adsorption on coal is a complex process influenced by many variables including coal rank, moisture content (or water content), pressure, temperature, adsorptive (CO_2) gas behaviour, and coal sample size considered during testing. The adsorption characteristics of the low permeable overburden (caprock system) are important to assess the CO_2 leak into sensitive subsurface environments. The caprocks may contain various rock and clay minerals. It was therefore necessary to thoroughly research the adsorption properties of various coal, rock, sand and clay minerals. A through literature review was conducted to identify knowledge gaps and the need for additional research in CO_2 adsorption and desorption in coal seams.

Scope and sequence of the review.

1. Section 2.2 discusses the literature review on the development of manometric/volumetric experimental setup and methodology.
2. Section 2.3 summarises the current knowledge pertaining the CO_2 adsorption capacity of powdered and intact coal samples of different ranks. The porous structure of the intact coal sample would have a greater effect on the CO_2 adsorption properties. The available literature revealed that there is a dearth of literature on the adsorption characteristics of large intact coal samples. Section

2.3.1 explores the literatures comparing the adsorption capacities of powdered and intact samples.

3. As CO_2 adsorption occurs in the gas and liquid phases at coal seam depths where the temperature and pressure are less than the critical parameters of CO_2 (31°C and 7.38 MP), the subcritical temperature/pressure adsorption behaviour of CO_2 is currently less understood. Section 2.3.2 discusses the existing literature on experimental results obtained at various pressure and temperature conditions. The coal rank and water content of the coal are the other important factors that influences the adsorption capacity of the coal. During the adsorption process, water molecules compete with CO_2 molecules. Many studies have been equilibrated powdered coal samples with moisture using methods that do not accurately represent field conditions. However, one of the goals of the current study is to investigate the effect of water on intact coal samples and compared to that of the powdered samples of different rank coal samples. The scope of the current research was established by the literature review discussed in section 2.3.3. Section 2.3.3.1 provides an overview of previous research on the water retention properties of different coal samples and how CO_2 interacts with adsorbed water and coal.
4. The adsorption-desorption hysteresis pattern and adsorption-desorption kinetic data are important because they reveal the reversibility and pore trapping capacities of various coal samples at specific temperature and pressure ranges. The above-mentioned context was the basis for the literature review, which is presented in sections 2.3.4 and 2.3.5.
5. In section 2.4, the literature on CO_2 adsorption on caprock, sandstone and clay minerals were reviewed in the context of the caprock system's adsorption properties. Experiments with sandstone rock cores from a coal field demonstrated that a bacterial species (*Bacillus mojavensis*) indigenous to coal seams is resistant to CO_2 at varying pressure range. This established a framework and motivated the investigation of *Bacillus mojavensis*'s effect on the CO_2 adsorption behaviour of sand.
6. Section 2.5 discusses the fundamentals of gas adsorption as well as existing adsorption isotherm models (the Langmuir and Brunauer–Emmett–Teller

(BET) theories) and kinetic models relevant to CO_2 adsorption. Section 2.5.4 discusses the theoretical basis of the characteristic curve based on the potential theory of adsorption. Section 2.5.5 also summarises the background literature for the characteristic curve developed based on the varying adsorbed phase density of CO_2 as a function of the equilibrium gas phase pressure.

Based on the literature review, gaps in the current knowledge have been identified and summarised in the concluding remark section (section 2.6) as the primary objectives of the current research.

2.2 CO_2 adsorption measurement methods

Numerous experimental techniques, including volumetric/manometric, gravimetric, volumetric-gravimetric, oscillometery, and impedance spectrometry, have been used to determine gas adsorption (Keller and Staudt 2005). The volumetric/manometric method was used in this study to determine the adsorption on coal and rock minerals.

The early designs of volumetric measurement apparatus were intended to determine the volumes of irregular shapes. Pohl (1940) created an instrument that served as a prototype for the modern volumetric adsorption measurement apparatus. Many manometric/volumetric devices have been developed and used to measure CO_2 adsorption on coal (Krooss et al. 2002; Busch et al. 2003a; Siemons and Busch 2007; Li et al. 2010; Busch and Gensterblum 2011; Battistutta et al. 2012; Merkel et al. 2015).

The concept of the manometric/volumetric method is a known amount of CO_2 gas stored in a reference vessel and expanded into a vessel containing a sample of sorbent (e.g., coal sample) that was initially vacuumed. The CO_2 gas is then partially adsorbed on the surface of the coal sample (external and internal surfaces). As the gas molecules disappear from the gas phase into the adsorbed phase, the pressure drops. The amount of adsorbed CO_2 in volumetric or manometric gas adsorption is simply calculated by the amount of CO_2 that has disappeared from the vapour phase under

given P-V-T conditions. The amount of CO_2 adsorbed can be expressed as excess, absolute, or net (Sudibandriyo et al. 2003; Keller and Staudt 2005 and Meyers 2014). Excess adsorption is determined experimentally as described below and can be calculated using Equations (2.1) and (2.4). (Ozdemir et al. 2003; Sakurovs et al. 2007; Ozdemir and Schroeder 2009 and Meyers 2014).

Figure 2.1 illustrates a simplified schematic of the volumetric/manometric experimental setup. The apparatus is made up of a gas supply, an adsorption apparatus with a reference cell (RC), a sample cell (SC), and pressure transducers for measuring the pressure drop. The entire setup is contained within a thermostat (water bath) to maintain a constant temperature (Figure 2.1). A known mass (m_s) of adsorbent (coal) that has been vacuum degassed to remove any trapped gas in the sample. A known quantity (n_t) of gas (CO_2) is injected into the RC, expanded into the SC, and adsorbed on the adsorbent. The coal samples are highly fractured, and not all gas molecules are adsorbed. A small amount of gas remains in the gas phase at equilibrium. The amount adsorbed is the difference between the amount of gas in the gas phase (n_{eq}) and the known amount (n_t) of gas (CO_2) injected into the RC (Keller and Staudt 2005; Meyers 2014).

The He-pycnometry method is used to approximate the void volume (v_d) available for gas molecules in the RC and SC by injecting He into the adsorption cell at the experimental ambient temperature and pressure. Then the void volume can be calculated using perfect gas law, Equation (2.1) (Sudibandriyo et al. 2003; Keller and Staudt 2005; Meyers 2014).

$$v_d = \frac{n_{He} R T Z_{He}}{P_{He}} \qquad (2.1)$$

where n_{He} is the number of moles of He injected (mol), v_d is the void volume available for gas (m^3), P_{He} is the pressure (Pa), Z is compressibility factor of He and R-gas constant 8.314 (J/K mol).

The calculated v_d is used to estimate the total amount of CO_2 injected ($n_t^{CO_2}$; Equation 2.2) and amount present in the gas phase ($n_e^{CO_2}$; Equation 2.3) at equilibrium and difference between $n_t^{CO_2}$ and $n_e^{CO_2}$ is adsorbed amount ($n_{equ,ad}^{CO_2}$; Equation 2.4).

$$n_t^{CO_2} = \frac{p^{CO_2}}{RTZ_{(p,v)}} v_{rC} \qquad (2.2)$$

$$n_e^{CO_2} = \frac{p_{eq}^{CO_2}}{RTZ_{(p,v)}} v_d \qquad (2.3)$$

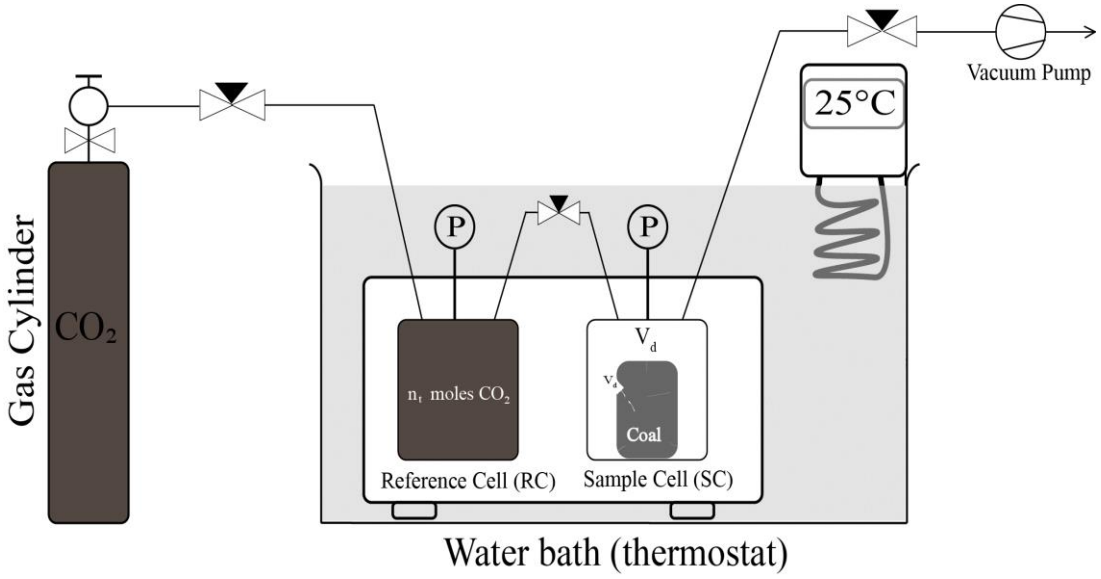

Figure 2.1. Schematic of monomatric/volumetric adsorption experimental setup.

Keller and Staudt (2005) described the Equations (2.2 and 2.3) can be combined as described in Equation (2.4) to accommodate experimental parameters.

$$n_{equ,ad}^{CO_2} = \frac{n_t^{CO_2} - \frac{p_{eq}^{CO_2}}{RTZ_{(p,v)}} v_d}{m_s} \qquad (2.4)$$

where $n_t^{CO_2}$ is the known amount present in the gas phase at the beginning of the adsorption experiment (mol), $n_e^{CO_2}$ is number of moles of CO_2 at equilibrium stage (mol), $n_{equ,ad}^{CO_2}$ is amount of CO_2 adsorbed over known mass of adsorbent (mol/kg), v_d

is void volume available for gas, (v_d is sample cell volume with sample loaded + reference cell volume), p^{CO_2} is pressure of CO_2 injected in RC, $p_{eq}^{CO_2}$ is equilibrium pressure of CO_2 (Pa) measured in RC+SC, v_{rC} is volume of reference cell (m^3), R is gas constant 8.314 (J/mol.K) and Z-is compressibility factor of CO_2. The compressibility factor (Z) was determined using the Peng-Robinson equation of state (Elliot and Lira 2012). The method for determining the compressibility factor (Z) and the theoretical background is discussed in detail in Chapter 3, section 3.3.4.

2.3 Factors affecting CO_2 adsorption on coal

Coal seams have been identified as a potential candidate for geological CO_2 storage due to physical adsorption capacity and their proximity to CO_2 generating industries (GCS 2018; White et al. 2005). The adsorption capacity and kinetics of CO_2 on coal are critical characteristics for determining the storage capacity of specific coal seams. The CO_2 gas adsorption capacity of coal samples is significantly influenced by the coal rank, moisture content, swelling characteristics, porosity, temperature, and operating pressures (Vangkilde-Pedersen et al. 2009; White et al. 2005; Masoudian 2016; Chen et al. 2020).

The following subsections provide the current knowledge garnered from the literature focusing on the influence of sample physical nature (intact and powdered) of coal samples, temperature, pressure and water on the adsorption capacity. The literature relevant to CO_2 adsorption characteristics of rock, sand and clay minerals at varying biogeological conditions were also discussed in this section.

2.3.1 Effect of sample condition (powder and intact)

The small blocks or core samples with undisturbed physical structure are referred as to intact sample in the current thesis. Experimental investigations to date have mainly focused on the gas sorption capacity and kinetics of powdered coals. There have been a few studies conducted on the CO_2 adsorption behaviour of intact coal samples (Pone et al. 2009; Espinoza et al. 2014; Zagorščak 2017). Experiment

performed with 44 mm diameter 53 mm heigh core samples by Zagorščak (2017) showed 1.82 mol/kg at the maximum applied pressure of 3.5 MPa. Keleman (2009) reported the adsorption capacities for small intact bituminous coal specimens as 44.01 g of CO_2/kg of coal (1 mol/kg) at 296 K and at equilibrium pressures of 1.8 MPa. The difficulty in coring fractured coal blocks to obtain representative coal samples, the longer time required to reach thermodynamic adsorption equilibrium, the influence of permeability, pore diffusion/condensation, and CO_2-compatible components for the experimental set-up are all possible explanations for the scarcity of data on intact samples (Espinoza et al. 2014). Coal has a porous matrix as well as a natural fracture system (cleats) (Puri et al. 1991; Clarkson and Bustin 1996; Li et al. 2012; Mitra et al. 2012; Ramandi et al. 2016; Pirzada et al. 2018). The physical nature of the coal can be altered or lost when the samples are pulverised and (Xu et al. 2015; Tan et al. 2018) would have an impact on the CO_2 adsorption properties (Liu et al. 2020).

Powdered samples are expected to have a higher adsorption capacity due to their high surface area. When intact coal samples are powdered, their pore network (channel-like and interconnected pores) is lost (Zhao et al. 2014) and affects the adsorption capacity (Majewska et al. 2009). Because pore diffusion and condensation of CO_2 have a large influence on the adsorption capacity of coal samples, the fractured and porous structure of the coal is critical for CO_2 adsorption. This effect was found to be more pronounced in intact samples of bituminous coal (38 mm dia. core) from the Hazard No. 9 coal seam in Perry County, Western Kentucky Coalfield (Pone et al. 2009). The intact sample of the bituminous coal showed 61.6 g of CO_2/kg of coal compared to 52.8 g of CO_2/kg of the powdered coal sample at 3.1 MPa injection pressure.

2.3.2 Effect of temperature and pressure

Many studies on carbon dioxide sorption on powder samples of various coal ranks at varying temperatures and pressures have been conducted (Stevenson et al. 1991; Arri et al. 1992; Yee et al. 1993; Hall et al. 1994; Nodzenski 1998; Clarkson and Bustin 1999, 2000; Krooss et al. 2002; Busch et al. 2003; Goodman et al. 2004;

Ozdemir et al. 2004; Fitzgerald et al. 2005; Mosleh 2014). These studies demonstrated that increasing the pressure increased the CO_2 adsorption capacity of coal up to the critical region. While other studies have focused on adsorption behaviour at higher pressures, it has been shown that the decreasing trend in the isotherm pattern at pressures near and above the critical pressure (7.38MPa at temperature of 304.1K) (Krooss et al. 2002; Fitzgerald et al. 2005; Siemons and Busch 2007; Lee et al. 2013; Zagorščak 2017). In general, CO_2 gas adsorption on coal can be explained by physical adsorption, in which the adsorption capacity increases as pressure increases.

A sorption capacity of 70 STD cm^3 CO_2/g of coal was obtained for dry coal samples using volumetric adsorption measurements performed at 20 MPa pressures and temperatures of 313 K, 324 K and 353 K (Krooss et al. 2002). An extensive study carried out on activated carbon by Sudibandriyo et al. (2003) published excess adsorption capacities of varying pressures at 318.2 K, which provided the basis for the adsorbed volume of CO_2 at varying pressure for carbonous materials. Busch et al. (2003) reported the increase in excess adsorption with increasing pressure for coal samples that reached an adsorption capacity of 96.82 g of CO_2/kg of coal at a pressure of 4.5 MPa at 295 K.

When comparing the adsorption-desorption isotherms at different pressures, the hysteresis pattern showed a positive deviation, which was attributed to the metastable state of the sorbent/sorbate system, and the adsorbate gas is not readily released to the corresponding thermodynamic equilibrium values (Busch et al. 2003). Figure 2.2 shows the CO_2 adsorption-desorption measurement carried out on a medium volatile bituminous coal at 22℃ and up to the pressure range of 5.1 MPa. The plot in Figure 2.2 depicts the general pattern of the CO_2 adsorption-desorption isotherm pattern upon varying equilibrium pressure range as reported in Busch et al. (2003).

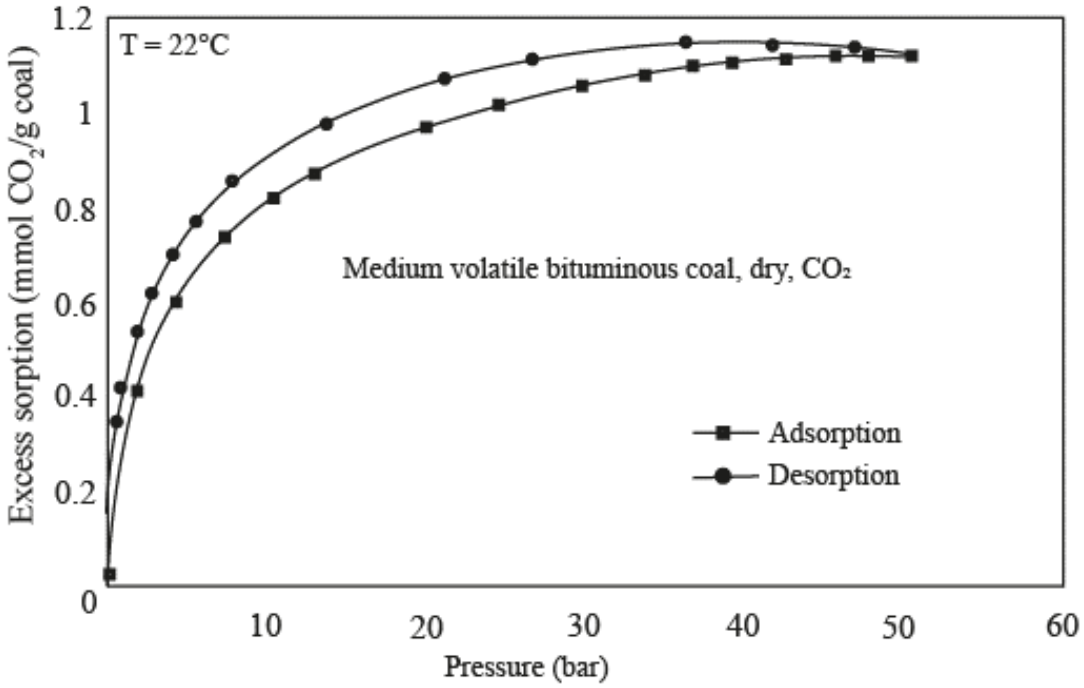

Figure 2.2. CO_2 adsorption-desorptiom isotherms of medium volatile bituminous coal at varying pressures (Busch et al. 2003).

Most of the previous studies were performed at higher temperatures to achieve super critical CO_2 (308.15 K, 318.15 K, 328.15 K and 377.15 K; Guan et al. 2003; Li 2010) and very limited works are available at lower temperatures (290.15 K and 298.15 K) (Mastalerz et al. 2004 and Day et al. 2008a). At lower temperatures, the bituminous coal showed an adsorption capacity of 24.6 m^3/tonne of coal (Mastalerz et al. 2004). The experimental and theoretical model fit of adsorption isotherms observed for a low rank coal at different temperatures are presented in Figure 2.3. In general, adsorption capacity increased upon decreasing temperature (Figure 2.3) (Guan et al. 2003).

Day et al. (2008a) explored the correlation between equilibrium pressure, CO_2 adsorption capacity, and coal swelling. Swelling increased up to 10 MPa in experiments conducted at pressure values ranging from 8 to 10 MPa, with no further swelling observed as CO_2 adsorption increased. At 6 MPa and 298.15 K, the observed volume expansion was approximately 1.5 percent of the void volume of the coal sample.

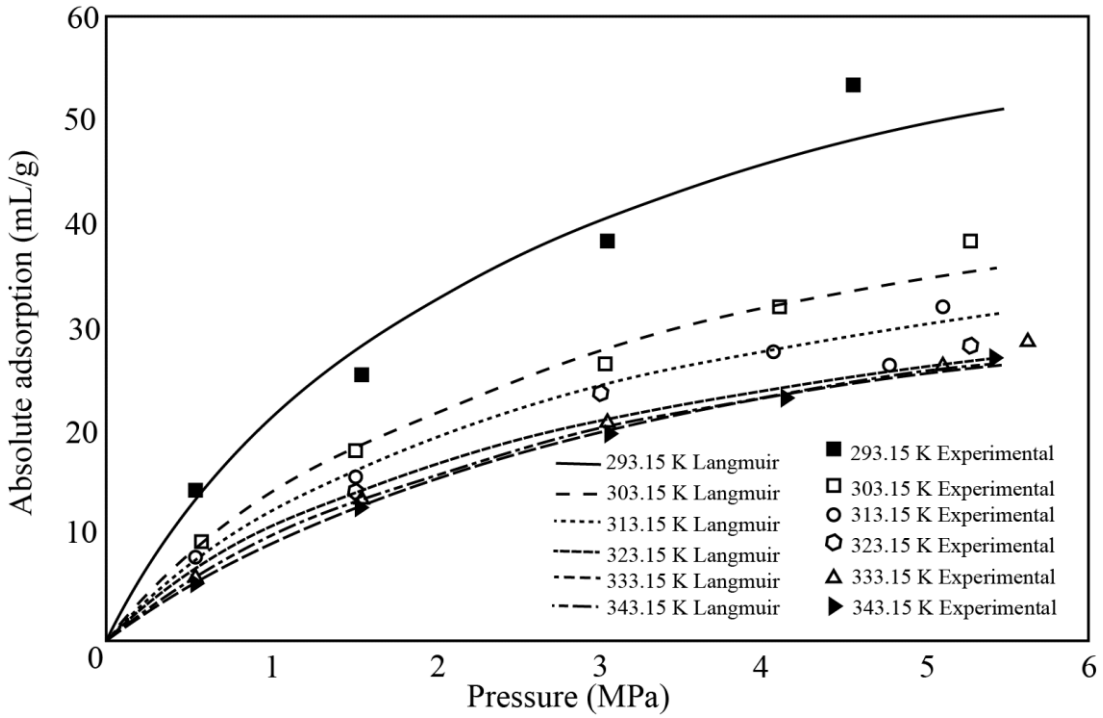

Figure 2.3. Adsorption isotherms of coal at varying temperatures (Guan et al. 2003).

Because CO_2 adsorption is a gas phase adsorption at coal seam depths where the temperature and pressure values are less than the critical parameters of CO_2 (31°C and 7.38 MP), the subcritical temperature/pressure adsorption behaviour of CO_2 is currently less understood (Bachu 2010). The density of CO_2 is extremely sensitive near the critical point (van der Waals loop region) of CO_2 (Eliot and Lira 2012), where the coexistence of the liquid and vapour phases of CO_2 would influence CO_2 adsorption in general and the calculations of adsorbed phase molar volume, and eventually the isotherm patterns (De Silva and Ranjith 2014). This is critical for estimating the amount of CO_2 adsorbed and comprehending the mechanism of CO_2 adsorption on coal. Furthermore, there are limited number of adsorption-desorption kinetic data at this temperature-pressure range (subcritical (6.1 MPa) near critical; 6.1 MPa to 6.49 MPa at 298.15 K) has been published.

2.3.3 Effect of coal rank and moisture

Adsorbed water may limit the mobility of adsorbed CO_2 (Day et al. 2008b and Gensterblum et al. 2014). A reduction in CO_2 adsorption capacity of coal has been found to be correlated with the amount of pre-adsorbed water on the coal samples (natural water content), with the reduction in adsorption capacity being greater for low rank coal and lower for high rank coal. Adsorption capacity has been shown to decrease by approximately 7.3 kg of CO_2/tonne of coal for every 1% increase in water content of the coal sample (Day et al. 2008b).

Figure 2.4 presents the adsorption isotherm of various coal rank samples (lignite, sub-bituminous and high volatile bituminous). In general, adsorption capacity reduced upon increasing moisture content (Figure 2.4; Ozdemir and Schroeder 2009). The simple volumetric expulsion of adsorbate (CO_2) by water molecules explains the loss of adsorption capacity. The water molecules that are adsorbed on the polarised sites on the coal surface have a high heat of adsorption and displace the CO_2 molecules (Day et al. 2008b). However, the CO_2 molecules can penetrate into the moist coal and remove the water. Figure 2.5 correlates the amount water expelled upon 1 mol of CO_2 adsorbed with coal ranks (%C = carbon content) (Ozdemir and Schroeder 2009). It can be seen from the Figure 2.5 the water expulsion is higher in low rank coal so the adsorption capacity higher than the high rank coal. The correlation of water expulsion, adsorption capacity and coal rank was further investigated by Gensterblum et al. (2013) using dried and moisture-equilibrated powdered bituminous and anthracite coal samples at temperatures of 45°C, 61°C and 76°C (318 K, 334 K and 350 K) at pressure up to 20 MPa. It was found that moisture had a decreasing effect on CO_2 adsorption capacity as coal rank increased, which was related to the presence of carboxylic functional groups and oxygen content.

Other experimental results, however, showed that CO_2 prefers H_2O sites (CO_2 competes with water), particularly in bituminous coal (Pone et al. 2009). According to a nuclear magnetic resonance study, CO_2 dissolves in capillary water and enters the coal matrix. The mass of water replaced by CO_2 was related to the Langmuir

adsorption capacity of CO_2 and increased as the adsorption capacity increased (Sun et al. 2015).

When comparing the dry samples with moisture equilibrated coal samples, the excess adsorption capacity of moisture equilibrated coals was 0.8 to 1.2 mmol of CO_2/g of coal, which was 17% lower than the adsorption capacity of dry coal samples (Weigner et al. 2012). According to Wang et al. (2011), the amount of CO_2 adsorbed in wet coal was reduced by 69 % to dry coal (0.45 mmol/g of dry coal and 0.14 mmol/g of wet coal). Vábová et al. (2012) discovered a similar effect in high volatile bituminous coal samples. Wang et al. (2007), Lee et al. (2013), and Pan et al. (2010a) highlighted the importance of moisture content and site conditions on CO_2 adsorption characteristics on coal.

Sudibandriyo et al. (2003) and Goodman et al. (2006) emphasised that the presence of water in coal samples influenced the physical structure of the coal and its CO_2 adsorption behaviour, and that this effect warrants further investigation. Zhang et al. (2019) investigated the effect of water on intact coal using constructed coal specimens. There is a scarcity of data on the adsorption of CO_2 on wet intact coal samples. Some coal seams are naturally wet, and flowing groundwater has been discovered in some of them (Sadasivam et al. 2019). As a result, additional research on the adsorption characteristics of large intact coal samples with varying water content was required.

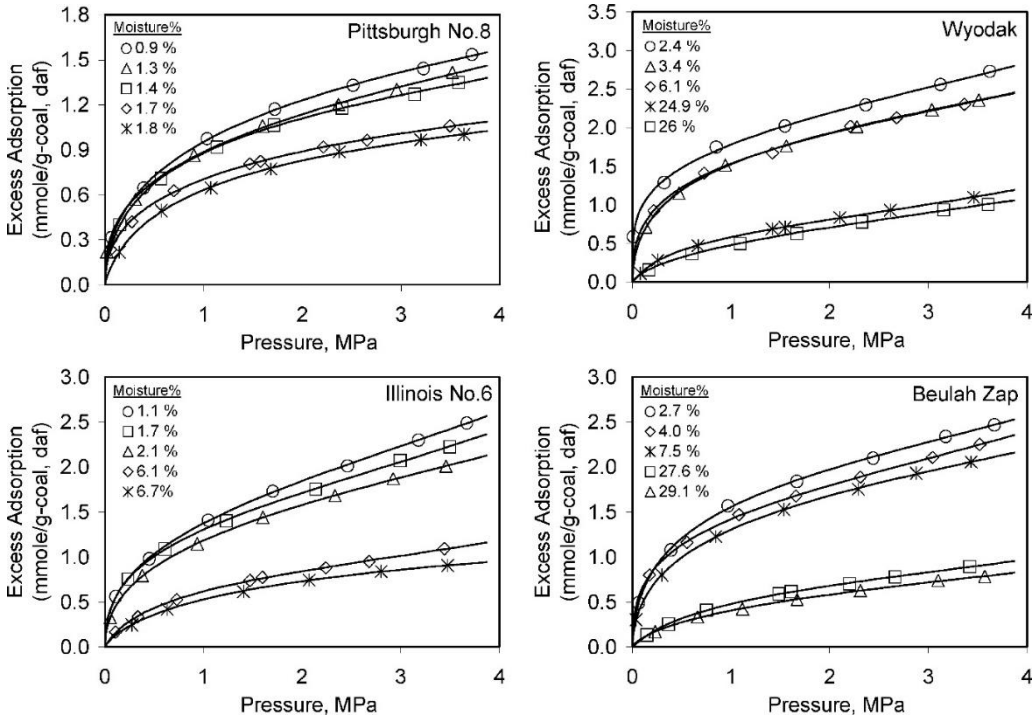

Figure 2.4. Comparision of moisture effect on adsorption capacities of various coal ranks (Pittsburgh No.8 = high volatile bituminous, Wyodak = subbituminous, Illinois No.6 = high volatile bituminous and Beulah Zap = lignite) at vaious pressures (Ozdemir and Schroeder 2009).

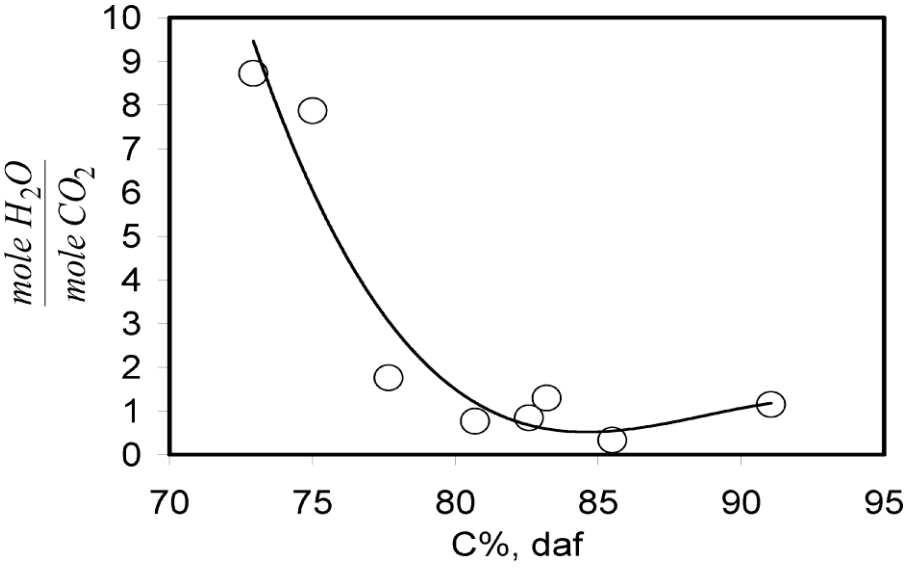

Figure 2.5. Schematic of the volume expulsive behaviour upon one mole of CO_2 adsorbed as the coal rank varies (C% carbon content; Ozdemir and Schroeder 2009)

2.3.3.1 Water retention characteristics of coal

The coal seams are naturally filled with water, and the moisture content decreases with increasing coal rank (Rajput and Thakur 2016). The high-water content of low rank coals is due to the high number of functional groups and polar groups found in low rank coals. Water molecules form hydrogen bonds with the functional groups on the coal surface. The higher the amount of polar functional groups such as OH-, carboxyl (COOH), methoxy (-OCH3), and carboxyl (C=O) groups present in bituminous coal, the more hydrophilic it is (Mahajan and Walker 1971; Allardice and Evans 1971; Nishino 2001; Qi and LaVan 2005; Miura et al. 2005; Kodigolu and Varamaz 2003). The carbon-containing groups mentioned above decompose and increase the carbon content of high-rank coal while decreasing its hydrophilicity (Stach et al. 1982; Allardice 1991; Olayinka 1993; Murata 2000; Allardice et al. 2003; Charriere and Behra 2010).

Increased water adsorption on the coal surface increases with water relative pressure and temperature (Charriere and Behra 2010; vábová et al. 2011). Water adsorption energy on coal-based carbon material was found to be approximately 21 kJ/mol (Salame et al. 1999), which is attributed to the energy of physical adsorption. This water holding capacity of coal can vary with coal rank and has a significant impact on how CO_2 is adsorbed on the coal surface.

The availability of pores in bituminous coals increases water retention capacity, whereas the decomposition of functional groups in anthracite coal blocks pores and reduces water retention capacity (Kaji 1986). The study of the water retention characteristics of coal under varying water content would provide insight into the water holding capacity of the coal samples at the elevated pressure ranges (Ferrari et al. 2014) . The relationship between the suction and water content of soils has been studied using Chilled-mirror water potentiometer (WP4C) apparatus (Leong et al. 2003; Tripathy et al. 2021; Ferrari et al. 2014; Moghadam et al. 2020).Water retention behaviour was only examined for soils and there is no literature available on water retention on coal. As a result, the current study attempted to obtain water retention characteristics of intact and powdered coal samples at varying moisture content and correlate the adsorption capacity with CO_2 adsorption isotherms obtained

from moist and dry anthracite and bituminous coal specimens at varying pressure ranges.

The dissolution of CO_2 on adsorbed water can increase the carbonic acid content and possibly dissolve the mineral content in coal, particularly alkaline (Ca, Na, K, and Mg bearing) minerals. This process would result in the mineralisation of CO_2 with calcium as $CaCO_3$ (Massarato et al. 2010). Investigating the phenomenon further would provide information to correlate with the adsorption capacity obtained from moist coal samples.

2.3.4 CO_2 adsorption-desorption hysteresis

When the amount of CO_2 adsorbed at a given equilibrium pressure during the adsorption process is not equal to the amount adsorbed at the same equilibrium pressure during desorption, the adsorption-desorption isotherm exhibits hysteresis. The typical hysteresis observed for CO_2 adsorption-desorption isotherms is depicted in Figure 2.6 (a) (Ren et al. 2022). The filling and emptying of adsorbates in and out of adsorbent pores and fractures is also associated with hysteresis loops. The observed positive deviation (hysteresis) indicates that the adsorbed CO_2 was not easily released from the coal's pores or microfractures (Wang et al. 2014).

The positive hysteresis gap was attributed primarily to the porous structure of the specific coal (Ren et al. 2022). Harpalani et al. (2006) demonstrated that the linear increase in the CO_2 adsorption isotherm is caused by pore condensation and CO_2 diffusion in the coal structure. The observed adsorption-desorption hysteresis pattern was also attributed to the coal matrix shrinking/swelling (Busch et al. 2003; Ozdemir et al. 2004; Harpalani et al. 2006; Pan et al. 2010; Dutta et al. 2011). Other factors such as equilibrium pressure, temperature, and water content all have an impact on the type of hysteresis pattern observed (Wang et al. 2014; Busch et al. 2003).

Figure 2.6 (a) shows the adsorption-desorption hysteresis observed for two different types of coals by Ren et al. (2022). It can be seen that the hysteresis observed for the low rank coal had a higher positive index than the high rank coal, implying that the pore structure determines the desorption pattern observed. Figure 2.6 (b) illustrates

the likely adsorption mechanisms of CO_2 that reflect the hysteresis pattern observed. Ren et al. (2022) defined the pore trapping mechanisms such as pore blockage, gas cavitation, adsorption induced deformation, and pore network effect (ink bottle effect) that affect the hysteresis pattern.

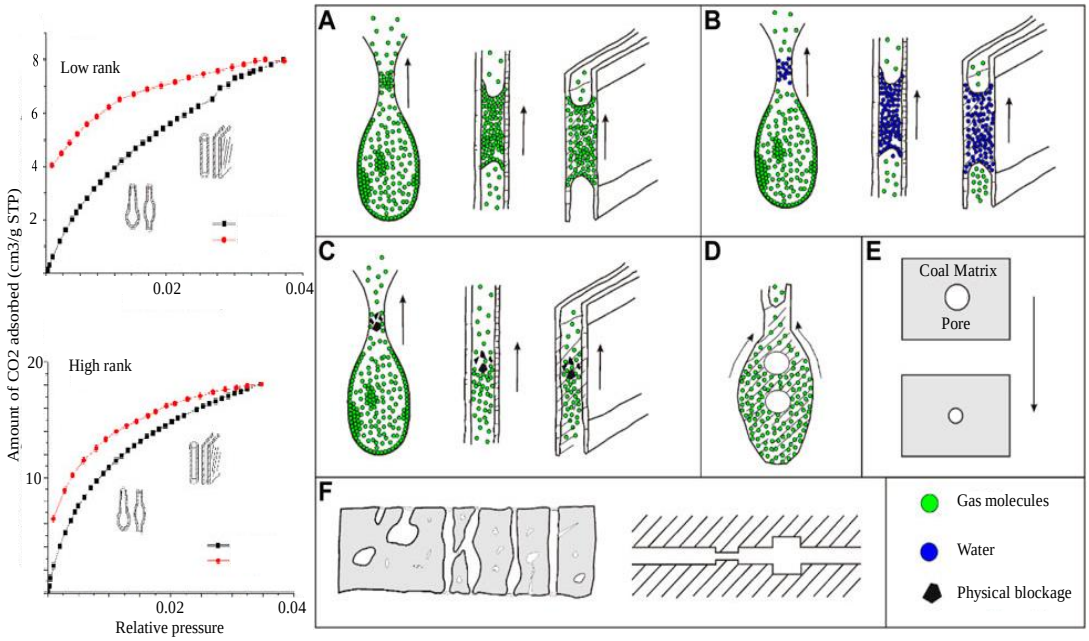

(a) (b)

Figure 2.6. (a) Adsorption-desorption hysteresis pattern observed for two different rank coaland (b) Likely adsorption mechanisms that reflects on the hysteresis pattern; pore blockage (A-C), gas cavitation (D), adsorption induced deformation (E) and pore network effect (F) that affects the hysteresis pattern (Ren et al. 2022).

2.3.5 CO_2 adsorption kinetics

The kinetics of CO_2 adsorption are critical for extrapolating laboratory data to the field. The kinetics of CO_2 adsorption were investigated by measuring the time versus pressure decay or amount of CO_2 adsorbed. Gruszkiewicz et al. (2008) compared the CO_2 adsorption kinetics to the methane adsorption kinetics and found that CO_2 adsorption on a water saturated coal was faster than CH_4 adsorption and that water saturation reduced the CO_2 adsorption rate. Li et al. (2010) investigated the CO_2 adsorption kinetics of powdered bituminous and anthracite coal samples using

manometric adsorption. The experiments were conducted at temperatures of 308 K, 318 K, and 328 K and pressures ranging up to 25 MPa and demonstrated that the adsorption kinetics were not temperature dependent.

Pseudo-first-order (PFO) and pseudo-second-order (PSO) kinetic models have been widely applied and are well suited for predicting CO_2 physical adsorption on coal (Alvarez-Gutierrez 2017). Among the two dominant models, the PSO model fit the experimental data the best. Shi et al. (2020) compared experimental data to the PSO model for an intact bituminous coal sample using the manometric adsorption experiment method at pressures up to 5 MPa and temperatures of 298.15 K, 308.15 K, and 318.15 K. The experiments corroborated the model well (Figure 2.7 (a) and (b)).

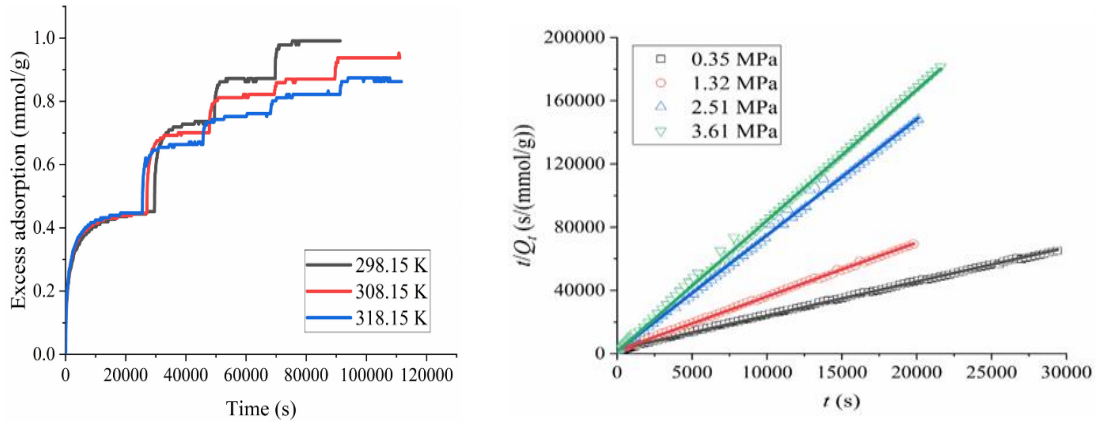

Figure 2.7.(a) Kinetic data of CO_2 adsorption on a bituminous coal measured using manometic adsorption aparatus, and (b) experimetal data fitted in PSO model (Shi et al. 2020).

Attempts have been made to develop a new kinetic equation to demonstrate that pore diffusion determines the rate of CO_2 adsorption on coal samples (Marecka and Mianowski 1998). Hou et al. (2020) investigated the CO_2 adsorption kinetics and hysteresis of powdered samples of bituminous coal using the manometric/volumetric experimental method. The study demonstrated the physical meaning of the PSO model by demonstrating the CO_2 adsorption process (the rate limiting factor) on coal, as well as the hysteresis pattern of adsorption-desorption. The study explained how the

hysteresis pattern correlated with the CO_2 adsorption kinetics, revealing CO_2 pore diffusion/condensation as the rate limiting factor.

There have been very few studies conducted to investigate the desorption kinetics. The experiments on the desorption kinetics indicated the CO_2 pore trapping capabilities of bituminous coal samples. A significant amount of CO_2 gas molecules remained in the coal structure (Figure 2.8) (Majewska et al. 2009). Desorption kinetics can also be used to investigate the reversibility of pore-trapped CO_2 as well as evidence of pore diffusion and condensation.

Based on the information gathered, it is more appropriate to consider the PFO and PSO models to compare the experimental results of CO_2 adsorption on coal samples and use the models to correlate with hysteresis patterns to understand the influence of pore diffusion and condensation on CO_2 adsorption on coal as defined in the IUPAC description of isotherm patterns (De Boer 1958; Sing et al. 1985; Majewska et al. 2009). There is limited information available on the desorption kinetics data fitted into PFO and PSO models. Yet, modified PFO and PSO equations (Njikam and Schiewer 2012) are available to represent the desorption kinetics. Therefore, the reversibility of the pore trapped CO_2 and the rate determining step for the desorption can be predicted by using the modified PFO and PSO models. The mathematical forms of the PSO and PFO models are presented in Chapter 3, section 3.5.

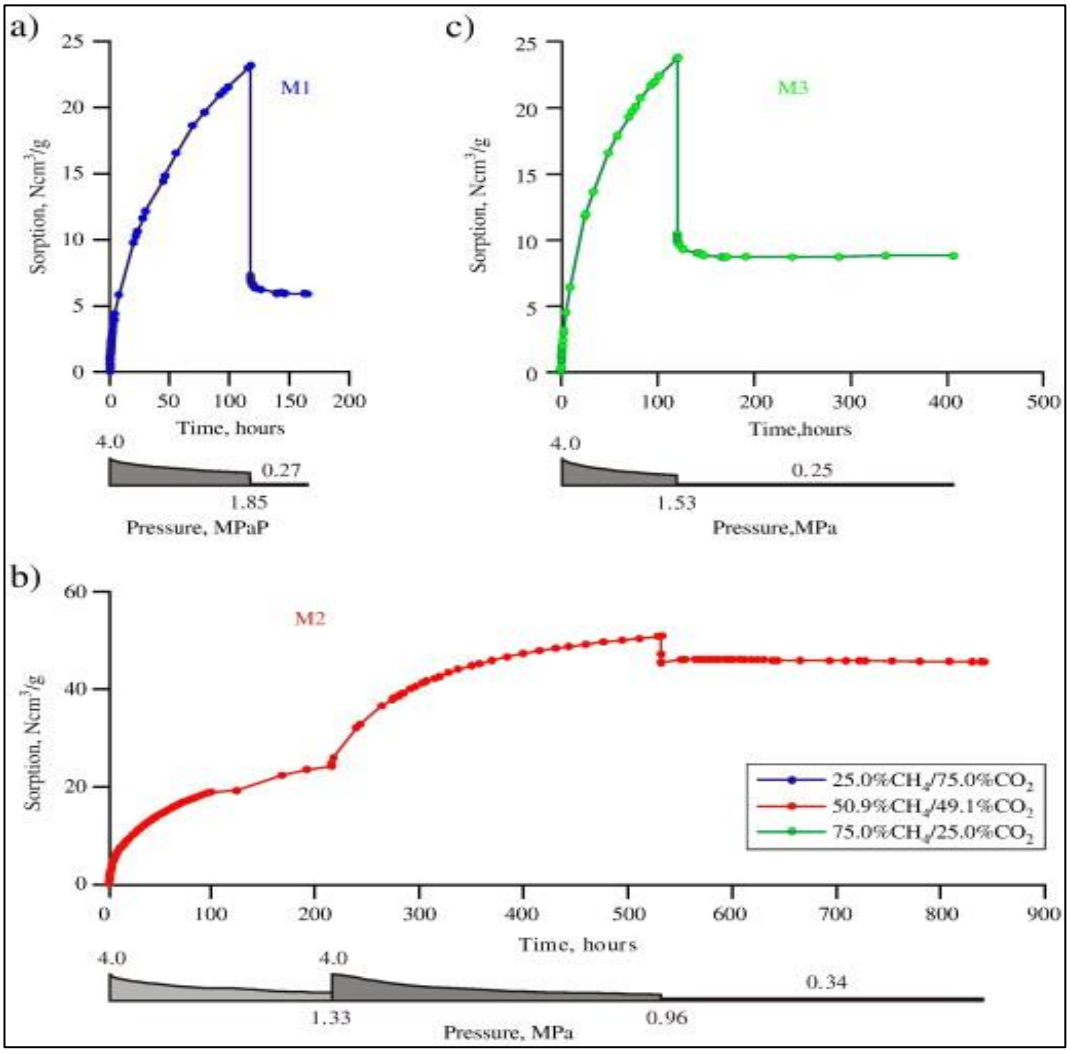

Figure 2.8. Adsorption desorption kinetics of CO_2 on bituminous coal. The drop and straight line show the desorption section and the corresponding value shows the volume of CO_2 remaining in the sample (Majewska et al. 2009).

2.4 CO_2 adsorption on caprocks

The CO_2 adsorption capacity of the rocks has been studied in the context of geological CO_2 storage potential. The rock strata overlaying the un-mineable coal seams consist of sandstone and mudstone formations. Quartz is the primary mineral composition of the sandstone with a small proportions of clay minerals (e.g., bentonite and kaolinite). Thus, studying the CO_2 adsorption capacity of rock samples, sand and

clay minerals would improve the current knowledge on CO_2 storage in un-mineable coal seams. This section reviews the literature on the CO_2 adsorption capacity of rock, sand, and clay minerals.

2.4.1 CO_2 adsorption on rock

The CO_2 gas can permeate, trapped in the porous structure of the rock, chemically interact with water, and adsorbed on the rock minerals (DePaolo 2013). Sedimentary rocks showed considerable CO_2 adsorption capacity which was influenced by various biogeological conditions such as depth, clay content, mineral composition, water content, and biofilm content (Botan et al. 2010; McGrail et al. 2009; Kwak et al. 2011; Loring et al. 2011; Shao et al. 2011; Tokunaga and Wan 2013; Kanihira et al. 1987; Enomoto et al. 1997; Zhang et al. 2006). In general, physical adsorption of CO_2 on rock samples observed with Langmuir type isotherms (Tajnik et al. 2012; Jedli et al. 2016; Fakher and Imqam 2020).

2.4.2 CO_2 adsorption on sand

In terms of CO_2 adsorption on sand, atomic simulation studies revealed that CO_2 adsorption on the silica surface is affected by pore structure and pore network accessibility. CO_2 confinement in silica pores can increase the density of the adsorbed phase (Melnichenko et al. 2010; Cole et al. 2010; Kim et al. 2010; Cole et al. 2010; Rother et al. 2012). When exposed to humid conditions, the hydrophilic nature of silica affects CO_2 adsorption on rocks by forming thin films of water on the mineral surface (McGrail et al. 2009; Kwak et al. 2011; Loring et al. 2011; Shao et al. 2011; Tokunaga and Wan 2013). However, the effect of sand's dry or wet state on adsorption capacity has not been clearly explained in available experimental research. Numerous molecular simulation studies revealed that the adsorbed water film on silica has a high isosteric heat of adsorption and a low diffusivity, which influences CO_2 adsorption on sandstone bearing rocks (Wensink et al. 2000; Rahaman et al. 2008; Malani and Ayappa 2009; Kerisit et al. 2012). The paucity of data available from experimental simulations of CO_2 adsorption on dry and wet sand makes it an area that needs to be

explored through experimental investigations that focus solely on adsorption properties.

2.4.3 Biofilm influence on the CO_2 adsorption on sand

The formation of biofilms on the mineral surfaces of rocks can have an impact on the interaction of CO_2 with the minerals. The mechanism by which CO_2 reacts with the biofilm can influence the adsorption characteristics of rock minerals. Baseline studies at potential CO_2 reservoirs have confirmed naturally occurring microbial activities, which have implications for the fate and transport mechanism of CO_2 at potential GCS sites (Morozova et al. 2010; Lavalleur and Colwell 2013; Peet et al. 2015).

The supercritical nature of CO_2 can be used to disinfect microorganisms. Biofilms formed by *Bacillus mojavensis* bacteria, on the other hand, can withstand supercritical CO_2. *Bacillus mojavensis* is the native microorganism found in the sandstone cores from coal field and can withstand high pressure conditions (Kanihira et al. 1987; Enomoto et al. 1997; Zhang et al. 2006; Mitchell et al. 2009). The results of the experiments revealed that *Bacillus mojavensis* was more CO_2 resistant than any other microbe (Mitchell et al. 2008). This finding highlights the importance of conducting additional experiments on *Bacillus mojavensis* biofilm-loaded sand samples at various pressure ranges to examine the impact of the biogeochemical nature of the rock strata on CO_2 adsorption capacity.

2.4.4 CO_2 adsorption on bentonite and kaolinite

CO_2 adsorption capacity of bentonite and kaolinite is influenced by numerous factors, including interlayer exchangeable cations, saturation state, the charge on the clay surface, and interlayer distance (Jin and Firoozabadi 2013; Lin et al. 2013; Zhang 2016; Volzone and Ortiga 2004; Rutherford et al. 1997). CO_2 adsorption in clay nanopores has been studied primarily in the absence of water (Wang et al. 2003). The amount of CO_2 trapped in Na-montmorillonite by a single layer of adsorbed water is

dependent on the density of the CO_2 in the bulk fluid. Figure 2.9 illustrates the mechanism of CO_2 adsorption in the interlayer spacing of Na-montmorillonite. Due to the swelling properties of hydrated clay, CO_2 penetration into nanopores was slowed because the adsorbed cations were not completely solvated by the CO_2 and remained close to the surface (Figure 2.9) (Yang and Yang 2011).

Botan et al. (2010) used molecular simulations to investigate the CO_2-water-montmorilonite interaction and discovered that CO_2 enters the water saturated clay nanopores through diffusion and dissolution due to the water holding capacity of the clay. Furthermore, experimental results show that CO_2 adsorption is affected by the initial water content of the clay minerals. CO_2 adsorption experiments on montmorillonite were conducted at elevated temperatures and pressures (318 K, 328 K; up to 12 MPa) (Jeon et al. 2014). The kaolinite experiments were carried out at very low-pressure range (0.1 MPa) (Chen and Lu 2015) and the maximum CO_2 adsorption was obtained at 298.15 K.

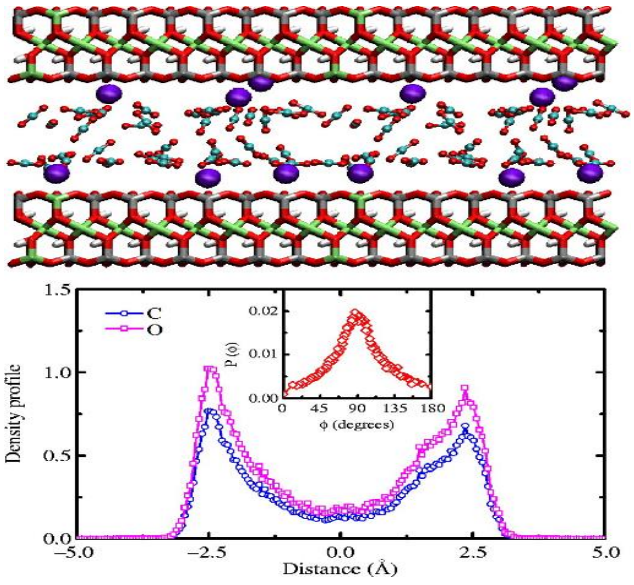

Figure 2.9. Molecular simulation of CO_2 in the interlayer spacing of a two-layer hydrated (basel spacing of 17.4Å) Na-montmorillonite. The violet balls are Na^+ cations remain at the surface and the ball and stick inside the layer represents the CO_2. The image below shows the density of CO_2 from the surface (Yang and Yang 2011).

2.5 Adsorption principles for CO_2 adsorption on coal

Adsorption is a vital process that is used in gas retention and storage, liquid purification, environmental protection, and solid-state reactions (Debrowski 2001). Adsorption is a surface phenomenon; it is a separation process in which specific molecules from a fluid phase are transferred to the surfaces of solids (Ruthven 1984 and Smith et al. 2004). In simple gas adsorption, small uncharged gas molecules accumulate at the solid-gas interface (Figure 2.10).

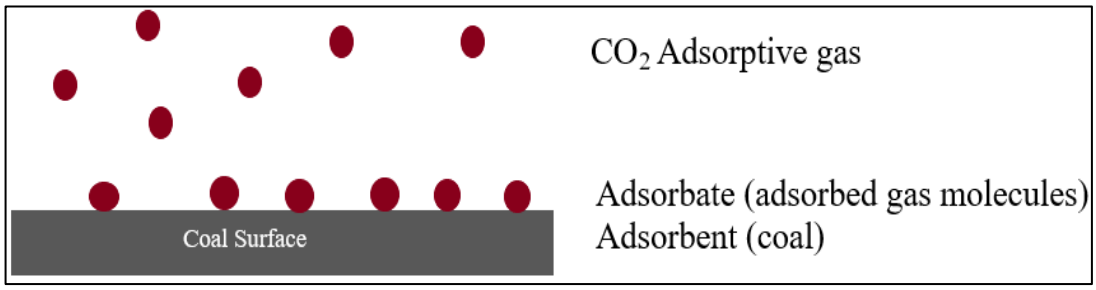

Figure 2.10. Schematic of the adsorption process.

The gas molecules that have been adsorbed are referred to as adsorbates (accumulated on a solid surface). The adsorbates accumulate in single molecule layer or multilayers (Figure 2.11). The gas molecules that will be adsorbed are referred to as adsorptive gas (gas phase; before they accumulate on the surface). The solid surfaces (e.g., coal) are referred to as adsorbents in this study (Figures 2.10 and 2.11) (Rouquerol et al. 2013 and Tien et al. 2019). Table 2.1 summarises the key definitions presented in the literature which are used in the current study to describe adsorption process.

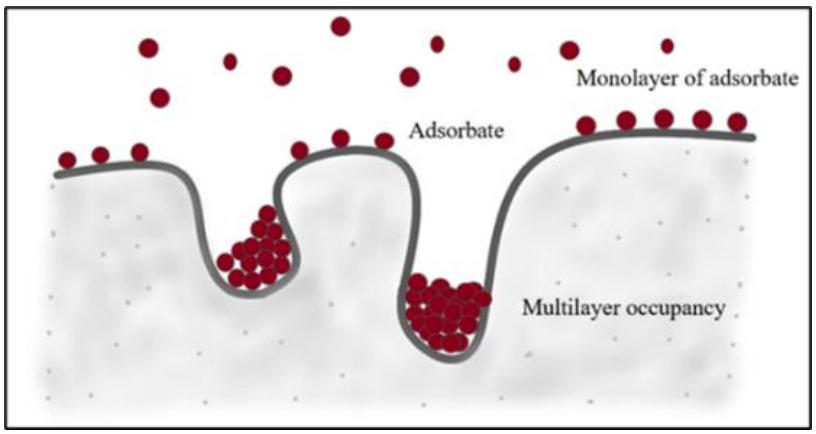

Figure 2.11. Schematic of the gas adsorption process (mono and multilayer occupancy assumptions).

Adsorption of gas molecules on solid surfaces is caused by physical forces of attraction such as van der Waals/London dispersion attraction forces and is referred to as physical adsorption. Physical adsorption has an energy range of -20 kJ/mol to -40 kJ/mol. Adsorbate can diffuse through the porous structure of the adsorbents in gas adsorption. Physical sorption achieves equilibrium between the adsorbed and gas phases quickly and, more importantly, it is reversible. However, the reversibility of adsorbed gas molecules in porous and micro fractured solid adsorbents is a partial or slow process. Chemical sorption, on the other hand, is irreversible and defined by a specific chemical reaction at a specific site. The adsorption energy varies between -100 and -400 kJ/mol (Ralph 1987 and Butt et al. 2003).

The adsorption process is examined in this study from the standpoint of CO_2 adsorption on coal. The key question is how many CO_2 molecules are adsorbing on the surface of coal. In general, the amount adsorbed varies with temperature. At constant temperature, the amount of gas adsorbed by a known mass of solid adsorbent is determined by the equilibrium pressure. When the temperature is constant, a plot of the amount of CO_2 adsorbed/kg of coal versus the corresponding equilibrium pressure in the gas phase gives a better overview of the gas adsorption process. The gas adsorption isotherm is the plot of the amount adsorbed versus the equilibrium pressure (Figure 2.12) (Freundlich 1909).

Table 2.1. Definitions of the terminology used in gas adsorption process.

Terminology	Definitions
Adsorption	Accumulation of one or more gas molecules at the solid-fluid interface (CO_2 in the current study).
Adsorbate	Gas (CO_2) molecules in the adsorbed state.
Adsorbent	Solid adsorbents on which adsorption occurs. Coal is the adsorbent in the current study.
Physical adsorption (Relevant to gas adsorption)	Adsorption by physical attraction forces such as the van der Waals/London dispersive force of attraction. Adsorption occurs in the absence of chemical bonding.
Chemical adsorption	Adsorption involving chemical bonding between adsorbate and adsorbent.
Monolayer	On a solid surface (coal), a single layer of adsorbed gas (CO_2) molecules.
Multilayer	There are multiple sites available, and the gas can reach a high enough pressure to form liquidlike layers of adsorbate at the interface.
Specific surface area	Available surface area for the specific gas molecule (CO_2) based on the cross-sectional occupancy of the molecule.
Adsorbed phase	Describes the state of the fluid molecules that have been adsorbed.
Adsorbed phase density	Adsorbed phase molar density (mol/m^3) is the number of moles retained in a specific volume at the solid-fluid interface at a given pressure and temperature.
Adsorbed phase molar volume	Specific volume occupied by moles retained at the solid-fluid interface (m^3/mol) at a given pressure and temperature. Reciprocal of the molar density of the adsorbed phase.

The IUPAC (International Union of Pure and Applied Chemistry) classifies many experimentally derived isotherm shapes. The different types of isotherm shapes can be found in early literatures on adsorption of van der Waals gases on solid surfaces (Figure 2.12) (Brunauer 1940; Sing et al. 1985; Thommes et al. 2015). The gas adsorption behaviour is generally explained by a combination of one or more types of isotherms.

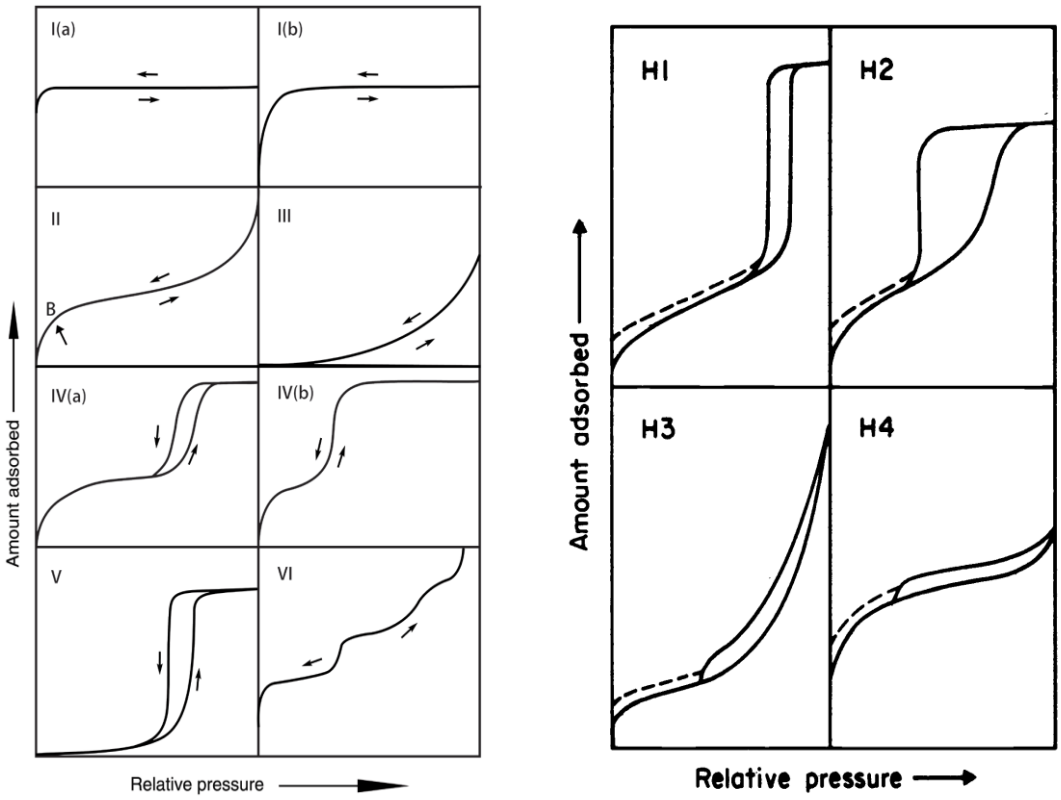

Figure 2.12. Classification of physical sorption isotherms and hysteresis loops by IUPAC as presented in Thommes et al. (2015) and Sing et al. (1985).

Type I (a and b) has a concave pattern, rising steeply at low pressures and plateauing. The adsorption capacity is limited by the adsorption sites in this type of adsorption, and the indication of the limited area of pores and surface area is commonly referred to as monolayer adsorption type.

Type II has a concave pattern in relation to relative pressure and becomes linear and convex as pressure increases. This type is observed when the density of the adsorbed layer approaches that of a liquid or solid. If a sharp knee is observed (the inflection point marked as B in the type II pattern in Figure 2.12), it is thought to

indicate that the monolayer has been completed and that multimolecular adsorbed layers have formed.

Type III has a convex pattern with no inflection point, indicating unfavourable adsorption and is uncommon.

Adsorptions of type IV a. and IV b have been observed with mesoporous adsorbents. These patterns are caused by the adsorbate's pore filling and condensation.

Type V isotherms were observed due to the adsorbent's weak interaction with the adsorbate.

Type VI isotherm usually shows the different mechanisms of adsorption at diverse pressure ranges.

Adsorption isotherms are obtained experimentally by gradually increasing pressures and measuring the amount adsorbed at relevant equilibrium pressures. Desorption experiments can also yield the adsorption isotherm pattern. Following the completion of the adsorption tests, the desorption isotherms were obtained by lowering the pressures and measuring the amount of gas adsorbed. During desorption tests, the amount of adsorbed gas molecules generally traces back on the isotherm pattern. Adsorption-desorption hysteresis occurs when the amount of gas adsorbed during adsorption does not match the amount adsorbed during desorption (Sing et al. 1985 and Thommes et al. 2015).

The physical nature of the adsorbent and the adsorption process are responsible for the different types of adsorption hysteresis. Figure 2.12 depicts the IUPAC classification of adsorption-desorption hysteresis. When condensation occurs in adsorbents with a narrow range of uniform mesopores, the type H1 loop is observed (ink bottle type pores). Type H2 pore structures are more complex and are caused by pore-blocking and delayed condensation in pore necks. The two types of H3 loops that are similar to the type II isotherm are frequently found at slit-like pores. Type H4 hysteresis loops are frequently associated with narrow slit-like pores containing adsorbents, but they are also related to the type I isotherm (Sing 1985). As stated above, the original four types have been extended and further classified by IUPAC and are presented in Thommes et al (2015).

According to the reported CO_2 adsorption isotherm patterns derived from coal samples, the CO_2 adsorption process can be explained by a combination of type I (monolayer) at low and intermediate pressures and type II (multilayer type) with H1 and H3 hysteresis loops at elevated pressures. (Harpalani et al. 2006; Ozdemir et al. 2004; Zutshi and Harpalani 2004; George and Barakat 2001 and Harpalani 1995).

Equations were developed for a better understanding of monolayer and multilayer isotherms, and they are based on a specific theoretical model. Langmuir (1915, 1916, 1917, and 1918) published the most important theory, which explains type I monolayer adsorption. Brunauer et al. (1938) published the BET model to consider vapour and liquid like adsorption (type II multilayer adsorption type).

Other theories, in addition to the Langmuir and BET theories, have been considered to construct characteristic curves to explain CO_2 gas adsorption on coal. The background literature is discussed in sections 2.5.3 and 2.5.4 and is detailed in Chapter 3.

2.5.1 Langmuir isotherm model

The Langmuir model assumes that the adsorbent surface has a certain number of sites per unit area (A), mol/$m^{2,}$ or 1/m^2 (Figure 2.13).

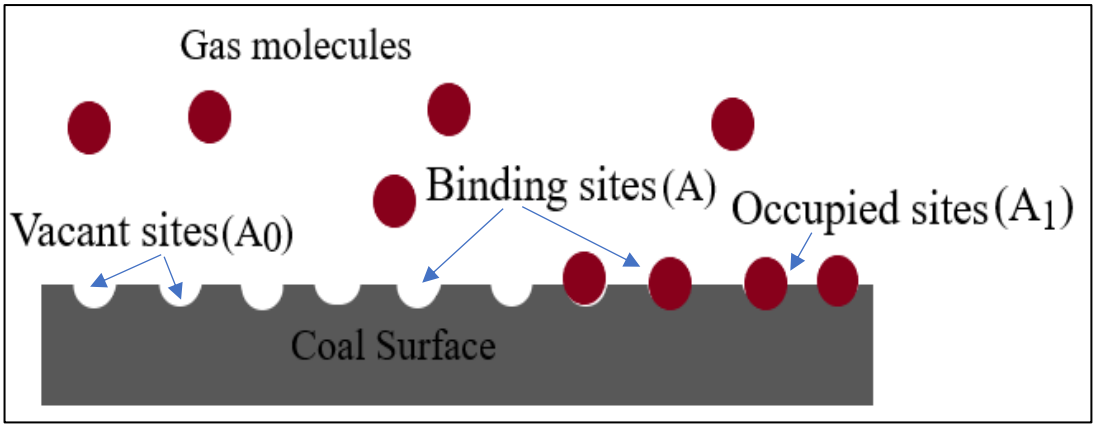

Figure 2.13. Representation of the Langmuir model.

If the adsorbents occupy A1 of the binding sites, the vacant sites are A_0 = A-A_1. According to Langmuir's (1915) kinetic theory of adsorption, the rate of adsorption is proportional to the number of vacant sites and the corresponding equilibrium gas phase pressure (Equation 2.5).

$$Rate\ of\ adsorption\ r_a = k_{ad} P_{eq} (A - A_1) \qquad (2.5)$$

Meanwhile, the rate of desorption is proportional to the adsorbed molecules or occupied sites (A_1) (Equation 2.6).

$$rate\ of\ desorption\ r_d = k_{de} A_1 \qquad (2.6)$$

where k_{ad} and k_{de} are the adsorption and desorption rate constants, respectively. A and A_1 can be replaced by the maximum amount of gas that can be adsorbed on the adsorbent (m_∞- Langmuir maximum capacity, mole or g of adsorbate/kg of coal) and the equilibrium amount adsorbed (m_{eq}) at a relative equilibrium pressure, respectively.

At equilibrium, the rate of adsorption (r_a) and rate of desorption (r_d) are equal, Equation (2.7)

$$r_a = k_{ad} P_{eq} (m_\infty - m_{eq}) = r_d = k_{de} m_{eq} \qquad (2.7)$$

Solving the Equation (2.7) for the equilibrium amount adsorbed (m_{eq}); Butt et al. 2003a), Equation (2.7) becomes Equation (2.8) or (2.9), the non-linear Langmuir model.

$$m_{eq} = m_\infty \frac{k_{ad} P_{eq}}{k_{de} + k_{de} P_{eq}} \qquad (2.8)$$

$$m_{eq} = m_\infty \frac{bp}{1 + bp} \qquad (2.9)$$

where b is Langmuir constant = k_{ad}/k_{de} (adsorption constant over desorption), Langmuir parameter b is also reciprocal of half-loading pressure (Pa^{-1}), P equilibrium

pressure (Pa), m_∞ is limiting value of mass adsorbed at a constant temperature, also the mass of a maximum monolayer adsorbate covering the surface of the sorbent (mol or g/kg), and m_{eq} is mass adsorbed at given equilibrium pressure (mol or g/kg).

The Langmuir parameter b is related to the energy of adsorption. The energy of adsorption (ΔH_{ad}) and Gibbs free energy (ΔG_{ad}^{0}) of adsorption can be calculated based on the Langmuir parameter b obtained from fitting the experimental data in isotherm model using Equation (2.9) and the kinetic theory of adsorption (Equation 2.10 and 2.11) (Butt et al. 2003a). Gibbs free energy (ΔG_{ad}^{0}, kJ/mol) can be calculated using equation (2.12);

$$b = b_0 \exp\left(\frac{\Delta H_{ad}}{RT}\right) \tag{2.10}$$

$$b_0 = \frac{N_m \sigma_A \tau_0}{\sqrt{2\pi MRT}} \tag{2.11}$$

$$\Delta G_{ad}^{0} = -RTlnb^{-1} \tag{2.12}$$

where b_0 is the exponential factor (pa-1), b Langmuir constant or reciprocal of half-loading pressure (pa-1), ΔH_{ad} is energy of adsorption (J/mol), τ_0 is vibration period related to the residence time of the adsorbed CO_2 molecule (typically in the order of 10^{-13} s), N_m is Number of molecules adsorbed (related to m_∞ and the Avogadro's number), σ_A is cross sectional area covered by one CO_2 molecule (m^2), M is molecular mass of CO_2 (0.04401 kg/mol), R is universal gas constant (8.314 J/mol K), and T is temperature 298.15 K.

2.5.2 BET multilayer model.

Langmuir model is unrealistic for the liquid-like adsorbed phase density of the adsorbates, since the Langmuir isotherms are saturated at high pressures (type I). Brunauer et al. (1938) developed the BET model to overcome the shortcomings of the Langmuir model. The BET model isotherm equation derived for the multimolecular adsorption of gases which includes the Langmuir isotherm. The theory assumes that

the heat of the first layer (Q_1) has a specific value and the subsequent layers (Q_2) have the heats of adsorption values related to the condensation of the fluid (Figure 2.14).

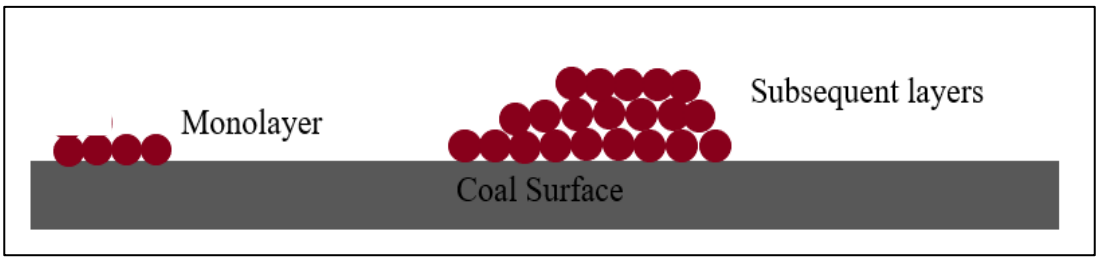

Figure 2.14. Representation of the BET model.

The BET model also assumes that adsorption and desorption are related to the corresponding layer. The kinetics of adsorption and desorption of monolayer is defined in Equations (2.13) and (2.14), which is theoritically the Langmuir isotherm.

Rate of adsorption to vacant surface sites is $r_{ad}^{1} = k_{ad}^{1} P_{eq} A_0$ (2.13)

At equilibrium rate desorption from the first layer is $r_{de}^{i} = a_1 A_1 e^{-Q_1/RT}$ (2.14)

At equilibrium, the rate of desorption from the first layer is equal to the rate of adsorption of the first layer. Similarly, for the i^{th} layer, rate of adsorption to the i^{th} layer is

$$r_{ad}^{i} = k_{ad}^{i} P_{eq} A_{i-1} \quad (2.15)$$

At equilibrium, rate desorption from the i^{th} layer is:

$$r_{de}^{i} = a_i A_i \, e^{-Q_2/RT} \quad (2.16)$$

where a_1 and a_i are the frequency factors related to the residence time of the gas molecules interacting with the surface, k_{ad}^{i} adsorption equilibrium constant, A_0, A_{i-1} and A_i are empty sites, monolayer occupancy, and i^{th} layer occupancy, respectively.

Equation (2.17) is obtained by solving the above equations for the amount adsorbed in layers.

$$\frac{\frac{P_{eq}}{P_0}}{n(1-\frac{P_{eq}}{P_0})} = \frac{1}{cn_{mon}} - \frac{(1-c)}{cn_{mon}} \times \frac{P_{eq}}{P_0} \quad \text{(or)} \quad n = \frac{n_{mon} c \frac{P_{eq}}{P_0}}{\left(1-\frac{P_{eq}}{P_0}\right)\left[1-(1-c)\frac{P_{eq}}{P_0}\right]} \qquad (2.17)$$

where n is amount adsorbed (mol), n_{mon} is number of moles to cover monolayer adsorption (mol), P is equilibrium pressure (Pa), P_0 is saturation pressure (Pa), c is dimensionless parameter related to heat of adsorption. The parameter c also related to the energy of adsorption ($c \approx e^{\left[\frac{Q_1 - Q_2}{RT}\right]}$), where Q_1 is the heat of adsorption on the bare surface (J/mol) and Q_2 is heat of adsorption for physisorption of the overlaying layers (heat of condensation) (J/mol).

The c and n_{mon} values were acquired from the plot of $\frac{\frac{P_{eq}}{p_0}}{n(1-\frac{P_{eq}}{p_0})} vs \frac{p}{p_0}$ or nonlinear regression analysis by fitting the experimental data into Equation (2.17) to validate the adsorption process. Figure 2.15 compares the typical Langmuir and BET adsorption isotherm shapes reported for experiments conducted for CO_2 adsorption on four bituminous coal samples (Harpalani et al. 2006).

There are very limited litrature available for experiments performed at 298.15 K. Since adsorption isotherms are temperature dependent, it is important to choose an appropriate model to evaluate the CO_2 isotherm. Most of the litrature explains the CO_2 adsorption by the Langmuir model. Wang et al. (2009), White (2005) and De Silva et al. (2012) fitted the CO_2 adsorption in the multilayer BET model.

Harpalani et al. (2006) Ozdemir. et al. (2004), Zutshi and Harpalani (2004), George and Barakat (2001) and Harpalani (1995) reported the adsorption isotherm and hysteresis for experiments conducted at 318.15 K and 328.15 K and indicated that the pore condensation, diffusion, and thermodynamic behaviour of CO_2 play a crucial part in the isotherm patterns.

Comparing the reported isotherms and the adsorption-desorption hysteresis of CO_2 on coal, obtained at 298.15 K, the CO_2 adsorption can be explained by type I (Langmuir model) and type II combining with H3 (Figure 2.12 and 2.15). In a molecular simulation study, Yang et al. (2016) observed a monotonic increase in the absolute adsorption isotherms at 298 K for all pore widths. The reported isotherms (Figure 2.15) depict the type II isotherm pattern which can be explained by BET model.

Furthermore, the current study conducted the experiment in the near critical region (van der Waals loop region) of the temperature isotherm (298.15 K) of CO_2 (Eliot and Lira 2012), where the coexistence of the liquid and vapour phases of CO_2 would influence the adsorption of CO_2 in general, as well as the calculations of adsorbed phase molar volume and, ultimately, the isotherm patterns (De Silva and Ranjith, P.G. 2014). This is critical for estimating the amount of CO_2 adsorbed and comprehending the mechanism of CO_2 adsorption on coal.

Further reviews were conducted based on the gathered knowledge from the literatures on the fundamental behaviour of CO_2 at 298.15 K to devise a calculation method to produce the adsorption isotherm for near critical region adsorption (6.1 MPa to 6.4 MPa) and presented in section 3.3.4 of Chapter 3.

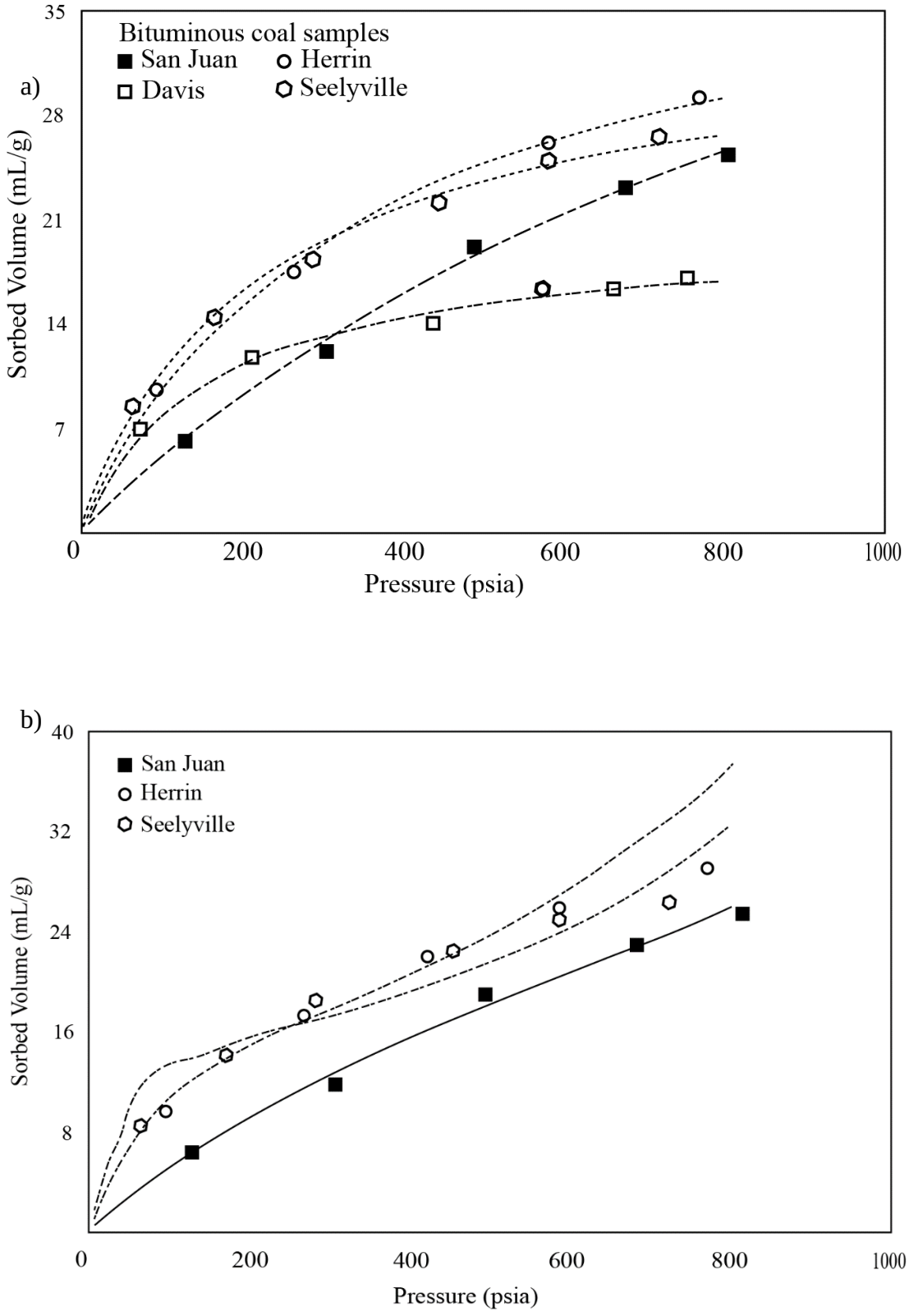

Figure 2.15. Typical (a) Langmuir and (b) BET models compared with experimental isotherms (Harpalani et al. 2006).

2.5.3 CO_2 adsorption characteristic curve based on P-V-T behaviour

A characteristic curve was developed on the assumption that the molar volume of CO_2 adsorbed varies with changing gas phase pressure in equilibrium. At intermediate pressures of 0.5 MPa to 6.5 MPa, the molar volume of adsorbed phase approaches the liquid-like density of CO_2 inside the pores (Brunauer et al. 1940). Adsorption on the pore walls of adsorbents can significantly densify the fluid phase of CO_2 trapped in the nanoscale pores (Cole et al. 2010; Chialvo et al. 2012; Gruszkiewics et al. 2012). This type of adsorption is limited by the point at which the fugacity of the adsorbed phase equals the fugacity of the gas phase, at which the adsorption achieves equilibrium. An empirical equation is constructed based on the hypothesis and presented in Chapter 6; section 6.4, along with the calculation method and results.

2.5.4 Characteristic curve based on the potential theory of adsorption

The potential theory of adsorption takes into account the adsorbed phase thickness and the number of moles spreading over a specific surface area, which are affected by the state of chemical equilibrium and physical attraction between the sorbent and the sorbates (Equation 2.18) (Yang 1987; Tóth 2002; Butt et al. 2003a, b; Atkins et al. 2017; Tien 2019). Physical attraction forces such as van der Waals and London dispersion forces are significant in coal-CO_2 interactions.

$$\Gamma = \frac{x}{V_m^L} = \frac{1}{V_m^L}\sqrt[3]{\frac{C_p}{RT\ln\left(\frac{p_0}{p}\right)}} - \frac{D_0}{V_m^L} \qquad (2.18)$$

where Γ is moles adsorbed over the specific surface area (mol/m$^{2)}$, x is the thickness of the liquid like adsorbed layer related to density and effective surface area by adsorbents (m), C_p is a constant specific to the solid-gas adsorption system, is related to internal energy of the surface (involving physical attraction forces quantities) (Jm^3/mol), p_0 and p are saturation and equilibrium pressures, respectively, R is gas constant 8.314 (J/mol.K), T is temperature and D_o is the effective radius of the CO_2

molecule, (m). Equation (2.18) can be used to predict the number of CO_2 moles adsorbed over a unit surface area of coal.

2.6 Concluding remarks

A literature review on CO_2 adsorption on coal suggested that un-minable coal seams have the potential for CO_2 sequestration to reduce CO_2 emissions. CO_2 storage in coal seams is primarily determined by adsorption-desorption properties of the specific coal type. Several factors influence coal adsorption capacity, including injection pressure, temperature, moisture, coal rank, and the type of organic matter present in the coal. However, due to the brittleness of coal and other experimental difficulties, most studies have used powdered samples. Nonetheless, powdered samples do not represent intact coal samples from deep coal seams, and data on intact coal samples is limited. Further laboratory adsorption tests on intact coal samples are required to obtain more reliable CO_2 adsorption properties of coal.

In terms of temperature and pressure, most studies have been carried out at 318 K, 328 K, 338 K, and 378 K. There are only a few literatures available for temperatures around 298.15 K. Because of the geothermal gradient, un-mineable coal seams at depths ranging from 500 m to 1000 m will have temperatures ranging from 293.15 K to 298.15 K. As a result, from a thermodynamic standpoint, conducting adsorption experiments at 298.15 K will indeed greatly contribute to current understandings.

Most previous studies used the Langmuir monolayer model to describe CO_2 adsorption, with only a few studies using the BET isotherm model. Understandably, the isotherm pattern must be revisited because the sample condition (intact) and thermodynamic conditions used in the current study differ from previous studies.

There is a scarcity of information on adsorption-desorption kinetics in the current literature. Furthermore, the adsorption-desorption hysteresis pattern can reveal the CO_2 pore trapping capabilities of specific coal samples. To demonstrate pore diffusion and CO_2 condensation during adsorption, detailed adsorption-desorption kinetics data are required.

The moisture influence on intact coal samples needed to be studied further in terms of understanding the influence of water present in the coal seams. The water retention behavior of coal influences the adsorption properties of coal. Studying the water retention characteristics along with the buffering capacity of coal provides a further understanding of the CO_2-water-coal interaction.

Caprock for the CO_2 storage reservoir is formed by the rock strata above the un-mineable coal seams. It is necessary to investigate the adsorption capacity of rock samples to gain insight into the scenario of CO_2 permeating adjacent strata. Additionally, there is little or no data on the effect of biofilms on the CO_2 adsorption properties of rock minerals, and experiments using biofilm-coated minerals would provide first-hand information.

Chapter 3

Materials and Methods

3.1 Introduction

This chapter introduces the materials and experimental methods that were used to achieve the research objectives. For the adsorption tests, an anthracite (Aberpergwm) coal and a bituminous (Big Pit) coal samples were obtained from South Wales Coalfield. Following the adsorption test, a desorption test was conducted for the anthracite coal samples. The British Geological Survey (BGS) provided rock samples from the East Irish Sea. Additionally, a commercially available sand, MX80 bentonite and Speswhite kaolin were used to study the CO_2 adsorption behaviour.

Prior to the adsorption experiments, the properties of the materials used (coal rank, geological background, proximate, ultimate coal analysis, chemical composition, and mineralogy of the rock and clay specimens) were characterised using the standard methods described in section 3.2. Sections 3.2.1 to 3.2.5 describe the sample preparation methods for powder and intact coal samples and coal samples with various water contents, biofilm loaded coal and sample characterisation methods for rock samples. Sections 3.2.6–3.2.8 describe the preparation of dry and wet sand samples, biofilm loading on the sand samples, and the properties of the clay minerals used in the study.

Section 3.3 describes the manometric adsorption method, apparatus and experimental setup. This section describes the step-by-step He-pycnometer procedure for measuring the volume available for gases in the adsorption cell with and without adsorbent loaded (section 3.3.1). Section 3.3.2 demonstrates step-by-step procedures for CO_2 injection and adsorption/desorption measurements by monitoring the CO_2 gas pressure in the adsorption cell. Section 3.3.3 details the procedure for calculating the

amount of CO_2 adsorption using the compressibility factor (Z) at a CO_2 temperature isotherm of 298.15 K.

Sections 3.4 and 3.5 discuss the theoretical methods used to evaluate CO_2 adsorption on coal by fitting experimental data into existing adsorption isotherm and adsorption kinetic models.

The chilled-mirror dew point method was used to comprehend the water retention characteristics of the coal samples-in order to correlate the influence of water retention properties on the adsorptive behaviour of coal in the presence of water in the coal seam. The experimental method used for determining the water retention characteristics of coal samples is described in section 3.6.

Section 3.7 provides a general outline of the experimental program for this study.

3.2 Properties of the materials used and preparation methods

3.2.1 Properties of coal samples

Coal samples were collected from two coal mines in South Wales Coalfield, Wales, the United Kingdom. The anthracite coal samples were obtained from the Aberpergwm coal mine (51°44'28.8"N 3°38'36.0"W), which is operated by Energybuild and owned by Walter Energy, and the bituminous coal was obtained from the Big Pit coal mine (51.7724°N 3.1050°W), which is closed and has been converted into a National Coal Museum.

Coal blocks were extracted from two coal seams at Aberpergwm colliery: a 9 feet seam located at a depth of 550 m and an 18 feet seam located at a depth of 500 m. These samples will be referred to as 9ft AB and 18ft AB hereafter. Small chunks of coal measuring approximately 5 cm x 7 cm x 4 cm were collected from the Big Pit coal museum and referred to as BP. These small blocks and the coal core samples extracted from larger samples are referred to as intact samples.

The proximate and ultimate analyses were conducted in accordance with the British Standards Institution (BSI) and American Society for Testing Materials

(ASTM) standards (BS 1016-104.3 1998, BS 1016-104.4 1998, BS 1016-104.1 1998, BS 1016-104.1 1999, BS 1016–106.1.1 1996, BS 1016–106.4.2 1996, and ASTM D3302/D3302M 2015). Table 1 summarises the properties of the coal samples.

On the basis of carbon content, volatiles, and gross calorific value, the Aberpergwm samples (9ft AB and 18ft AB) were classified as anthracite coal (high rank). Big Pit (BP) coal was identified as bituminous sample (Green and Perry 2019 and ASTM D388-99 1999).

Table 3.1 Proximate and ultimate analysis of the coal samples from 9ft and 18ft Aberpergwm.

Analytical		18ft Aberpergwm Coal	9ft Aberpergwm Coal	Big Pit Coal
Proximate analysis				
Water Content	% mass	0.78	0.91	0.96
Ash Content	% mass	1.38	4.62	12.7
Volatiles content	% mass	5.08	5.73	
Calorymetry				
High calorific value	Mj/kg	35.04	35.60	33.68
Low calorific value	Mj/kg	34.30	32.89	
Ultimate analysis				
Total Carbon	%mass	92.05	89.5	83.87
Total sulphur	% mass	0.73	0.87	
Sulphur combustion	% mass	0.01	0.25	
Sulphur after full combustion	% mass	0.72	0.62	
Combustible sulphur	% mass	92.05	89.5	
Total hydrogen	% mass	3.31	3.16	
Nitrogen	% mass	1.27	1.31	3.3
Oxygen	% mass	0.5	0.33	
Petrography				
Vitrinite reflectance	% Vol	2.72	2.84	
Vitrinite content	% Vol	86	86	
Liptynite (egsynite)	% Vol	0	0	
Inertynite	% Vol	14	14	
Mineral matter content	% Vol	0	0	
As received				
Transient moisture	% mass	0.84	0.65	
content	% mass	1.61	1.56	
Total moisture	% mass	1.37	4.59	
Ash content	% mass	5.04	5.69	
Volatile matter content	% mass	0.72	0.86	
Total sulphur content	Mj/kg	33.99	32.66	
Low calorific value				
Dry state				
Ash	% mass	1.39	4.66	
Total sulphur	% mass	0.74	0.88	
Daf state				
Volatile matter content	% mass	5.19	6.07	
High calorific value	% mass	33.82	35.57	

3.2.2 Coal powder sample preparation

Coal samples were ground into powder (<250 μm) (Figure 3.1 a), and separate aliquots were mixed with varying amounts of water to create coal-water mixtures with varying water contents. The mixtures were wrapped in cling film, placed in a locked bucket, and covered with a wet cloth. Following equilibration, a subset of samples was used to determine the water content using ASTM standard methods (ASTM D3302/D3302M–19 2019).

3.2.3 Coal intact sample preparation

Coal cores were drilled from large coal blocks using a core drill machine equipped with a 5 cm internal diameter diamond saw-tipped core drilling bit. Prior to adsorption experiments, samples were air dried to simulate dry test conditions and designated as dry intact samples. The image in Figure 3.1 (b) shows the coal core sample. The core samples were saturated with water using an oedometer to prepare coal samples with water content (Figure 3.1 C and d). The core samples were left in the cells for 21 days to attain saturation equilibrium and are referred to as wet samples.

(a)

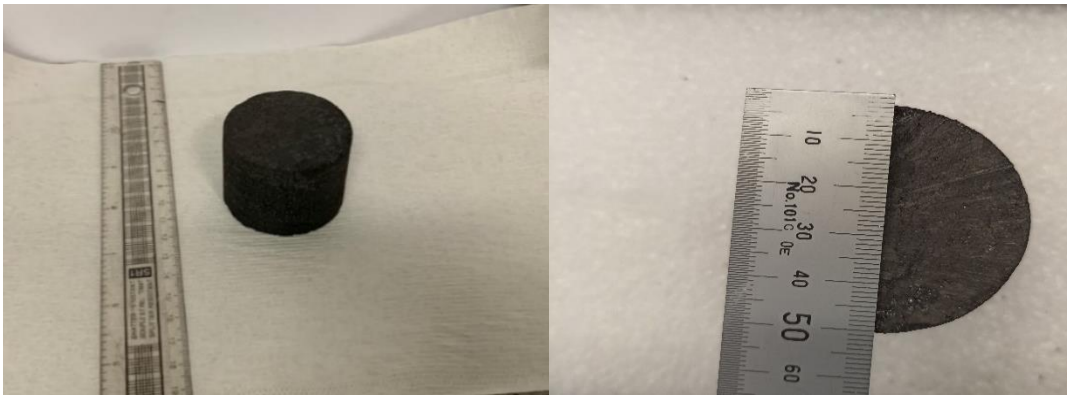

(b)

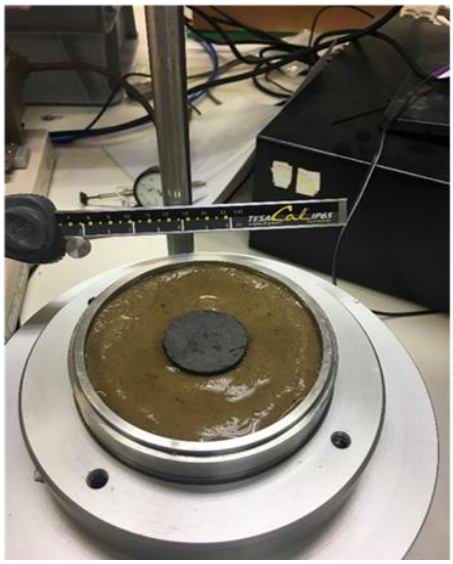

(c)

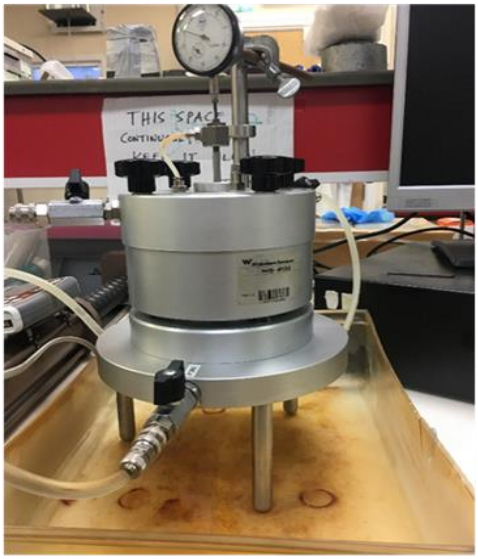

(d)

Figure 3.1. Images of (a) powdered (b) core coal samples, (c) and (d) water saturation of coal samples using oedometer.

3.2.4 Biofilm loading on coal samples

Previous research has shown that native bacteria (*Bacillus mojavensis*) found in coal seams are resistant to high pressure CO_2 environments. As a result, the impact of biomineralization or biologically influenced mineralisation of CO_2 cannot be overlooked during the adsorption process. This study used SEM (scanning electron microscope) to identify *Bacillus mojavensis* on the natural coal sample and the coal sample with a laboratory-grown bacterium. The method for growing *Bacillus mojavensis* on coal samples is discussed in this section, and the SEM analysis is discussed in the subsection (3.2.4.1). The results are presented in Chapters 5 (section 5.4.2) and 6 (section 6.6).

The starter cultures were incubated overnight at 30°C. *Bacillus mojavensis* starter cultures were prepared in 2 x 5 ml Nutrient Broth (NB). The following day, coal fragments were spread across two rectangular Petri dishes (single well cell culture plate) for each coal sample, one dish for each bacterium. Additionally, two 50 ml Falcon tubes were filled with coal fragments to serve as negative or medium controls. Each plate received two millilitres of starter culture, which was pipetted specifically onto the coal fragments. After 20 minutes of standing at room temperature, the lidded dishes were removed to allow bacteria to attach to the coal. Each dish received approximately 50 ml of Nutrient Broth (NB) media, while the Falcon tube negative controls received 5 ml of media. All samples were incubated for 11 days at 30°C (static). The growth medium was decanted and the coal fragments in the rectangular dishes were transferred to 50 ml Falcon tubes on the eleventh day. All samples were covered with a 5 ml solution of phosphate buffered saline (PBS), and controls were fixed with 25% glutaraldehyde to a final concentration of 1.5 %. The rectangular dishes with coal fragments are depicted in Figure 3.2.

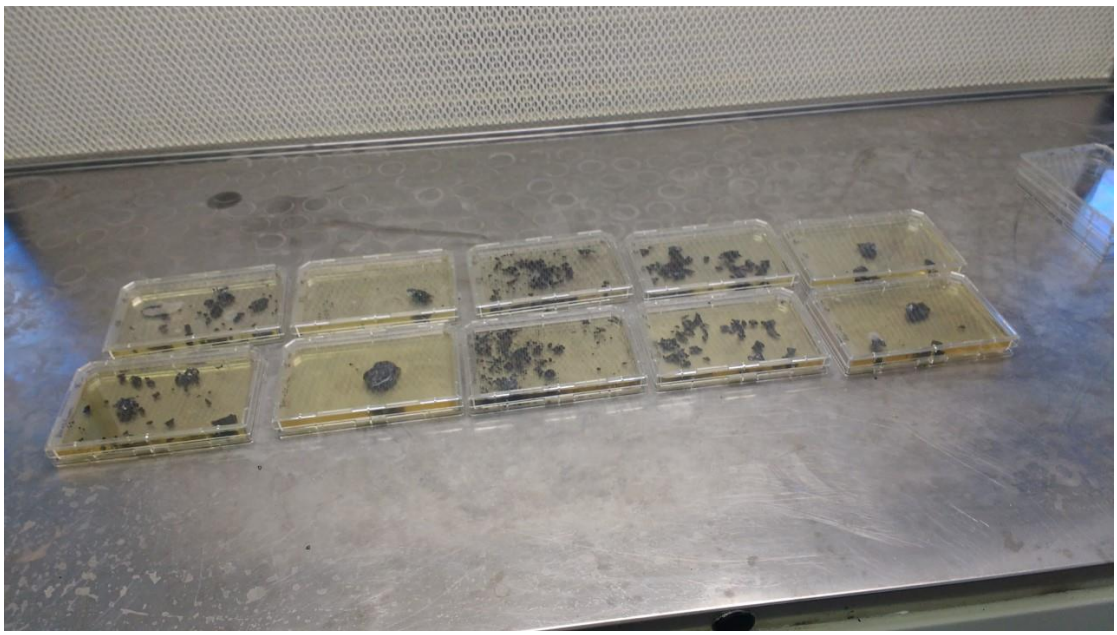

Figure 3.2 Coal fragments loaded with Bacillus Mojavensis stored in rectangular dishes prior to the imaging.

3.2.4.1 Scanning electron microscope (SEM) imaging of coal samples

SEM was used to image the 9ft, 18ft AB and BP coal samples to determine the presence of bacteria. There were two types of samples used: (1) the coal samples as received, and (2) coal sample with laboratory-grown *Bacillus mojavensis* on the sample. Secondary electron images of the intact and powdered coal samples were obtained using a Zeiss Sigma HD Field Emission Gun Analytical high-resolution SEM (samples as received). The samples were coated with a very thin layer of gold to reduce the charging effect, and the images were used to visualise the nano pores to substantiate the CO_2 pore condensation phenomenon in the intact sample. The secondary electron images of the bacteria-loaded coal samples were captured using a focused ion beam - Zeiss 1540xB SEM.

3.2.5 Characterization of East Irish Sea rock samples

The British Geological Survey (BGS) provided rock core samples from the East Irish Sea that measured 2.54 cm in diameter. Prior to the mineralogical and elemental analysis, powdered rock samples (< 75 μm) were dried at 100 °C for 24

hours. A Phillips Xpert powder X-ray diffractometer was used to obtain XRD patterns of powdered rock samples from the East Irish Sea to identify mineralogy. The elemental composition of the rock samples was quantified using an Olympus X-5000 energy dispersive X-ray fluorescence (XRF) spectrometer. Chapter 7 discusses the results of mineralogical identification and chemical analysis (section 7.2).

3.2.6 Wet sand samples preparation methods

The sand samples were dried at 105°C for 24 hours. To avoid microbial growth, a dried portion of sand was equilibrated with water and stored in a freezer. One day prior to the adsorption tests, the samples were transferred to a refrigerator. These samples were designated as wet sand samples.

3.2.7 Preparing biofilm-laden (*Bacillus mojavensis*) sand sample

Bacillus mojavensis grown in Nutrient Broth E was added to the sand samples. The samples were prepared at the University of Aberystwyth's microbial geochemistry facility.

The biofilm was developed in syringe sand columns (Figure 3.3). Each sand column was filled with 50 mL of fine sand. Prior to biofilm loading, the sand was heated to 150°C. The assembly is designed for single-pass flow of media, nutrients, and deionized water. The fluids were introduced into the system using a Watson-Marlow pump 205S multichannel pump (8 channels). To flush the system, autoclaved deionized water was run overnight. At 30°C, three millilitres of *Bacillus mojavensis* starter culture were prepared and left to grow overnight.

To grow the biofilm, six syringe columns were prepared, one of which served as a control. Four millilitres of the prepared *Bacillus mojavensis* culture were injected and washed down with liquid at a rate of 4.17 mL/min to wash out of the glass wool into the sand. The pump flow rate was then reduced to 0.056 mL/min to pump 60 mL of fluid, allowing a turn back time of 18 h to allow the bacteria to attach and form a biofilm on the sand. Following biofilm loading, the liquid was drained and sand portions were transferred to sterile 50 mL Falcon tubes and stored in a freezer prior to adsorption experiments. The samples were taken out of the freezer 24 hours prior to the adsorption experiments.

Figure 3.3. Photographs of the syringe sand columns with single-pass flow system for loading biofilm (Bacillus mojavensis grown in Nutrient Broth E).

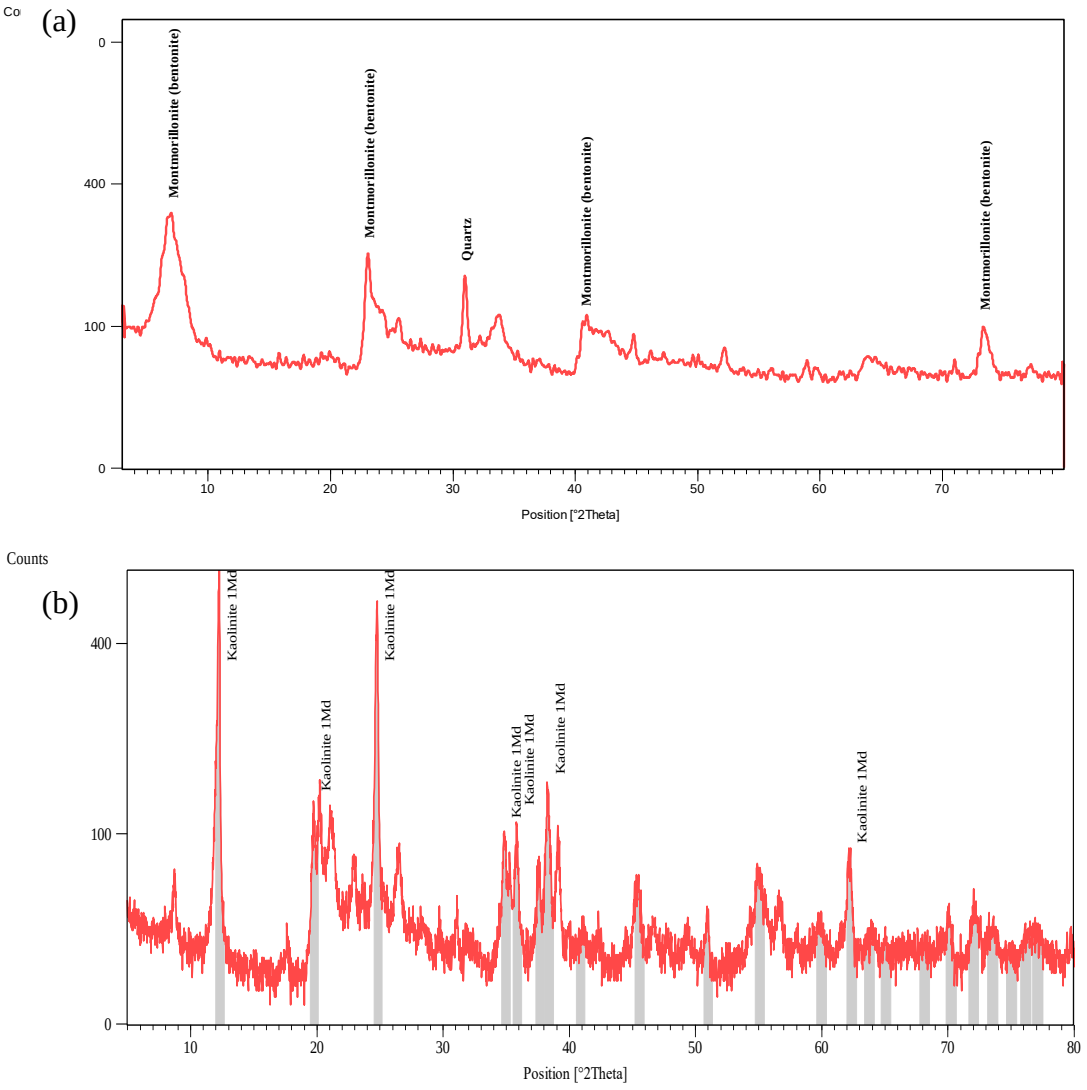

Figure 3.4. X-ray diffraction patterns of (a) MX80 bentonite and (b) Speswhite kaolin.

3.2.8 Properties of clays used

In this study, a commercially available MX80 bentonite and Speshwhite kaolinite were used. X-ray diffraction was used to identify the mineralogy of the clays. The bentonite contained 2:1 montmorillonite mineral and Speswhite kaolinite contained 1:1 kaolinite mineral (Figure 3.4 a and 3.4 b). The cation exchange capacity of the bentonite was found to be 109 meq/100 g of clay (Na = 50.11 meq/100 g, Mg = 14.03 meq/100 g, K = 1.7 meq/100 g, Ca = 44.07 meq/100 g). The Speswhite kaolin had 45.4% SiO_2, 39.8% Al_2O_3, 2.4% K_2O, 0.9% FeO, and 0.11% CaO by mass.

3.3 Adsorption /desorption experimental methods

The experimental techniques of pure CO_2 gas adsorption measurements using the volumetric or manometric method are outlined in this section. The theoretical background of volumetric gas adsorption experiments is described in Chapter 2, (section 2.2), and detailed in Keller and Staudt (2005). The current study utilised the manometric sorption apparatus housed at Seren Multipurpose Gas Laboratory, Cardiff University, which is capable of operating at pressures up to 20 MPa and temperatures up to 338 K (65°C) (Mosleh 2014; Zagorščak 2017). GDS Instruments of the United Kingdom designed and installed the adsorption cell system, and Mosleh (2014) explained the experimental setup in detail. The schematic of the system is shown in Figure 3.5 (a) and the photograph of the main components is shown in Figure 3.5 (b).

The manometric/volumetric adsorption test setup is instrumented with the following components: (1) a manometric unit consisting of a reference cell (RC) for preparing the known quantity of gas and a sample cell (SC) for placing the adsorbent material, (2) needle valves for connecting and isolating the RC and SC, (3) pressure transducers and data loggers for communicating with the computer, (4) a water bath with a temperature controller for maintaining the temperature of 298.15 K, and (5) A calibration cell (known volume = 0.0004892 m^3) was used to determine the void volumes of RC and SC, as well as the volumes with sample loaded, using helium pycnometry method. The calibration cell heater is kept at a constant temperature of 298.15 K. Figure 3.5 (a) depicts the overall connection scheme for the adsorption experiments.

Manometric adsorption is a mass balance technique that utilises precise pressure, volume, and temperature measurements (Sudibandriyo et al. 2003). The experimental concept is as follows: (i) Determination of the reference and sample cells void volumes (v_d) using helium pycnometry method, (ii) Prepare a known quantity of CO_2 gas in RC expanding into SC while monitoring the pressure drop and repeat the procedure by progressively increasing the pressure in RC and (iii) Calculate the adsorbed amount using the appropriate equation of state (EoS) for CO_2 and the perfect gas law.

The general procedure is as follows: a known amount of CO_2 gas is stored in a reference vessel (RC) and expanded into a vessel (sample cell, SC) containing a previously degassed sample of adsorbent (e.g. coal sample). CO_2 gas is partially adsorbed on the surface of the coal sample after expansion (on external and internal surfaces). The pressure decreases as the gas molecules transition from the gas phase to the adsorbed phase. Continuous pressure drop measurements are taken in manometric apparatus designed to determine gas adsorption. The equilibrium pressure was defined as the value of the pressure that remained stable for a minimum of four hours. After achieving equilibrium, the RC and SC were isolated in order to increase the pressure in the RC for the subsequent expansion stage. The adsorption experiments were conducted by gradually increasing the CO_2 pressure in stages starting at 0.5 MPa and ending at 6.5 MPa. CO_2 desorption experiments were conducted following a pressure step down procedure from the maximum adsorption equilibrium pressure to the null pressure. Every ten seconds, the change in gas phase pressure caused by adsorption and desorption was recorded and used to determine the rate of adsorption and desorption. The adsorption-desorption experiments on powdered and intact samples conducted at two different injection pressure ranges (< 6.1 MPa and up to 6.4 MPa). Details of the experimental procedures and calculation methods are illustrated and explained in the subsequent sections with examples.

Figure 3.6 shows the sample loading and preparation of the adsorption cell. A 5 cm diameter filter paper with a pore diameter of 20 μm was kept in the bottom of the reference and sample cells. The sample cell was loaded with the core sample. O-rings were installed with the vacuum seal applied, and a 55 mm diameter filter paper with a pore diameter of 2.5 μm was kept on top of both cells to avoid particles clogging into the high-pressure line. The entire system is sealed gas-tight with the top cover (Figure 3.5 b) of the adsorption cell.

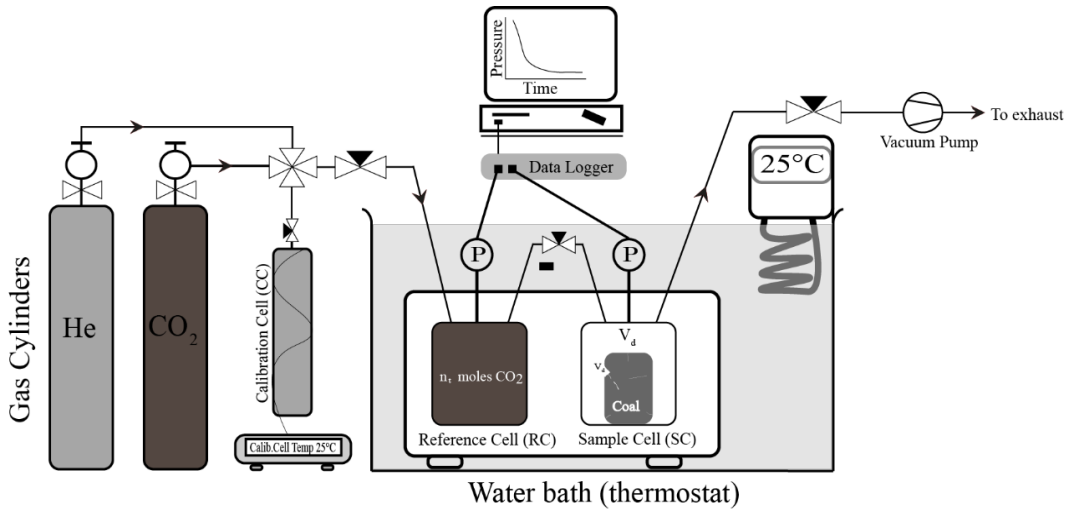

(a)

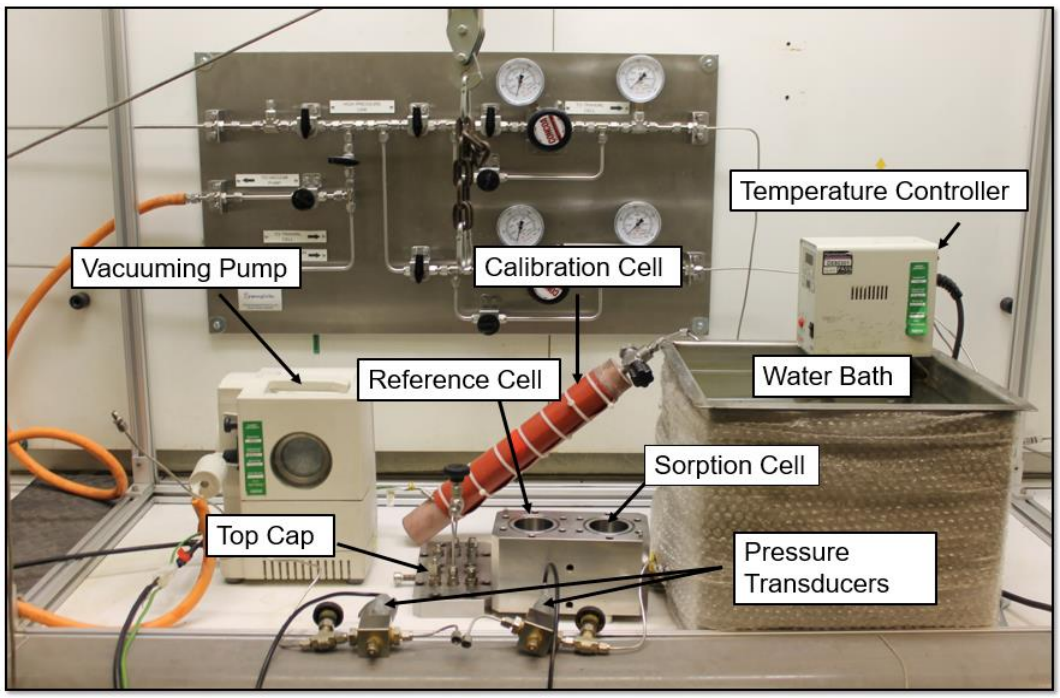

(b)

Figure 3.5. (a) Schematic of the manometric adsorption experimental setup and (b) the photograph of the main components of the manometric adsorption set up.

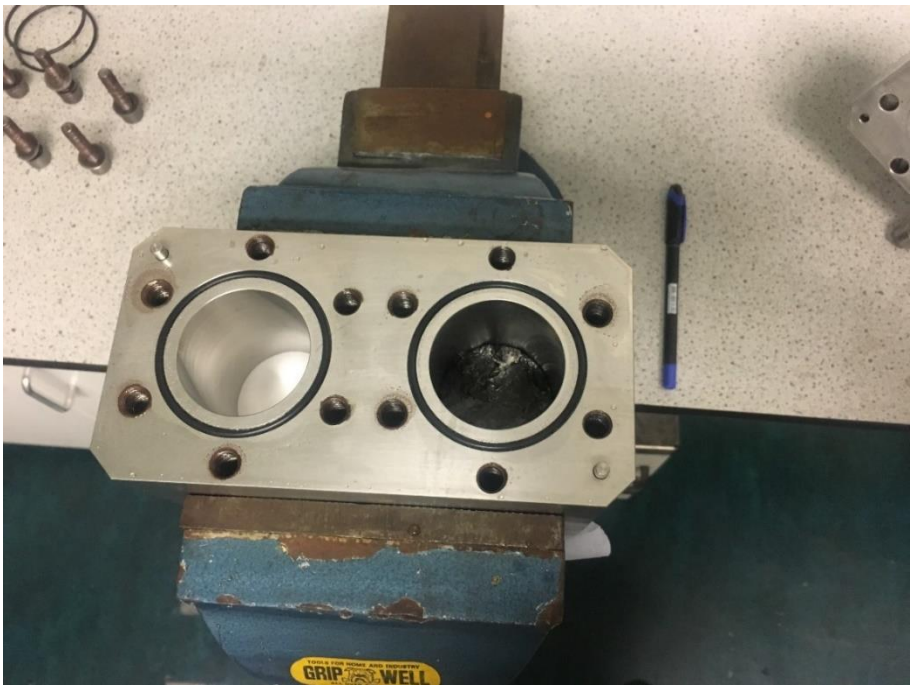

Figure 3.6. adsorption cell preparation.

3.3.1 Modified helium pycnometer method

The helium pycnometer method (DIN method. 2001. DIN 51913:2001; Sudibandriyo et al. 2003; Keller and Staudt 2005; Meyers 2014; ASTM D4892-14 2019) was used to determine the void volumes of the reference (V_{rc}) and sample cells (V_{sc}), as well as the void volume of the cells with sample loaded (v_d) as described in the following sub-sections.

3.3.1.1 Determining the volume of the voids in the empty reference (V_{rc}) and sample cells (V_{sc})

The He-pycnometry technique is a straightforward method, utilising Boyle's law variant of the perfect gas law (PV=ZnRT). The void volume of the reference cell (V_{rc}) and the sample cell (V_{sc}) were calculated as described below using an illustrated example (Figure 3.7).

(*i*) A vacuum pump was used to evacuate the entire adsorption system for 24 h. Before the test, the pipeline connecting the system to the helium gas cylinder was vacuumed for 15 minutes.

(*ii*) The calibration cell was connected to the gas line, and its temperature was kept constant at the same level as the water tank (298.15 K). A known volume of He gas (calibration cell volume V_{cc}= 0.0004892 m^3) is prepared in the calibration cell (CC) (Figure 3.7 a). Valve V1, V2, and V3 (Figure 3.7) have been closed to isolate the calibration cell (CC), reference cell (RC), and sample cell (SC).

(*iii*) The calibration cell was injected with a known amount of helium gas (He) (2.5 MPa in the example given; Figure 3.7 a). Despite the fact that the gas pressure display quickly levels off, the measurement is scheduled to take around 20 minutes. The pressure value is abbreviated as P_{cc}.

(*iv*) To expand the He gas into the RC, valve V1 was opened (Figure 3.7 b). Pressure was decreased by following the volume expansion gas law at constant temperature (1.9 MPa, for the given example). A period of 20 minutes was allowed to ensure that the pressure value remained constant for an extended period of time, thereby avoiding any determinate errors caused by system failure (leaks). Pressure values (designated as (P_{cc}+P_{rc})) were recorded in order to determine the volume of the reference cell (V_{rc}) (Figure 3.7 b).

(*v*) Then the valve V2 was opened to expand the He gas into the sample cell (SC). After 20 minutes, the pressure values (designated as P_{cc}+P_{rc}+P_{sc}) were recorded and used to calculate the sample cell volume (V_{sc}) (Figure 3.7 c).

(*vi*) Once the test was completed. The calibration cell (CC) and the helium gas line from the main gas supply cylinder, RC, and SC were evacuated for about 10 minutes using a vacuum pump through valve V3.

To eliminate the indeterminate experimental errors, the preceding procedures was repeated three times.

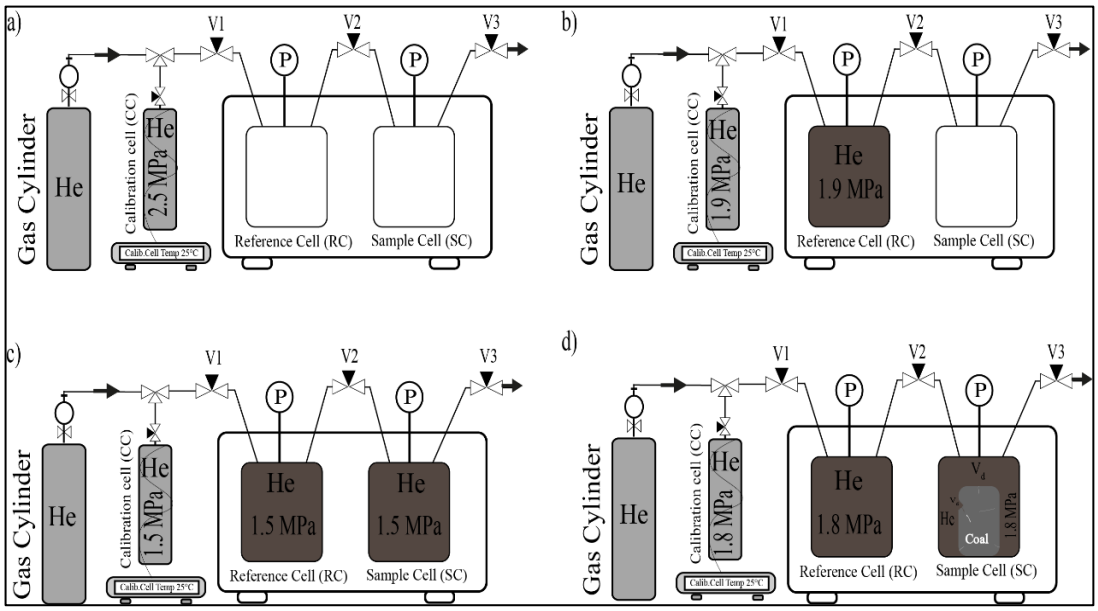

Figure 3.7. He-pycnometry method; (a) Preparating He gas in the CC (P_{cc} = 2.5 MPa), (b) Expanding He gas into RC (P_{cc}+P_{rc} = 1.5 MPa), (c) Expanding He gas from CC and RC to SC (P_{cc}+P_{rc}+P_{sc} = 1.5 MPa) and (d) with sample loaded (Pcc+Prc+Pscv= 1.8 MPa).

3.3.1.2 Determination the Void volume of adsorption cell with sample loaded

The steps for determining the void volume of the adsorption cell with sample loaded (v_d) were similar to those described in section 3.3.1.1. The only difference in this case was that the sample cell (SC) was loaded with the sample of adsorbent, and the pressure measured as P_{cc}+P_{rc}+P_{scv} (shown in Figure 3.7 d) was used to calculate the available volume (v_d) for the adsorbate gas (CO_2). The volume calculation method is explained in the section that follows.

3.3.1.3 Volume calculation for He-Pycnometry method

Pressure values generated from the He-pycnometry method described in the previous section was used in the perfect gas law (Equation 3.1) to calculate the volume of the reference cell (V_{rc}) and the sample cell (V_{sc}).

Step 1: The number of moles injected into the calibration cell was calculated using Equation (3.1).

$$n_{He} = \frac{p_{cc}V_{cc}}{ZRT} \quad (3.1)$$

where n_{He} is number of moles of He (mol), P_{cc} pressure measured from CC (Pa), V_{cc} is volume of CC = 0.0004892 (m^3), Z is compressibility factor of He, gas constant 8.314 ($Pa.m^3/(K.mol)$ and T is temperature (298.15 K).

The Peng-Robinson Equation of State was used to calculate the compressibility factor (Z) (Elliot and Lira 2012) and substituted in Equation (3.1).

$$n_{He} = \frac{p_{cc}V_{cc}}{ZRT} = \frac{258300\ pa \times 0.0004892\ m^3}{1.0007 \times 8.314\ \frac{pa\ m^3}{°K\ mol} \times 298.15\ °K} = 0.509 \text{ moles}$$

Step 2: The number of moles obtained from the above calculations (n_{He}), as well as the pressure values P_{cc} + P_{rc}, were entered into Equation (3.2) to calculate the volume of V_{rc} and V_{sc}. The reference cell volume was calculated by subtracting V_{cc} (0.0004892 m^3) from V_{cc}+V_{rc}.

$$V_{cc} + V_{rc} = \frac{n_{He}ZRT}{p_{cc}+p_{rc}} \quad (3.2)$$

where $P_{cc} + p_{rc}$ pressure meassured from CC+RC (Pa), $V_{cc} + V_{rc}$ is volume of CC +RC (m^3).

Step 3: Similar procedures as depicted in step 2 were followed to calculate the void volume with sample loaded (Equation 3.3). As the empty volumes of the $V_{cc} + V_{rc} + V_{sc}$ was known from steps 1, The volume of CC+RC+SC with a sample loaded was calculated using pressure values of $p_{cc} + p_{rc} + p_{svc}$. Subsequently, the void volume of RC+SC with sample loaded (v_d) was was calculated by subtracting the void volume of CC.

$$V_{cc} + V_{rc} + V_{scv} = \frac{n_{He}ZRT}{p_{cc}+p_{rc}+p_{scv}};\ v_d = V_{rc} + V_{scv} \quad (3.3)$$

where $p_{cc} + p_{rc} + p_{svc}$ pressure meassured from CC+RC+SC with sample loaded, $V_{cc} + V_{rc} + V_{scv}$ is volume of CC+RC+SC (m^3) with sample loaded and v_d is volume of RC+SC with sample loaded. v_d is the volume available for the gas in the adsorption cell and used in the CO_2 adsorption calculations.

3.3.2 CO_2 injection for adsorption measurements

CO_2 gas adsorption experiments were conducted in a manner similar to that described in section 3.3.1 for helium gas expansion. Helium was neither adsorbed nor absorbed onto the coal, indicating that the adsorption cell's pressure was not decreasing. With respect to carbon dioxide, the spontaneity of gas adsorption or desorption can be determined by increasing and decreasing the pressure of the adsorbate (CO_2) gas. The sample cell was filled with a known mass of adsorbents (adsorbents: coal, rock, dry sand, wet sand, bacteria-loaded sand, MX80 bentonite, and Speswhite kaolin). Section 3.3 discussed sample and adsorption cell preparation methods. The following are the major stages of the procedures.

(*i*) Before the test, the entire adsorption system was vacuumed for 24 h, and the pipeline connecting the system to the CO_2 gas cylinder was evacuated for about 15 minutes.

(*ii*) To isolate the sample cell, valves V2 and V3 (Figure 3.8) were closed. The vapour phase CO_2 from the cylinder was injected using a gas heater.

(*iii*) RC was filled with a known amount of CO_2 ($n_t^{CO_2}$ moles) (Figure 3.8 a). The volumes of RC and SC were known and the molar volume of the gas was calculated using the gas law (PV=ZnRT).

(*iv*) Valve V1 was closed after filling RC with CO_2, and the gas pressure in RC was measured. The gas is then expanded to the SC by opening the valve V2 (Figure 3.8 b).

(*v*) After expanding the gas into the RC, the gas pressures in the RC and SC were continuously monitored and recorded using GDS Instruments' application software. The sorptive gas (CO_2) pressure was reduced in proportion to the adsorption rate. The CO_2 gas was allowed to equilibrate with the sorbent, and the equilibrium gas pressure was determined when the gas pressure values were constant for at least 4 h.

The gas pressure versus time data is discussed in Chapters 4, 5, and 7. The equilibrium gas pressure values were used to calculate the amount of CO_2 at the equilibrium (Figure 3.8 c). The amount adsorbed ($n_{equ,ad}^{CO_2}$) was calculated by subtracting the number of injected moles ($n_t^{CO_2}$ moles) from the number of moles at equilibrium (n_{eq} moles) (Equation 3.4).

(*vi*) The aforementioned steps were repeated for injecting CO_2 at pressures ranging from 0.5 MPa to 6.5 MPa. In stage 1, for example, a gas pressure of 0.5 MPa is injected into the RC, which is then connected to the SC and equilibrated with the adsorbent (similar procedure as described in the above steps). After equilibration, the valve V2 was closed to prepare the RC for stage 2 by injecting at a pressure greater than 0.5 MPa. Following the filling of the RC, the pressure in the SC and RC is separately recorded to calculate the total number of moles available at the start of the new stage (Figure 3.8 d). Valve V3 was eventually opened, allowing the system to reach equilibrium. The preceding procedure was repeated for each subsequent stage up to the injection pressure range of 6.5 MPa was reached.

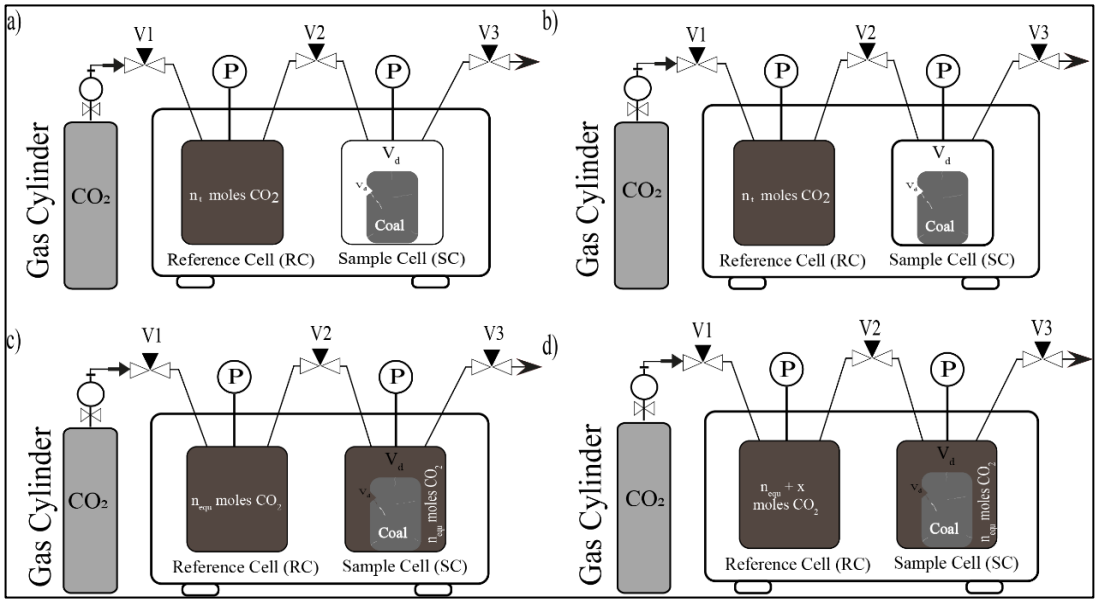

Figure 3.8. Illustration of CO_2 adsorption pressure step-up stage (a) Filling the RC with a known amount of CO_2, (b) Expanding into SC, (c) Illustrating the equilibrium of the first stage and (d) illustrating the next pressure step up stage.

3.3.3 Desorption experimental method

The CO_2 desorption experiments were carried out using a pressure step down procedure similar to that described in section 3.3.2 for adsorption pressure step up procedures. After the final stage of the adsorption experiment was completed, the valve V2 was closed to isolate the SC from the RC. Then, valve V2 was opened to connect RC and SC and allow equilibrium to occur. Pressure increased gradually during desorption as CO_2 molecules were released from the adsorbents. After achieving equilibrium, the procedures were repeated. Every ten seconds, the change in gas phase pressure caused by adsorption and desorption was recorded and used to determine the rate of adsorption and desorption.

The amount of CO_2 adsorbed/desorbed was calculated using Equation (3.4) and (3.5).

$$n_{equ,ad}^{CO_2} = \frac{n_t^{CO_2} - \frac{p_{eq}^{CO_2}}{RTZ_{(p,v)}} v_d}{m_s} \quad \text{the amount adsorbed} \qquad (3.4)$$

$$n_{equ,de}^{CO_2} = \frac{\frac{p_{eq}^{CO_2}}{RTZ_{(p,v)}} v_d - n_t^{CO_2}}{m_s} \qquad \text{amount desorbed} \qquad (3.5)$$

where $n_{equ,ad}^{CO_2}$ is number of moles of CO_2 at equilibrium stage (mol/kg), v_d is void volume available for gas (m^3) *(v_d* = sample cell volume with sample loaded + reference cell volume), $p_{eq}^{CO_2}$is equilibrium pressure of CO_2 (Pa), Z is compressibility factor of CO_2, and R is gas constant 8.314 (Pa m^3)/(K mol), T is temperature (298.15 K), m_s is mass of adsorbent (kg) and $n_t^{CO_2}$is the known amount present in the gas phase at the beginning of the adsorption experiment (mol).

The values of the compressibility factor were determined using the Peng-Robinson equation of state (PR-EoS). The following section discusses the rationale for selecting the equation of state.

3.3.4 Consideration of CO_2 gas thermodynamics

The cubic form (Equation 3.7) of the Peng-Robinson equation of state (PR EoS) (Equation 3.6) was solved to estimate the molar volume and compressibility factor. The values were compared to NIST (National Institute of Standards and Technology, USA) values for CO_2 derived from the Span Wagner EoS. (Span and Wagner 1996). The density values calculated by Span and Wagner EoS exhibits a shift at near the critical pressure range of the temperature isotherm of 298.15 K (Meng et al. 2019; NIST Chemistry WebBook, SRD 69, 2021) while the PR EoS consider the liquid and vapour co-existence region. Therefore, for the current study, the PR EoS is more appropriate to calculate the amount adsorbed for injections in the pressure range of up to 6.4 MPa. The PR EoS is a modified version of the Redlich-Kwong equation of state (Equation 3.6).

$$P = \frac{RT}{V-b} - \frac{a(T)}{V(V+b)+(V-b)} \qquad (3.6)$$

$$a(T) = \alpha a(T_c)\,,\ a(T_c) = 0.45723553\ \frac{\alpha R^2 T_c^2}{P_c}$$

$$b = 0.07779607\frac{RT_c}{P_c}, \alpha = (1 + \varkappa(1 - \sqrt{\frac{T}{T_c}})^2\,, \varkappa = 0.37464 + 1.54226\,\omega - 0.26992\omega^2$$

Cubic form of the equation is as follows.

$$Z^3 - (1-B)\,Z^2 + (A-3B^2-2B)Z - (AB - B^2 - B^3) = 0 \qquad (3.7)$$

$$Z = \frac{PV}{RT}\ ,\ A \equiv \frac{aP}{R^2T^2}, B = \frac{bP}{RT}\ ,\ b\rho = \frac{B}{Z}; \frac{a\rho}{RT} = \frac{A}{Z}$$

where Z is compressibility factor, P is pressure (Pa), V is volume (m^3), R is gas constant (J/mol.K), T is temperature in K (298.15 K), ρ is gas density (mol/m^3), Pc and Tc are critical constants, *a*, *b*, *A*, and *B* are the dimensional equation of state

parameters and constants, ω is acentric factor α and $\varkappa$ are the parameters for Peng-Robinson equation of state.

The pressure-volume curves were plotted for the purpose of the current study to determine the P-V-T behaviour of CO_2 using the Peng-Robinson equation of state for different temperatures prior to the experiments (Figure 3.9). Many of the CO_2 adsorption studies were performed at temperatures of 318.15 K and 328.15 K or higher temperatures and pressures, where the temperature isotherms of CO_2 show a linear pattern. However, the van der Waals loop occurs near the critical pressure range (6.1 MPa to 6.4 MPa at 298.15 K; Figure 3.9), in which liquid and vapour CO_2 coexist and differ in molar volumes. Critical pressure value of CO_2 shifts to 6.4 MPa at 298.15 K. (Span and Wagner 1996). Above this point, the coexistence of liquid and vapour is impossible. This is a key technical aspect that affects adsorption results as overestimation or underestimation of CO_2 excess adsorption calculations. To overcome this phenomenon, the following theoretical consideration was used in the current study to calculate the amount of CO_2 adsorbed in the near critical region (6.1MPa to 6.4MPa at 298.15K).

When the vapour and liquid in equilibrium, the chemical potential and Gibbs free energy of both liquid and vapour phases are equal for pure substances, and they are thermally (T) and mechanically (P) in equilibrium. The calculated molar volumes of liquid (n_L) and vapour (n_v) phases by PR-EoS at a given temperature and pressure were used in Equation (3.8) to calculate the volume fraction (v^F) of vapour phase CO_2 (Eliott and Lira 2012; Gmehling et al. 2019).

$$v^F = \frac{n_v}{n_v - n_L} \tag{3.8}$$

The volume fraction ratio of vapor and liquid CO_2 was used to calculate the total number of moles injected at near critical phase region.

For example, the injection pressure of 6.42 MPa into the reference cell, as of the Equation of State, the molar volume of the liquid CO_2 is 70.4161 cm^3/mol, and molar volume of vapour CO_2 is 181.184 cm^3/mol at 6.42 MPa. The volume fraction

of liquid is approximately 0.281, the volume fraction of vapour is 0.7189. This ratio is used to calculate the total number of moles at the injection stage.

Abide By the above discussed procedure based on fundamental principles of gas thermodynamics, the amount of adsorption was calculated correctly at near-critical region of CO_2.

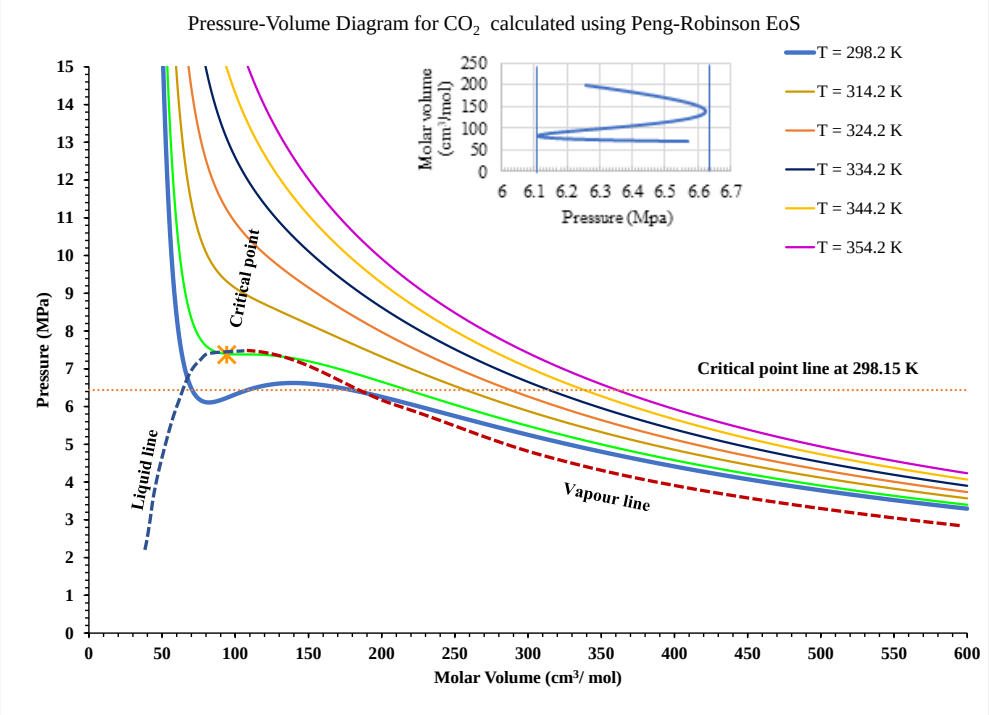

Figure 3.9. Isothermal P-V curves of CO_2. The insert is the region of liquid-vapour coexistance where the molar volume of CO_2 does not have single value - calculated based on Peng-Robinson EoS (Elliot & Lira 2012).

3.4 Evaluation of CO_2 adsorption by Langmuir and BET models

The theory of adsorption and existing isotherm models have been discussed in Chapter 2 (section 2.5). The current study used the nonlinear form of the Langmuir isotherm model (Langmuir 1916, 1917, 1918) and compared the experimental data with the model (Keller and Staudt 2005) (Equation 3.9).

$$m_{eq} = m_{\infty} \frac{bP}{1+bP} \quad (3.9)$$

where P is Equilibrium pressure (Pa), m_{eq} is mass of CO_2 adsorbed at given equilibrium pressure (g/kg). m_{∞} is limiting value of mass adsorbed at temperature is constant, also mass of a maximum monolayer adsorbate covering the surface of the sorbent (g/kg), b is Langmuir parameter, which is also reciprocal of half-loading pressure, Pa^{-1}.

The m_{∞} and b values were obtained from the nonlinear regression analysis. The values were used in Equation (3.9) for validating the model with the experimental data.

The thermodynamic parameters, the heat of adsorption (ΔH_{ad}) and Gibbs free energy (ΔG_{ad}^{0}) were calculated based on the Langmuir parameters (m_{∞} and b) obtained from the isotherm model fit and kinetic theory of adsorption. (Equation 3.10 and 3.11) (Butt et al. 2004a; Rouquerol et al. 2014; Ruthven 1984).

$$b = b_0 \exp\left(\frac{\Delta H_{ad}}{RT}\right) \quad (3.10)$$

$$b_0 = \frac{N_m \sigma_A \tau_0}{\sqrt{2\pi MRT}} \quad (3.11)$$

where b_0 is the exponential factor (Pa^{-1}), b Langmuir constant or reciprocal of half-loading pressure (Pa^{-1}), ΔH_{ad} is energy of adsorption (J/mol), τ_0 is vibration period related to the residence time of the adsorbed CO_2 molecule (typically in the order of 10^{-13} s), N_m is Number of molecules adsorbed (related to m_{∞} and the Avogadro's number), σ_A is Cross sectional area covered by one CO_2 molecule (m^2), M is Molecular mass of CO_2 (0.04401 kg/mol), R is universal gas constant (8.314 J/mol K), and T is temperature 298.15 K.

The Langmuir constant b related to the equilibrium constant of the adsorption process is at equilibrium, and the Gibbs free energy (ΔG_{ad}^{0}, kJ/mol) can be calculated using Equation (3.12) (Butt et al. 2003a);

$$\Delta G_{ad}^{0} = -RTlnb^{-1} \quad (3.12)$$

For BET model, the multi-layer adsorption assumption (Brunauer 1938), the nonlinear form of the model was used (Equation 3.13):

$$\frac{\frac{P}{P_0}}{n(1-\frac{P}{P_0})} = \frac{1}{cn_{mon}} - \frac{(1-c)}{cn_{mon}} \times \frac{P}{P_0} \text{ (or) } n = \frac{n_{mon} c \frac{P}{P_0}}{\left(1-\frac{P}{P_0}\right)\left[1-(1-c)\frac{P}{P_0}\right]} \quad (3.13)$$

where n is Adsorbed moles (mol), n_{mon} is Number of moles to cover monolayer adsorption (mol), P is equilibrium pressure (Pa), P_0 is saturation pressure (Pa), c is dimensionless parameter related to heat of adsorption. The c and n_{mon} values were acquired from the plot of $\frac{\frac{p}{p_0}}{n(1-\frac{p}{p_0})} vs \frac{p}{p_0}$, and fit into Equation (3.13) or nonlinerar regression analysis using nonlinear form of Equation (3.13) to validate the model.

The present study also calculated the specific surface area as follows. The surface area of 1 mol of CO_2 in the liquid state is calculated by Equations (3.14) and (3.15) (Yang 1987; Tien 2019);

$$a_s = 1.091 (V_m^L)^{\frac{2}{3}} \quad (3.14)$$

where a_s is effective surface area covered by 1 mol of CO_2 (m^2/mol), V_m^L is liquid molar volume of CO_2 (m^3/mol). The number 1.091 is the packing factor of 12 neighbouring molecules in a bulk liquid and six on a plane (Yang 1987).

$$A_s = a_s \times n_{mon} \quad (3.15)$$

where A_s is Specific surface area (m^2/kg), and n_{mon} is number of moles required to complete the monolayer coverage per kg of coal sample, moles/kg.

3.5 Adsorption kinetics

Data acquired from the experiments was fitted into the pseudo-first-order (PSO) and pseudo-second-order rate Equations (3.16 and 3.17) (Guo 2017; Hu 2020; Liu and Wang 2017).

$$\text{PFO: } q_t = q_e(1 - e^{-k_{a1}t}) \tag{3.16}$$

$$\text{PSO: } q_t = \frac{t}{\frac{1}{q_e}t + \frac{1}{k_{a2}q_e^2}} \tag{3.17}$$

where q_t is mass adsorbed per mass of adsorbent at time t, g of CO_2/kg of coal, q_e is mass adsorbed per mass of adsorbent at time equilibrium, g of CO_2/kg of coal, k_{a1} *is* first-order rate constant, h^{-1}, and k_{a2} is second-order rate constants, kg g^{-1} h^{-1}.

Desorption kinetics data were fitted in to the modified equations of PFO and PSO kinetics models (Equations 3.18 and 3.19). The equations are modified on the basis that the amount of CO_2 adsorbed on the coal is the rate determining factor (Njikam and Schiewer 2012).

$$\text{PFO: } q_t = q_e / e^{k_{d1}t} \tag{3.18}$$

$$\text{PSO: } q_t = \frac{q_e}{(1 + (k_{d2}q_e t)} \tag{3.19}$$

where q_t is mass adsorbed per mass of adsorbent at time t, g of CO_2/kg of coal, q_e is mass adsorbed per mass of adsorbent at time equilibrium, g of CO_2/kg of coal, k_{d1} is first-order rate constant for desorption, h^{-1}. and k_{d2} is second-order rate constants for desorption, kg g^{-1} h^{-1}.

The adsorption experimental data is fit into the Bangham model to predict the influence of the pore diffusion (Equation 3.20) (Bangham and Burt 1924, 1925; Bangham and Sever 1925).

$$q_t = q_e(1 - \exp(-k_b t^n)) \quad (3.20)$$

where q_t is mass adsorbed per mass of adsorbent at time t , g of CO_2/kg of coal, q_e is mass adsorbed per mass of adsorbent at time equilibrium, g of CO_2/kg of coal, k_b (h^{-1}) and n are constants of the model. The adsorption isotherm and kinetics modelling results have been discussed in Chapter 6.

3.6 Coal-water interaction

3.6.1 pH buffering capacity of coal

The water content of coal and the chemical interaction between coal and water would influence its CO_2 adsorption capacity. The injected CO_2 would react with the water present in coal, producing carbonic acid and lowering the pH (Appelo and Postma 2005). The acidic pH of coal can dissolve the minor mineral constituents. Alkaline minerals such as calcium, sodium, potassium, and magnesium would dissolve to neutralise the pH. This behaviour of coal is significant because dissolved CO_2 mineralizes as $CaCO_3$ when it reacts with calcium, affecting the CO_2 adsorption capacity of moist coal. The above-mentioned pH buffering capacity of coal was investigated by equilibrating 10 g of powdered coal sample (size <75μm) with 10 mL of water samples for 24 hours at varying pH values ranging from 2 to 11, the results of which are discussed in Chapter 5.

3.6.2 Water retention behaviour

The water retention characteristics of the coal specimens were experimentally established to understand the influence of coal type on water retention and to study the effect of presence water on the CO_2 adsorption/desorption on coal. Before saturation process of the samples, coal samples were prepared according to the procedure described in section 3.2. then the samples were prepared using the methods explained in the subsequent sections.

3.6.2.1 Preparation of wet powdered coal samples

The powdered coal samples (9ft AB and BP) were mixed manually with various quantities of distilled water to achieve the required water content. Then samples were sealed using polyethylene bags covered with wet clothes and stored in sealed bucket for 24 h to equilibrate. The coal samples were prepared for WP4C test by statically compacting coal-water mixtures at various water contents. The prepared mixtures were statically compacted in WP4C device cups to achieve desired dry densities (Figure 3.10 b). The coal samples were compacted to different dry densities. The achieved dry densities were relatively similar to that of intact coal samples. The targeted dry densities of 9ft AB coal were 1700 kg/m^3 and 900-1000 kg/m^3, while for BP were 1500 kg/m^3 and 1700 kg/m^3 (Figure 3.10).

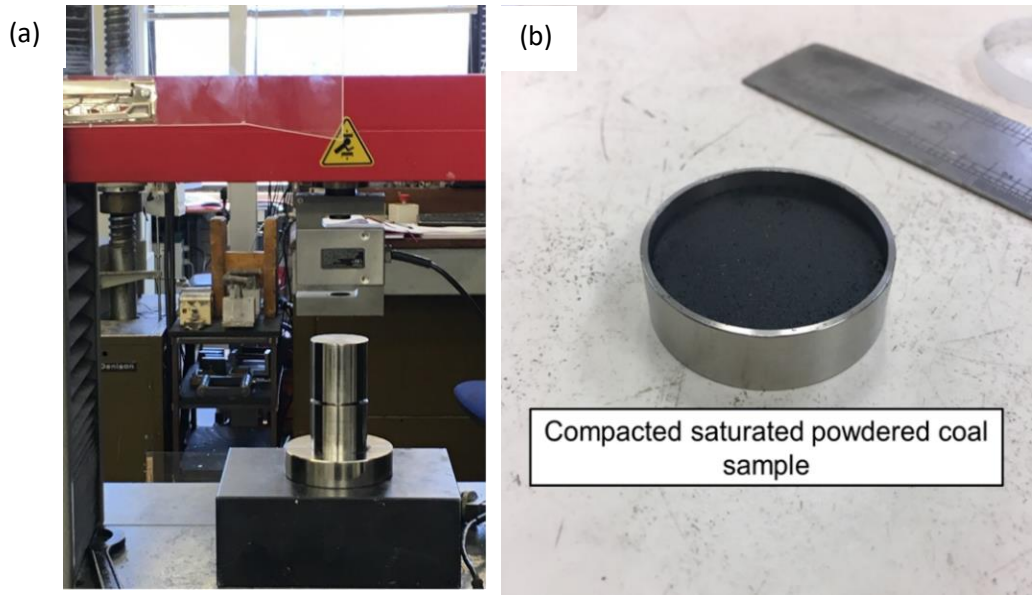

Figure 3.10. (a) static compaction of coal-water mixtures and (b) compacted powdered samples for WP4C.

3.6.2.2 Preparation of wet intact coal samples using oedometer

A commercially available oedometer cell was used in this study (CONTROLS Group Ltd). An intact 9ft AB sample with a dry density of 1380 kg/m^3 was used to study the water retention properties of an intact coal sample. Intact samples were

drilled from the coal blocks using a core drill with a 3.6 cm internal diameter diamond core bit. Upon extraction, cores were cut to a length of approximately 0.5 cm using a diamond saw. The saturation process was done by placing inside the oedometer cell with sand fillings using de-aired water with two ceramic porous stones on top and bottom of the sample. The samples were subjected to a pressure of 1 MPa for at least three weeks. Figure (3.11) shows a schematic diagram of the saturation process using oedometer.

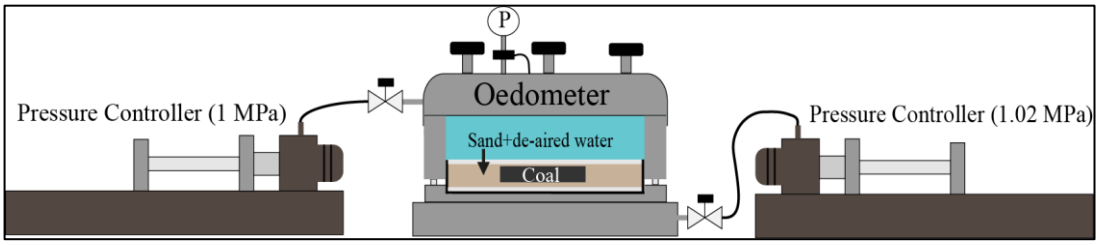

Figure 3.11. schematic for intact coal saturation procedure using oedometer.

3.6.2.3 Preparation of wet intact coal samples using vacuum desiccator

The small, thin, intact core samples were saturated by placing them in test tubes filled with distilled water. Then test tubes were left in a vacuum desiccator and the water content was checked every week (Figure 3.12).

Figure 3.12. Images of vacuum desiccator containing coal disks for water.

3.6.2.4 Suction measurement using Chilled-mirror dew point water potentiometer (WP4C)

The water retention properties of coal samples were determined using the chilled-mirror dew point method specified in American Society for Testing and Materials (ASTM) standards (ASTM D6836-16 2016). Chilled-mirror dew point water potentiometer (WP4C) apparatus has been used to establish suction-water content relationship of soils (Leong et al. 2003; Ferrari et al. 2014; Moghadam et al. 2020; Tripathy et al. 2021). Figure 3.13 shows an image of the chilled-mirror water potential meter (WP4C) apparatus. The WP4C apparatus was calibrated using a 0.5 M KCL solution to obtain a standard total suction value of 2.22 ± 0.05 MPa at 25°C in accordance with ASTM standards (ASTM E104-02 2003).

Coal samples with varying water content were placed in a 40 mm diameter stainless steel container and inserted into the temperature-controlled chamber of the WP4C apparatus, where they were left to thermodynamically equilibrate with the chamber environment. The temperature of the mirror in the chamber is reduced to the dew point by a cooling system, and the first point of condensation on the mirror is detected by a photoelectric cell. A thermocouple and an infrared thermometer are used to measure the dew point temperature and the chamber temperature. From the measured temperatures, the vapour pressure in the chamber and the saturated vapour pressure at the relevant temperature were calculated. Kelvin's equation (Equation 3.21) is used to calculate total suction (Fredlund et al. 2012). The device performs the calculations internally, and the total suction is displayed.

$$\Psi = \frac{RT\rho_w}{\omega_v} \ln\left(\frac{\mu_v}{\mu_{v0}}\right) \qquad (3.21)$$

where Ψ is soil suction (or total suction) (Pa), R is universal (molar) gas constant (8.31432 J/mol.K), T is absolute temperature (K), ρ_w is density of water (kg/m^3), ω_v is molecular mass of water vapor (i.e., 18.016 kg/k mol), μ_v partial pressure of pore-water vapor, (Pa), and μ_{v0} is saturation pressure of water vapor over a flat surface of pure water at the same temperature (Pa).

The procedure was repeated for various coal water contents. The wet coal mass was measured as soon as it was removed from the apparatus. The coal samples were then dried in a hot air oven for 16 hours at 105°C before being removed from the oven and placed in a desiccator to cool. Once the samples had cooled sufficiently, the mass of the dry coal was measured to calculate the water content. The SWCC was calculated by plotting total suctions versus water content of coal samples.

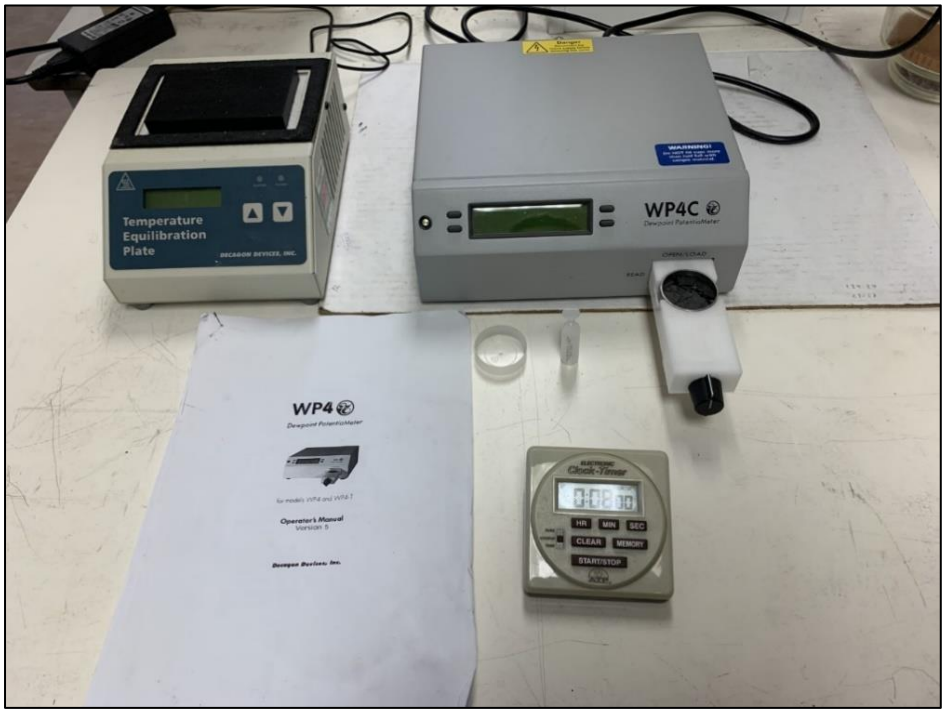

Figure 3.13. Images of chilled-mirror water potentiometer (WP4C) apparatus.

3.7 Outline of the experimental programme

Adsorption experimental plan matrix is presented in Table 3.2. Adsorption experiments were also conducted on rock samples, sand, bentonite, and kaolinite clay minerals, in addition to coal samples. The results are discussed in relevant chapters as follows.

1. Chapter 4 discusses the CO_2 adsorption-desorption experimental results obtained from powdered and intact coal samples,
2. Chapter 5 presents the water retention characteristics and adsorption-desorption experimental results of wet coal samples, and

3. Chapter 7 presents the CO_2 adsorption results obtained from East Irish Sea rock samples, dry sand, wet sand, *Bacillus mojavensis* loaded sand, MX80 bentonite and Speswhite kaolin samples.

Table 3.2. Experimental plan program.

Sample type/ Description	Adsorption	Desorption	WP4C	Sample type/ Description	Adsorption	Desorption
9ft Aberpergwm				Clays		
Powder - dry	x	-	x	MX80 bentonite	x	-
Powder - wet	-	-	x	Speswhite kaolin	x	-
Intact -dry	x	x	x			
Intact -wet	x	-	x			
18ft Aberpergwm				Sand		
Powder - dry	x	x	-	Pure sand - dry	x	-
Powder - wet	x	x	-	Pure sand - Wet	x	x
Intact -dry	x	x	-	Pure sand - with meduim	x	x
Intact -wet	x	-	x	Pure sand - with meduim and bacteria	x	x
Big Pit				East Irish Rocks		
Powder - dry	x	-	x	SSK69016	x	-
Powder - wet	-	-	x	SSK69020	x	-
Intact -dry	x	-	-	SSK69021	x	-

3.8 Concluding remarks

In the framework of CO_2 sequestration in un-mineable coal seams, experimental investigations and characterization methods were developed to meet the objectives. The following is a summary of the materials and methods used in the current study.

Two anthracite coals, a bituminous coal, three rock samples, dry, wet sand and sand loaded with *Bacillus mojavensis* bacteria, MX80 bentonite and Speswhite kaolinite were used as adsorbents in the CO_2 adsorption experiments.

A volumetric/manometric adsorption apparatus was used for CO_2 adsorption experiments. Adsorption-desorption experiments were conducted at pressures ranging from subcritical to near critical (up to 6.5 MPa) at 298.15 K. Desorption tests were carried out following the adsorption tests for the two anthracite coals sand samples. To better understand the rate determining step of CO_2 adsorption and desorption, kinetic data (time versus amount adsorbed) were obtained.

A Chilled mirror dew point water potentiometer WP4C equipment was used to obtain the water retention characteristics curves of coal to gain a better understanding of the water holding capacity of coal, which may affect the CO_2 adsorption characteristics of coal.

To evaluate the adsorption-desorption processes, experimental data were fitted to existing adsorption isotherm models (Langmuir and Brunauer-Emmett-Teller (BET) isotherm models), CO_2 adsorption characteristics curves, and kinetic models (pseudo-first-order, pseudo-second-order and Bangham pore diffusion kinetic models).

The significant findings from the experiments are discussed in Chapter 4, 5,6 and 7.

Chapter 4

CO_2 adsorption and desorption behaviour of coals

4.1 Introduction

Un-mineable coal seams have been considered as one of the potential mediums for carbon dioxide sequestration (Bachu et al. 1996; Metz et al. 2005; White et al. 2005). Therefore, studies related to CO_2 adsorption and desorption behaviour of coal are crucial to understand some key aspects, such as (*i*) the approximate storage capacity in specific coal type, (*ii*) the effect of sample condition (intact and powdered) on the CO_2 adsorption and (*iii*) the effect of subcritical (liquid/gas) pressure range on CO_2 adsorption at 298.15 K.

Manometric, volumetric and gravimetric methods have been widely used for measuring CO_2 adsorption/desorption of coal (Busch and Gensterblum 2011; Mukherjee and Misra 2018; Mosleh et al. 2017; Zagorščak and Thomas 2018). Many studies have been conducted on CO_2 adsorption on powder samples of various coal ranks at varying range of temperature and pressure (Stevenson et al. 1991; Arri et al. 1992; Yee et al. 1993; Hall et al. 1994; Nodzenski 1998; Clarkson and Bustin 1999; Clarkson and Bustin 2000; Busch et al. 2003; Goodman et al. 2004; Ozdemir et al. 2004; Krooss et al. 2002 and Fitzgerald et al. 2005; Mosleh 2014). These studies showed that the adsorption capacity of coal increased simultaneously within subcritical pressure range. While Other studies looked at adsorption behaviour at higher pressures and found that the excess adsorption isotherm showed a declined trend near and above the critical pressure (7.38 MPa at temperature of 304.1K) (Krooss et al. 2002; Fitzgerald et al. 2005; Siemons and Busch 2007; Lee et al. 2013; Zagorščak 2017).

A review of the literature presented in Chapter 2 suggested that most of the experimental investigations so far have mainly focused on gas adsorption capacity and

kinetic measurements of powdered coals. Only a very few investigations on CO_2 adsorption behaviour on intact coal samples have been performed (Pone et al. 2009; Espinoza et al. 2014; Lin et al. 2017; Zagorščak 2017). Powder samples of coal do not represent the actual fabric and structure of insitu coal seams and hence the results obtained from adsorption tests on powder coal samples may not be considered reliable for quantifying the CO_2 adsorption capacity of coal seams. Studies of the CO_2 adsorption and desorption on intact coal samples are crucial as it would provide a good reflection of the insitu conditions. Hence, it would provide a better understanding of the real field process.

The main objectives of the investigation presented in this chapter are:

1. To experimentally investigate the effect of coal sample conditions (powder/ intact) on the CO_2 adsorption behaviour with insight of effects of pressure, temperature, and coal rank (bituminous and anthracite).
2. To experimentally study the carbon dioxide desorption in anthracite coal.
3. To understand the effect of near critical injection pressure (6.1 to 6.4 MPa) at 298.15 K.
4. To study the adsorption-desorption hysteresis to assess the stability of CO_2 within coal pores for anthracite coal.

Section 3.3 of Chapter 3 describes in detail about the coal samples used in experimental investigations, the sample preparation methods, and the methodology adopted for adsorption and desorption experiments. Nonetheless, for the purpose of completeness the key aspects of the experimental investigations and the analysis methods used are summarised in section 4.2.

The results obtained from the adsorption experiments are presented in section 4.3. Section 4.3.1 discuss the effect of sample conditions (intact and powdered) on the CO_2 adsorption capacity. Additionally, this section presents the results from adsorption experiments and covers the parameters that affect CO_2 adsorption, such as coal rank, pressure, and temperature. Section 4.3.2 presents the results obtained for adsorption experiments performed up to near critical pressure range of CO_2 at 298.15 K temperature. Section 4.3.3 presents pressure decay kinetic plots for the adsorption

showing the rate of adsorption at varying equilibrium pressures. The results obtained from desorption experiments are presented in Section 4.4. Adsorption - desorption hysteresis aspect is presented in section 4.4.1. Section 4.4.2 displays the pressure-time curves observed for determining the rate of desorption. Section 4.5 presents the key findings emerged from the chapter.

4.2 Experimental programme

The coal samples were procured from two coal mines from the South Wales Coalfield, Wales, UK. The anthracite coal samples were procured from Aberpergwm coal mine that were from two different coal seams (9ft and 18ft), whereas the bituminous coal samples were collected from Big Pit coal mine.

The intact coal samples were covered with cling film and stored in a wooden box in the laboratory. Coal samples from 9ft Aberpergwm (9ft AB), 18ft Aberpergwm (18ft AB), and Big Pit (BP) were crushed, and sieved as described in Chapter 3, section 3.2. These crushed and sieved samples produced are called powder samples. The gravimetric water contents of the coals were determined using the method described in ASTM standard (ASTM D3173-11 2017). The gravimetric water contents of 9ft AB, 18ft AB and BP samples were 0.9%, 0.78% and 0.96%, respectively. Cores were drilled out of 9ft AB, 18ft AB and BP coal blocks using a core drill machine with diamond saw tip core drilling bit of 50 mm internal diameters. These samples are called as intact samples.

A manometric adsorption apparatus was used in this study to establish adsorption and desorption capacity curves and the data were used to produce the pressure decay curves. The temperature was set to 298.15 K in all experiments and kept constant throughout the tests. The maximum pressure used was about 6.6 MPa. The minimum sample mass required for the apparatus to conduct an adsorption experiment is 0.05 kg. Therefore, all powdered and intact coal samples used were above 0.05 kg in mass. Table 4.1 presents the experiments carried out for each coal sample. Adsorption tests were carried out on both powder and intact samples of all the

selected coals. Due to the lengthy test duration, only three anthracite samples were tested for desorption tests in order to obtain comprehensive desorption data..

Table 4.1. Details of the coal samples that were used for adsorption and desorption tests.

Coal sample/Location	9ft Aberpergwm		18ft Aberpergwm		Big Pit	
Sample description	Powder	Intact	Powder	Intact	Powder	Intact
Adsorption test	x	x	x	x	x	x
Desorption test	-	x	x	x	-	-

The void volumes of the reference cell and sample cell were measured using the helium pycnometry method according to ASTM procedure (ASTM D4892-14 2019; DIN method. 2001. DIN 51913:2001). The calculation of the volumes of reference and sample cells are presented in Chapter 3, section 3.4.1. The calculated void volumes of the reference and sample cells for the tested samples are summarised in Table 4.2. The volume values were later used to calculate the CO_2 adsorption and desorption values as explained in section 4.2.1. Samples were vacuumed at -100 kPa for 24 hours before and after the helium pycnometry test to remove any residual gases from the system. The system was injected with CO_2 gas with an increasing pressure in a step-wise manner from 0.5 to 6.5 MPa followed by decreasing the pressure step-wise to study the adsorption and desorption behaviour CO_2 in coal.

Table 4.2. Void volume of various coal samples measured by helium pycnometry.

Sample condition	Reference Cell Void Volume, V_R (m^3)	Sample Cell Void Volume, V_S (m^3)	Reference + Sample Cells Void Volume, V_{R+S} (m^3)
9ft Aberpergwm			
Powder	165.52×10^{-6}	132.07×10^{-6}	297.64×10^{-6}
Intact	166.18×10^{-6}	85.61×10^{-6}	251.76×10^{-6}
18ft Aberpergwm			
Powder	165.55×10^{-6}	109.83×10^{-6}	274.93×10^{-6}
Intact	165.02×10^{-6}	89.13×10^{-6}	254.13×10^{-6}
Big Pit			
Powder	165.64×10^{-6}	127.78×10^{-6}	293.32×10^{-6}
Intact	165.56×10^{-6}	107.79×10^{-6}	272.85×10^{-6}

4.2.1 Method of analysis

The amount of CO_2 gas adsorbed on coal can be categorized as (*i*) the absolute adsorption, (*ii*) the Gibbs excess adsorption, and (*iii*) the net adsorption. The Gibbs excess and the net adsorption are measured by experimental means, whereas the absolute adsorption requires detailed analysis of the pore volume of the adsorbents. Thorough discussion on the experimental procedures and calculation methods along with the gas physical adsorption data have been presented by Keller and Staudt (2005), Gregg and Sing **(**1982); Ruthven (1984), Rouquerol et. al. (1999), Sing et al. (1984), Sing et al. (1994), Myers and Monson (2014) and Toth (2012).

The Gibbs excess adsorption is calculated using the results obtained from the manometric experiments as described in the previous section and Chapter 3 (section 3.4). The amount of CO_2 adsorption and desorption can be calculated as follows.

$$n_{equ,ad}^{CO_2} = \frac{n_t^{CO_2} - \frac{p_{eq}^{CO_2}}{RTZ_{(p,v)}} v_d}{m_s} \quad \text{the amount adsorbed} \qquad (4.1)$$

$$n_{equ,de}^{CO_2} = \frac{\frac{p_{eq}^{CO_2}}{RTZ_{(p,v)}} v_d - n_t^{CO_2}}{m_s} \quad \text{amount desorbed} \qquad (4.2)$$

where $n_{equ,ad}^{CO_2}$ is number of moles of CO_2 at equilibrium stage (mol/kg), v_d is void volume available for gas (m^3) (v_d = sample cell volume with sample loaded + reference cell volume), $p_{eq}^{CO_2}$ is equilibrium pressure of CO_2 (Pa), Z is compressibility factor of CO_2, and R is gas constant 8.314 (Pa m^3)/(K mol), T is temperature (298.15 K), m_s is mass of adsorbent (kg) and $n_t^{CO_2}$ is the known amount present in the gas phase at the beginning of the adsorption experiment (mol).

Considering the P-V-T (pressure, volume and temperature) behaviour of CO_2 and for the convenience of substituting the gas pressure data obtained from the experiments and the compressibility factor in the current study, Equation (4.2) was modified to account for the experimental parameters, as shown below.

$$n_{CO_2 ad.} = \frac{\left(n_{CO_2 rc_0} + n_{CO_2 sc_0}\right) - \left(n_{CO_2 [rc+sc]_{equ}}\right)}{m_s} \qquad (4.3)$$

where $n_{CO_2 ad.}$ is the moles adsorbed over kg mass of adsorbent, (mol)/kg, $n_{CO_2 rc_0} + n_{CO_2 sc_0}$ is the number of moles in RC+SC at the beginning of each stage, and $n_{CO_2 [rc+sc]_{equ}}$ is the number of moles in RC+SC at the end of each stage (equilibrium).

The number of moles of CO_2 in the reference cell (RC) and sample cell (SC) were calculated using the real gas law (Equation 4.4).

$$n_{CO_2 rc_0} = \frac{p_{rc} V_{rc}}{Z_{rc} RT} \;;\; n_{CO_2 sc_0} = \frac{p_{sc} V_{sc}}{Z_{sc} RT};\; n_{CO_2 [rc+sc]_{equ}} = \frac{p_{rc+sc} V_{rc+sc}}{Z_{rc+sc} RT} \qquad (4.4)$$

where $n_{CO_2 rc_0}$ is the number of moles of CO_2 in RC at the beginning of each stage (mol), $n_{CO_2 sc_0}$ is the number of moles of CO_2 SC at the beginning of each stage (mol), $n_{CO_2 [rc+sc]_{equ}}$ is the number of moles at the end of each equilibrium stage (mol), P_{rc}+P_{sc} is the sum of pressures in RC and SC (Pa), V_{rc} and V_{sc} are the volumes of RC

and SC (m^3) and Z_{rc} and Z_{sc} are the compressibility factors for RC and SC, respectively.

Each data point presented in the adsorption and desorption isotherm patterns in this chapter was calculated as described. The compressibility factor can be calculated using an appropriate equation of states or from the experimentally derived generalised compressibility factor charts (Rao 1997, Elliott and Lira 2012). Not many CO_2 adsorption experiments performed at 298.15 K have been reported in previous studies. At 298.15 K and in the near critical pressure range (6.1 MPa to 6.4 MPa), the coexistence of the gaseous and liquid phases of CO_2 is unavoidable. This can be defined as the problem of estimating the right amount of injected moles in RC and finally the amount of CO_2 adsorbed. This basic thermodynamic behaviour of CO_2 under certain state functions (pressure-volume-temperature) was anticipated (Engel and Reid 2019) and confirmed by control experiments performed at 6.1 MPa to 6.4 MPa. The current study resolves this difficulty by developing a simple method to calculate the volume fractions and molar volume of liquid and gaseous CO_2 calculation based on Peng-Robinson Equation of State.

4.3 Adsorption behaviour

This section presents the experimental results of carbon dioxide adsorption tests in various types of coal. The effects of sample conditions (powder and intact) and coal rank are presented in section 4.3.1. The rate of adsorption and the pressure decay kinetics curves during the adsorption experiments are presented in section 4.3.2.

4.3.1 Effect of sample conditions (powder and intact) and coal rank

Gas adsorption in porous media occurs through the bulk diffusion of gas molecules into the porous medium surface, followed by migration into the pores, where they are attached by adsorption forces to form monolayers or multilayers. Adsorption in coal is controlled by micropore-filling process (Mazzotti et al. 2009). Swelling behaviour exhibited by coal affects the adsorption capacity (Harpalani 1995;

George and Barakat 2001; Ozdemir et al. 2004; Zutshi and Harpalani 2004). The magnitude of swelling depends upon the coal rank and usually high in bituminous coal and low in anthracite and lignite coals. The swelling deformation is linearly related to pressure and inversely related to temperature and reflects on the adsorption capacity (Walker et al. 1988; Ranathunga et al. 2017; Mukherjee and Misra 2018).

Figures 4.1, 4.2 and 4.3 present the equilibrium pressure versus CO_2 adsorbed by 9ft AB, 18ft AB and BP coal samples, respectively. In each case the adsorption behaviour of powder and intact samples are shown. The maximum applied pressure was less than 5.0 MPa in each case. Additionally, the adsorption test results of 9ft AB coal (both powder and intact) reported by Zagorščak (2017) are shown in Figures 4.4 and 4.5 for comparison.

It can be seen in Figures. 4.1 to 4.3 that, the amount of CO_2 adsorbed increased with an increase in the injection pressure for all coal types. The powder samples of 9ft and 18ft AB coal exhibited a greater CO_2 adsorption capacity than the intact samples (Figures 4.1 and 4.2). In contrast, the trend was reversed in the case of the Big Pit coal, where the intact sample exhibited a greater CO_2 adsorption capacity than the powder sample (Figure 4.3). With an increase in the injection pressure, the difference between the CO_2 adsorption capacities of intact and powder coals increased.

Table 4.3 shows the adsorbed amount of CO_2 in the coal samples at the maximum applied injection pressures adopted in the tests. It can be seen in Table 4.3, the CO_2 adsorption capacities of powder samples of the 9ft and 18ft AB coal were about 21% and 36% higher than that of intact samples, respectively. The results show that more adsorption sites are available in the powdered samples compared with the intact samples. The case is different when comparing powder and intact for bituminous BP samples. The effect of swelling and microporous structure on adsorption capacity was comparatively less in anthracite coal than bituminous (Harpalani 1995; George and Barakat 2001; Ozdemir et al. 2004; Zutshi and Harpalani 2004) and hence, the intact bituminous (BP) coal has higher adsorption capacity than the powdered coal (Figure 4.3).

The CO_2 adsorption capacity of powder sample of BP coal was 16% lower than the intact sample for experiments conducted up to equilibrium pressures of 3.6 MPa. Similar behaviour for bituminous coal has been reported by Pone et al. (2009), where the adsorption capacity of powdered sample was 14% lower than the intact sample at applied pressure of 3.1 MPa. Zhao et al. (2014) reported that bituminous coal has channel-like and interconnected pores. Such pore structures are observed for both high- and low-volatile bituminous coals. Xu et al. (2015) and Tan et al. (2018) suggested that during sample grinding process, powdered samples lost most of the macropores and the fracture network. The porous matrix difference between the intact and powdered resulted in higher adsorption capacity observed in intact than the powdered sample.

The bituminous BP intact coal sample showed similar adsorption capacity of 1.15 mol of CO_2/kg (84% carbon) to that of the anthracite 18ft AB coal (92% carbon content) samples with adsorption capacity of 1.11 mol of CO_2/kg of coal and lower than the 9ft AB (89% carbon) anthracite sample (1.6 mol of CO_2/kg) (Table 4.3; Figure 4.4). The adsorption capacities of the samples correlated with respective carbon content and coal pore structure.

Table 4.3. Summary of carbon dioxide adsorption capacity of 9ft Aberpegwm, 18ft Aberpergwm and Big Pit coal samples for subcritical and near-critical pressure ranges.

Sample size	Adsorption capacity for sub critical pressure (< 6.1MPa) (mole/kg)	Powder / intact percentage difference %	Adsorption capacity for near-critical pressure (6.1 - 6.5 MPa) (mole/kg)	Powder / intact percentage difference %
9ft Aberpergwm				
Powder	1.937	21%	-	
Intact	1.597		-	
18ft Aberpergwm				
Powder	1.494	36%	1.843	45%
Intact	1.115		3.328	
Big Pit				
Powder	0.966	16%	-	
Intact	1.15		-	

The results from the adsorption tests clearly showed that the powdered and intact samples of coals considered in this investigation exhibited different adsorption capacities. Therefore, testing intact samples is more appropriate for determining the adsorption capacity since it reflects the fabric and structure of in-situ coal seam.

To explore the effect of temperature on CO_2 adsorption, the adsorption isotherm (at 298.15 K) of powdered and intact samples of 9ft AB were compared with the experimental results reported by Zagorščak (2017) at temperature of 313 K. A difference in the CO_2 adsorption capacity can be noted for the 9ft AB powder coal sample in this study (1.9 mol/kg) and that reported by Zagorščak (2017) (1.82 mol/kg) at the maximum applied pressure of 3.5 MPa (Figures. 4.4). Similarly, at a pressure of 3.5 MPa, a difference in the adsorption capacity can be noted for the intact sample in this study (1.6 mol/kg) and that reported by Zagorščak (2017) (0.75 mol/kg) (Figure 4.5). A comparison of the results indicated that the adsorption capacity of the coal decreased upon increasing temperature which is in line with studies reported by Krooss et al. (2002), Busch et al. (2004), Ottiger et al. (2006), Li et al. (2010), Zhang et al. (2011), Weniger et al. (2012), Santarosa et al. (2013) and Mukherjee and Misra (2018).

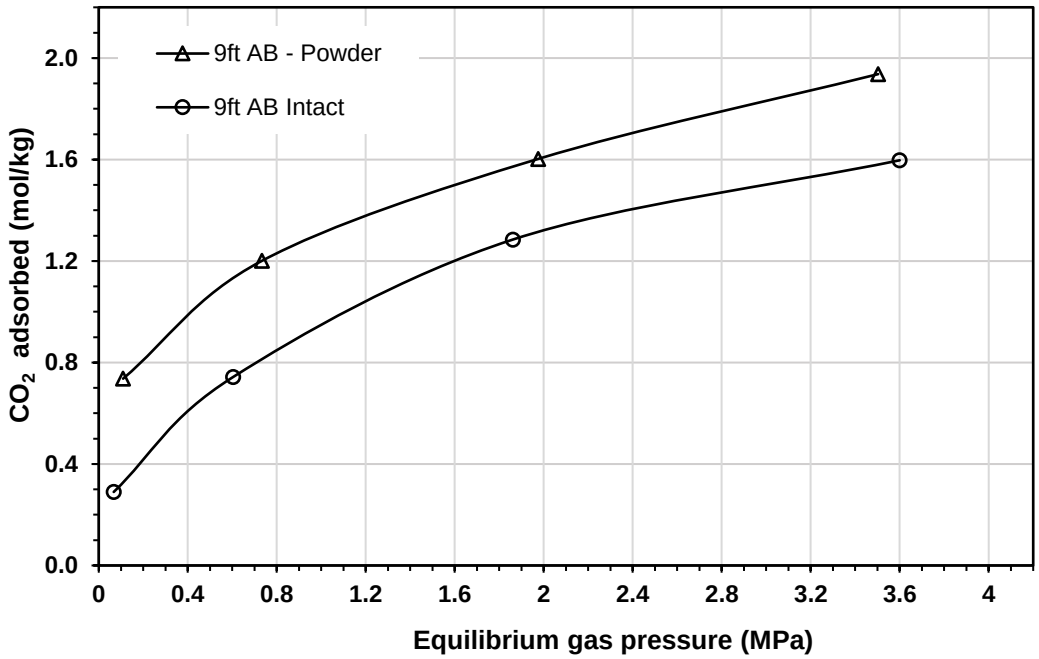

Figure 4.1. CO_2 adsorption isotherm of 9ft Aberpergwm coal samples (powder and intact).

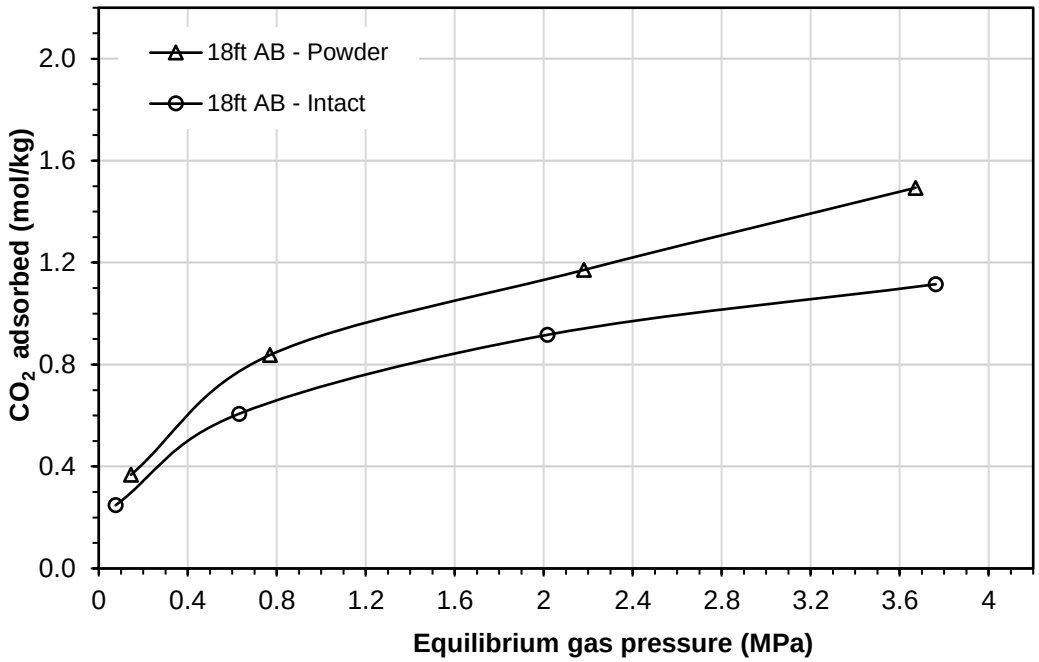

Figure 4.2. CO_2 adsorption isotherms of 18ft Aberpergwm coal samples (powder and intact).

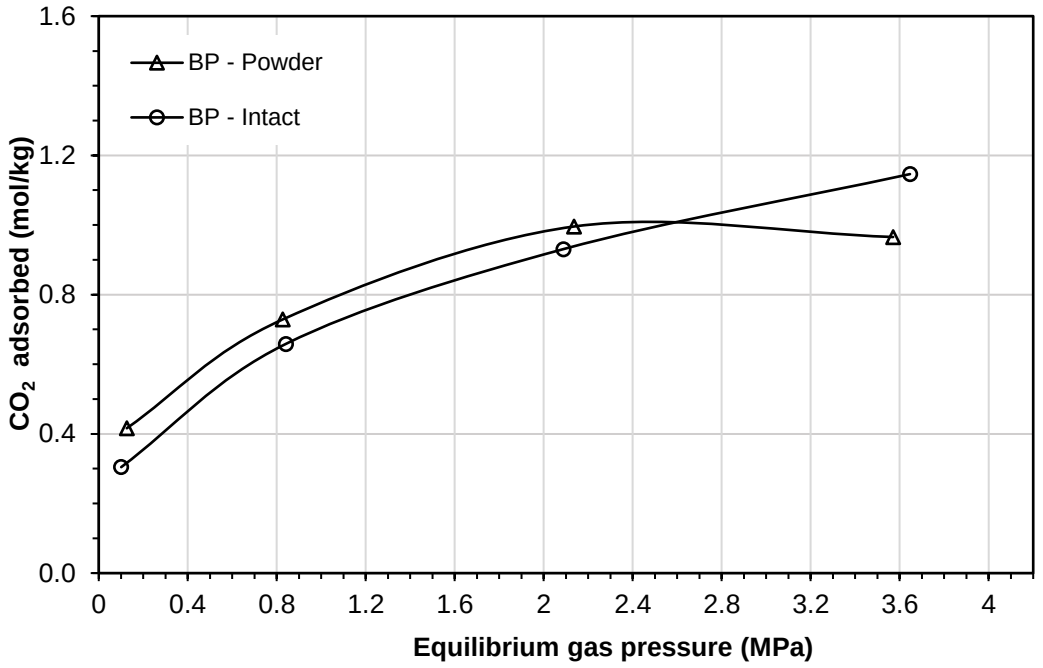

Figure 4.3. CO_2 adsorption isotherm of Big Pit coal (powder and intact).

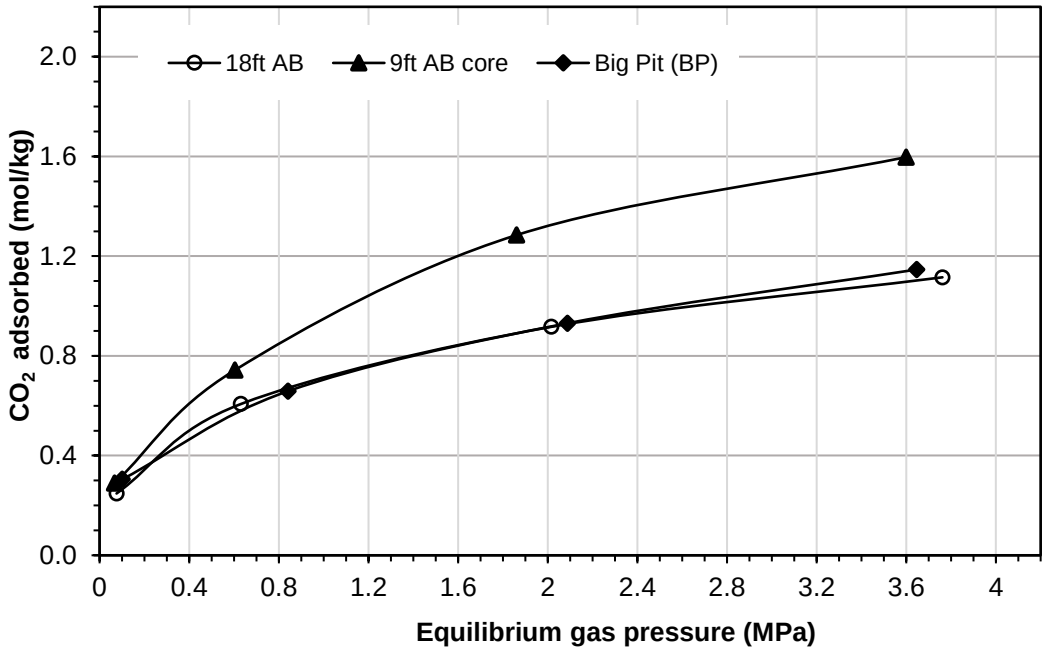

Figure 4.4. CO_2 adsorption isotherm of intact 9ft Aberpergwm, 18ft Aberpergwm and Big Pit coal.

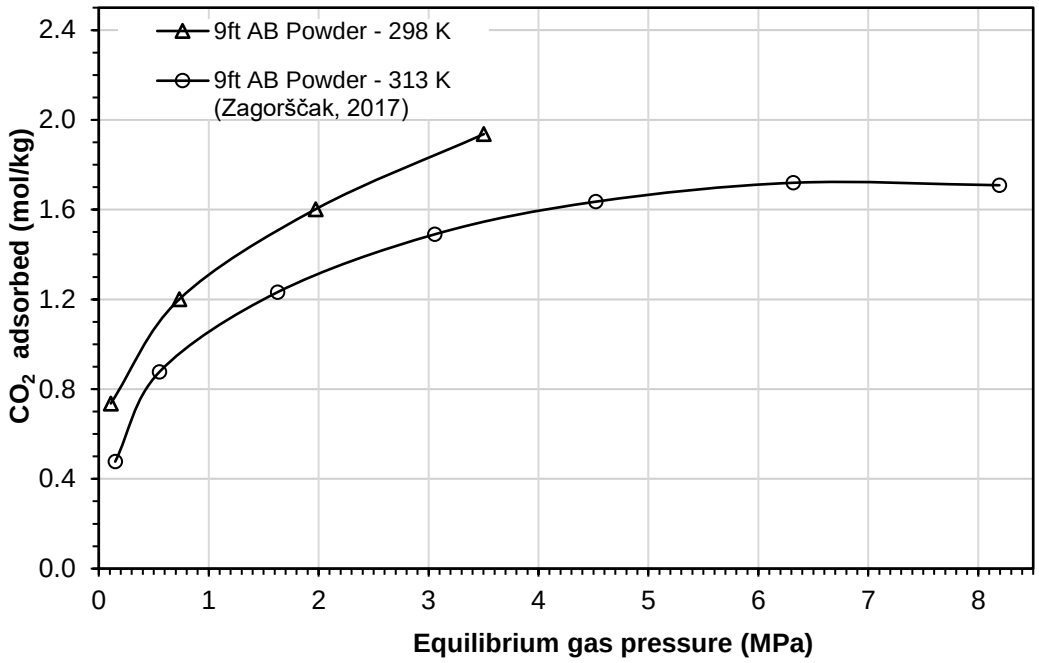

Figure 4.5. Adsorption isotherms of powder samples of 9ft Aberpergwm coal at temperatures of 298.15 K and 313 K

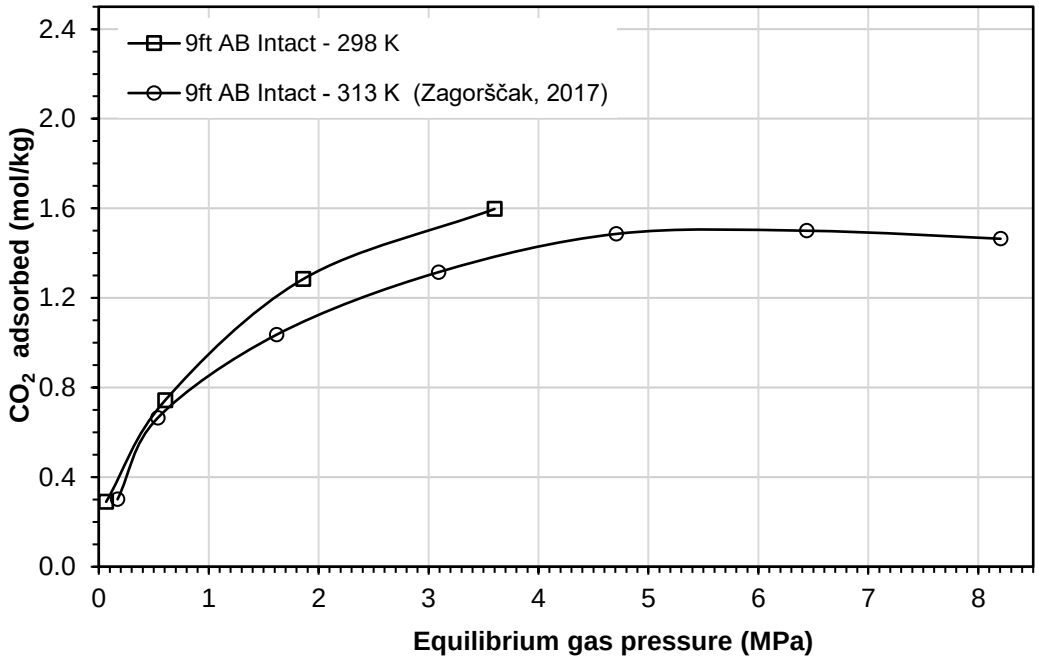

Figure 4.6. Adsorption isotherm of intact 9ft Aberpergwm coal at temperatures 298.15 K and 313 K.

4.3.2 Effect of near critical injection pressure (6.1 to 6.4 MPa) at 298.15 K

The injection-pressure is considered as one of the key parameters that affects the adsorption capacity of coals. For pressures lower than the critical pressure, only gas phase would be exist in the system. At higher pressures, that is, near the critical region, the co-existence of liquid and vapour phases of CO_2 is evident. In order to study the effect of injection pressure on CO_2 adsorption, experiments were carried out on intact and powder 18ft AB coal for injection pressure range of 0.5 to 6.4 MPa.

At injection pressure above 6.1 MPa up to 6.4 MPa, that is, the region of near critical pressure for CO_2 at temperature of 298.15 K, isothermal compression occurs in the RC forming both liquid and gas CO_2 of different volumes. This effect will reflect on calculating the accurate amount of CO_2 injected in RC since the molar volume of liquid and gas phases differ. Therefore, the fractions of liquid and gas volume were calculated using Peng-Robinson equation of state as described in section 4.2 and chapter 3 (section 3.3.4). The liquid fraction was approximately 0.28 and the volume fraction of gas was 0.72 and the molar volume of the liquid CO_2 is 70.42 cm^3/mol and molar volume of vapour phase CO_2 is 181.18 cm^3/mol. The calculated molar volumes of liquid and gas phase were used to calculate the accurate amount of CO_2 injected in the RC. After connecting the RC and the SC, isothermal expansion that occurred in the system formed only gas phase of CO_2 (liquid CO_2 evaporates).

The adsorption isotherms at high injection pressures (>6.1 MPa) were established based on the fundamental principles of gas thermodynamics as described above. The adsorption isotherms of 18ft AB powder and intact coal for an injection pressure range of 0.5 MPa to 6.4 MPa are presented in Figure 4.7. It can be seen from Figure 4.7 that the 18ft AB intact specimen showed maximum capacity of 3.328 mol of CO_2/kg of coal and the powdered specimen exhibited 1.843 mol of CO_2/kg of coal. It is noted that, at lower pressures (<6.1 MPa), the powdered sample showed higher adsorption capacity than the intact sample. However, at near critical injection pressure range (6.1 to 6.4 MPa), the intact sample showed higher adsorption capacity than the powder. This is due to pore diffusion and condensation occurs and CO_2 adsorb at higher density in the microfractures of intact samples and signify the influence of the

coal samples physical nature. This mechanism further explained in Chapter 4.4 (section 4.4.1) with desorption data and in Chapter 6.6 (section 6.5) with desorption kinetics data.

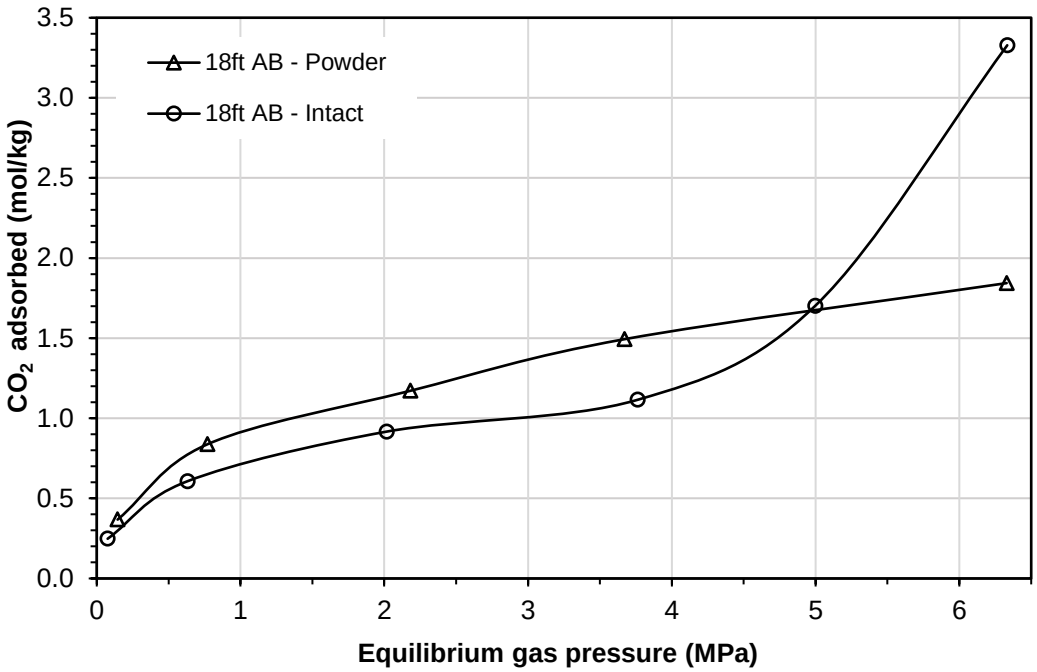

Figure 4.7. CO_2 adsorption isotherm of 18ft Aberpergwm coal powder and intact for injection pressure up to 6.5 MPa.

4.3.3. Pressure decay curves of CO_2 Adsorption experiments

The pressure-time curves are crucial for understanding the rate of CO_2 adsorption in coals. Knowledge of the adsorption rate plays a significant role in designing the injection process in the field. The patterns provide general idea of the equilibrium pressure and equilibrium time for the corresponding injection pressures. Therefore, pressure versus time data has significant usage in designing the field injection and monitoring strategy.

For ease of understanding, representative plots (pressure-time curves) of 18ft AB powder and 18ft AB intact are presented in this section to compare the rate of CO_2 adsorption by intact and powdered samples.

For powdered and intact 18ft AB, four to six steps of injection pressure were applied (0.6, 1.5, 3, 4.5, 5.5, 6.5 MPa) and the pressures in both RC and SC were monitored after connecting the RC to SC. The pressure spikes related to the adiabatic (Joules-Thomson) cooling of the injected gas, which would appear for a few seconds immediately after connecting the adsorption cells, have been removed from the results.

Figures 4.8 to 4.13 show the pressure-time response of the powder and intact samples of 18ft AB coal. It can be seen across all stages that the powdered samples needed shorter time to reach equilibrium than the intact sample as shown in the Table (4.4). The pressure vs time experimental data observed for the adsorption tests were converted to amount of CO_2 adsorbed on coal and fitted to adsorption kinetic models (pseudo-first order and pseudo-second order) to obtain the rate constants and to predict the adsorption rate determining step. The results were discussed in Chapter 6 along with adsorption isotherm model

Table 4.4. Equilibrium time for each injection pressure step for 18ft Aberpergwm (powder and intact).

Sample condition	Pressure range (MPa) (Injection pressure – Equilibrium pressure)	Time to reach equilibrium (h)
18ft Aberpergwm - Powder	0.68 - 0.15	15
	1.65 - 0.77	20
	3.22 - 2.18	20
	4.52 - 3.67	17
	6.34 - 6.33	2
18ft Aberpergwm - Intact	0.58 - 0.08	24
	1.53 - 0.63	24
	3.04 - 2.02	25
	4.60 - 3.76	25
	5.52 – 5.00	25
	6.35 - 6.33	10

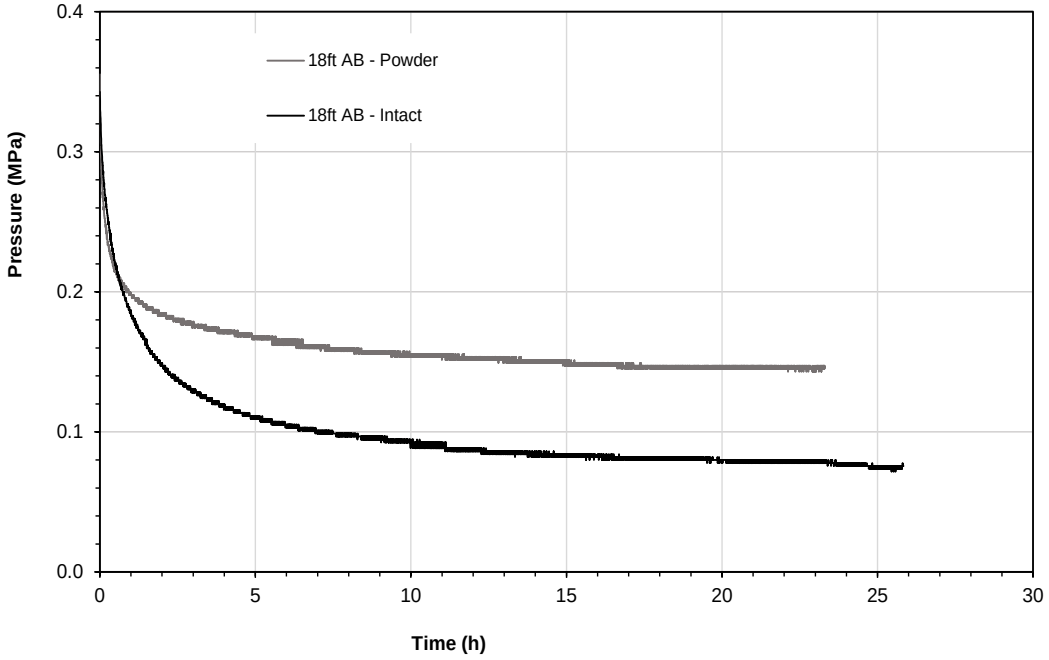

Figure 4.8.Pressure decay curves for powder and intact 18ft Aberpergwm samples - Injection pressure of ≈0.6MPa at 298.15K.

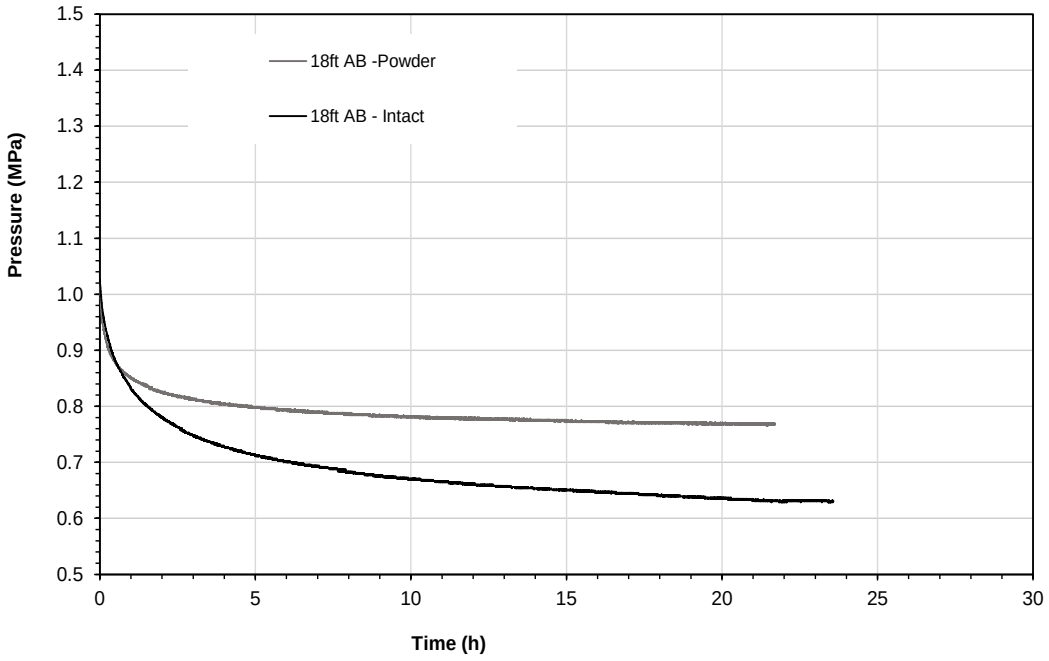

Figure 4.9. Pressure decay curves for powder and intact 18ft Aberpergwm samples - Injection pressure of ≈1.6MPa at at 298.15K.

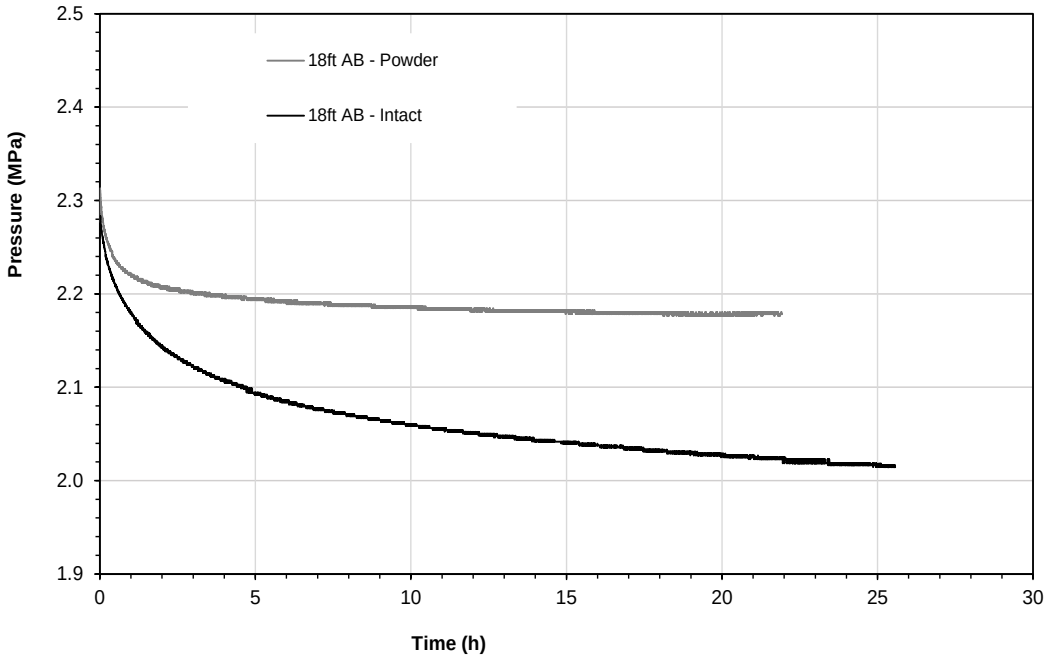

Figure 4.10. Pressure decay curves for powder and intact 18ft Aberpergwm samples - Injection pressure of ≈3 MPa at 298.15K

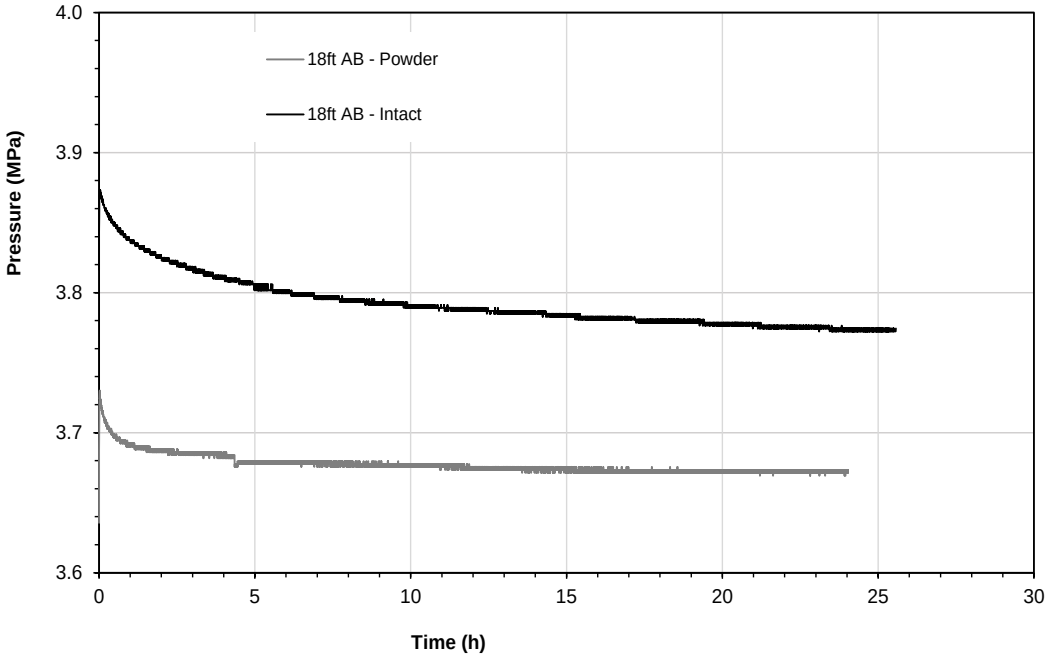

Figure 4.11. Pressure decay curves for powder and intact 18ft Aberpergwm samples - Injection pressure of ≈4.5MPa at 298.15 K.

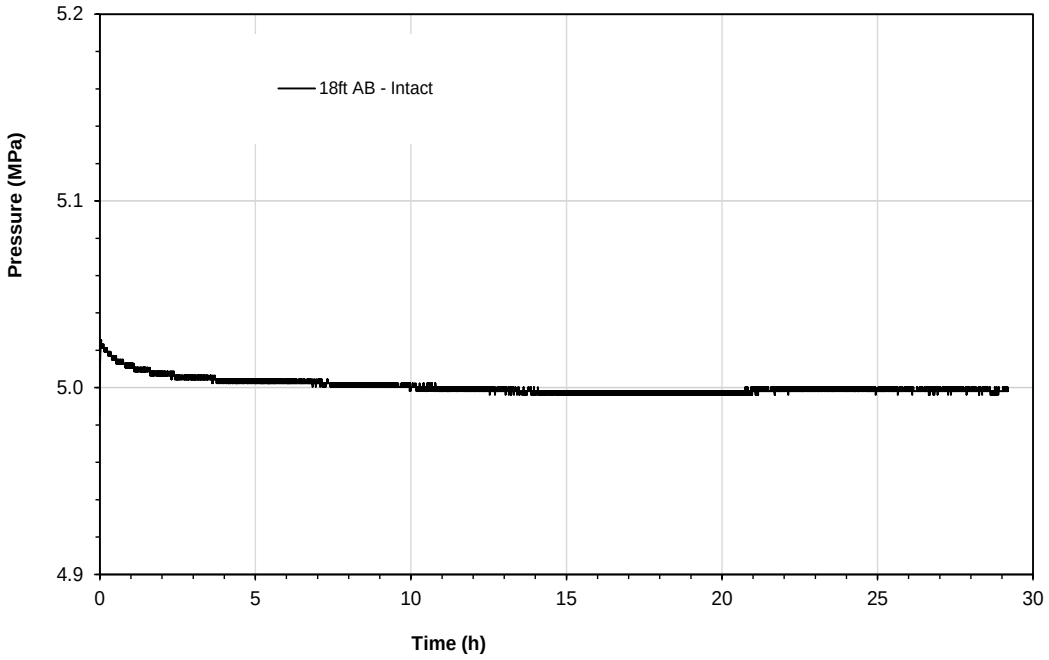

Figure 4.12. Pressure decay curves for powder and intact 18ft Aberpergwm samples - Injection pressure of ≈5.5MPa at 298.15 K.

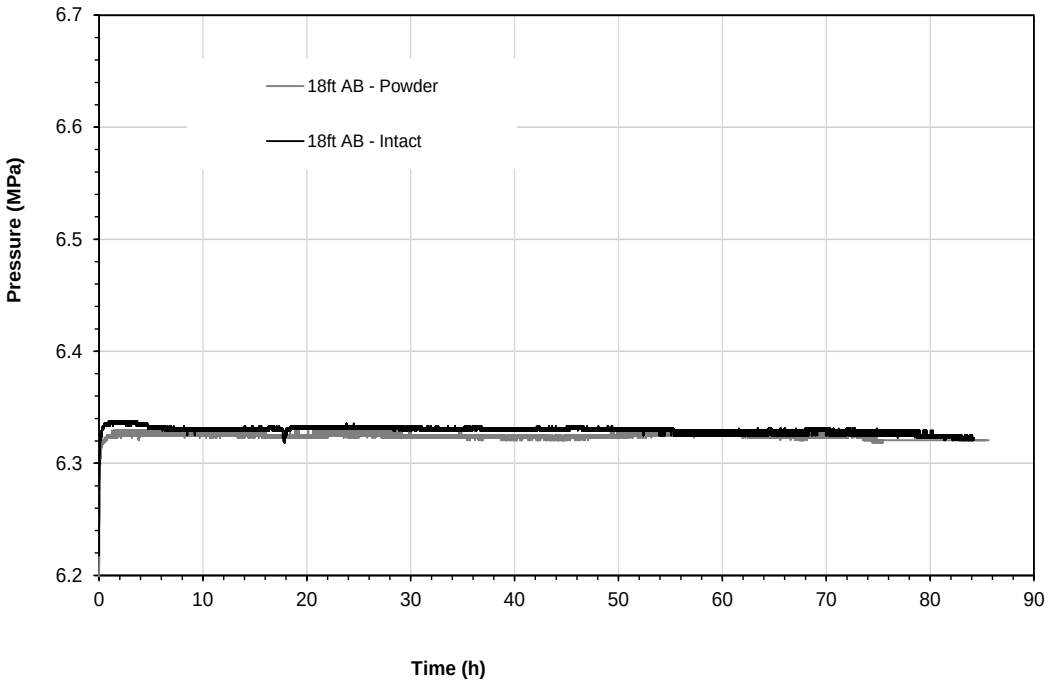

Figure 4.13. Pressure decay curves for powder and intact 18ft Aberpergwm samples - Injection pressure of ≈6.3MPa at 298.15 K.

4.4 Desorption Behaviour

This section presents carbon dioxide desorption behaviour of anthracite coal (intact 9ft AB, powder and intact 18ft AB) (section 4.4.1). The pressure versus time curve obtained during desorption experiments were presented in section 4.4.2 to understand the rate of desorption at each step-down pressure stage.

4.4.1 CO_2 adsorption –desorption hysteresis

The reversibility of CO_2 physical adsorption was studied by performing desorption experiments. Desorption experiment was conducted after completing the adsorption experiments on the same coal sample. Desorption characteristics of CO_2 from the coal samples were established by progressively decreasing the pressure in a stepwise manner and determining the adsorbed amount of CO_2. This section also discusses the effect of near critical (6.1 MPa and 6.4 MPa) pressure on the adsorption-desorption of CO_2 on anthracite 18ft AB coal samples, both intact and powdered.

A review of the literature suggested that the desorption patterns do not track back the adsorption isotherm pattern, but lie above the adsorption isotherm plots, often called hysteresis loops. The hysteresis arises when the amount of CO_2 adsorbed at a given equilibrium pressure during the adsorption process is different than the amount of CO_2 desorbed at the same equilibrium pressure (Sing et al. 1985; Rouquerol et al. 1999). The hysteresis loops are primarily associated with the filling and emptying of adsorbates in and out of the pores and the fractures of adsorbents (Busch et al. 2003; Ren et al. 2022).

The adsorption and desorption isotherms of intact 9ft AB, intact 18ft AB and powdered 18ft AB coal samples are presented in Figures 4.14, 4.15 and 4.16. The amount of CO_2 adsorbed during desorption was not the same as the amount of CO_2 measured during the adsorption process. Figures 4.14 to 4.16 showed that, at the same equilibrium pressures the amount of CO_2 adsorbed during desorption was higher than the amount of CO_2 adsorbed. The positive deviation in the hysteresis indicates that some amount of CO_2 still adsorbed in the porous structure of the coal. This pattern

also depicts the Type II and H3 adsorption-desorption pattern described by IUPAC classification for pore diffusion/condensation dominated adsorption process (Sing et al. 1985; Thommes et al. 2015), see Chapter 2, section 2.4.

Comparing the powder and intact samples of 18ft AB for the experiments conducted up to 6.4 MPa, the adsorption hysteresis patterns differ attributing to high dense adsorbed phase formation in intact coal fracture system and micropores. Comparatively the lower adsorption capacity observed with powdered 18ft AB shows the effect of the physical nature of the intact sample and the effect of near critical pressure range (6.1 MPa to 6.4 MPa; liquid and gas coexistence) CO_2 adsorption at 298.15 K (Figures 4.15 and 4.16).

The adsorption-desorption hysteresis patterns were found to be consistent with previous work (Busch et al. 2003; Ozdemir et al. 2004; Harpalani et al. 2006; Pan et al. 2010; Dutta et al. 2011; Mukherjee and Misra 2018). The current study experiments and findings reveal that the physical nature of coal and the thermodynamic nature of CO_2 provide a pathway to a deep pore matrix in which CO_2 molecules are trapped. Because CO_2 can enter through supermicropores (<2 nm), the ink bottle effect was observed in the hysteresis pattern of both intact and powdered samples (Ren et al. 2022). As a result, the slow release of CO_2 trapped in the pores is observed as a positive deviation in the adsorption-desorption hysteresis pattern.

Moreover, it is important to calculate the residual amount of CO_2 remained in the coal during desorption to ascertain the CO_2 trapping capability of the coal seams. The residual values for intact 9ft AB, intact18ft AB and powder 18ft AB coal samples were 1.05 mole/kg, 0.9 mole/kg and 1.18 mole/kg, respectively. The higher residual amount of CO_2 adsorbed for the powdered sample for the 18ft AB was attributed to the adsorption of CO_2 in the exposed (when the samples are powdered) super micropores (<2 nm) and evidence of ink bottle effect (Pajdek et al. 2019).

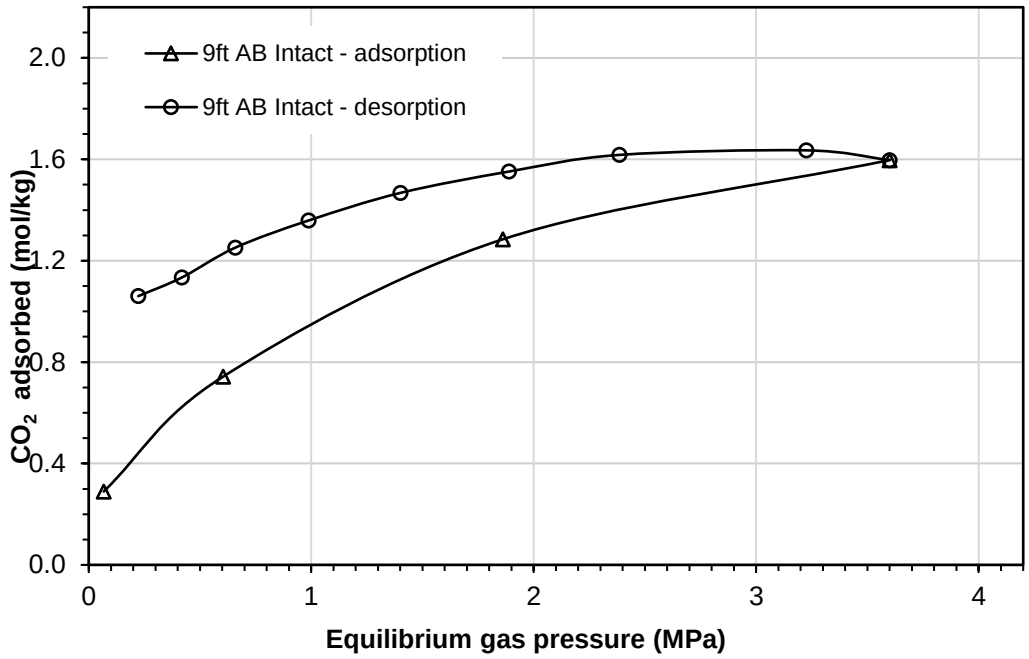

Figure 4.14. CO_2 adsorption and desorption behaviour of intact 9ft Aberpergwm coal.

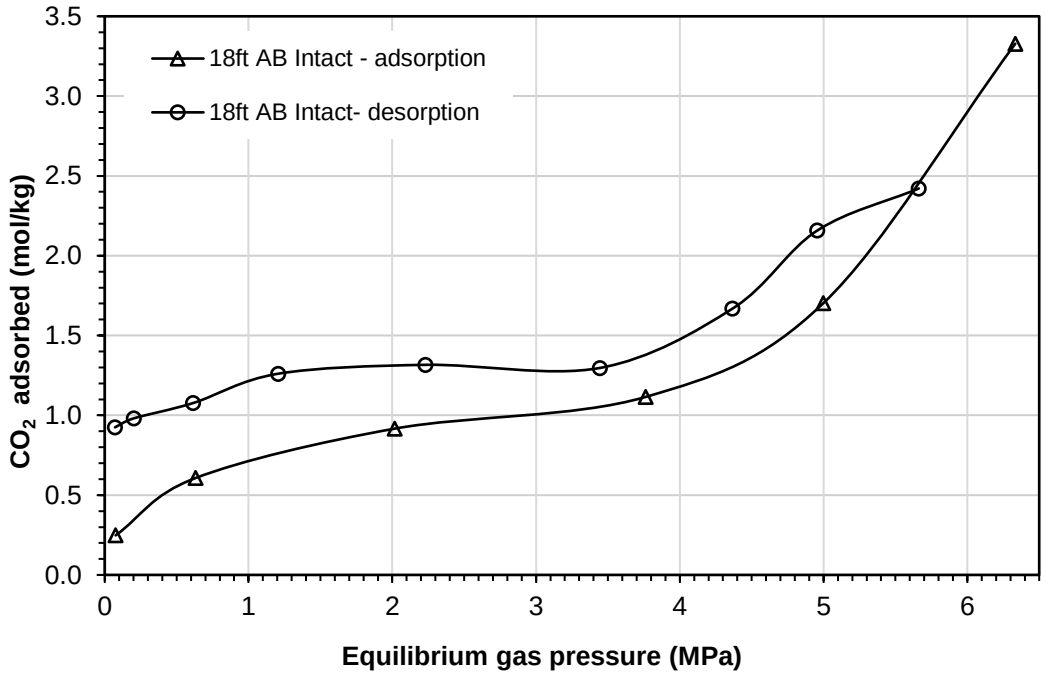

Figure 4.15. CO_2 adsorption and desorption behaviour of intact 18ft Aberpergwm coal

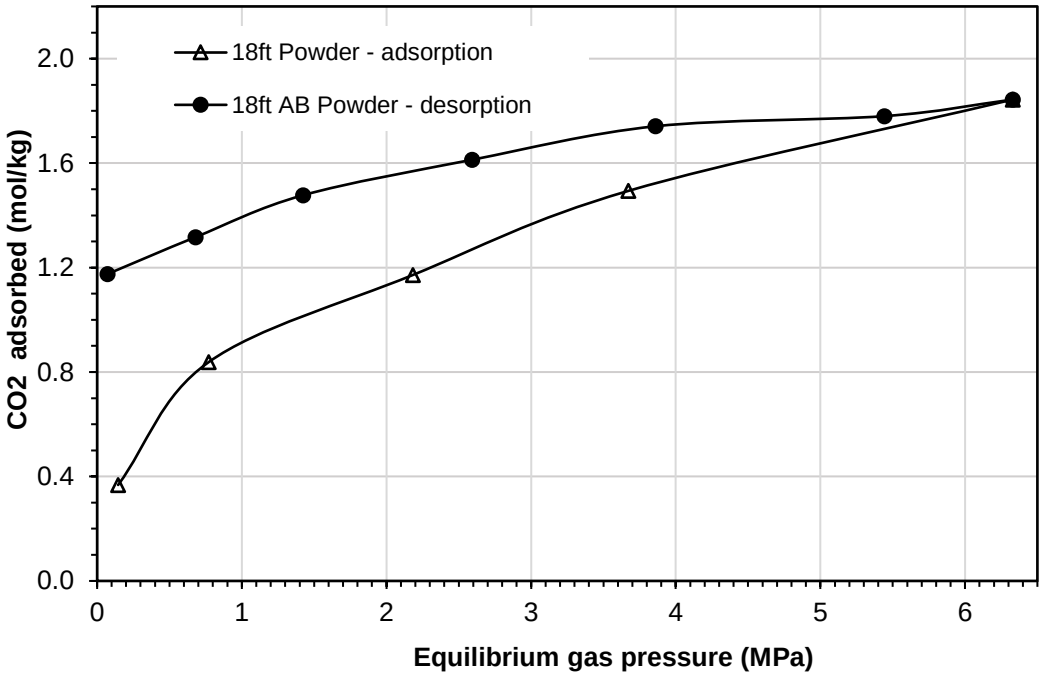

Figure 4.16. CO_2 adsorption and desorption behaviour of powdered 18ft Aberpergwm.

4.4.2 CO_2 desorption pressure-time curves

During the desorption experiments, the pressure increases in the adsorption cell recorded for every 10 seconds. The pressure-time curves are monitored in order to explore the rate of desorption. The most important observation of the pressure-time data is to determine the residual gas molecules trapped in the coal, which provide the pore-trapping capabilities of the specific coal sample.

Figures 4.17 to 4.24 present the pressure versus time data for the 9ft AB intact coal sample during the desorption experiments. Table 4.5 presents the injection pressures and equilibrium time to attain the corresponding equilibrium.

Table 4.5. Equilibrium time for each gas release pressure step for 9ft Aberpergwm (intact).

Sample description	Pressure range (MPa) (Releasing pressure – Equilibrium pressure)	Time to reach equilibrium (h)
9ft Aberpergwm - Intact	3.06 - 3.23	23
	1.87 - 2.39	20
	1.54 - 1.89	18
	1.00 - 1.40	18
	0.60 - 0.99	17
	0.31 - 0.66	10
	0.10 - 0.42	23
	0 - 0.22	21

Figure 4.17 showed a pressure decrease with time pointed to a minor adsorption occurred rather than desorption at first gas release stage. Whereas, in Figures 4.18 to 4.24, pressure increasing trend was observed as the CO_2 gas molecules released from the coal sample (i.e., desorption).

In general, the slope of the pressure-time curves showed that the desorption rate increased with decreasing pressure (Figures 4.18 to 4.24). In all the pressure releasing steps, it took 10 h to23 h for desorption to attain equilibrium (Table 4.5). However, at low equilibrium pressures the desorption rate was slower because the CO_2 molecules trapped in the pores were not easily reversible (Figure 4.22 to 4.24). To further investigate these observations, both sample cell and reference cell were vacuumed for at least 10 seconds to create a negative pressure environment; however, CO_2 molecules released were observed as pressure increase. Figure 4.24 shows the release of desorption gas observed after evacuating the system to zero pressure. The sample was monitored for an extended period (nearly ten days) and the pressure increased to 235.5 kPa. This is an interesting finding, and it could be hypothesized that

the delay in releasing the CO_2 molecules is attributed to the evaporation/diffusion of the molecules condensed in the microporous structure of the coal specimen.

From the point of view of the adsorption kinetics, the desorption was first order regarding the amount of CO_2 still trapped in the pores. The pressure-time data were converted to amount of CO_2 adsorbed versus time to fit in to rate laws to ascertain the rate determining step and presented in Chapter 6.

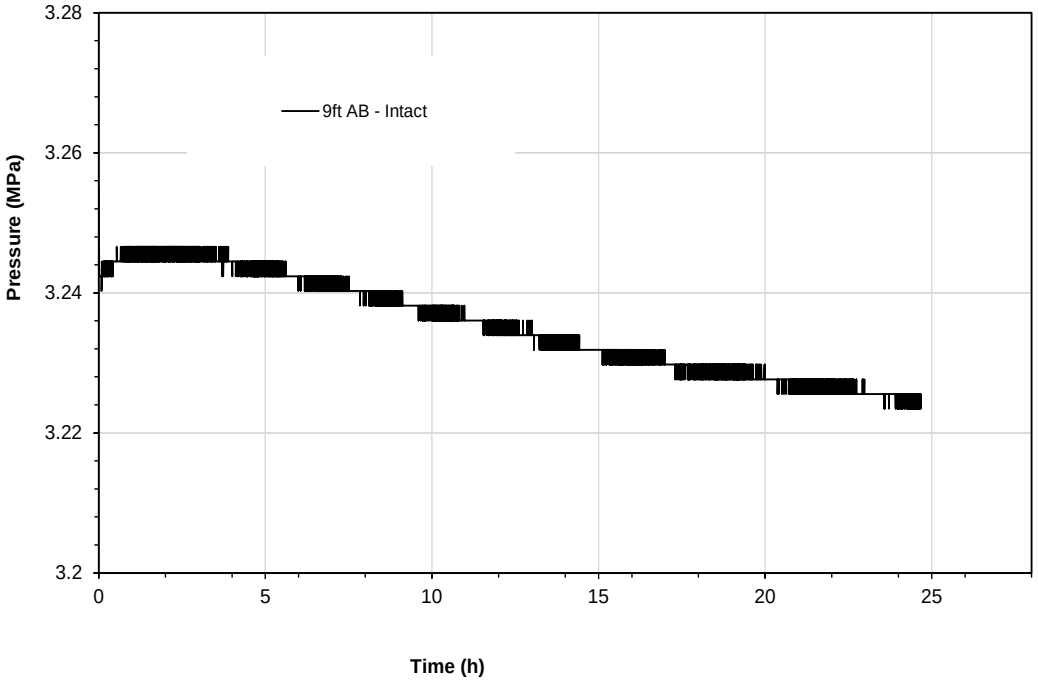

Figure 4.17. CO_2 desorption Pressure versus time curves for intact 9ft Aberpergwm sample - The 1st gas release step from 3.6MPa to 3.06MPa at 298.15 K.

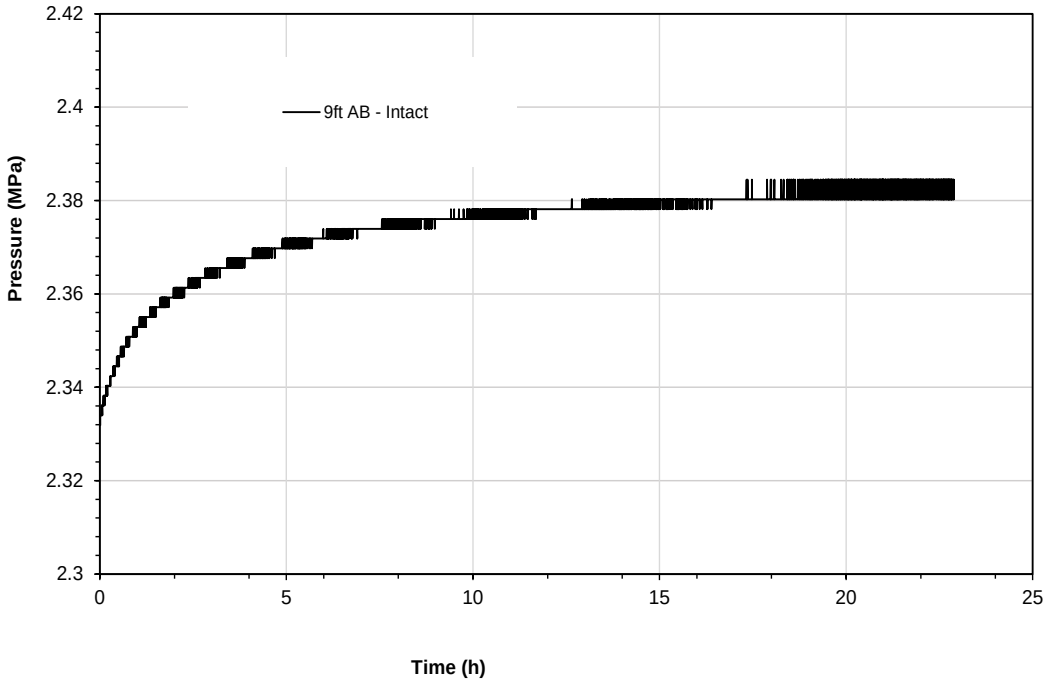

Figure 4.18. CO_2 desorption Pressure versus time curves for intact 9ft Aberpergwm sample - The 2nd gas release step from 3.23MPa to 1.87MPa at 298.15 K

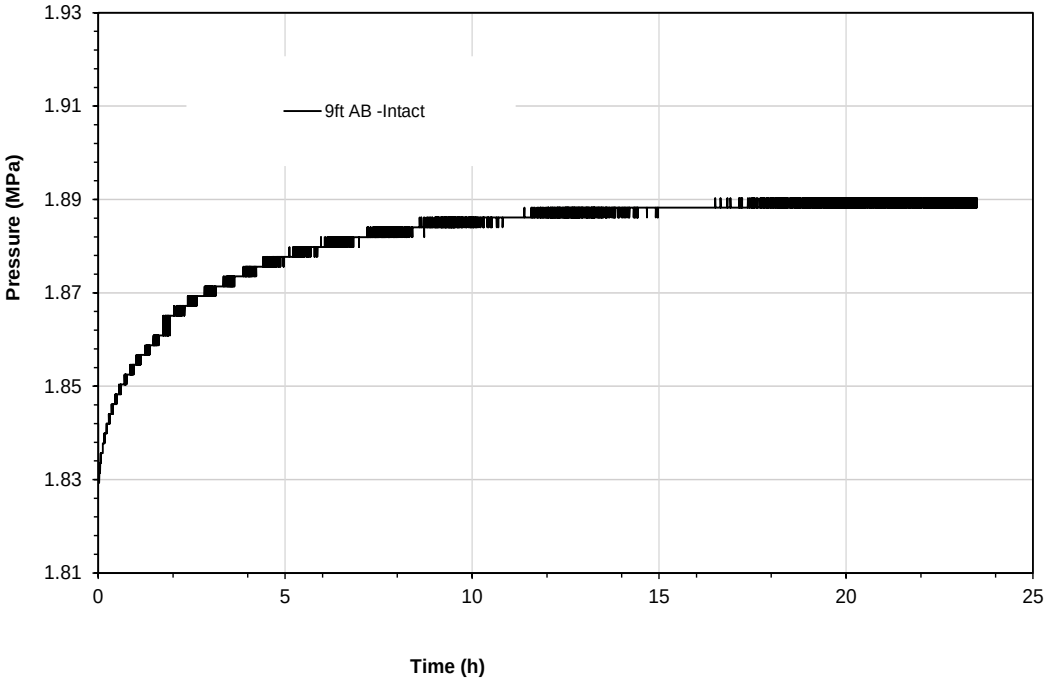

Figure 4.19. CO_2 desorption Pressure versus time curves for intact 9ft Aberpergwm sample - The 3rd gas release step from 2.39MPa to 1.54MPa at 298.15 K.

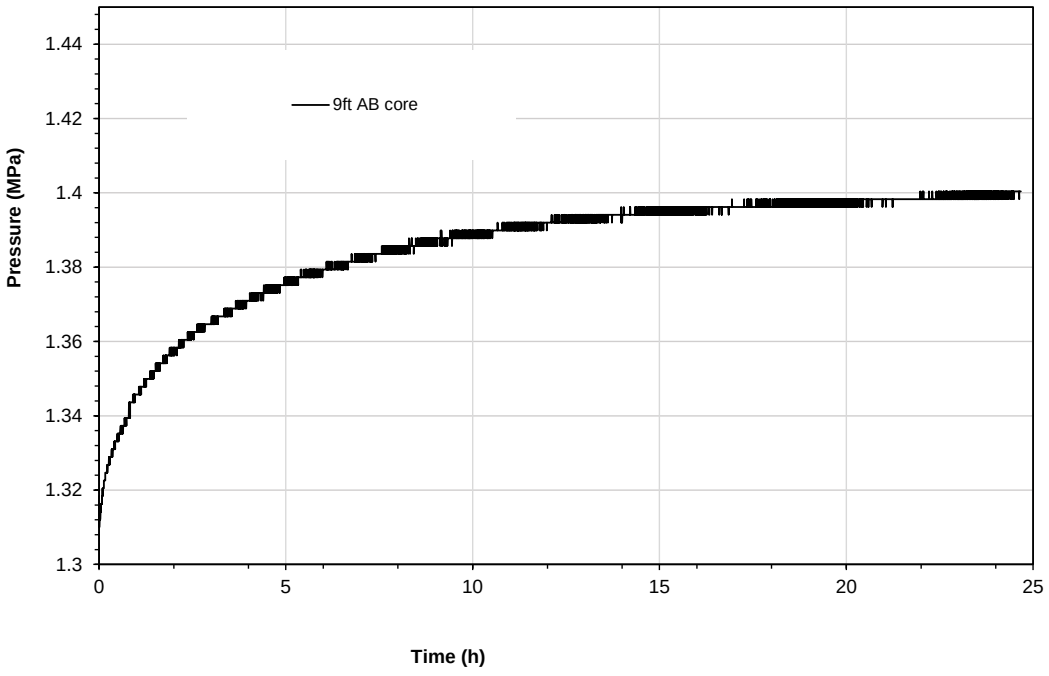

Figure 4.20. CO_2 desorption Pressure versus time curves for intact 9ft Aberpergwm sample - The 4th gas release step from 1.89MPa to 1MPa at 298.15 K.

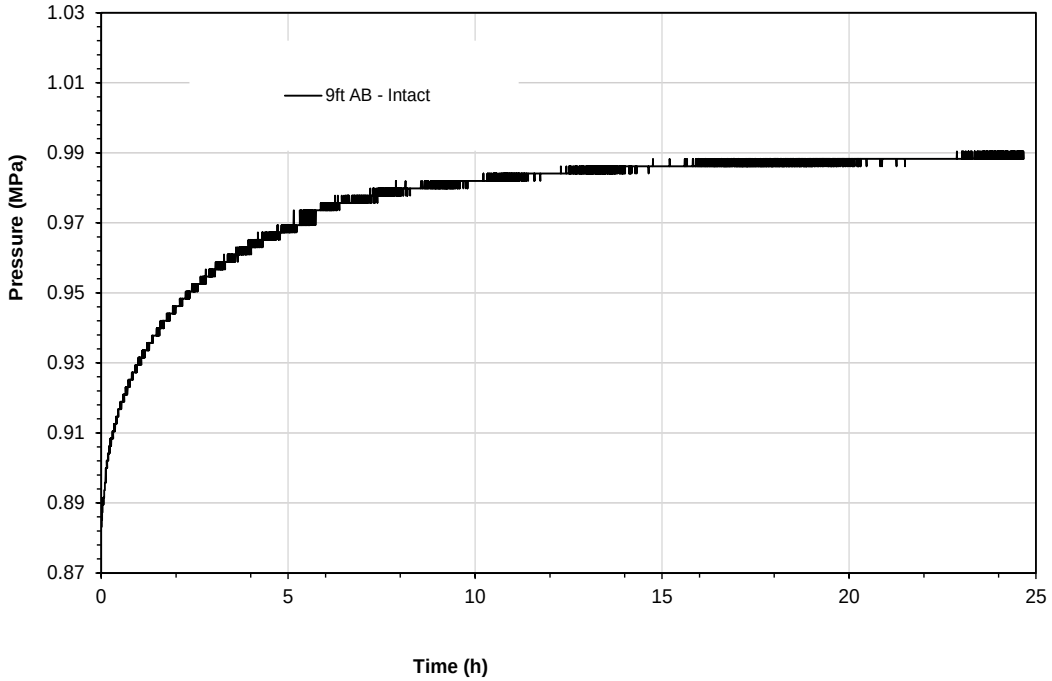

Figure 4.21. CO_2 desorption Pressure versus time curves for intact 9ft Aberpergwm sample - The 5th gas release step from 1.4MPa to 0.6MPa at 298.15 K.

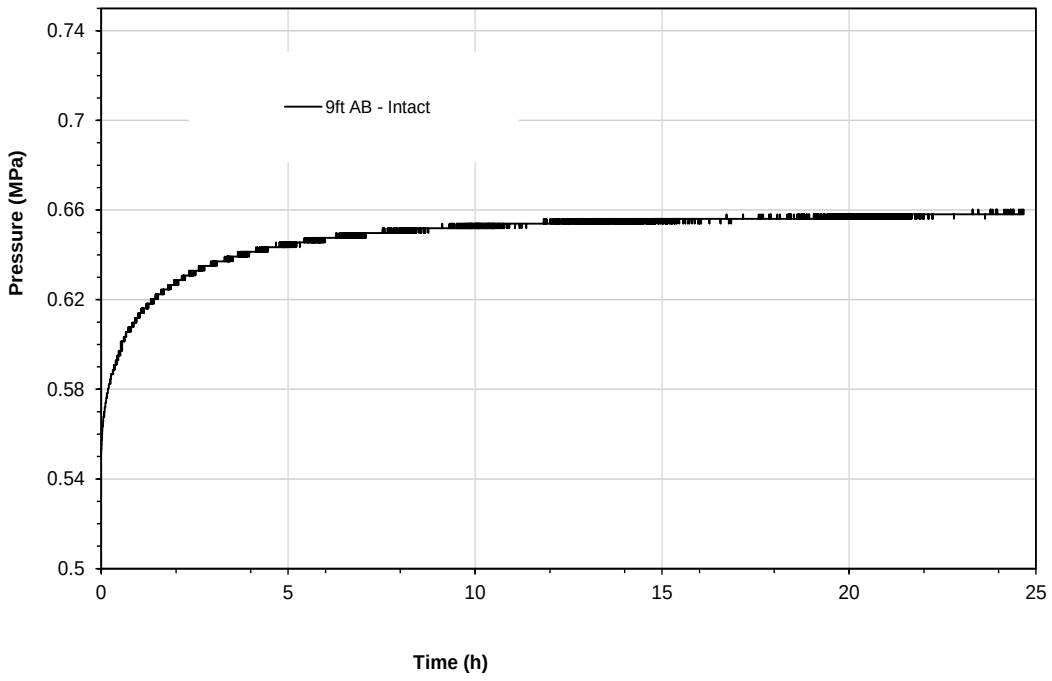

Figure 4.22. CO_2 desorption Pressure versus time curves for intact 9ft Aberpergwm sample - The 6th gas release step from 0.99MPa to 0.31MPa at 298.15 K.

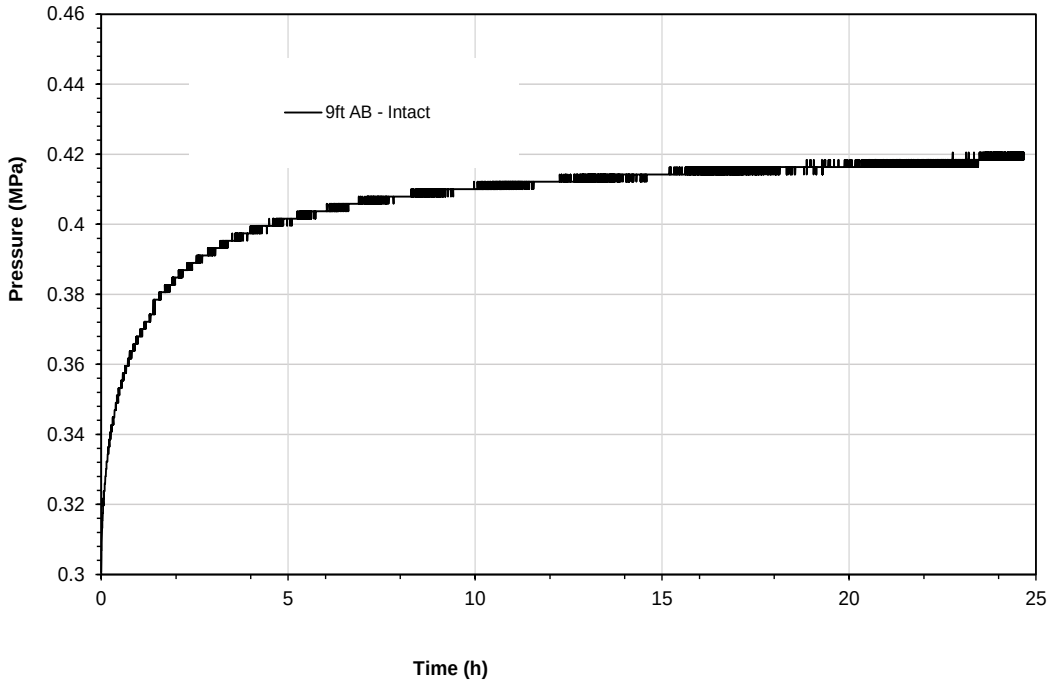

Figure 4.23. CO_2 desorption Pressure versus time curves for intact 9ft Aberpergwm sample - The 7th gas release step from 0.86MPa to 0.1MPa at 298.15 K.

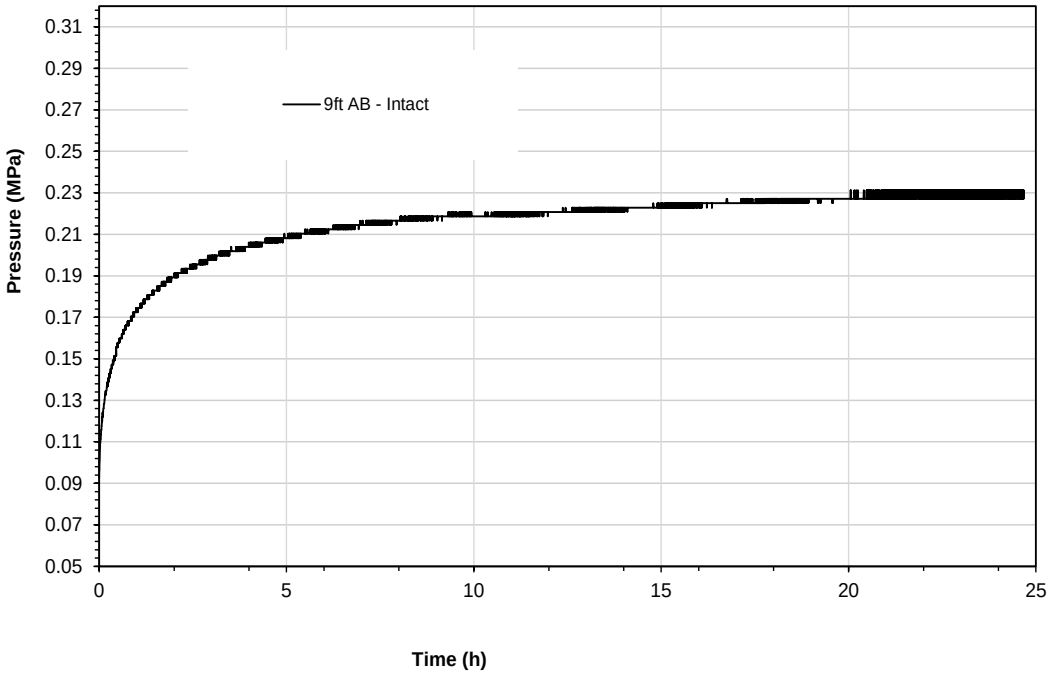

Figure 4.24. CO_2 desorption Pressure versus time curves for intact 9ft Aberpergwm sample - The 8th gas release step from 0.42MPa to 0MPa at 298.15 K.

4.5 Concluding remarks

This chapter presented the CO_2 adsorption patterns of powdered and intact specimens of anthracite (9ft AB and 18ft AB) and bituminous (BP) coals obtained at subcritical (<6.1 MPa), and near critical pressure range (6.1 MPa to 6.4 MPa) of CO_2 at temperature of 298.15 K using manometric/volumetric adsorption measurement method. The experimental results of the adsorption isotherm behaviour of large intact samples (50 mm diameter cores) of 9 ft AB, 18 ft AB and BP and were shown to represent the effect of the samples physical condition (intact and powder). The results obtained from intact specimens were compared with the powdered samples of corresponding coal samples. The key points derived from the investigation are:

1. The CO_2 adsorption capacity of powdered samples of anthracite samples showed higher adsorption capacity than that of intact samples due to the increased surface area which exposes the polarising sites of anthracite coal. However, the intact bituminous (BP) coal showed a higher adsorption capacity than the powdered samples. An increased adsorption capacity of the intact specimen of bituminous coal compared with the powder samples are anticipated as the intact specimen have channel-like micro pores which induces the pore condensation diffusion, where the CO_2 adsorb as a whole phase (Pone et al. 2009; Zhao et al. 2014). Pulverising the sample destroys the microfracture network that is specific to bituminous coals (Xu et al. 2015; Tan et al. 2018; Lu et al. 2020) and the results observed in this study demonstrated the effect of different porous network of anthracite and bituminous coal samples on the CO_2 adsorption capacity. Comparing the powdered samples of bituminous and anthracite, the bituminous showed lower adsorption capacity than the anthracite strengthening the aforementioned explanation.

2. Comparing the adsorption capacities of intact samples by coal rank showed that the adsorption capacity was more closely associated with the carbon content of the respective samples than with the coal rank. The enhanced adsorption capacity observed for intact bituminous coal is attributed to variations in the coal matrix with rank (Perera and Ranjith 2012; Harpalani et al. 1995). The matrix swelling makes way

to the CO_2 to access the microfractures and nanopores of the coal structure (Days et al. 2008a; Ren et.al. 2022) which ultimately contributes to the adsorption capacity.

3. Hysteresis was observed in CO_2 adsorption-desorption isotherms. The possible reason is that the CO_2 gas molecules trapped in the coal structure are not fully released to the corresponding equilibrium pressure and temperature values (Bush et al. 2003). This study estimated the amount of CO_2 remained in the coal after the desorption experiment. The estimated values for intact 9ft AB, intact18ft AB and powder 18ft AB coal samples were 1.05 mole/kg, 0.9 mole/kg and 1.18 mole/kg, respectively.

4. The adsorption-desorption hysteresis patterns observed for intact and powdered samples at near critical pressure ranges (6.1 MPa and 6.4 MPa) revealed a significant difference in shape, indicating the formation of high dense adsorbed phase CO_2 in the microfracture volume of the intact sample. The powdered sample, on the other hand, demonstrated the effect of adsorption on the exposed nanopores (<2 nm) and by displaying a large gap in the hysteresis (Wang et al. 2014; Wang et al. 2016; Ren et al. 2022).

5. The pressure versus time curves showed the CO_2 adsorption equilibrium was attained faster with the powdered samples than the intact samples due to the larger surface area in the powder sample. The pressure versus time curves observed for the desorption experiments showed the increasing trend for the experiments began with zero initial pressure values which attribute to the slow release of CO_2 condensed or diffused into the narrow pores. This observation strengthens the pore entrapment of CO_2 and not all the trapped CO_2 were released.

Chapter 5

Effect of the presence of water on the CO_2 adsorption behaviour of coals

5.1 Introduction

The presence of water in coals affects the CO_2 adsorption capacity (Wang et al. 2011; Sun et al. 2016). The amount of water present in coal seams during the formation process and the water-holding capacity of coals depend upon the rank of the coal. The availability of functional groups, such as OH and carbon-containing groups such as carboxyl (COOH), methoxy (-OCH3), and carboxyl (<C=O) on the coal surface vary depending on the coal rank, which in turn influence the amount of water present. The hydrophilicity of bituminous coal is higher than that of anthracite coal since the proportion of the aforementioned carbon-containing groups in bituminous coal are higher (Mraw and Naas-O'Rourke 1979; Stach et al. 1982; AllardRice 1991; Olayinka 1993; Murata 2000; Allardice et al. 2003; Charriere and Behra 2010). Studies of the influence of coal rank and the amount of water in coal on the CO_2 adsorption enhance the confidence level in understanding the long-term CO_2 sequestration in coal seams.

In the past a few investigations have been undertaken on the influence of moisture on the gas adsorption in coal seams (Joubert et al. 1974; Clarkson and Bustin 2000; Krooss et al. 2002; Day et al. 2008b; Weniger et al. 2012; Romanov et al. 2013; Gensterblum et al. 2014; Weishauptova et al. 2015). These studies have shown that the existence of moisture in coal would tend to decrease the CO_2 adsorption capacity. Most of the studies in the past have examined the effect of moisture on the CO_2 adsorption properties of pulverized coal samples. The tests have been undertaken by following the ASTM standard (ASTM D1412-07 2007) to add moisture to the coal samples. The sample preparation method adopted in the earlier research studies

suggested that the pulverized samples were exposed to a specified relative humidity to prepare the moist coal.

The pulverisation process for various laboratory tests tends to dry coal samples, which in turn destroys the physico-chemical nature of the coal. The naturally occurring adsorbed water which was lost during the drying process might interact differently with the intact coal samples.

The investigation reported in this thesis approached the problem from a broader perspective by examining the natural water-holding capacity of coal samples for a large range of suction (water potential) and examining the bio-geological state of intact coal samples. The key ideas in the current work are (*i*) using an alternative method of increasing water in coal samples to understand the influence of water and field conditions on CO_2 adsorption of coals, (*ii*) water retention behaviour of coal, (*iii*) studying the chemical interaction of CO_2, water and coal, and (*iv*) identifying if there any biological activities in coals.

Concerning the presence of water in coals the following are some key aspects: (*i*) a very high pressure may be required to drive out the adsorbed water from a coal and hence even under ambient conditions, there may be a certain amount of water present in coals, (*ii*) CO_2 may have to compete with H_2O for specific adsorption sites, (*iii*) CO_2 dissolves in water to form carbonic acid and mineralise with alkali minerals, especially calcium minerals dissolved from coal due to the pH buffering effect of coal, and (*iv*) high-pressure resistant bacterial colonies and the adsorbed water may induce the biomineralisation of CO_2; therefore, it is necessary to study the effect of water on intact coal samples to reflect site conditions.

The investigations reported in this thesis include studying the interaction of CO_2, water and coal by (*i*) experimental determination of the water retention characteristic curves of 9ft AB and BP coals, (*ii*) alkaline mineral dissolution from 9 ft AB coal by pH buffering to determine CO_2 mineralization, (*iii*) CO_2 adsorption capacity of moist 9ft AB and 18ft AB coals, and (*iv*) identify native bacteria present in AB coal samples using the secondary electron image obtained from a scanning electron microscope (SEM). The obtained results are interpreted to comprehend the CO_2-water-coal system.

The main objectives of the chapter are as follows.

1. Perform laboratory water retention tests and establish water retention characteristic curves of coal samples for a large range of suction using the chilled-mirror dew-point technique. A commercially available WP4C device from METER Group was used for this purpose.
2. Conducting laboratory tests to determine the pH buffering capacity of coal. The dissolved ions from coal at different pH values were quantitatively measured using an ICP-OES (inductively coupled plasma-optical emission spectrometry) equipment.
3. Study the microstructure of the coal specimens utilizing a scanning electron microscope (SEM) to identify the existence of any native bacteria present in coals.
4. Conducting CO_2 adsorption measurements using coal samples at different water contents. Samples of intact 9ft Aberpergwm (9ft AB) and intact and powder 18ft Aberpergwm (18ft AB) to study CO_2 adsorption behaviour. The maximum equilibrium pressures considered was up to 6 MPa and at a temperature of 298.15K.

5.2 Experimental programme

Suction measurements were performed using a chilled-mirror dew-point potentiometer, WP4C device. The device is available from METER Group and has been frequently used to establish water retention behaviour of soils and industrial wastes (Decagon Devices 2010; Fredlund et al. 2012). The types of coal sample used are given in Table 5.1. The sample preparation method and the experimental methods for WP4C are described in Chapter 3, section 3.6.2.

Table 5.1. Samples used in chilled-mirror dew-point (WP4C) water potentiameter tests.

Coal sample/Location	9ft Aberpergwm (AB)		Big Pit (BP)	
Sample type	Powder	Intact	Powder	Intact
Suction measurement	x (3)	-	x (3)	-

For the adsorption experiments, coal samples were prepared at different gravimetric water contents. The water content of intact 9ft AB sample was about 2.34%, intact 18ft AB was about 4.07% and powder samples of 18ft AB was about 1.2%. The description of the samples is presented in Table 5.2 and the sample preparation method is described in Chapter 3, in sections 3.2.2 and 3.2.3. These samples are referred to as wet samples. Adsorption studies were not performed on Big Pit samples. A check mark in Table 5.2 indicates that the test was completed, the cross mark indicates the test was not performed. The results are compared with the similar samples with lower water content of 0.78% (18ft AB) and 0.91% (9ft AB); these samples are referred to as dry samples (Chapter 4, section 4.3.1). Adsorption and desorption measurements using the wet and dry samples were performed using the manometric adsorption apparatus.

The pH buffering capacity of coal was performed as described in Chapter 3, section 3.6.1, and biofilm loading on coal and sample preparation method for SEM imaging are detailed in Chapter 3, section 3.2.4.

Table 5.2: Samples used in adsorption and desorption measurement using manometric sorption apparatus.

Coal sample/Location	9ft Aberpergwm		18ft Aberpergwm	
Sample type	Powder	Intact	Powder	Intact
Adsorption test	-	x	x	x
Desorption test	-	-	x	-

5.3 Water retention characteristics of coal samples

Natural groundwater percolating through the coal seam would significantly affect carbon sequestration in the coal (Wang et al. 2007; Pan et al. 2010 and Lee et al. 2013). The water retention properties of coal reflect the ability to retain water in the porous system, which is critical for understanding the CO_2-water-coal interaction.

Powdered and intact samples of 9ft AB coal were tested for establishing their water retention characteristics curves while only powdered samples of BP coal were considered. Suction was measured using a WP4C device. Coal-water mixtures were prepared at several water contents and the water contents of the mixtures were verified using oven drying method (ASTM D2216-19, 2019). The saturation water content (ω_s) for the powdered 9ft AB samples were about 18% (dry density = 1700 kg/m^3) and 20.9% (dry density = 900-1000 kg/m^3). The saturation water content (ω_s) for the intact sample of 9ft AB was about 7.11% and for the bituminous BP samples were about 11.95% (dry density = 1700 kg/m^3) and 19.71% (dry density = 1500 kg/m^3).

The curves depict the typical curve observed for unsaturated soil samples in which the suction ranges from zero to 10^6 kPa (Fredlund et al. 2012). The van Genuchten (1980) equation (Equation 5.1) was used to best-fit the experimental data to get the best-fit parameters ($a_{vg}, \omega_s, \omega_r,\ n, and\ m$). Microsoft Excel Solver was used to generate best-fit parameters.

$$\theta_n = \frac{1}{[1+(a_{vg}\psi)^n]^m}$$

where, $\theta_n = \frac{w(\psi)-w_r}{w_s-w_r}$

Therefore, $$w(\psi) = w_r + \frac{w_s-w_r}{[1+(a_{vg}\psi)^n]^m} \quad (5.2)$$

where θ_n is the volumetric water content (%), *w* is the gravimetric water content (%), ψ is suction pressure MPa, w_s is saturation gravimetric water content (%), w_r is residual gravimetric water content (%), a_{vg} is fitting parameter primarily related to the inverse of air-entry value (MPa^{-1}), *n* is fitting parameter related principally to the rate of water extraction from the coal once air-entry value has been exceeded and *m* = 1 - (1/*n*).

Figures 5.1 to 5.4 show the water retention characteristic curves and the best-fit parameters for the 9ft AB coal sample that were compacted at dry densities of 1700 kg/m^3 and 900-1000 kg/m^3 and BP coal samples compacted at dry density of 1700 kg/m^3. The van Genuchten parameters a_{vg}, *n* and *m* obtained for 9ft AB coal sample with a dry density of 1700 kg/m^3 are 4 MPa^{-1}, 1.59 and 0.37, respectively. While these parameters are 16 MPa^{-1}, 1.54 and 0.35 for 9ft AB sample with a dry density of 900-1000 kg/m^3. The parameters calculated for intact samples of 9ft AB with a dry density of 1362 kg/m^3 are 0.05 MPa^{-1}, 2.74 and 0.64, respectively. The parameters (a_{vg}, *n* and *m*) obtained for the bituminous BP samples are 1.42 MPa^{-1}, 4.63, 0.78 (dry density of 1700 kg/m^3) and 3.1 MPa^{-1}, 1.98, 0.49 (dry density of 1500 kg/m^3).

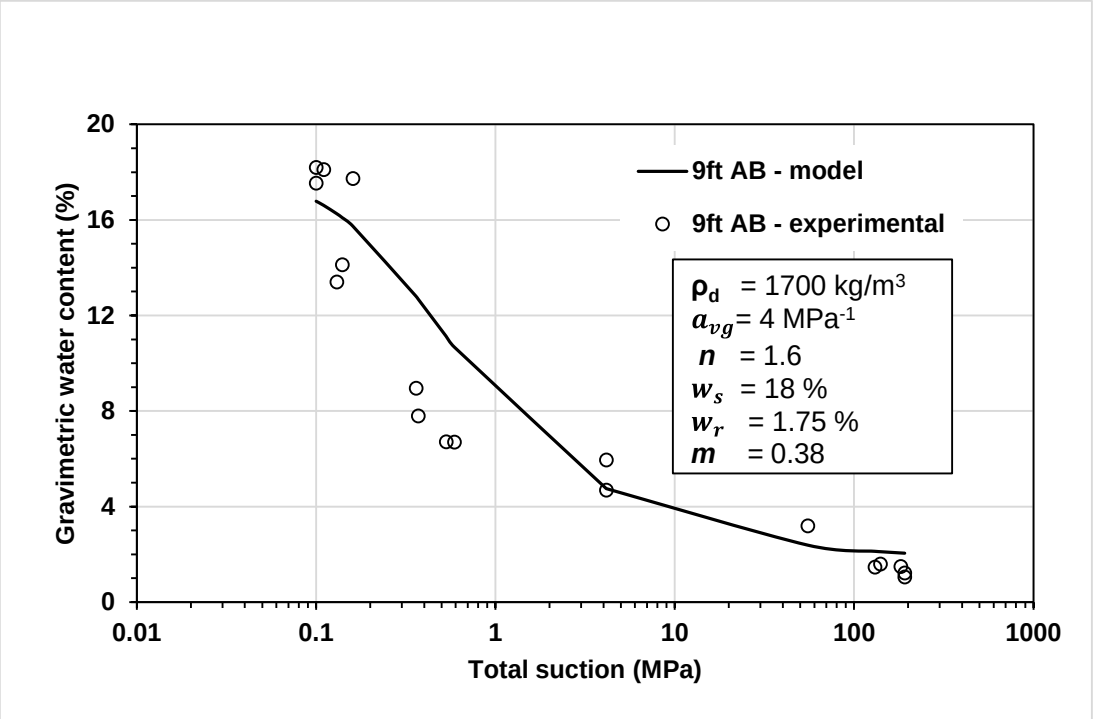

Figure 5.1. Suction versus water content curves obtained from experimental and van Genuchten model for powdered 9ft Aberpergwm coal (dry density=1700 kg/m^3).

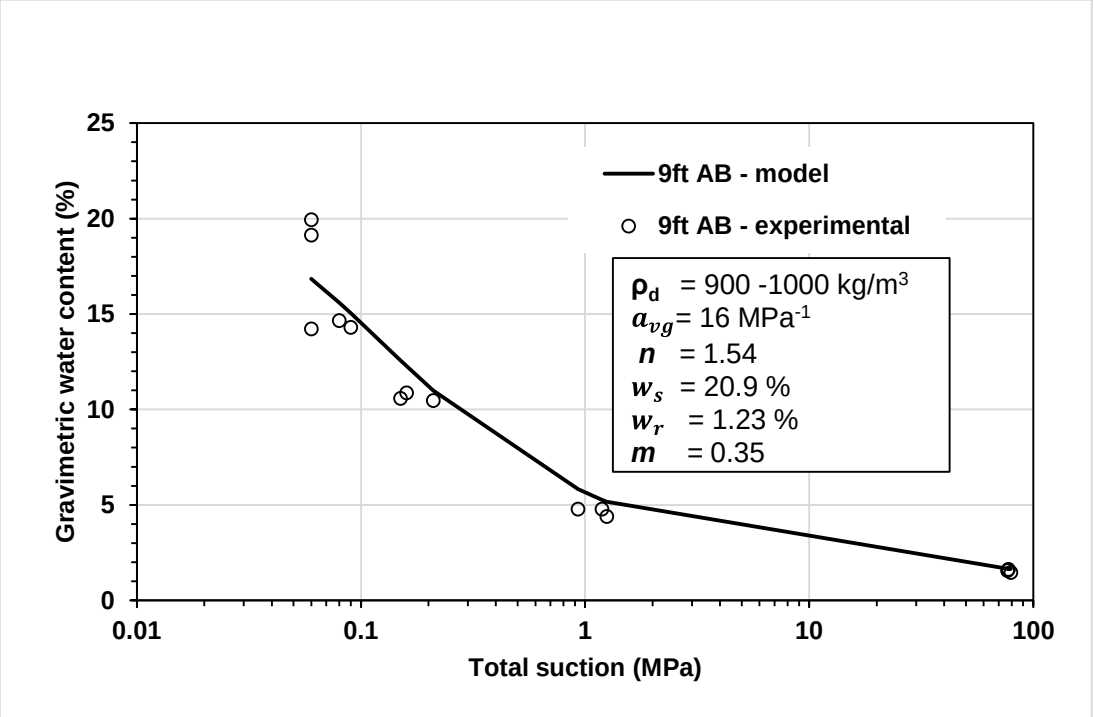

Figure 5.2. Suction versus water content curves obtained from experimental and van Genuchten model for powdered 9ft Aberpergwm coal (dry density=900-1000 kg/m^3).

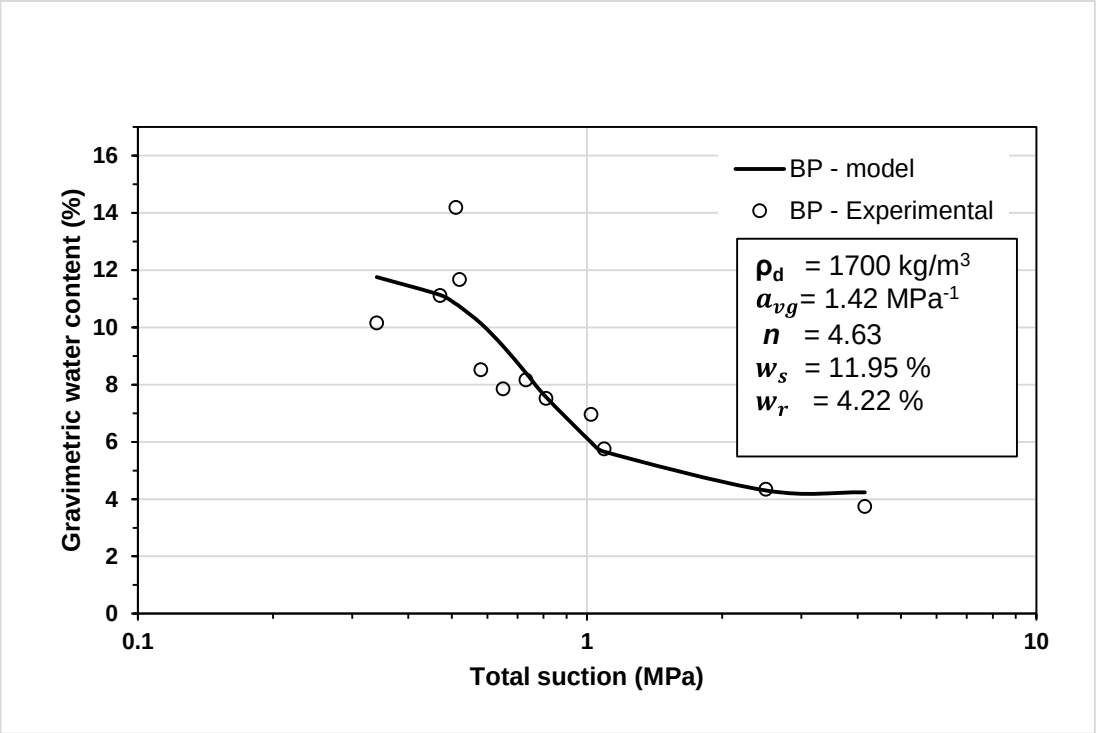

Figure 5.3. Suction versus water content curves obtained from experimental and from van Genuchten model for powdered Big Pit coal (dry density=1700 kg/m^3).

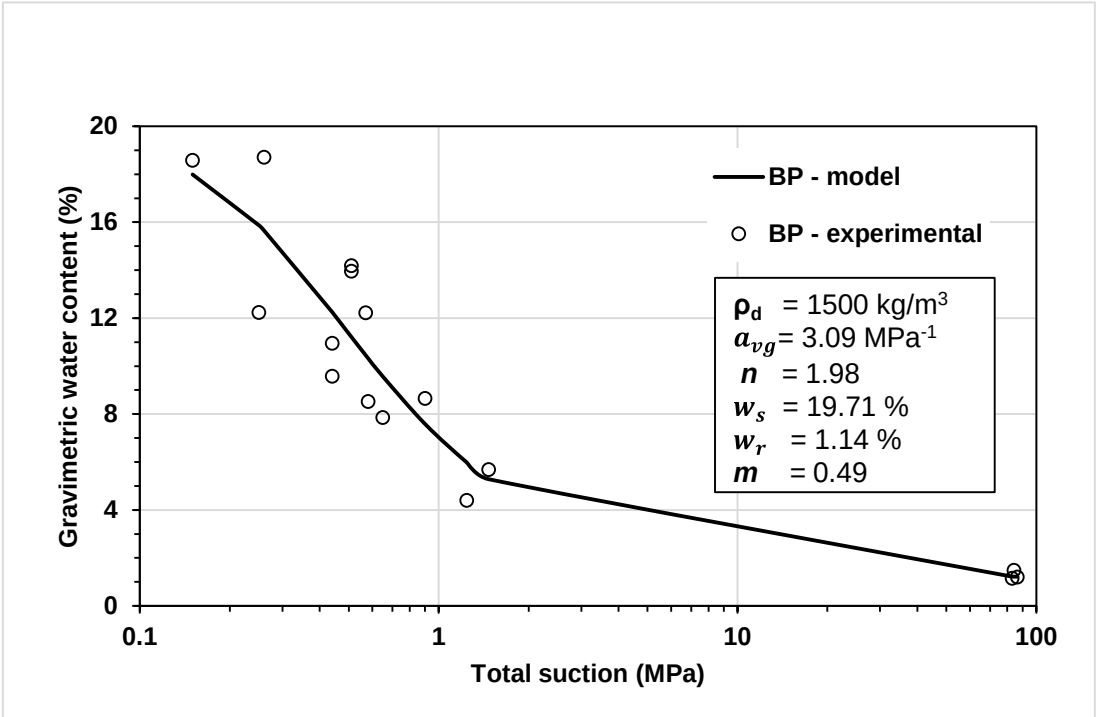

Figure 5.4. Suction versus water content curves obtained from experimental and from van Genuchten model for powdered Big Pit coal (dry density=1500 kg/m^3).

In the WP4C tests, the time required to obtain the final suction value depends upon the water content of coal samples. The equilibrium time in case of samples at low water contents was much longer than higher water content samples. For example, the time required to measure suction for the sample of 9ft AB coal with a water content of 2.11% was 4 hours and thirty minutes. The measured suction in this case was 40.74 MPa. During the suction measurement for this sample, a loss of moisture from the sample was about 0.3 g. The equilibrium suction measurement time for the sample with a water content of 7.1% was 12 minutes for a suction of 0.14 MPa. For the case of dry samples with less than 1% water content, the equilibrium time was 18 minutes for the measurement of a suction of 71.5 MPa.

5.4 CO_2-water-coal interaction

The adsorbed water may influence the way CO_2 interacts with coal and reflect on the adsorption measurement values (Day et al. 2008b). The water present in coals encourages biological activities. It is well known that *Bacillus mojavensis* bacteria are resilient to CO_2 and thrive at high-pressure and temperatures (Mitchell et al. 2008; Mitchell et al. 2009). This section explores the chemical interaction of CO_2-adsorbed water-coal and provides evidence for the biological activity in coal samples used in the current study.

5.4.1 Chemical interaction of CO_2 – water – coal

Upon in contact with water molecules, the injected CO_2 (gas) would become aqueous CO_2 (dissolved) to form carbonic acid (H_2CO_3). At a temperature of 298.15 K, the $CO_{2(g)}$ is the dominant species, but considering the amount of $CO_{2(g)}$ and pressure, some of them will dissolve in water and form carbonic acid (Appelo and Postma 2005).

$$CO_{2(g)} \rightarrow CO_{2(aq)}$$

$$CO_{2(g)} + H_2O \rightarrow H_2CO_3$$

The dissociation of carbonic acid releases protons,

$$H_2CO_3 \rightarrow HCO_3^- + H^+$$

$$HCO_3^- \rightarrow CO_3^- + H^+$$

These (H^+) protons eventually increase the solubility of the alkaline minerals (Ca^{2+}, Na^+, K^+, and Mg^{2+} bearing minerals) in the coal.

$$CO_{2(g)} + H_2O + coal - CaCO_3 \rightarrow Ca^{2+} + 2HCO_3^- + coal$$

In addition, this will create a complex system in which some of the CO_2 would precipitate as carbonate minerals on coal surface.

$$Ca^{2+} + 2HCO_3^- + coal \rightarrow coal - CaCO_3 \downarrow$$

This carbonic acid effect was tested in a separate experiment in this study. The pH buffering capacity and inorganic ions on the coal surface were examined by equilibrating 10 g of a powdered 9ft AB coal sample (<75µm size) with 10 mL of water samples for 24 h at varying pH ranging from 2 to 11. The initial and final pH of coal-water mix is plotted in Figure 5.5. The cations dissolved from the coal at different pH values were measured using ICP-OES equipment and the results are presented in Table 5.3.

Figures 5.5 presents the pH buffering capacity trend of 9ft AB coal. It can be seen in Figure 5.5 that the pH of the water samples was increased after equilibrating with coal because of mineral dissolution. The concentrations of cations released from the coal during the equilibration indicate the possible dissolution of alkali minerals (example, dissolution of calcium increases alkalinity) from the coal surface. For example, Carbonic acid (H_2CO_3) causes the pH 5.8 of the deionised water which should be neutral pH 7 . After equilibrating with coal, the pH rises to 6.58 (Table 5.3). The measured cations concentration for the corresponding coal-water mix confirms the alkali mineral dissolution (Table 5.3) is the reason for the pH neutralisation. The dissolution of alkali minerals from coal was previously studied by Massarotto et al. (2010). Their results were similar to that obtained in this study.

From the experimental results, it was observed that the dissolved CO_2 would increase the acidity of the adsorbed water in coal. Consequently, the acidic pH was neutralised by the alkali minerals released from the coal. This clearly suggests that the

released alkali mineral from the coal, particularly calcium, would interact with H_2CO_3 to precipitate as $CaCO_3$. This is very important in terms of carbon sequestration where CO_2 will be mineralised.

Table 5.3: pH buffering capacity of 9ft Aberpergwm coal

Initial pH	pH after 24 h	Ca (mg/g of coal)	Na (mg/g of coal)	K (mg/g of coal)	Mg (mg/g of coal)	Mn (mg/g of coal)	B (mg/g of coal)	Ba (mg/g of coal)
2.73	6.96	0.031	0.005	0.013	0.005	0.0004	0.0002	0.00009
3.69	7.6	0.018	0.004	0.01	0.002	0.0002	0.0002	0.00002
4.26	7.4	0.019	0.005	0.011	0.003	0.0002	0.0002	0.00036
5.8	6.56*	0.02	0.004	0.004	0.007	0.0003	0.0002	0.00001
11.85	11.26	0.001	**	0.012	0	0	0.0001	0.0002

* Natural pH with DI water, **NaOH is used for adjusting the pH

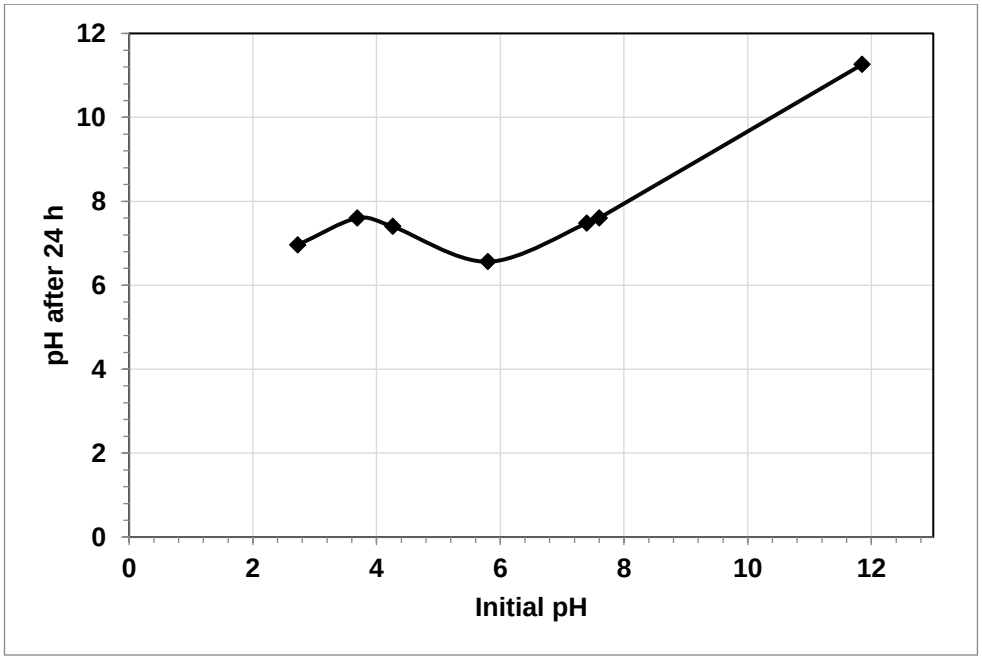

Figure 5.5. pH buffering capacity of 9ft Aberpergwm coal using ICP-OES equipment.

5.4.2 Evidence of biological activity on moist coal based on SEM study

One of the objectives of this chapter was to investigate the morphological diversity of the coal and to identify native bacterial growth on the coal seam. Scanning Electron Microscopy (SEM) was used to scan on 9ft AB coal to identify any signs of bacteria on the coal surface.

The SEM images of 9ft AB coal samples were obtained using methods describes in Chapter 3, section 3.2.4. The scanning electron microscope images of coal samples are shown in Figure 5.6.

Figure 5.6 (a) shows evidence of some biofilm on the surface cracks of the coal sample. The naturally growing bacterial activities can be identified. Bacteria grew on small chunks of coal, and the images clearly show the presence of live bacteria. Figure 5.6 (b) shows the rod-shaped species, most likely belonging to the *Bacillus* family, usually found in coal seams (Mitchel et al. 2008; Mitchel et al. 2009).

To confirm the *Bacillus* family bacterium presence, the images obtained with natural coal sample were compared with SEM images obtained with coal samples with laboratory grown bacterium (*Bacillus mojavensis*). Bacteria was grown on the 9ft AB coal using laboratory procedure described in Chapter 3, section 3.2.4. The scanning electron microscope images of the laboratory grown *Bacillus mojavensis* on 9ft AB coal sample is shown in Figures 5.7. The *Bacillus mojavensis* has been identified in previous works as resilient to high pressure CO_2 (Mitchel et al. 2008; Mitchel et al. 2009). The typical length of *Bacillus mojavensis* is 2 µm to 4 µm and a width of 0.5 µm to 1 µm (Roberts et al. 2017).

a)

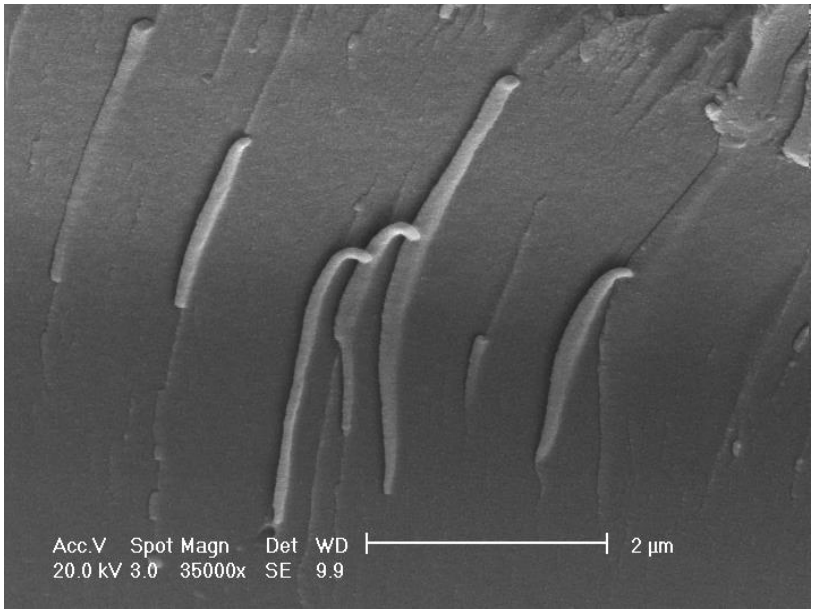

b)

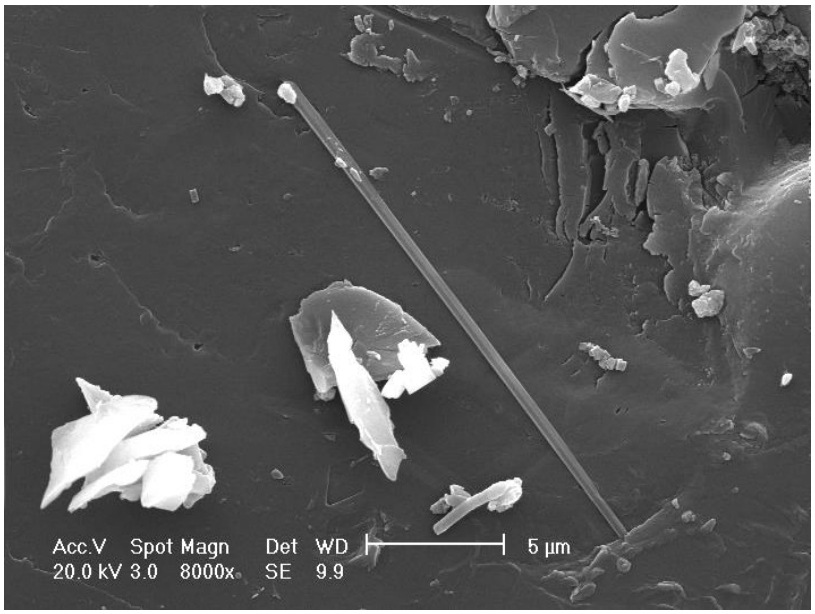

Figure 5.6. Scanning electron photomicrographs of intact 9ft Aberpergwm coal showing: a) sign of biofilm on the surface cracks, b) rod-shaped species, probably belonging to the Bacillus family.

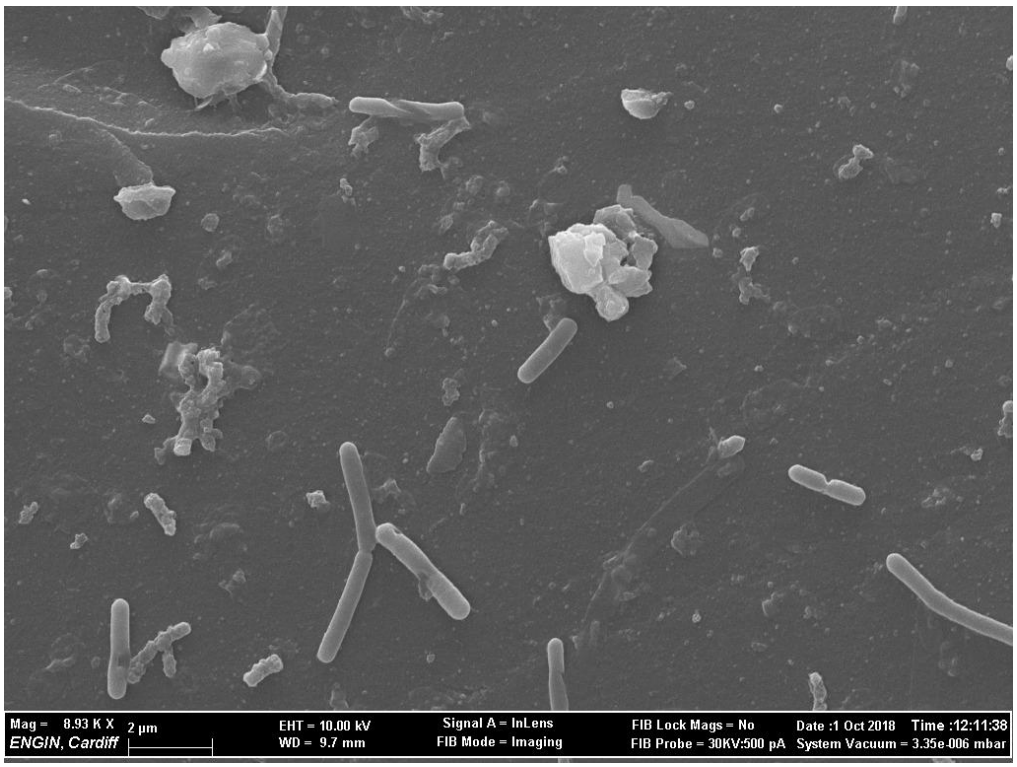

Figure 5.7. Scanning electron photomicrographs of the laboratory grown bacteria on 9ft Aberpergwm coal.

The presence of bacterium can induce biomineralization of CO_2 (Figure 5.8). Biomineralization can occur in many ways: (*i*) Biologically controlled mineralisation: The CO_2 dissolved in water produces HCO_3, and the calcium adsorbed on the cell membrane can react with HCO_3 and precipitate as $CaCO_3$ (Figure 5.8 a), (*ii*) Biologically induced mineralisation: calcium present in the bacterial cell can diffuse out and form $CaCO_3$ and precipitate on the organic matrix (coal) (Figure 5.8 b) and (*iii*) Biologically influenced calcium precipitation: The dissolved CO_3^{2-} interact with the calcium adsorbed on the dead mass of the bacterial biofilm (Dupraz et al. 2008; Castro Alonso et al. 2019). Based on the discussion, the CO_2 mineralisation can be classified as inorganic mineralisation (discussed in section 5.4.1) and biomineralization (discussed in section 5.4.2).

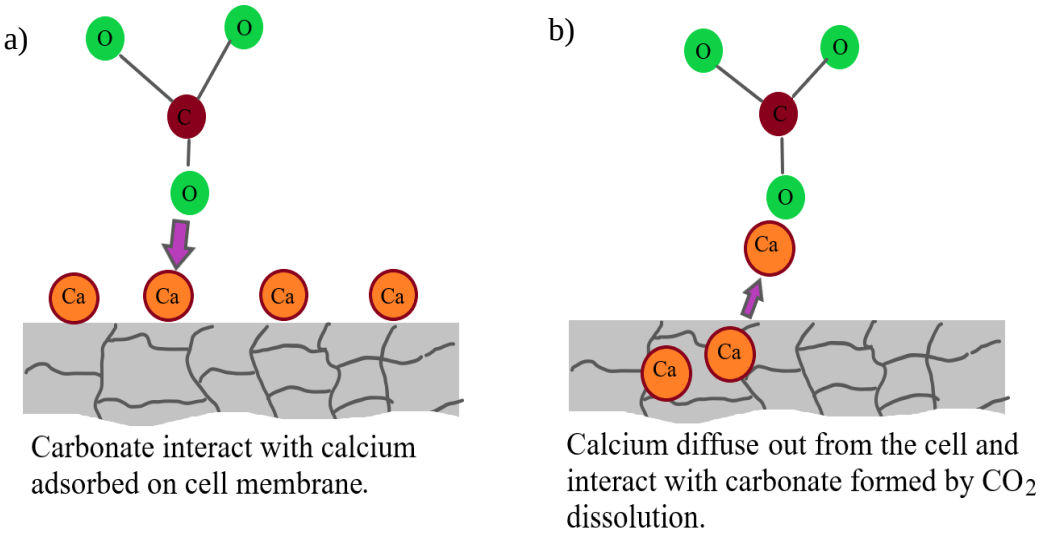

Figure 5.8. Mechanism of biomineralization; CO_2 interaction with a) Calcium adsorbed on the cell wall, b) calcium diffused out of the cell.

5.5 CO_2 adsorption and desorption behaviour of moist coal

Previous studies on moist coal revealed that the adsorbed water was replaced by CO_2 and the gas molecules diffuse/dissolve through the adsorbed water to reach the interior of the coal matrix (Sun et al. 2015). On the other hand, CO_2 adsorption capacity of coal is reduced in several ways, including the adsorbed water limiting the mobility of the adsorbed CO_2 (Day et al. 2008b), the volumetric expulsion of adsorbate (CO_2) by water molecules, and the water molecules adsorbed on the polarised sites on the coal surface have a high heat of adsorption, displace the CO_2 molecules (Day et al. 2008b and Gensterblum et al. 2014). As noted previously, based on the biogeological conditions seen in coal seams, the influence of inorganic and biomineralization on CO_2 adsorption on wet coal should not be overlooked (section 5.4). As a direct consequence, the current work conducted CO_2 adsorption studies on coal samples with different water contents to better understand the effect of field conditions. Adsorption experiments on wet powder and intact samples of 18ft AB and 9ft AB coals were conducted and compared to dry samples of the same coals.

5.5.1 Carbon dioxide adsorption in moist coal samples

The CO_2 adsorption isotherms of intact 9ft AB dry (water content = 0.91%) and wet (water content = 2.35%) coal samples are depicted in Figure 5.9. When the adsorption isotherms of dry and wet samples were compared, a marginal increase in CO_2 adsorption was observed for the wet sample in the higher-pressure range. At an equilibrium pressure of 3.6 MPa, the wet sample adsorption capacity was about 1.8 mol CO_2/kg, whereas the dry sample adsorption capacity was about 1.6 mol CO_2/kg. The wet sample had a lower adsorption capacity than dry samples at equilibrium pressures below 2 MPa. The likely explanation for this behaviour is that the water content affects the bulk pore diffusion, the primary mode of adsorption mechanism at low pressures. At increased pressures, the increased adsorption capacity can be attributed to complex mechanisms such as CO_2 adsorption at water activated sites by expelling the adsorbed water (Day et al. 2008b; Sun et al. 2015) and mineralisation of CO_2.

A similar adsorption isotherm pattern was observed with intact samples of 18ft AB, with 4.07% water content (Figure 5.10). The sample showed an increased adsorption capacity than the sample with a much lower water content of 0.78% at elevated pressures of 3.6 MPa. The 18ft AB sample with 4.07% water content showed an adsorption capacity of 1.6 mol of CO_2/kg of coal and 0.78% water content exhibited an adsorption capacity of 1.1 mol of CO_2/kg of coal (Figure 5.10).

The intact wet samples of both 9ft AB and 18ft AB anthracite coals had comparable isotherm patterns (Figure 5.11). However, the marginally enhanced adsorption capacity seen above 1 MPa equilibrium pressures with 9ft AB samples is correlated with the sample's low carbon content (89.5 %) in comparison to 18ft AB (92.05 %). The low carbon content coals contain higher polarised sites with functional and carbon containing groups where CO_2 and water molecules generally prefer to adsorb (Mahajan and Walker 1971; Allardice and Evans 1971; Nishino 2001; Kodigolu and Varamaz 2003; Qi and LaVan 2005; Miura et al. 2005; Day et al. 2008b).

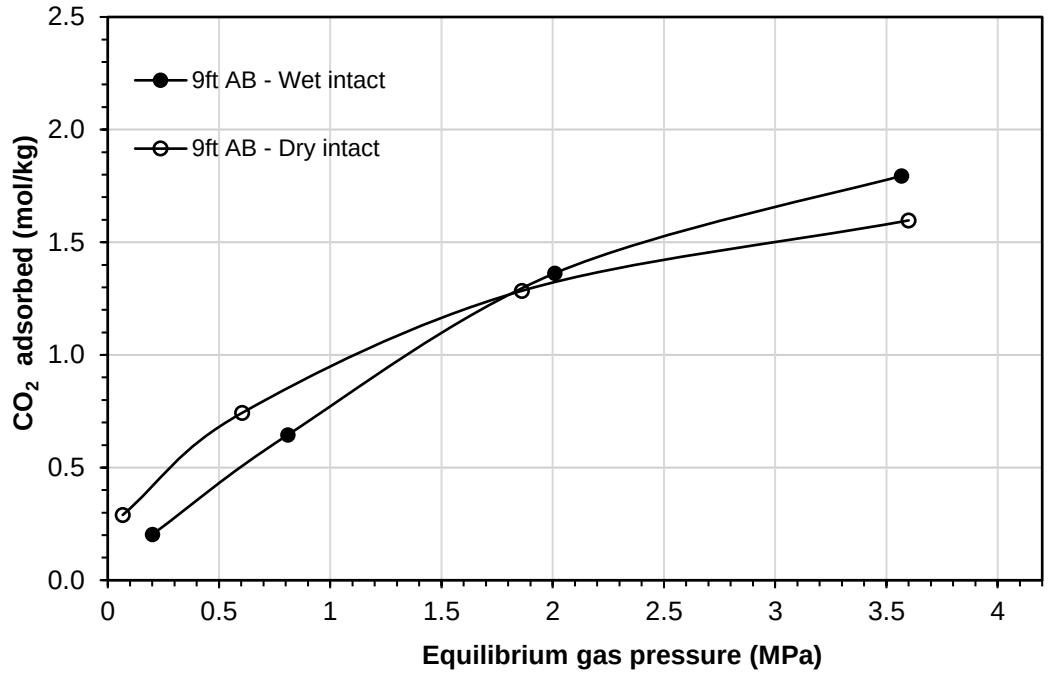

Figure 5.9. CO_2 adsorption isotherm of intact 9ft Aberpergwm coal (dry and wet with water content of 0.9% and 2.35%, respectively).

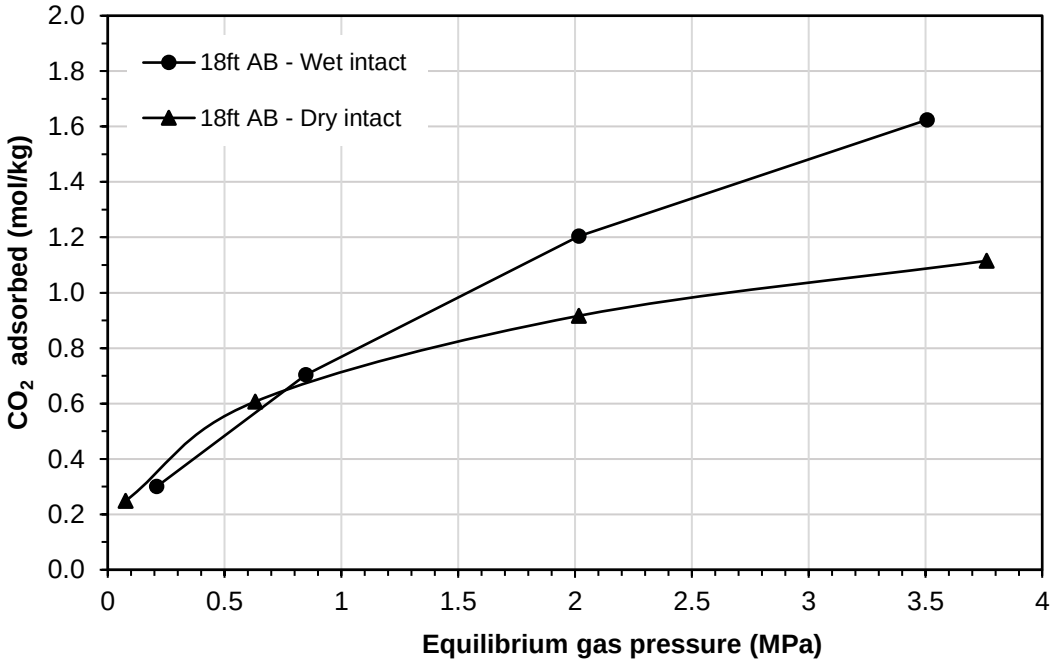

Figure 5.10. CO_2 adsorption isotherm of intact 18ft Aberpergwm coal (dry and wet with water content of 0.78% and 4.07%, respectively).

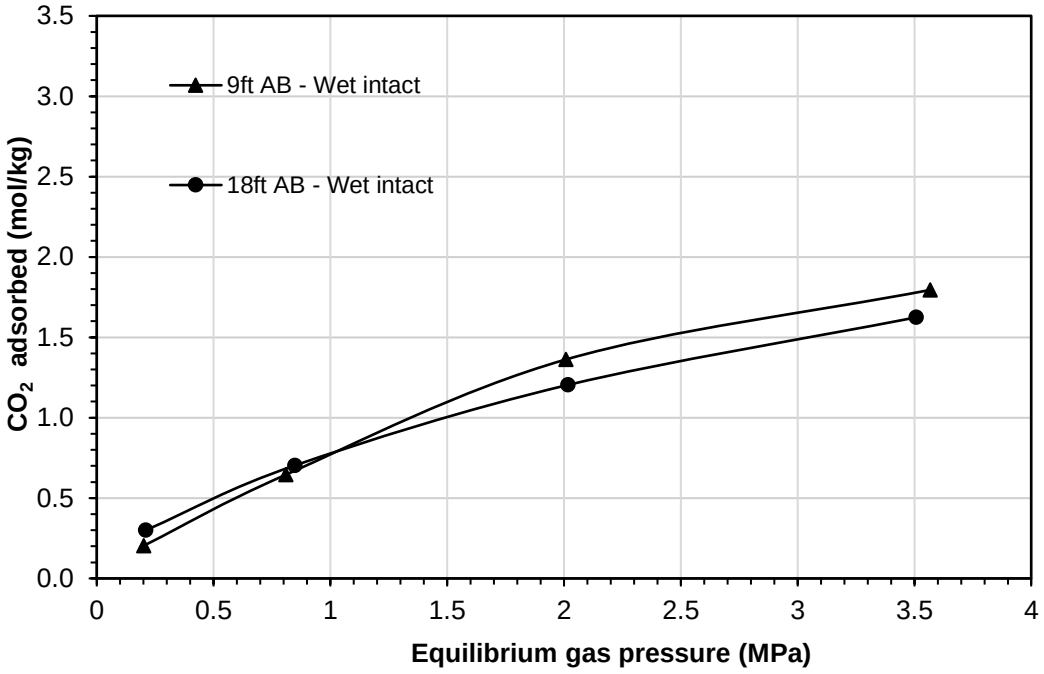

Figure 5.11. CO_2 adsorption isotherm of wet intact 9ft and 18ft Aberpergwm coal (with water content of 2.34% and 4.2%, respectively

Figure 5.12 compares the isotherm patterns of dry and wet powdered 18ft AB coal samples. The adsorption capacity of the dry powdered sample was significantly greater than that of the wet samples. When the pressure was increased, the disparity in adsorption capacity grew. Powdered samples of 18ft AB with 0.78% water content adsorbed 1.5 mol of CO_2/kg of coal, while samples with 1.2% water content had an adsorption capacity of 1.1 mol of CO_2/kg of coal at 3.5 MPa, a 33% reduction in adsorption capacity (Figure 5.9). This pattern reflects the findings of Wang et al. (2011), who found that the amount of adsorbed CO_2 on wet coal samples was reduced by 69% when compared to dry powdered samples.

The trends observed for the intact and powdered samples (Figures 5.9 to 5.12) is expected as the adsorbed water forms hydrogen bonds with the polar functional group and carbon-containing groups of coal structure (Mahajan and Walker 1971; Allardice and Evans 1971; Nishino 2001; Kodigolu and Varamaz 2003; Qi and LaVan 2005; Miura et al. 2005). By pulverising the coal samples, these polarisation sites are

exposed for water to absorb. Since H_2O molecules have a high heat of adsorption, it is difficult for CO_2 to replace the water molecules adsorbed on the polarised sites on the coal surface of the powdered samples (Day et al. 2008b).

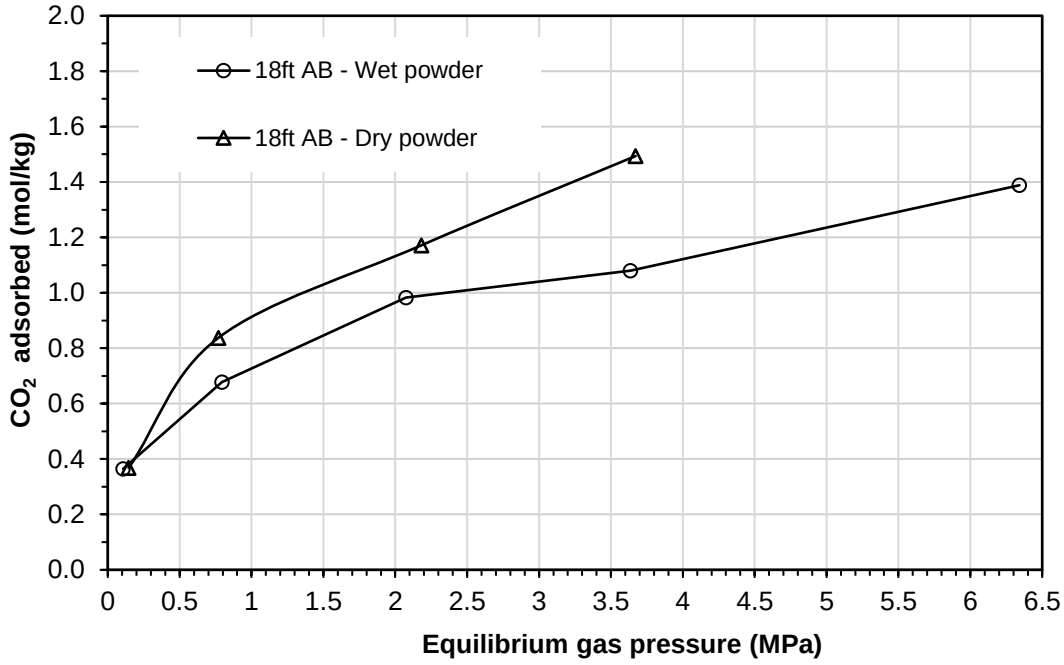

Figure 5.12. CO_2 adsorption isotherm of powder 18ft Aberpergwm coal (dry and wet with water content of 0.78% and 1.2%, respectively).

The observations made during the adsorption experiments with wet samples are represented in Figure 5.13. After completing the adsorption-desorption tests on wet intact 18ft AB with water content (4.07%), the sample cell's bottom was found to be wet (Figure 5.13 a). The possible reason of water expulsion from the coal structure is that CO_2 can diffuse/dissolve into capillary water to access the coal matrix interior, causing the water molecules to desorb from the surfaces of nano, micro and mesopores (Figure 5.13 b - insert shows the image of nanosized pores and micro cleats found in anthracite coal).

This volume expulsion behaviour was previously reported in a study of CO_2 gas-water exchange experiments performed at pressures up to 4.5 MPa and temperatures up to 298.15 K (Sun et al. 2015), which are similar to the parameters set up in the current investigation. Sun et al. (2015) found a link between the volume of

water replaced and adsorption capacity, and they found that decreasing temperature and increasing pressure enhance water-CO_2 exchange.

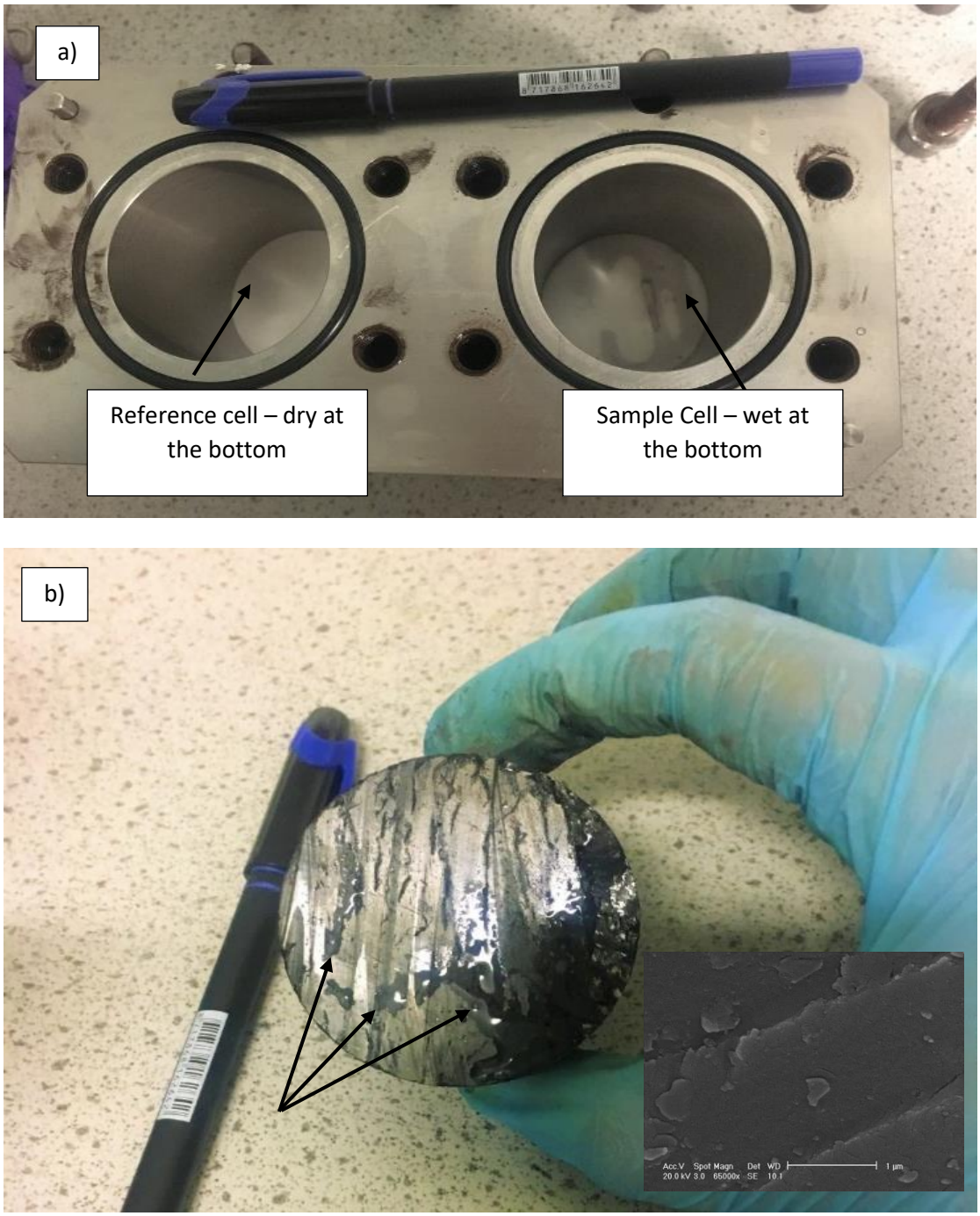

Figure 5.13. Signs of residual water after CO_2 adsorption test on intact 18ft coal - a) at the bottom on the adsorption cell, b) at the bottom of the sample core (insert show the SEM images of nanosized fractures).

5.5.2 CO_2 desorption results

Desorption isotherms are generally presented along the adsorption isotherms obtained for the specific sample. Figure 5.14 depicts the CO_2 desorption isotherm of a wet powdered sample of 18ft AB coal, as well as the CO_2 adsorption isotherm for the same sample. The isotherm pattern displayed the type II adsorption isotherm and H3 hysteresis pattern described by IUPAC (Chapter 2, section 2.5). The adsorption-desorption isotherm showed hysteresis by exhibiting a positive deviation in the lower pressure range (< 2 MPa). The wet coal did not exhibit the substantial positive deviation observed with the dry powdered samples. The reason for this could be that in wet samples, CO_2 must compete with water molecules at activated sites and be easily released from weakly adsorbed external sites at higher pressures (> 2 MPa). The CO_2 molecules adsorbing inside the narrow pores were not ready for desorption at lower pressure range (< 2 MPa) (Figure 5.14).

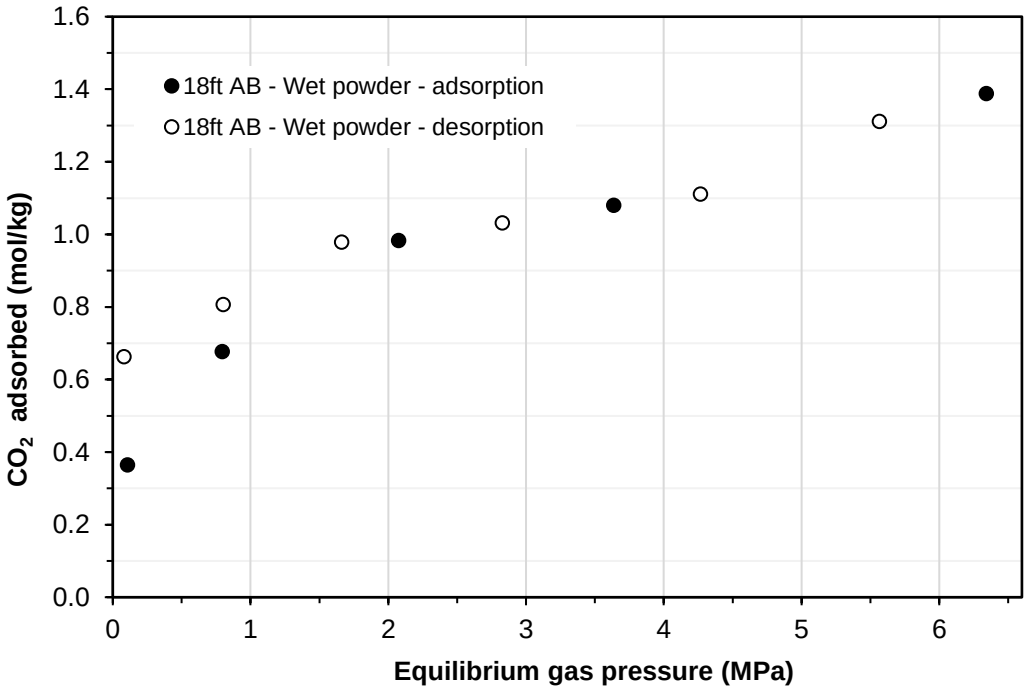

Figure 5.14. CO_2 adsorption-desorption isotherm of wet powder 18ft AB coal - water content 1.2%.

The calculated amount of CO_2 adsorbed at zero pressure during desorption is referred to as residual CO_2. The intercept of the vertical axis by the desorption isotherm pattern in Figure 5.14 represents the residual quantity of CO_2 (0.65 mol/kg) retained in the coal. When the residual amount of CO_2 on the powdered dry sample of 18ft AB coal was compared to the wet sample of 18ft AB coal, the dry sample had 1.18 mol/kg of coal retained at the end of desorption (Chapter 4, section 4.22), while the wet sample had 0.65 mol/kg coal retained in the coal. These findings support the discussion of less amount of CO_2 enter the nano/micropores that has been occupied by the water.

5.5.3 Adsorption pressure versus time observations

The amount of CO_2 gas adsorbed is calculated using the pressure versus time data collected during the adsorption experiments. The recorded pressure versus time data provides information about the kinetics of the adsorption process, as well as information for the CO_2 injection strategy in the field application and identifies uncertainties (leaks and coal deformation induced pressure change) in pressure step-up injection adsorption experiments. The effect of water content on the time required to reach equilibrium was compared in this section for powdered and intact samples of 18ft AB dry and 18ft AB wet.

The equilibrium time obtained for each injection pressure step is summarised in Table 5.4. According to the results obtained, the dry powdered sample of 18ft AB (water content = 0.78%) took longer to attain equilibrium than the wet samples with water content of 1.23%. When the 18ft AB dry (water content = 0.78%) and wet intact samples (water content = 4.5%) were compared, an opposite trend was noted, with the wet sample taking longer to reach equilibrium (Table 5.4). The enhanced adsorption capacity and a longer time to reach equilibrium show that the adsorption process with wet intact samples involves more than one adsorption rate determining steps. This can be explained by three mechanisms: (*i*) CO_2 molecules compete with water molecules for sites (Day et al. 2008b), (*ii*) CO_2 diffuses and dissolves to gain access to the coal matrix (Sun et al., 2015), and (*iii*) potential mineralization of water dissolved CO_2 (Appelo and Postma, 2005).

Table 5.4. Equilibrium time for each injection pressure step for powder and intact 18ft Aberpergwm (dry and wet).

Sample description	Pressure range (MPa) (Injection pressure – Equilibrium pressure)	Time to reach equilibrium (h)	Sample description	Pressure range (MPa) (Injection pressure – Equilibrium pressure)	Time to reach equilibrium (h)
18ft AB Powder- dry	0.68 - 0.15	18	18ft AB Intact - dry	0.58 - 0.08	25
	1.65 - 0.77	20		1.53 - 0.63	23
	3.21 - 2.18	16		3.03 – 2.02	23
	4.51 - 3.67	17		4.60 - 3.76	23
	6.33– 6.32	17		5.52– 5.00	10
				6.35-6.33	5
18ft AB Powder - wet	0.52 - 0.11	30	18ft AB Intact - wet	0.58 - 0.21	27
	1.55 - 0.79	12		1.58 - 0.85	35
	3.04 - 2.01	9		3.04 - 2.02	20
	4.57 - 3.63	2		4.52 - 3.51	20
	6.42 - 6.34	15			

5.5.4 Desorption pressure versus time observations

The equilibrium time and pressure vs time data obtained during the desorption experiments conducted on wet (water content = 1.2%) and dry (water content = 0.78%) powdered samples of 18ft AB are summarized in Table 5.5. Desorption pressure versus time curves provide information about the reversibility of the adsorbed CO_2 on wet coal.

Table 5.5. Equilibrium time for each desorption pressure step for powder 18ft Aberpergwm (dry and wet)

Sample description	Pressure range (MPa) (Releasing pressure – Equilibrium pressure)	Time to reach equilibrium (h)
18ft AB Powder- dry	4.86 - 5.44	90
	2.9 - 3.86	90
	1.42 - 2.59	140
	0.36 - 1.42	16
	0 - 0.68	10
	0 - 0.07	0.8
18ft AB Powder - wet	4.52 - 5.57	12
	2.84 - 4.27	22
	1.44 - 2.83	17
	0.54 - 1.66	13
	0 - 0.8	3
	0 - 0.08	23

In desorption pressure step-down experiments, it was found that the wet sample reached equilibrium more rapidly than the dry sample at higher pressures (Table 5.5). At lower pressures, however, the rate of desorption was slowed due to the longer time required for the wet sample to achieve equilibrium (Table 5.5). The shorter equilibrium time observed is corroborated with the discussion of the release of weakly adsorbed CO_2 due to the water molecule presence, which is reflected in the adsorption-desorption pattern without showing hysteresis of wet powdered 18ft AB sample at a higher-pressure range (>2 MPa; Figure 5.14, section 5.5.2). The longer equilibrium time observed at lower pressures was attributed to the release of the CO_2 into the pores

by expelling the water molecules, which was reflected as a positive hysteresis (<2 MPa; Figure 5.14, section 5.5.2).

5.6 Concluding remarks

This chapter presents and discusses the effect of presence of water in coal samples on CO_2 adsorption/desorption behaviour. This chapter also addresses the potential effects of inorganic and biomineralization of CO_2 on coal adsorption capacity in the presence of water.

1. The chilled-mirror dew-point technique was found to be suitable for establishing water retention curves of coal for a large range of suction. In the current study, for a water content range of 18.2% to 1.06%, the suction of 9ft AB anthracite coal (dry density 1700 kg/m^3) was found to vary between 0.1 MPa and 191 MPa. Similarly, for the 9ft AB coal (dry density 900-1000 kg/m^3), the suction was found to vary between 0.06 MPa and 79 MPa for a water content range of 19.94% and 1.46%. For the bituminous Big Pit coal (dry density 1700 kg/m^3), it was found to vary between 0.52 MPa and 4.15 MPa for a water content range of 11.67% and 3.75%. For the lower dry density, Big Pit coal (dry density of 1500 kg/m^3) was found to vary between 0.26 MPa and 86 MPa for a water content range of 18.7% and 1.2%.
2. The van Genuchten water retention model was successfully used to best-fit the water retention data. The model parameters for anthracite and bituminous coals were found to be different.
3. For anthracite coals (9ft AB and 18ft AB), it was found that the adsorption capacities of wet intact coal samples are slightly greater than that of dry samples. The wet samples of powdered coal (18ft AB), on the other hand, revealed a lesser adsorption capacity than that of dry samples.
4. Adsorption-desorption pattern of wet powdered 18ft AB sample at equilibrium pressures of 6.4 MPa to 2 MPa showed a reversible desorption pattern indicating the CO_2 molecules were weakly adsorbed. While at lower pressures, a positive deviation was observed similar to dry samples. These findings show that at lower pressures (2 MPa), CO_2 molecules had to compete with water

molecules, and that at higher pressures, CO_2 molecules can replace the water present in the pores and occupy the water activated sites (Day et al. 2008b).

5. The pH buffering capacity of coal and the quantification of alkali mineral dissolution underline the non-negligible influence of inorganic CO_2 mineralization on CO_2 adsorption in the presence of water. The pH vales of the samples were increased after equilibrated with coal for 24 h. For example, the sample of coal-water mixture with initial pH of 2.7 was increased to pH 7. The increase in pH values were attributed to the alkali mineral dissolution and neutralisation reaction. The calcium release from the coal was up to 0.02 mg/g of coal.
6. The SEM images indicated the presence of *Bacillus mojavensis*, a coal seam native species resistant to high pressure CO_2, identified in an intact 9ft AB intact sample. Therefore, it was hypothesized in this chapter that the increased adsorption capacity of wet intact 9ft AB samples than that of dry sample could be the result of biomineralisation and inorganic mineralisation of CO_2.
7. The longer time required to attain adsorption equilibrium pressure in wet coal samples suggested that other driving factors such as competitive adsorption at H_2O activated sites (Day et al., 2008b) and CO_2 mineralization are influencing the CO_2 adsorption behaviour of coal in the presence of water.

Chapter 6

Evaluation of CO_2 adsorption on coal by kinetics, isotherm models and characteristics curves

6.1 Introduction

This chapter presents the analyses of the experimental results presented in Chapters 4 and 5. Selected isotherm and kinetic models available in the literature were used to gain a better understanding of the CO_2 adsorption process in coal. The theoretical models applicable for monolayer or multilayer adsorption were used to improve understanding of the CO_2 adsorption processes in coal systems.

Langmuir (1915, 1916, 1917, and 1918) published the most important theory, which explains type I monolayer adsorption. Brunauer et al. (1938) developed the Brunauer–Emmett–Teller (BET) model to account for vapour and liquid-like adsorption (type II multilayer adsorption). The significance of the models is to calculate the maximum adsorption capacity, half-loading pressure that can load half of the maximum capacity on the coal, specific surface area, and thermodynamic parameters of the adsorption process. These parameters can be integrated into large-scale CO_2 injection modelling to create the best injection strategy.

As described by the International Union of Pure and Applied Chemistry (IUPAC), the CO_2 adsorption process in coal can be explained by a combination of type I (monolayer) at lower relative pressure and type II (multilayer type) with H1 and H3 hysteresis loops at elevated pressures (Sing et al. 1985; Harpalani 1995, George and Barakat 2001, Ozdemir et al. 2004, Zutshi and Harpalani 2004; Harpalani et al. 2006 and Thommes et al. 2015).

The current work also developed a strategy with the goal of explaining the CO_2 adsorption by characteristic curves developed based on the equations with parameters representing the thermodynamic nature of adsorbed phase CO_2 and physical forces of

attraction (van der Waals/London dispersion forces). To accomplish these objectives, the current study fitted the experimental adsorption test data into two characteristic curves. The first characteristic curve is based on the potential theory of adsorption (Butt et al. 2003), and the second is based on the gas phase pressure and adsorbed phase molar volume (Brunauer et al. 1940) calculated from the results obtained in the current study.

The adsorption/desorption kinetics data were fitted to pseudo-first-order (PFO) and pseudo-second-order (PSO) rate equations to predict rate-determining steps such as physical sorption, pore condensation/diffusion and surface interaction (Guo 2017; Hu 2020), and were also fitted into the Bangham model to predict pore diffusion as the rate-determining step for CO_2-adsorption on coal (Bangham and Sever 1925; Swan and Urquhart 1927). The theoretical foundations of existing adsorption isotherm models, characteristic curves and kinetic models were discussed in Chapters 2 and 3.

The primary objectives of the theoretical analysis presented in this chapter are as follows:

(*i*) To best-fit the experimental data with the Langmuir isotherm model to predict the maximum adsorption capacity and half-loading pressure of coal samples (section 6.2). To determine the dominant adsorption mechanism (physical/chemical) by calculating the heat of adsorption using Langmuir parameters.

(*ii*) To best-fit the experimental data with the BET isotherm model to evaluate the theory of liquid-like multilayer CO_2 adsorption on coal samples (section 6.3). To calculate the specific surface area available for CO_2 using the BET monolayer surface coverage and derive a possible explanation for CO_2 multilayer adsorption using the heat of adsorption values predicted by the BET model.

(*iii*) To best-fit the experimental data with characteristic curves to explain the CO_2 adsorption in terms of changing adsorbed phase molar volume with increasing gas phase pressure, surface potential/physical attraction forces (section 6.4).

(*vi*) To calculate the kinetic parameters for the corresponding pressure, step up (adsorption) and pressure step down (desorption) stages. To best-fit the experimental data with the Bangham model to predict the rate-determining step of pore diffusion (section 6.5). Specifically, the current work intends to investigate the desorption

kinetics of CO_2 from an intact sample, as no or limited data on CO_2 desorption from intact samples have been available from the earlier studies.

The results of the theoretical evaluation were utilised to analyse the most likely mechanism of CO_2 adsorption on coal (discussed in section 6.6).

6.2 Evaluation of CO_2 adsorption on coal using the Langmuir model

To validate the model, the CO_2 adsorption equilibrium data from the experiments were fitted with the mathematical expression nonlinear form of the Langmuir model (Equation 3.9; Chapter 3, section 3.4) and are shown in Figures 6.1-6.2 and Table 6.1. Figure 6.1 presents the samples with lower water content of 0.78% (18ft AB) and 0.91% (9ft AB); these samples are referred to as dry samples. Figure 6.2 presents the intact 9ft AB sample with a water content of about 2.34%, the intact 18ft AB sample with a water content of 4.07%, and a powder sample of 18ft AB with a water content of 1.2%. These samples are referred to as wet samples.

The Langmuir parameters, maximum CO_2 adsorption capacity of the coal samples ($m_\infty; g\ of \frac{CO_2}{kg} of\ coal$), and half-loading pressures (b; Pa^{-1}) were obtained from the best-fit of the nonlinear regression analysis (Equation 3.9; Chapter 3, section 3.4). Figure 6.1 shows the plots comparing the experimental data of dry intact and powdered samples of 9ft AB, 18ft AB and BP against results obtained from the Langmuir model. Figure 6.2 shows the plots comparing the experimental data of wet samples of intact 9ft AB, 18 ft AB and wet powdered sample of 18ft AB against results obtained from the Langmuir model. Table 6.1 summarises the Langmuir parameters.

At lower and intermediate pressures (< 6.1 MPa), there was good agreement between experimental and model results (Figures 6.1 a and c; Figures 6.2 a to c). The experimental results deviated from the model to show the multilayer build-up at high pressures (from 6.1 MPa to 6.4 MPa). This was evident in the intact samples of dry 18ft AB where high density CO_2 adsorption occurs within microfractures of intact coal (Figures 6.1 b), implying the effect of near critical pressure on intact samples. However, at a similar pressure range, the experimental results of the dry and wet powdered samples of 18ft AB were in good agreement with the Langmuir model,

indicating that water molecules prevent multilayer formation (Figure 6.1 b and Figure 6.1 C), showing the influence of sample fabric and water.

It was explained in Chapter 4 (section 4.3) why the bituminous intact coal sample had a slightly higher adsorption capacity than the powdered sample of the same coal, which was reflected in the calculated maximum capacity. The predicted Langmuir maximum adsorption capacity for the BP intact (bituminous) was 53.66 g of CO_2/kg of coal, while the powdered BP sample was 45.57 g of CO_2/kg of coal. The inverse of half-loading pressure of all the samples (Langmuir parameter *b*, Pa^{-1}), the predicted pressure at which half of the maximum adsorption capacity can be achieved, ranged from 10^{-6} to 10^{-7} Pa^{-1} (Table 6.1).

Half-loading pressure is an important economic parameter in coal seam CO_2 storage (Harpalani et al. 2006). Conducting an isobaric adsorption experiment at the half-loading pressure value predicted by the Langmuir model can yield half of the maximum adsorption capacity of the specific coal sample. Experiments at 1.18 MPa (half-loading pressure; reciprocal of *b*-value for 18ft AB dry intact) can, for example, achieve a loading of half the 65.94 g CO_2/kg of coal (Figure 6.1 (b); Table 6.1). Similarly, at 0.40 MPa (inverse of *b* value for 9ft AB dry intact; Figure 6.1 (a); Table 6.1), half of 80.54 g of CO_2/kg of coal can be loaded.

The observations discussed above imply that the monolayer was covered at pressures less than 0.5 MPa, and the isotherm pattern observed at intermediate pressures showed the type II isotherm slope (Sing et al. 1985) rather than the plateau typically observed in Langmuir type adsorption, representing the multilayer build-up that occurs at coal surfaces (Yang 1987). The type II isotherm pattern was visible with both wet and dry samples as the plots in Figures 6.1 and 6.2 showed a deviating uptrend from the Langmuir model, and it was more pronounced with the dry samples of 18ft AB at high pressures (up to 6.4 MPa) (Figure 6.1 b).

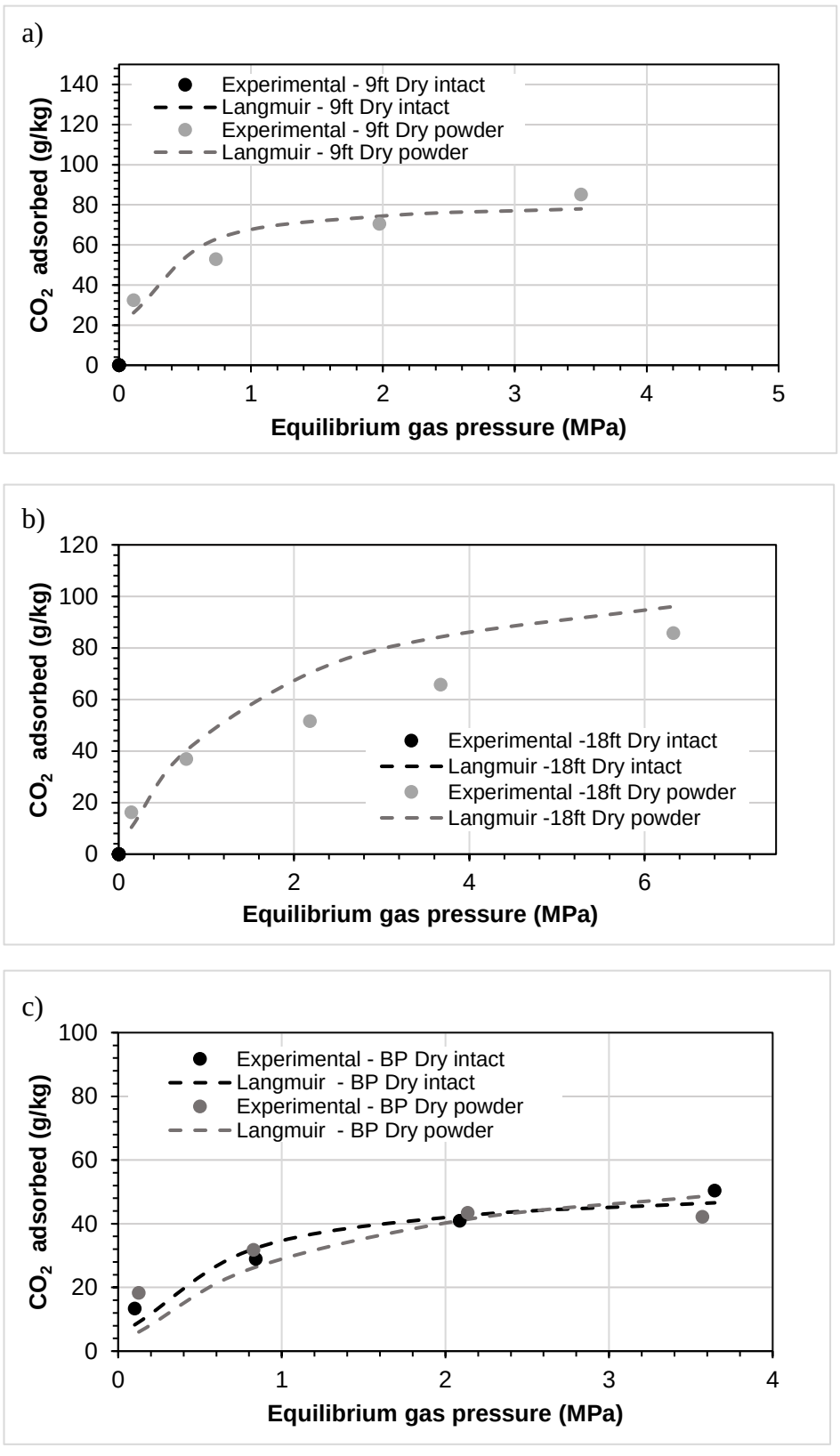

Figure 6.1. Experimental data fitted against Langmuir model: (a) 9ft AB dry (intact and powder), (b) 18ft AB dry (intact and powder) and (c) Big Pit intact and powder).

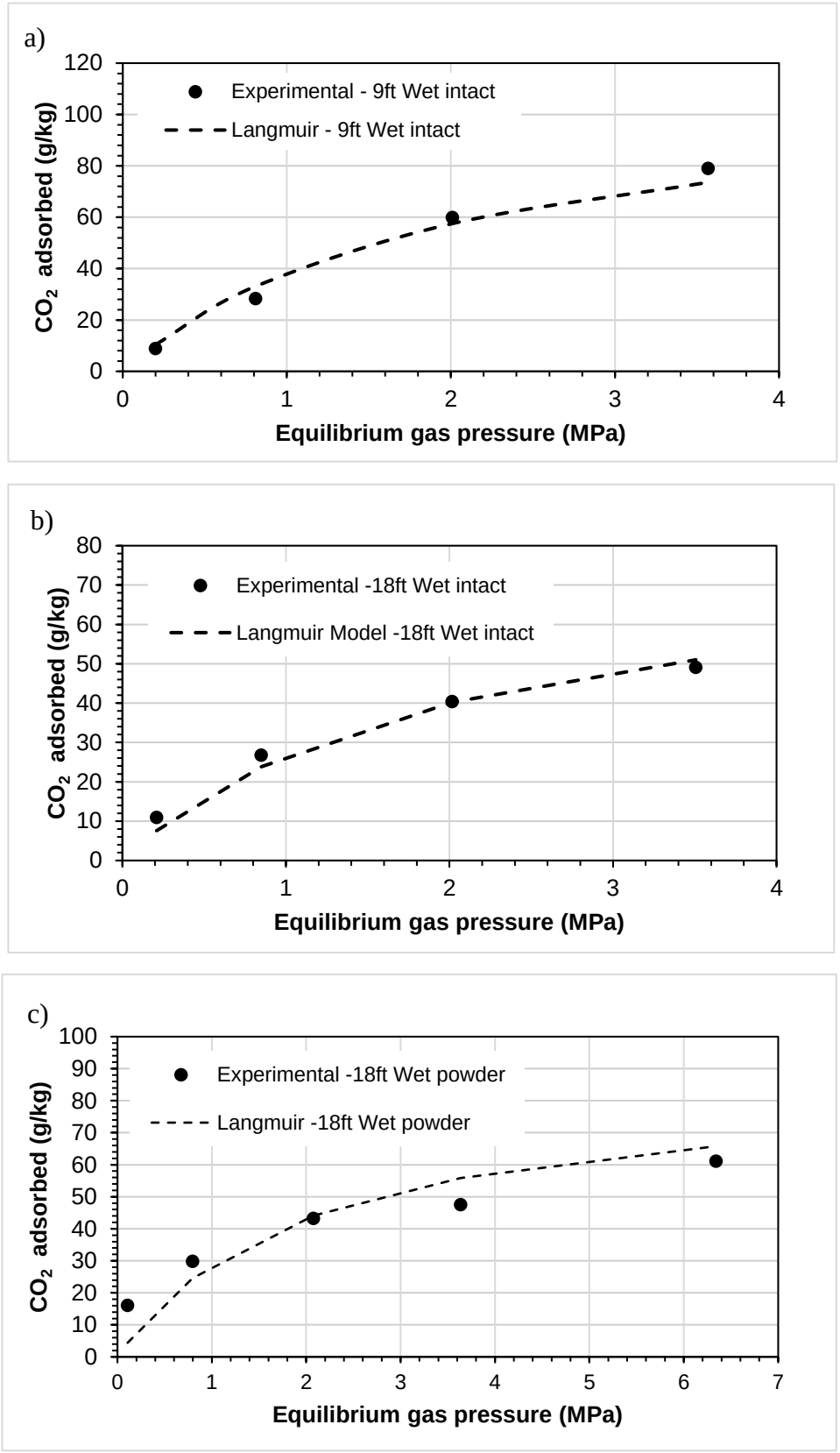

Figure 6.2. Experimental data fitted against Langmuir model: (a) 9ft AB wet intact, (b) 18ft AB wet intact, (c) 18ft AB wet powder.

Table 6.1. Langmuir parameters, b-half-loading pressure, and m_∞-maximum adsorption capacity, obtained from plots (Figure 6.1).

Sample description	Half-loading parameter *b*, Pa^{-1}	Maximum adsorption capacity, m_∞, g of CO_2/kg of coal
AB 18ft dry intact	8.50×10^{-7}	65.94
AB 18ft dry powder	6.61×10^{-7}	119.00
AB 18ft wet intact	5×10^{-7}	80.09
AB 18ft wet powder	5.0×10^{-7}	86.53
AB 9ft dry intact	1.56×10^{-6}	80.54
AB 9ft dry powder	2.49×10^{-6}	91.77
AB 9ft wet intact	2.95×10^{-7}	155.29
Big Pit intact	1.8×10^{-6}	53.66
Big Pit powder	4.29×10^{-6}	45.57

6.2.1 Energy of adsorption (Langmuir model)

The adsorption energy (ΔH_{ad}) was calculated using the Langmuir parameters obtained from the isotherm model fittings (maximum Langmuir adsorption capacity (m_∞) and the constant *b*). Chapter 3 presents the calculation method (Chapter 3, section 3.4). The heat of adsorption values was between -15 kJ/mol to -22 kJ/mol (Table 6.2), which attribute to the physical adsorption (enthalpy change of physical adsorption is in the range of -20 kJ/mol; Atkins et al. 2017).

Physical adsorption occurs when the CO_2 molecules are weakly held on the surface of the coal by the van der Waals forces (Butt et al. 2003b; Atkins et al. 2016). Therefore, it is appropriate to consider the theories (adsorption models) based on the surface potential energy caused by van der Waals forces (the potential theory of Polanyi; Butt et al. 2003a and b), which is further discussed in Section 6.4, under characteristic curve 2.

Table 6.2. Estimated values of energy of adsorption (based on Langmuir parameters and the kinetic theory of gases.

Sample description	ΔH_{ad} kJ/mol	ΔG^0_{ad} kJ/mol
AB 18ft dry intact	-16.38	-34.65
AB 18ft dry powder	-14.89	-35.27
AB 18ft wet intact	-17.22	-34.49
AB 18ft wet powder	-15.03	-33.93
AB 9ft dry intact	-17.99	-33.14
AB 9ft dry powder	-18.82	-31.98
AB 9ft wet intact	-12.23	-37.27
BP dry intact	-19.36	-32.8
BP powder	-21.91	-30.64

According to Langmuir theory, at equilibrium, the amount adsorbed equals the amount desorbed, and the Gibbs free energy is related to the equilibrium constant or the Langmuir constant (*b*, half loading pressure). The Gibbs free energy of CO_2 adsorption on coal was calculated using a modified version of the equation presented in Butt et al. 2003 (Equation 6.1) and shown in Table 6.2.

$$\Delta G^0_{ad} = -RTlnb^{-1} \qquad (6.1)$$

where ΔG^{0}_{ad} is Gibbs free energy of the adsorption, J/mol, R is gas constant J/mol K, T is temperature (298.15 K) and *b* is Langmuir constant, Pa^{-1}.

The adsorption energy/Gibbs free energy of adsorption are molar quantities that increase with the number of moles adsorbed. The findings were directly compared with previously reported findings on an 86% carbon content coal, where the enthalpy of adsorption ranged from 25.3 kJ/mol to 27.3 kJ/mol (Ozlemir et al. 2004), which is comparable with the current study's estimated values. The adsorption energy calculated in this work is similar to the numerical values of the heat of condensation of CO_2 (15.8 kJ/mol) (Speight 2017), indicating that liquid-like adsorption theories such as BET and potential theory of adsorption should be used to explain CO_2 adsorption on coal.

6.3 Evaluation of CO_2 adsorption on coal using Brunauer – Emmet - Teller (BET) model

Figure 6.3 shows plots comparing experimental data from dry intact and powdered samples of 9ft AB, 18ft AB and BP to results from the BET model. Figure 6.4 presents the plots comparing the experimental results with the results from the BET model of wet intact samples of 9ft AB, 18 ft AB and wet powdered sample of 18ft AB. For all the intact coal samples considered in this study (Figures 6.3 and 6.4 a, b), the BET model fitted well the experimental data, indicating multilayer CO_2 adsorption on coal surfaces. The BET model did not fit well with the powder samples of dry and wet 18ft AB (Figure 6.4 b and c). It is likely that the adsorbed water on the large surface area available for water molecules cannot be easily displaced by gas molecules, preventing multilayer formation in the pores (Figure 6.4 c). For a dry sample of 18ft AB (Figure 6.4 b), the lower density adsorbed phase reflected on the isotherm and fitted better with the Langmuir model than that of BET, signifying the influence of sample fabric. Table 6.3 provides a summary of the BET parameters of the coal samples.

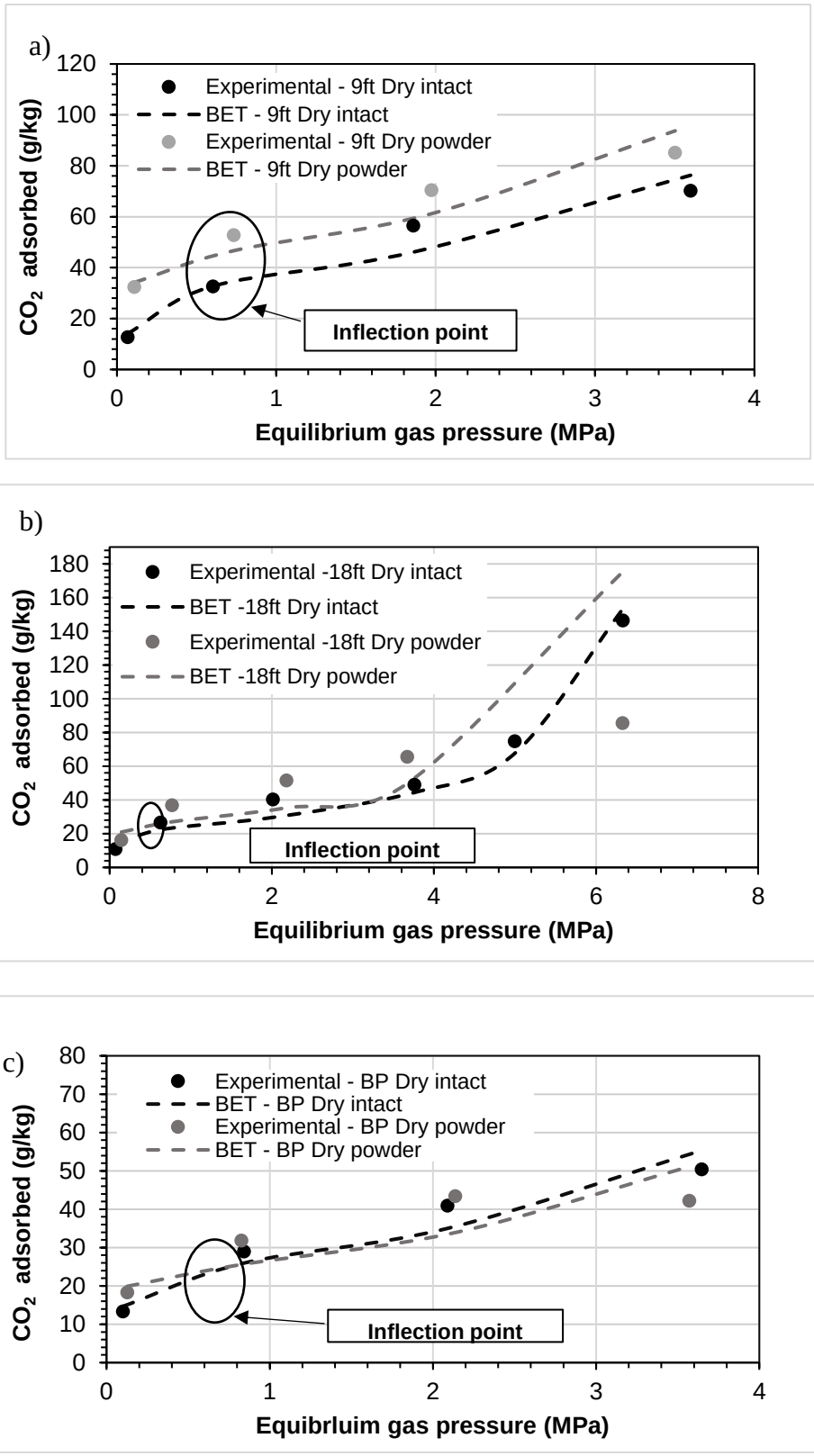

Figure 6.3. Experimental data fitted against Brunauer – Emmet -Teller (BET) model: (a) 9ft AB dry (intact and powder), (b) 18ft AB dry (intact and powder) and (c) Big Pit intact and powder).

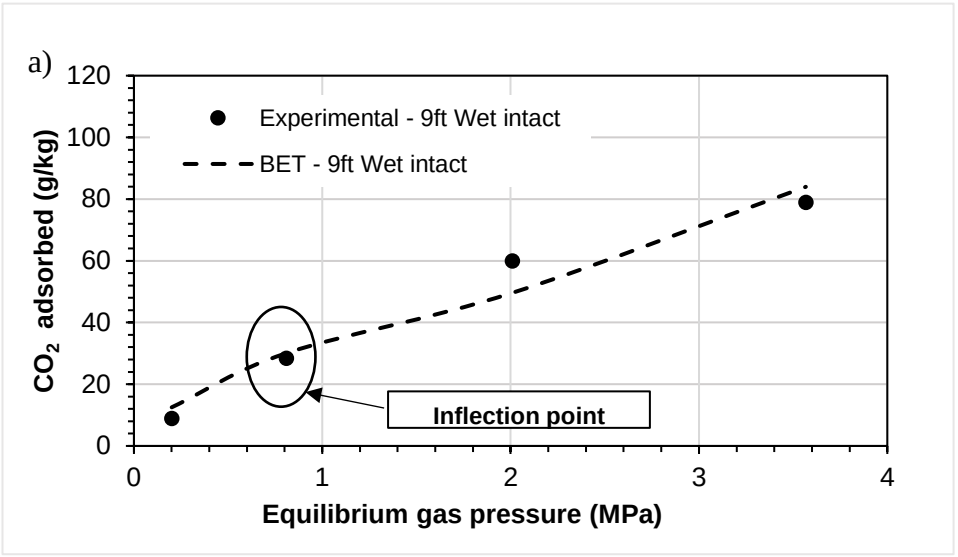

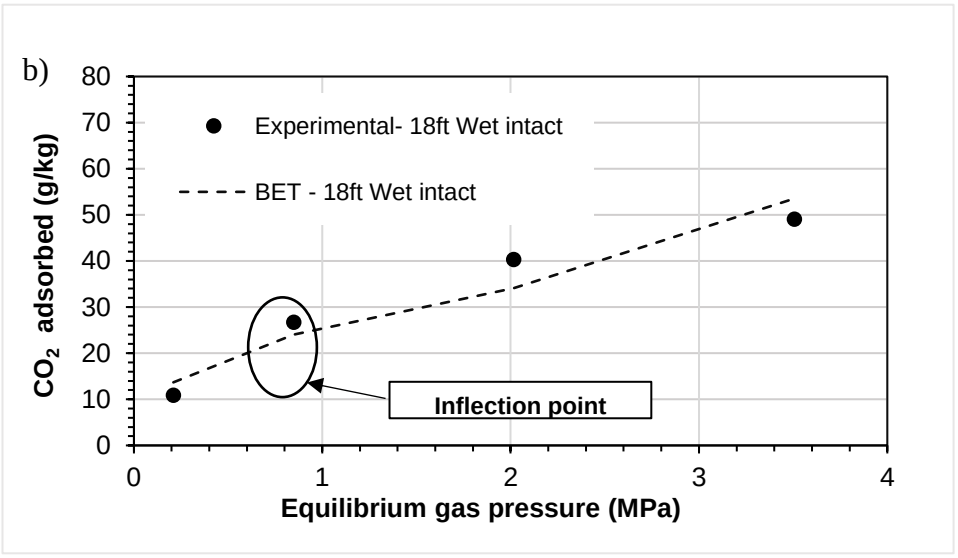

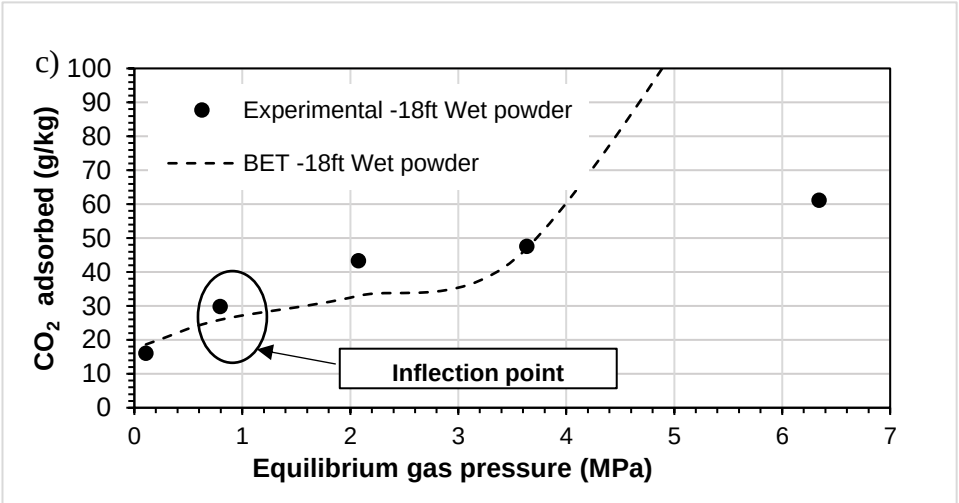

Figure 6.4. Experimental data fitted against Brunauer – Emmet -Teller (BET) model: (a) 9ft AB wet intact (b) 18ft AB wet intact, (c) AB 18ft wet powder.

Table 6.3. Brunauer - Emmet -Teller (BET)parameters of CO_2 adsorption on coal samples.

Samples description	BET dimensionless parameter, *c*	Adsorbed amount at monolayer coverage, n_{mon}, g of CO_2/kg of coal	Surface area, m^2/kg	Q_1-Q_2, (kJ/mol) *
AB 18ft dry intact	150	21.96	78408	-12.42
AB 18ft dry powder	222	25.17	89869	-13.39
AB 18ft wet powder	222	24	85692	-13.39
AB 9ft dry intact	52.95	38.79	121397	-9.839
AB 9ft dry powder	209	42.87	153067	-13.24
AB 9ft wet intact	13.7	39.61	141428	-6.49
AB 18ft wet intact	33.55	24.96	89120	-8.71
Big pit intact	93.5	24.16	86263	-11.21
Big pit powder dry	296.45	22.80	81407	-14.11

* Q_1-Q_2 is the difference between the heat of adsorption of the first layer and the subsequent liquid layers.

6.3.1 Specific surface area of coal

The monolayer coverage, n_{mon}, values show that the inflection point occurred well below 1.0 MPa (Figures 6.3 and 6.4). This could be the reasons that the intermediate pressure experiments fit the BET model well where the liquid like adsorption occurs above the inflection point. Because of the *c* values are greater than 20 (see Table 6.3), the obtained monolayer coverage values (n_{mon}) can be used to calculate the available surface area for CO_2 molecules (Pennell 2002).

Table 6.3 summarises the calculated available specific surface area on coal for the adsorption of gas molecules. The dry intact sample of bituminous BP coal (86263 m^2/kg) showed a higher surface area than the intact dry samples of anthracite 18ft AB (78408 m^2/kg) and lower than the 9ft AB (121397 m^2/kg) samples. The powdered samples of 9 ft AB had a higher specific surface area than the powdered samples of 18ft AB and BP samples. The intact sample of BP (86263 m^2/kg) exhibited higher specific microporous surface area than the powdered samples of BP (81407 m^2/kg). This is effect of the bituminous coal fabric (microporous porous network volume) on

the adsorption of CO_2 in intact bituminous sample which resulted in higher adsorption capacity. The obtained specific surface areas in the current work (78408 m^2/kg-153067 m^2/kg) are comparable with the specific surface area available for CO_2 obtained by Zhao et.al. 2016 (77400 m^2/kg to 198400 m^2/kg).

6.3.2 Energy of adsorption (BET model)

The dimensionless parameter *c* is related to the adsorption energy and is defined as (Brunauer et al. 1938):

$$c \approx e^{\left[\frac{Q_1 - Q_2}{RT}\right]} \qquad (6.2)$$

where *c* is the dimensionless BET parameter, Q_1 is the adsorption energy on the bare surface (monolayer adsorption) (J/mol), Q_2 is the energy of second and subsequent layers (J/mol), *R* is the gas constant (8.314 J/mol), and *T* is the temperature at the experiments conducted (298.15 K).

The magnitude of Q_2 is related to the heat of condensation or liquefaction of CO_2, which is constant. The value of Q_1 is associated with the energy of monolayer Langmuir adsorption (ΔH_{ad}). The differences between the energy of monolayer adsorption (Q_1 *or* ΔH_{ad} ; about 20 kJ/mol, Table 6.2) and the energy of condensation of CO_2 (Q_2) were comparable with the values obtained for ($Q_1 - Q_2$) from the dimensionless parameter *c* (Equation 6.2; Table 6.3). The heat of condensation of CO_2 is approximately 16.7 kJ/mol (NIST Chemistry WebBook, SRD 69, 2021). This analysis indicates that CO_2 pore condensation occurs above the inflection point (> 1 MPa; Figures 6.3 and 6.4).

6.4 Evaluation of CO_2 adsorption from characteristic curves

The Langmuir and BET isotherms represent the surface coverage and the build-up of multilayers of CO_2 molecules. The models do not represent for the effects of chemical potential, surface interfacial forces, and the P-V-T behaviour of adsorbed and free gas molecules on the isotherm pattern. As a consequence, the current study

attempts to study the CO_2 adsorption on coal using simple and reasonable theories, as described below.

The characteristic curve I is derived based on the theory that molar volume approaches the liquid-like density of CO_2 inside pores at 0.5 to 6.5 MPa (Brunauer et al. 1940) and that adsorption on pore walls can significantly densify CO_2 trapped in nanoscale pores of adsorbents (Cole et al. 2010; Chialvo et al. 2012: Gruszkiewics et al. 2012). The characteristic curve II was based on the potential theory of adsorption, which takes into account the number of moles spreading across a specific surface area of the adsorbent, which is influenced by the state of chemical equilibrium and physical attractive force between the sorbent and the sorbates (Yang 1987; Tóth 2002; Butt et al. 2003a, b; Atkins et al. 2017; Tien 2019). These are called characteristic curves 1 and 2.

Characteristic curve 1: In this case, the hypothesis assumed that as the pressure rises, the molar volume of the adsorbed phase of CO_2 ($v_m^{ad}\,\frac{m^3}{mol}$) varies as a function of the fugacity of the gas phase and the adsorbed phase of CO_2. The adsorption process on pore walls can significantly densify the entrapped CO_2 in the nanopores of the coal to liquid-like molar volume (Cole et al. 2010; Chialvo et al. 2012; Gruszkiewics et al. 2012). When the fugacity of the adsorbed phase and the gas phase are equal, adsorption reaches equilibrium and condensation occurs (Brunauer et al. 1938, Brunauer et al. 1940). Using the aforementioned theories, an empirical relationship was developed to explore the CO_2 adsorption on coal as it relates to the changing state functions (P and V) of CO_2. The empirical equation's theoretical formulation is as follows.

The molar volume of the adsorbed phase $v_m^{ad}\,\frac{m^3}{mol}$ was calculated using the number of moles adsorbed (n) in the available volume (v^a), Equation (6.3).

$$v_m^{ad} = \frac{v^a}{n} \tag{6.3}$$

where v_m^{ad} is the adsorbed phase molar volume ($\frac{m^3}{mol}$) , v^a is the volume available for CO_2 gas per kg of coal which is the void volume of the sample estimated by He-

pyconametry (m^3/kg) and *n* is number of moles of CO_2 adsorbed per kg of coal (mol/kg).

Then, using the BET monolayer coverage, the molar volume of the monolayer (v_m^{mon}) was calculated (Table 6.3, section 6.3). The empirical relationship presented in Equation 6.4 was formed by relating the molar volume of the adsorbed phase (v_m^{ad}) and the molar volume occupied by monolayer adsorption (v_m^{mon}) to the fugacity ratio of the gas phase and adsorbed phase. The gas phase and adsorbed phase fugacity were calculated using the Peng-Robinson equation of state for the pressure values measured during the experiments.

$$\frac{v_m^{mon}}{v_m^{ad}} \propto \frac{f_g}{f_a} \qquad (or) \qquad \frac{\rho^{ad}}{\rho_m^{ad}} \propto \frac{f_g}{f_a} \tag{6.4}$$

where v_m^{ad} and v_m^{mon} *are* the molar volumes of adsorbed phase and monolayer coverage ($\frac{m^3}{mol}$), ρ^{ad} and ρ_m^{ad}- are the densities of the adsorbed phase and monolayer coverage ($\frac{mol}{m^3}$) and f_g and f_a are the fugacity of the gas phase and liquid-like adsorbed phase.

The results obtained using the empirical relationship (Equation 6.4) for an intact coal sample of 18 ft AB are presented in Figure 6.5 (a). The illustration in Figure 6.5 (b) explains the hypothesis.

This approach is motivated to view CO_2 adsorption more realistically by taking into account the varying state functions at the adsorbed phase. The results presented in Figure 6.5 (a, b), and Equation (6.4) clearly explain the overall adsorption process that occurs in intact samples. The results presented in Figure 6.5 (a) show that multilayer build up occurs around the y-axis value of 1.0. The Y-axis of the characteristic curve can also be interpreted as the ratio of the adsorbed phase density of CO_2 at a given equilibrium pressure to the density of CO_2 found at complete monolayer coverage.

Another critical aspect of these theoretical assumptions is the relationship between the fugacity of the adsorbed (liquid) phase and the gas phase of CO_2 (x-axis

of Figure 6.5 a). When the fugacity of CO_2 in the gas phase equals that of the adsorbed phase (density of liquid CO_2) in the near-critical region of CO_2, pure fluid condensation of CO_2 must be considered (which can be located at the fugacity values reaches the value one along the X-axis).

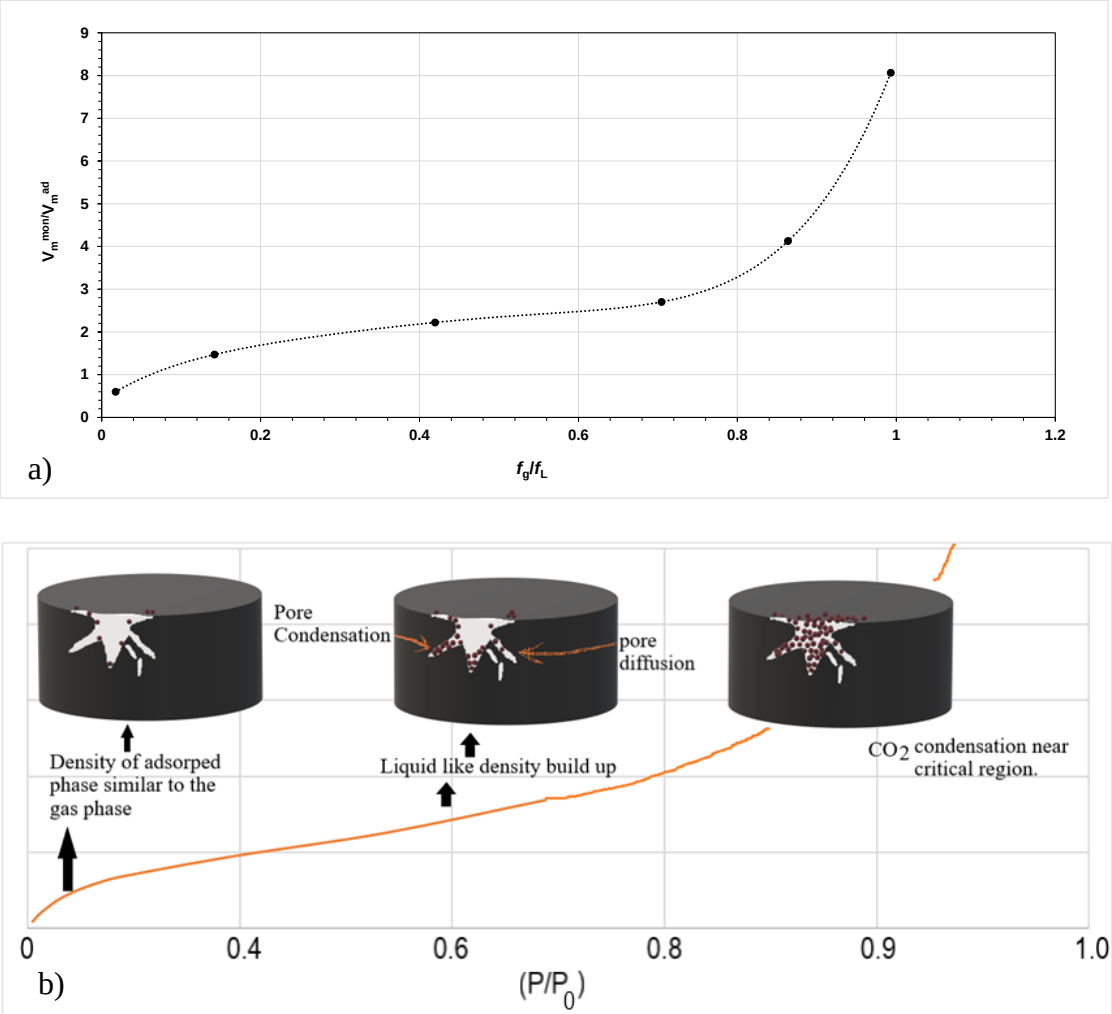

Figure 6.5. a) Adsorption characteristic curve based on equation (6.3) for 18ft Aberpergwm intact coal specimen and b) the pattern of the characteristic curve depicting the adsorbed phase density and influence of pore diffusion and surface condensation of CO_2 on the adsorption.

***Characteristic curve 2*:** In this case, the characteristic curve was constructed from the microscopic perspective of a single CO_2 molecule attracted to the coal's large body (The potential theory of Polanyi; Butt et al. 2003). The fundamental assumptions made for establishing the characteristic curve are as follows:

The potential theory assumes that the molecules near the coal surface has a physical attractive force similar to the gravitational field caused by van der Waals/London dispersion forces. The surface potential compresses the gas molecules isothermally. If this localized pressure is higher than the equilibrium pressure, the gas molecule will condense.

The condensed molecules adsorbed possess liquid-like densities. The molar volume of the liquid phase calculated using the appropriate equation of state (PR equation of state for the current study). The thickness of the adsorbed layers was related to the number of molecules adsorbed over a unit surface area. The moles of CO_2 adsorbed over a unit surface area held or attracted by the van der Waals force exerted by coal and that can be related and explained by Equation (6.5).

$$\Gamma \frac{mols\ adsorbed}{m^2} = \frac{x}{V_m^L} = \frac{1}{V_m^L}\sqrt[3]{\frac{C_p}{RT\ln\left(\frac{p_0}{p}\right)}} - \frac{D_0}{V_m^L} \qquad (6.5)$$

where x is thickness of the liquid-like adsorbed layer related to density and effective surface area by adsorbents (m), Γ is moles adsorbed over specific surface area (mol/m^2), V_m^L is molar volume of liquid like adsorbed phase, calculated using equation of state (m^3/mol), C_p is related to Hamaker constant for specific solid-gas system. Additionally, the parameter *C* is related to the internal energy (-Um(x)) of the surface (involving physical attraction forces quantities) $(-Um(x) = \frac{C}{(D_0+x)}$ (Jm^3/mol), $C_p = \frac{A_H}{3\pi\rho_A}$; A_H is Hamaker constant (J), D_0 is effective radius of the molecule = 0.33×10^{-9} m and ρ_A is density of adsorbed phase CO_2 (mol/m^3).

The predicted adsorbed CO_2 obtained from Equation (6.5) are plotted against the relative pressure and compared to the results obtained from experiments conducted up to 6.4 MPa for dry intact, dry and wet powdered samples of 18 ft AB samples in Figure 6.6 and experiments conducted below 6.1 MPa for dry and intact samples of 9ft AB, wet intact 18ft AB, dry intact and powdered samples of AB in Figure 6.7.

The results presented in Figures. 6.6 and 6.7 show that the potential theory of adsorption predicts the general shape of the isotherm and that the assumption of van der Waals attractive forces are significant in the CO_2-coal adsorption system. The

parameter C_p calculated from the isotherm plots was about $1 \times 10^{-27} \frac{Jm^3}{mol}$ (Equation (6.5); (Figures 6.6 and 6.7). The estimated value of the Hamaker constant was 4.42×10^{-23} J. The parameter C_p is of the order of $10^{-26} \frac{Jm^3}{mol}$, which is consistent with the assumption that only van der Waals forces act between a small molecule and a large surface (Butt et al. 2003 a, b).

The characteristic curves I and II demonstrate that selecting appropriate adsorption theories for understanding the fundamental nature of CO_2 adsorption on coal is important for CO_2 sequestration. The characteristic curve I shows the thermodynamic nature of adsorbed phase CO_2 as density changes with increasing gas phase and adsorbed phase pressure. The characteristic curve II, also known as the potential theory of adsorption, is an entirely different approach that assumes the van der Waals force of attraction exerted by coal on CO_2 molecules is significant, and the characteristic curve accurately predicts the isotherm for CO_2 on coal. The findings indicate that, in addition to the Langmuir monolayer and BET theories, other adsorption theories with more realistic experimental observations are needed to explain CO_2 adsorption on coal.

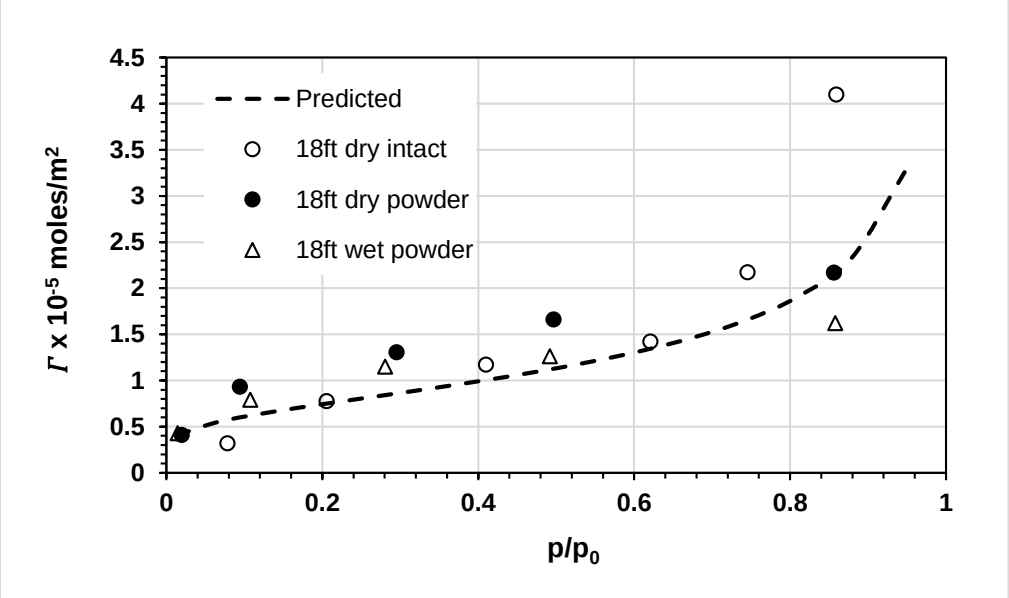

Figure 6.6. Adsorbed amount of CO_2 on coal specimens against values predicted by the equation based on the theory of Polanyi (Equation 6.5) which assumes the van der Waals forces are the major contribution of gas adsorption.

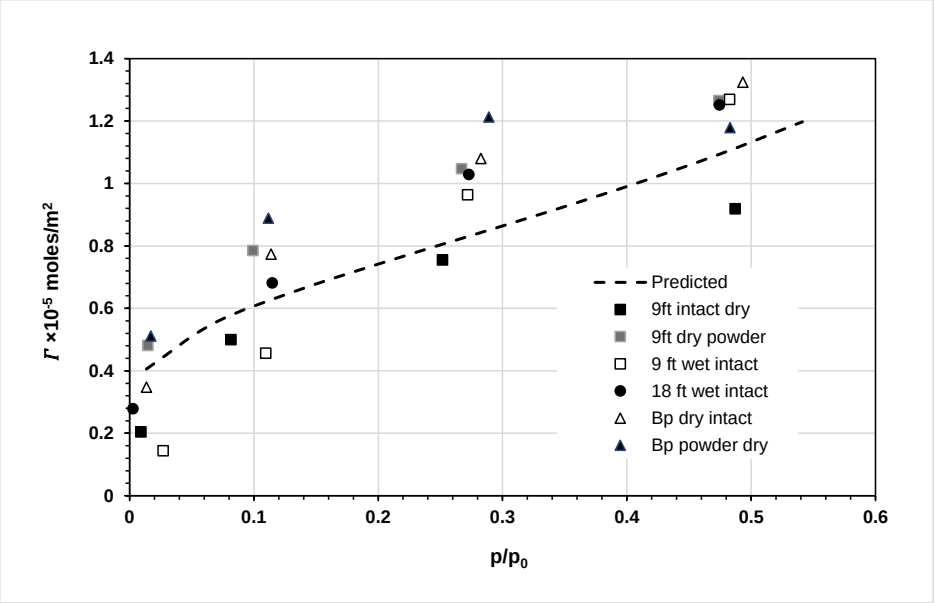

Figure 6.7. Adsorbed amount of CO_2 on coal specimens against values predicted by the equation based on the theory of Polanyi (Equation 6.5) which assumes the van der Waals forces are the major contribution of gas adsorption.

6.5 kinetics of CO_2 adsorption on coal

Pseudo-first-order (PFO) and pseudo-second-order (PSO) kinetic models were used to fit the experimental data (that is, the amount adsorbed CO_2 versus time). The adsorbed CO_2 predicted by the PFO and PSO models at time t (q_t, g adsorbed CO_2/kg coal) are plotted against the experimental values in Figures 6.8 to 6.12.

Figures 6.8, 6.9, 6.10, 6.11 and 6.12 show the results obtained for samples of 18ft AB dry intact, 18ft AB dry powder, 9ft AB dry intact, 9ft AB dry powder, and Big Pit powder dry, respectively. Tables 6.4, 6.5, 6.6 and 6.7 show the rate constants (K_{ad1}, K_{ad2} for adsorption, and K_{de1} for desorption), equilibrium concentration (q_e), R^2 values and standard error of estimate for the model fit for the 18ft AB dry intact, 18ft AB dry powder, 9ft AB dry intact, 9ft AB dry powder, and Big Pit powder dry, respectively. Column 1 in Tables 6.4 to 6.7 represents the adsorption injection and equilibrium pressure of the gas phase CO_2. Columns 2 and 5 represent the predicted equilibrium amount of CO_2 adsorbed on coal (q_e) and the rate constants for the PFO

and PSO models, respectively. Columns 4 and 7 in Tables 6.4 to 6.7 present the R^2 values of the fit and the standard error of estimate in the parentheses.

Gabruś et al (2021) published an experimental study on CO_2 adsorption on bituminous coal in which the results have been fitted into PFO and PSO models. The K_{ad1} and K_{ad2} values obtained at 298.15 K and 2 MPa equilibrium pressure were much higher than the values obtained in the current study. K_{ad1} was in the range of 1613×10^3 to 1011×10^3 h^{-1} and K_{ad2} was in the range of 5752×10^3 h^{-1} to 11851×10^3 h^{-1}. However, these experiments were conducted for less than 24 h equilibrium time to reach the maximum pressure range of 2 MPa whereas the current study allowed the equilibrium to occur for each pressure steps (0.5 MPa to 6.4 MPa).

Overall, the plots and the combination of standard error of estimate and correlation coefficient (R^2) indicate that the adsorption kinetics data agree well with the PSO model than the PFO model (Figures 6.8 to 6.12; Table 6.4 to 6.7). The PSO model implies that surface interaction and bulk pore diffusion dominate CO_2 adsorption on coal (Plazinski et al. 2013; Tang et al. 2016). The pressure dependence of K_{ad2} demonstrated that the pore diffusion being the rate determining step in the beginning and surface interaction being the slowest rate determining step at higher pressures (K_{ad1}, K_{ad2} values in Table 6.4 to 6.7).

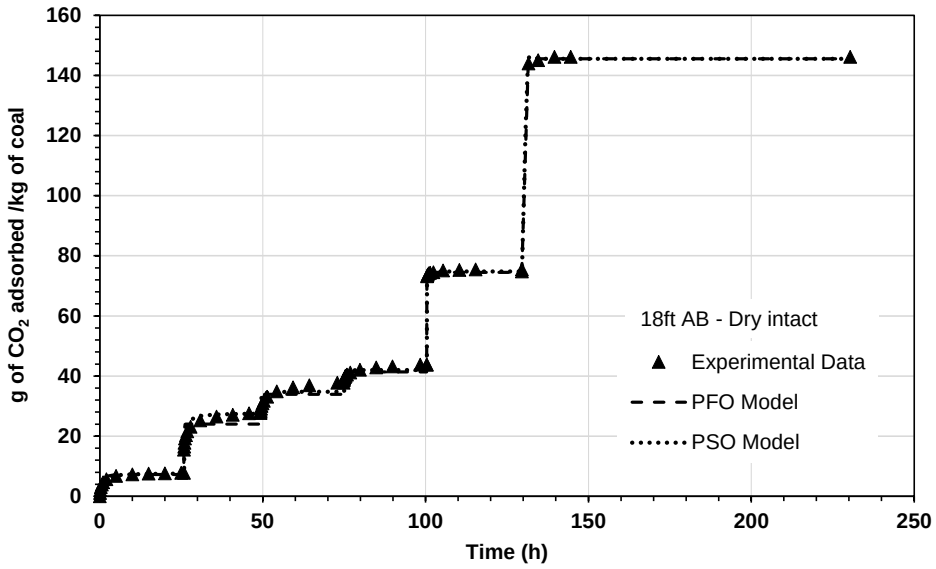

Figure 6.8. 18ft AB dry intact specimen, experimental data fitted against the PFO and PSO model. The equilibrium amount of CO_2 (qe) and rate constants (k_{a1} and k_{a2}) are summarised in Table 6.4.

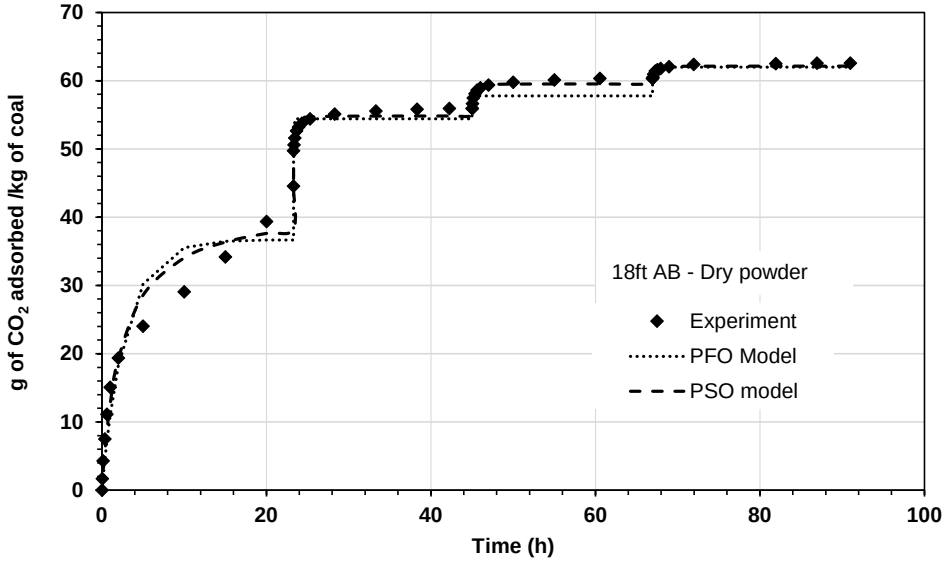

Figure 6.9. 18ft AB dry powder specimen, experimental data fitted against the PFO and PSO model. The equilibrium amount of CO_2 (qe) and rate constants (k_{a1} and k_{a2}) are summarised in Table 6.5.

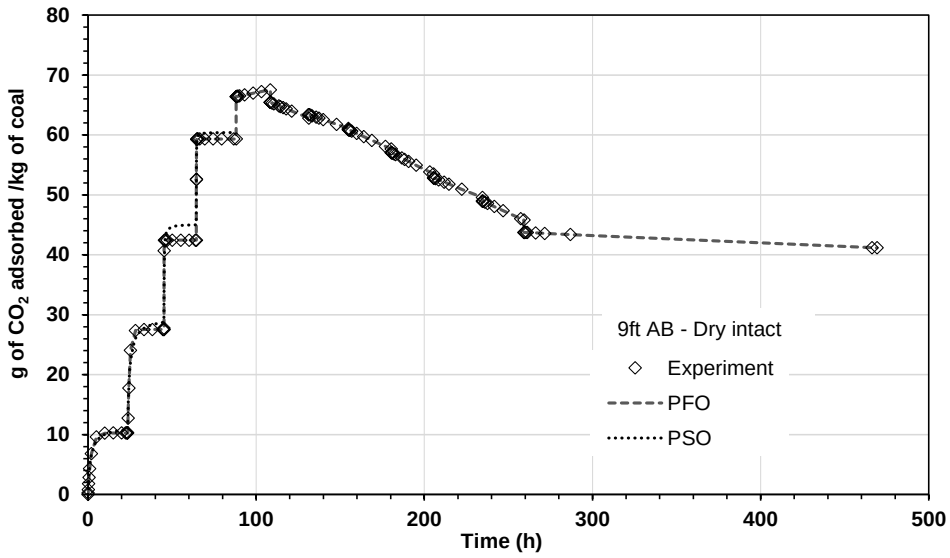

Figure 6.10. 9ft AB dry intact, experimental data fitted against the PFO and PSO adsorption-desorption kinetics model. The equilibrium amount of CO_2 (qe) and rate constants (k_{a1} and k_{a2}) are summarised in Table 6.6.

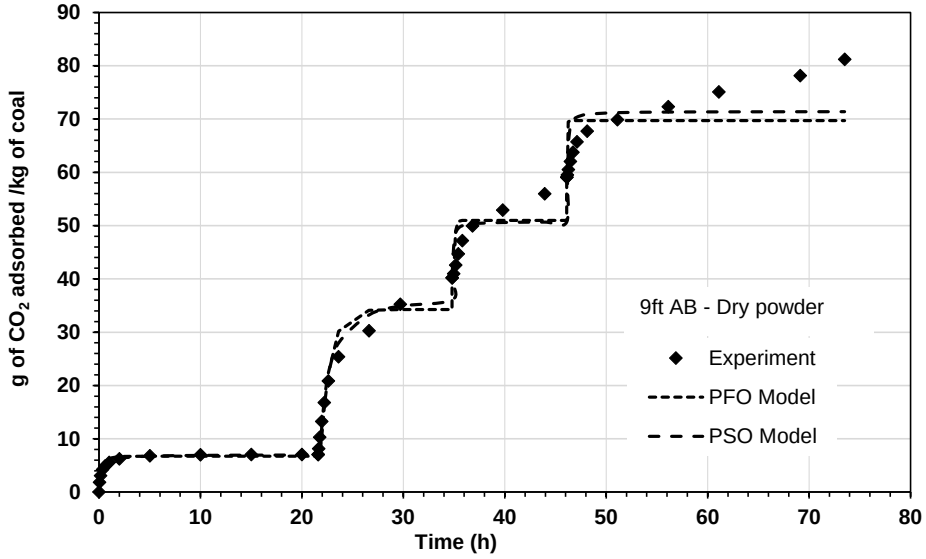

Figure 6.11. 9ft AB dry powder, experimental data fitted against the PFO and PSO model. The equilibrium amount of CO_2 (qe) and rate constants (k_{a1} and k_{a2}) are summarised in Table 6.7.

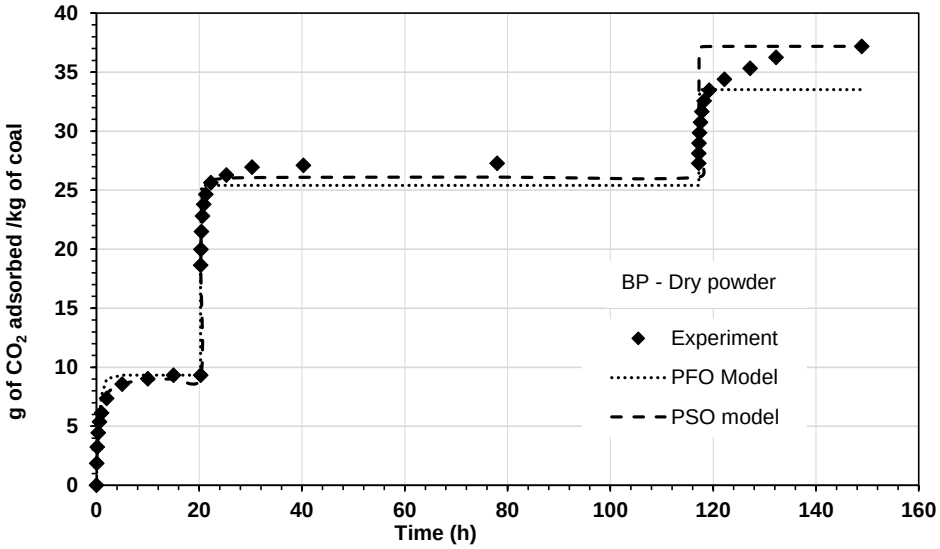

Figure 6.12. Big Pit powder dry, experimental data fitted against the PFO and PSO model. The equilibrium amount of CO_2 (qe) and rate constants (k_{a1} and k_{a2}) are summarised in Table 6.8.

Pore diffusion was more pronounced during the desorption kinetics, which fits the PFO model well. The rate-limiting step in the desorption process was the slow release of CO_2 molecules trapped in the pores (K_{de1} values; Table 6.7). It can be seen from the results presented in Figure 6.10 that the adsorption-desorption kinetics plots of 9ft AB dry intact, the model plot fitted very well with the desorption PFO kinetic model implying that the rate of desorption depends on the CO_2 trapped in the pores. There is no detailed desorption kinetics data that has been published so far to compare these results. Therefore, further studies would provide an improved understanding of desorption kinetics.

Table 6.4. PSO and PFO model parameters obtained for 18ft Aberpergwm dry intact

18ft AB dry intact, initial-equilibrium pressure (MPa)	Pseudo-first-order kinetics parameters			Pseudo-second-order kinetics parameters		
	q_e, equilibrium concentration, g of CO_2/kg of coal	Rate constant, k_{a1} (h^{-1})	R^2 and standard error of estimate	q_e, equilibrium concentration, g of CO_2/kg of coal	Rate constant k_{a2}, (kg g^{-1} h^{-1})	R^2 and standard error of estimate
0.58-0.08	7.25	1.21	0.95 (0.5)	7.75	0.23	0.99 (0.23)
1.53-0.63	23.97	17.64	0.49 (3.06)	27.73	0.19	0.99 (1.26)
3.04-2.02	33.37	31.57	0.25 (2.82)	37.83	1.68	0.60 (2.26)
4.59-3.76	41.36	410.9	0.02 (1.7)	42.04	4.14	0.55 (1.24)
5.52-4.99	74.47	346.91	0.92 (0.77)	74.82	9.5	0.99 (0.52)
6.35-6.33	145.54	346	0.99 (0.81)	145.54	346	0.99 (0.81)

Table 6.5. PSO and PFO model parameters obtained for 18ft Aberpergwm dry powder.

18ft AB dry powder, initial-equilibrium pressure (MPa)	Pseudo-first-order kinetics parameters			Pseudo-second-order kinetics parameters		
	q_e, equilibrium concentration, g of CO_2/kg of coal	Rate constant, k_{a1} (h^{-1})	R^2 and standard error of estimate	q_e, equilibrium concentration, g of CO_2/kg of coal	Rate constant k_{a2}, (kg g^{-1} h^{-1})	R^2 and standard error of estimate
0.68-0.15	36.68	0.35	0.97 (4.18)	42.08	0.01	0.95 (3.08)
1.65-0.77	54.39	52.93	0.99 (1.33)	54.85	3.48	0.91(0.95)
3.22-2.18	57.75	78.8	0.99 (1.59)	59.54	5.45	0.99 (0.61)
4.5-3.67	61.96	74.77	0.99 (0.35)	62.14	9.92	0.99 (0.49)

Table 6.6. PSO and PFO model parameters obtained for 9ft Aberpergwm dry powder.

9ft dry powder, initial-equilibrium pressure (MPa)	Pseudo-first-order kinetics parameters			Pseudo-second-order kinetics parameters		
	q_e, equilibrium concentration, g of CO_2/kg of coal	Rate constant, k_{a1}, h^{-1}	R^2 and standard error of estimate	q_e, equilibrium concentration, g of CO_2/kg of coal	Rate constant k_{a2}, kg g^{-1} h^{-1}	R^2 and standard error of estimate
0.75-0.11	6.72	2.87	0.92(0.49)	6.96	0.7	0.99 (0.19)
1.51-0.73	34.26	1.07	0.85(3.89)	37.99	0.04	0.99 (2.85)
3-1.97	50.98	9.24	0.35 (4.65)	50.74	1.27	0.99 (4.67)
4.51-3.5	69.71	37.13	0.2(6)	71.42	0.92	0.42 (5)

Table 6.7. PSO and PFO model parameters obtained for 9ft Aberpergwm dry intact.

9ft AB dry intact, initial-equilibrium pressure (MPa)	Pseudo-first-order kinetics parameters			Pseudo-second-order kinetics parameters		
	Equilibrium concentration (q_e) g of CO_2/kg of coal	Rate constant, k_{a1} (h^{-1})	R^2 and standard error of estimate	Equilibrium concentration (q_e) g of CO_2/kg of coal	Rate constant k_{a2} (kg g^{-1} h^{-1})	R^2 and standard error of estimate
Adsorption						
0.56-0.07	10.46	0.52	0.96 (0.84)	11.52	0.058	0.99 (0.48)
1.54-0.6	26.63	1.54	0.50 (5.12)	27.96	0.09	0.53(5.29)
3.03-1.86	44.99	4.86	0.25 (7.24)	47.94	0.14	0.7 (4.56)
4.51-3.6	58.71	953	0.01(4.80)	60.41	1.54	0.45 (3.80)
Desorption			k_{d1} (h^{-1})			
3.06-3.23	66.81	102	0.17 (0.24)	66.88	30.17	0.35 (0.26)
1.87-2.38	65.43	0.002	0.51(0.74)	65.44	2.79×10^{-5}	0.51 (0.74)
1.53-1.89	66.39	0.002	0.66 (0.52)	63.4	2.54×10^{-5}	0.66 (0.52)
1-1.4	60.89	0.002	0.76 (0.62)	60.9	3.63×10^{-5}	0.76 (0.61)
0.6-0.99	57.06	0.0025	0.65 (0.86)	57.07	4.67×10^{-5}	0.66 (0.87)
0.31-0.66	52.84	0.002	0.51 (0.99)	52.86	4.33×10^{-5}	0.52 (0.98)
0.1-0.42	48.96	0.003	0.61(0.84)	48.98	5.76×10^{-5}	0.62 (0.91)
0-0.22	43.73	0.0003	0.33 (1.41)	43.73	6.85×10^{-6}	0.33 (1.4)

Table 6.8. PSO and PFO model parameters obtained for Big Pit powder dry coal.

BP powder dry, initial-equilibrium pressure (MPa)	Pseudo-first-order kinetics parameters			Pseudo-second-order kinetics parameters		
	q_e, equilibrium concentration, g of CO_2/kg of coal	Rate constant, k_{a1}, h^{-1}	R^2 and standard error of estimate	q_e, equilibrium concentration, g of CO_2/kg of coal	Rate constant k_{a2}, kg g^{-1} h^{-1}	R^2 and standard error of estimate
0.53-0.13	9.33	1.70	0.99 (0.88)	9.25	0.28	0.99 (0.39)
1.54-0.82	25.4	28.75	0.46 (1.73)	26.11	1.84	0.99 (1.13)
3.12-2.13	33.52	39.1	0.45 (2.12)	37.18	40.99	0.98 (4.5)

In order to explore that the CO_2 adsorption is influenced by the mass transport phenomena of pore diffusion, the adsorption experimental data of 9ft AB were fitted to the Bangham model (Equation 6.6) (Bangham and Sever, 1925; Swan and Urquhart, 1927). The Bangham model assumes that pore diffusion influences the kinetics of the adsorption process. Equation 6.6 presents the non-linear form of the model. The correlation coefficient (R^2) from the best-fit indicates the pore diffusion and pressure dependency of the constants k_b (h^{-1}) and n indicate the rate determining step at the corresponding pressure range.

$$q_t = q_e(1 - \exp(-k_b t^n)) \qquad (6.6)$$

where q_t is adsorbed mass of CO_2 at time t , g of CO_2/kg of coal, q_e is adsorbed mass of CO_2 at equilibrium, g of CO_2/kg of coal, k_b (h^{-1}) and n are constants of the model.

The kinetic data acquired for the intact and powdered samples of 18ft AB dry, 9ft AB dry and powdered samples of BP dry was fitted with the model. Figures 6.13, 6.14, 6.15, 6.16, and 6.17 present results for 18ft AB dry intact, 18ft AB dry powder, 9ft AB dry intact, 9ft AB dry powder, and Big Pit powder dry, respectively.

The higher correlation coefficient (R^2) in Figures 6.13 to 6.17 show that the pore diffusion is one of the rate determining steps. The correlation coefficient (R^2) value obtained for high pressure experiments up to 6.3 MPa for dry 18ft AB coal was 0.84 (Figure 6.13), which was less than the values obtained for lower pressure

experiments for 18ft AB dry powder (R^2 = 0.98; Figure 6.14), 9ft AB dry intact (R^2 = 0.98; Figure 6.15), 9ft AB dry powder (R^2 = 0.98; Figure 6.16), and Big Pit powder dry (R^2 = 0.9; These findings indicate that at lower pressures, bulk pore diffusion is the primary rate determining step, while at higher pressures, surface interaction takes over, which is the slowest step (Tutem et al. 1998). Overall, the experimental data obtained from the current study fitted very well with PSO kinetic model and Bangham pore diffusion model indicating that surface interaction and pore diffusion/condensation are the rate determining steps in the CO_2 adsorption process on coal.

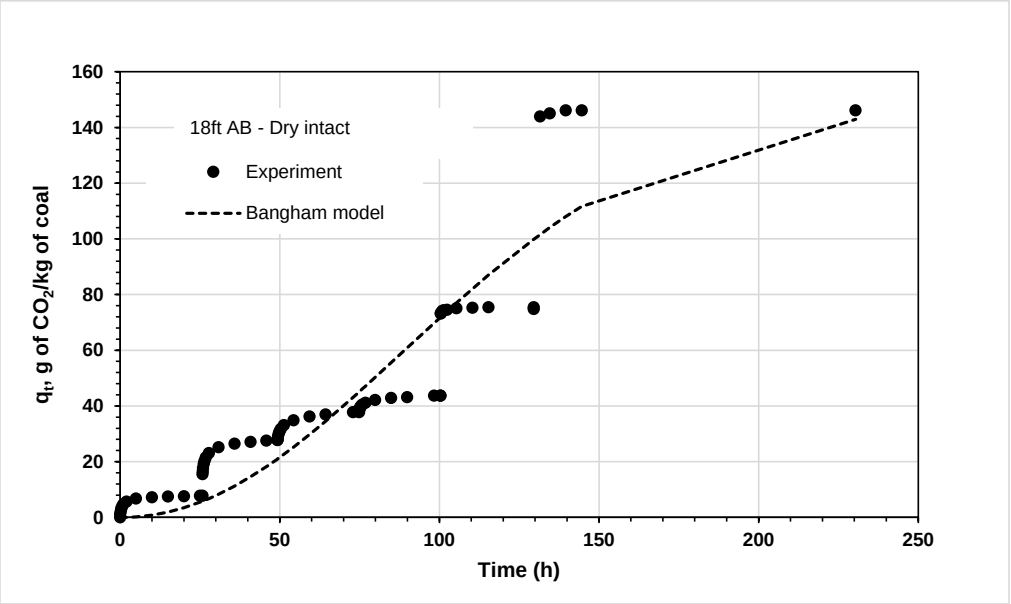

Figure 6.13. Bangham kinetic pore diffusion model fitting for the18ft AB dry intact (pressure range for up to 6.3 MPa).

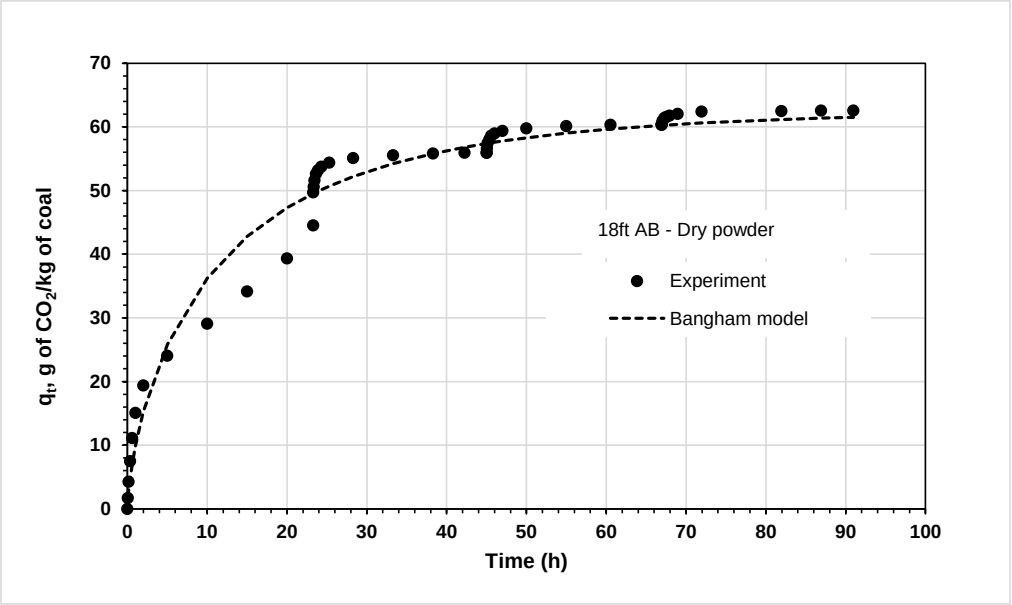

Figure 6.14. Bangham kinetic pore diffusion model fitting for the 18ft AB dry powder (pressure range for up to 6.3 MPa).

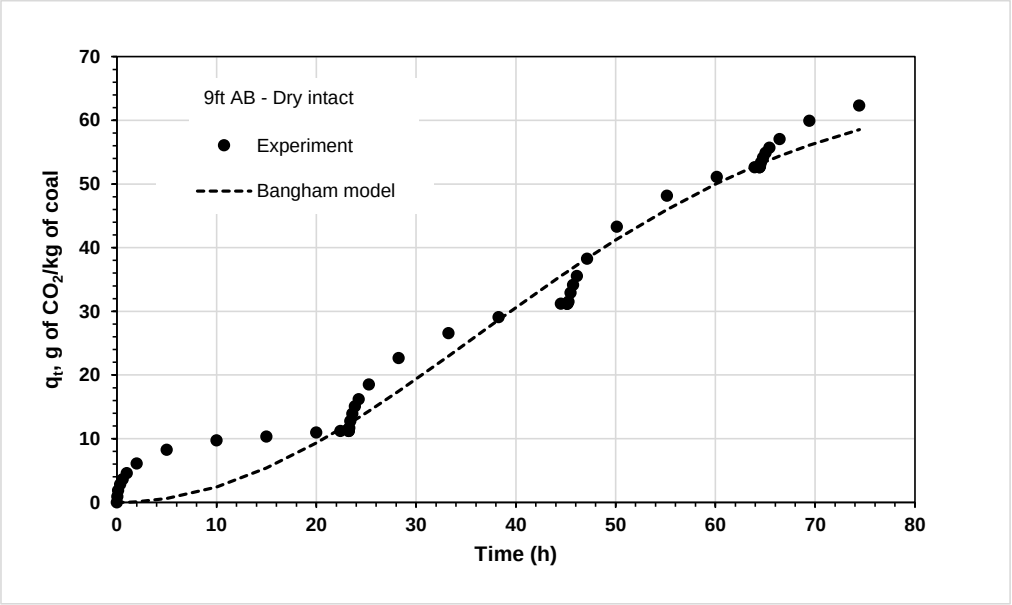

Figure 6.15. Bangham kinetic pore diffusion model fitting for the 9ft AB dry intact (pressure range for up to 4.5 MPa).

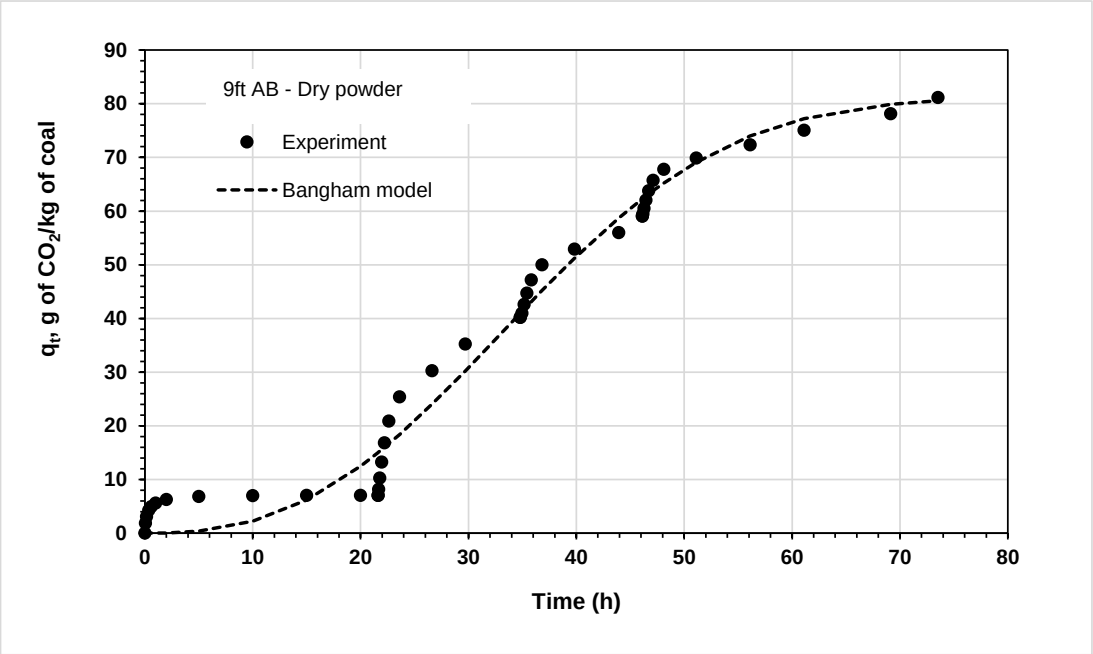

Figure 6.16. Bangham kinetic pore diffusion model fitting for the 9ft AB dry powder (pressure range for up to 4.5MPa).

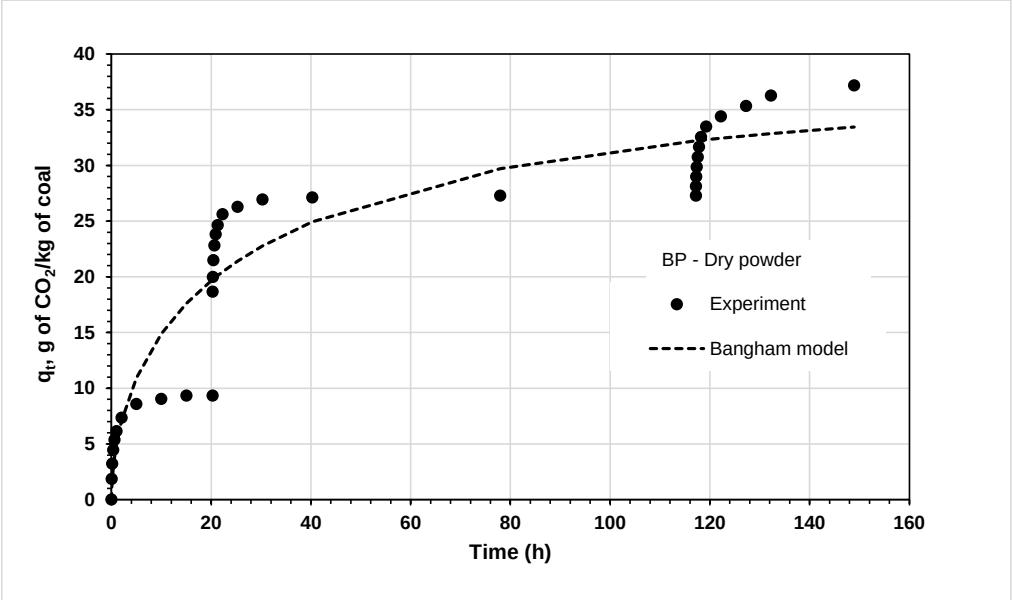

Figure 6.17. Bangham kinetic pore diffusion model fitting for the BP dry powder (pressure range for up to 4.5 MPa).

6.6 Mechanism of CO_2 adsorption on coal

According to the kinetic data analysis presented in section 6.5, it was found that the bulk pore diffusion of CO_2 followed by the surface interaction are the rate determining mechanisms in the CO_2 adsorption process on coal, which can be described as follows.

CO_2 could permeate not only through macropores but also the ultra-micropores/nanopores (< 2 nm) structure of the coal due to the molecular diameter (Cui et al. 2004). The CO_2 condenses in the pores, and when the pressure rises, the adsorption process is controlled by the diffusion mass transfer phenomenon. This was demonstrated during the desorption kinetics tests, in which the delayed release of CO_2 molecules from the coal was detected even after the manometric system had been completely evacuated (Figure 6.18 a, b and c).

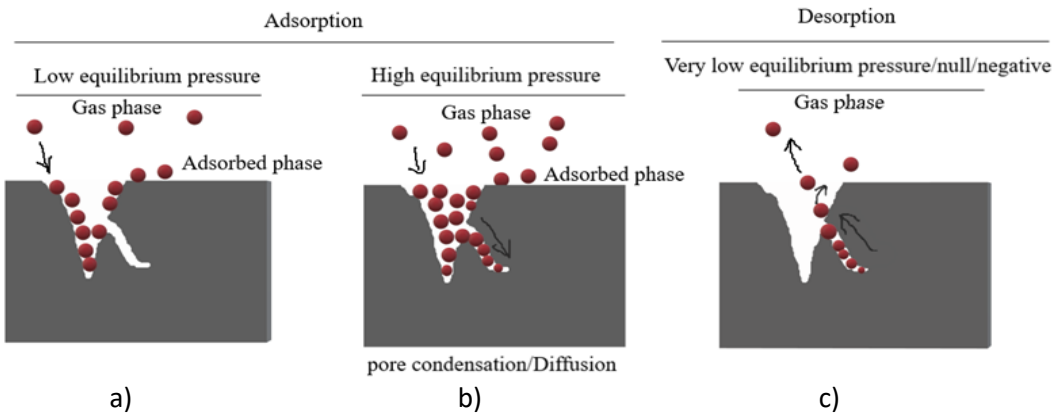

Figure 6.18. Schematic of the pore condensation diffusion during adsorption-desorption kinetics measurements at a) low adsorption equilibrium pressure, b) high adsorption equilibrium pressure and c) very low desorption equilibrium pressure.

The CO_2 molecules near the coal surface attracted by a potential from the coal surface caused by van der Waals/London dispersion force of attraction (Figure 6.19 a). The adsorption on carbon materials is dominated by the interaction of π-electrons with strong contributions of the van der Waals interaction (London dispersion forces) (Wang et.al. 2020). (Figure 6.19 a). The London dispersion forces induce the polarisation of CO_2 molecules and attract the molecules towards the surface in the

same way as gravity works. Then the CO_2 molecules tend to occupy the surface in two ways spreading and clustering (Figure 6.19 b).

The effective contact area of a CO_2 molecule on the coal surface is 0.260 nm^2 (calculated using the critical parameters 298.15 K and 6.43 MPa and taking the packing factor of CO_2 packed closely together into account) and the collision contact area is 0.52 nm^2 (Figure 6.19 c) (Yang 1987; Pennell 2002; Butt et al. 2003; Atkins et al. 2017). This surface interaction becomes the rate determining step following the initial pore diffusion.

To substantiate the prediction of pore diffusion and condensation, the SEM images of the powdered coal samples and intact samples were taken to identify the nano/micro pores. Figure 6.20 presents the SEM images for 9ft AB intact and powdered samples. The large micro size fractures (Figure 6.20 a) and surface cracks are clearly visible in the intact specimens (Figure 6.20 b). Further magnifications clearly show the nano-sized pores/fractures/cleats (Figure 6.20 d) and channel-like pore openings (entrance) (Figure 6.20 e). When the coal specimens are powdered, this pore structure will be lost, and huge inter particle pores (Figure 6.20 c) will develop for CO_2 gas transport and adsorption.

Due to the huge amount of space available in powdered samples, CO_2 adsorbs at a lower adsorbed phase density, whereas in intact specimens, pore diffusion and condensation occur in the channel-like pores and the CO_2 adsorbs at a higher adsorbed phase density. This behaviour was detected as enhanced adsorption capacity with intact bituminous specimens and reflected on the adsorption-desorption hysteresis pattern, which depicts the H3 pattern of the IUPAC description of adsorption process controlled by pore condensation/diffusion.

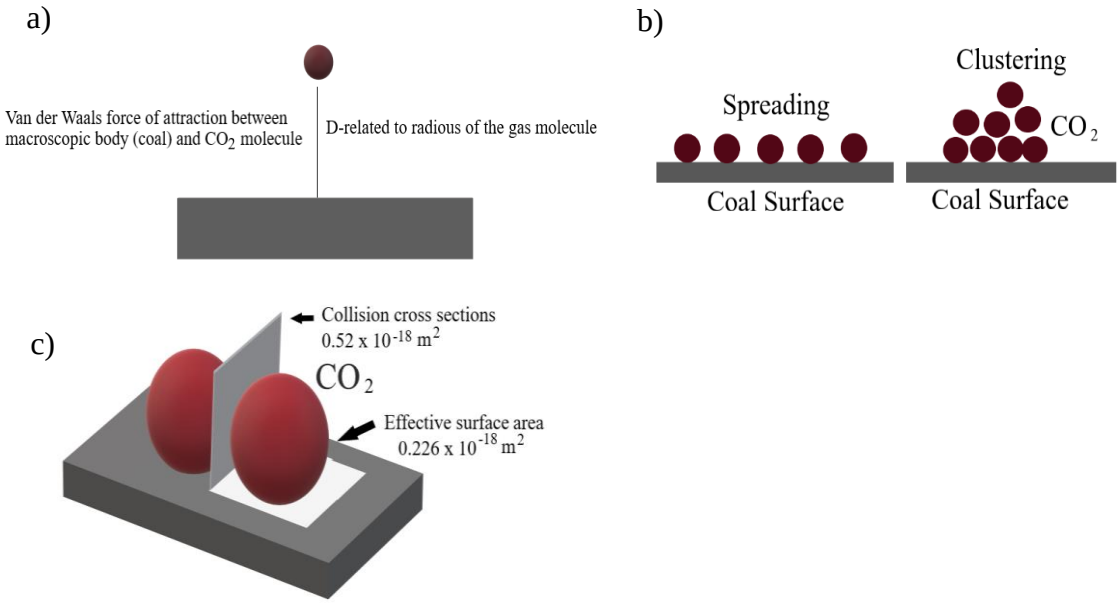

Figure 6.19. Illustration of a) van der Waals forces (London dispersion forces) exerted by coal acting on CO_2, b) spreading and clustering CO_2 molecules on coal surfaces, and c) collision cross-section and effective surface area of CO_2.

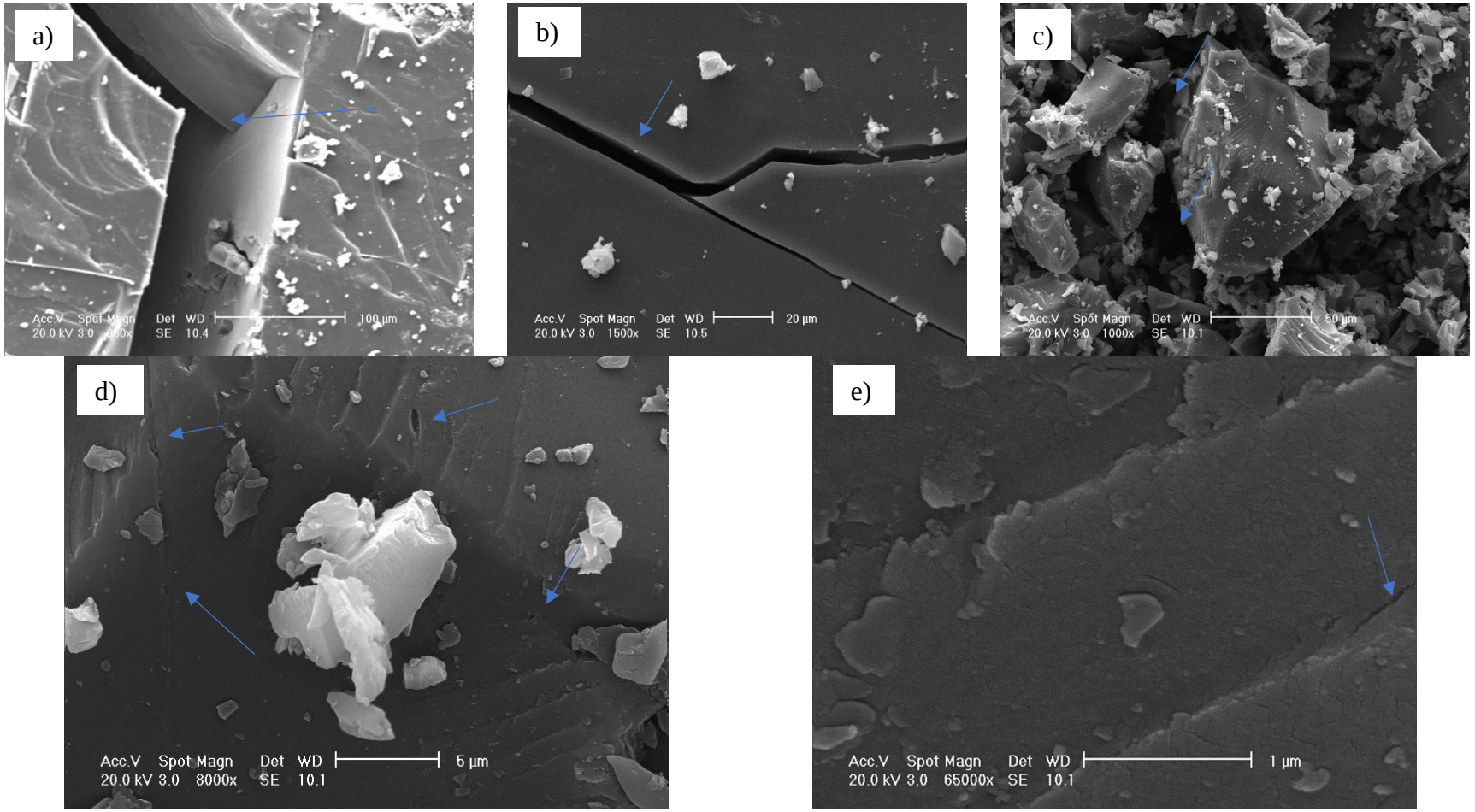

Figure 6.20. SEM for 9ft Aberpergwm a) large µm size fractures on intact sample. b) surface cracks on intact sample, c) powdered sample, d) openings (entrance) of channel like pores and e) nano pores/fractures in intact sample.

6.7 Concluding remarks

The theoretical adsorption isotherm and kinetic model fitting analyses, as well as the mechanisms and rate determining steps in CO_2 adsorption on coal samples, were presented in this chapter. Adsorption experimental data for dry intact and powdered samples of 9ft AB, 18ft AB, and BP, as well as wet samples of intact 9ft AB, 18ft AB, and wet powdered sample of 18ft AB, were fitted with Langmuir and BET models using nonlinear regression analysis. To determine the rate determining step, the experimental kinetics data for the 18ft AB dry intact, 18ft AB dry powder, 9ft AB dry intact, 9ft AB dry powder, and Big Pit powder dry samples were fitted with PFO, PSO, and Bangham kinetic models. The pore diffusion mechanism was described, along with SEM images of intact and powdered 9ft AB. The following are the key findings from this chapter.

1. At low pressures (<6.1 MPa), the Langmuir model fitted the experimental data very well. The Langmuir parameter (*b*; inverse of half-loading pressure) and the Langmuir maximum adsorption capacity of the coal samples were predicted (m_∞) using the model fitting. The Langmuir parameter *b* was ranging between 10^{-6} to 10^{-7} MPa for the maximum adsorption capacities ranging from 45 to 155 g of CO_2/kg of coal. The Langmuir half-loading pressure (b^{-1}) and the maximum adsorption capacity are important economic parameters to assess the CO_2 sequestration in coal seams (Harpalani et al. 2006; Zhou et al. 2019).

2. Adsorption energy calculated using Langmuir isotherm model parameters showed the values consistent with physical reversible adsorption (ΔH_{ad} was about -20 kJ/mol).

3. The experiments conducted up to near critical pressure range (up to 6.4 MPa) for intact 18ft AB showed that the experimental data were better fitted with the BET model than the Langmuir model, indicating that CO_2 adsorption on intact sample is driven by liquid-like condensation CO_2 on the coal surfaces (external and pore surfaces). The energy of adsorption calculated by using BET model was attributed to the energy of condensation of CO_2.

4. The specific surface area available for CO_2 of each coal sample were determined using the BET model. the surface area was in the range of 78408 m^2/kg-153067 m^2/kg

which is comparable previously published values by Zhao et.al. 2016 (77400 m^2/kg to 198400 m^2/kg).

5. The characteristic curves I and II showed the importance of considering the appropriate adsorption theories for understanding CO_2 adsorption on coal. The characteristic curves showed that the adsorption of CO_2 on coal can be influenced by the following factors: (*i*) varying adsorbed phase molar volume upon pressure rise, and (*ii*) physical attraction forces such as van der Waals/London dispersion forces (the force exerted by the coal surface to polarise the CO_2 molecules).

6. The experimental results were fitted to PFO, PSO and Bangham pore diffusion kinetic models, which showed that surface interaction and pore diffusion mechanisms are the rate-determining mechanisms of CO_2-coal adsorption processes.

7. The high-resolution SEM images show the presence of nanopores and substantiate the hypothesis of CO_2 pore diffusion/condensation occurs in intact specimens.

Chapter 7

CO_2 adsorption behaviour of rocks and clays

7.1 Introduction

The interaction of CO_2 with cap rocks (overburden) is an important aspect of the geological storage of CO_2 in un-mineable coal seams. Figure 7.1 depicts the conceptual movement of CO_2 in coal seams and the surrounding rock strata. With reference to Figure 7.1, the CO_2 (1) permeate to the adjacent rock strata, (2) trapped in porous structure of coal, (3) chemical interact with rock mineral, (4) interact with water and rock and (5) adsorbed on rock minerals.

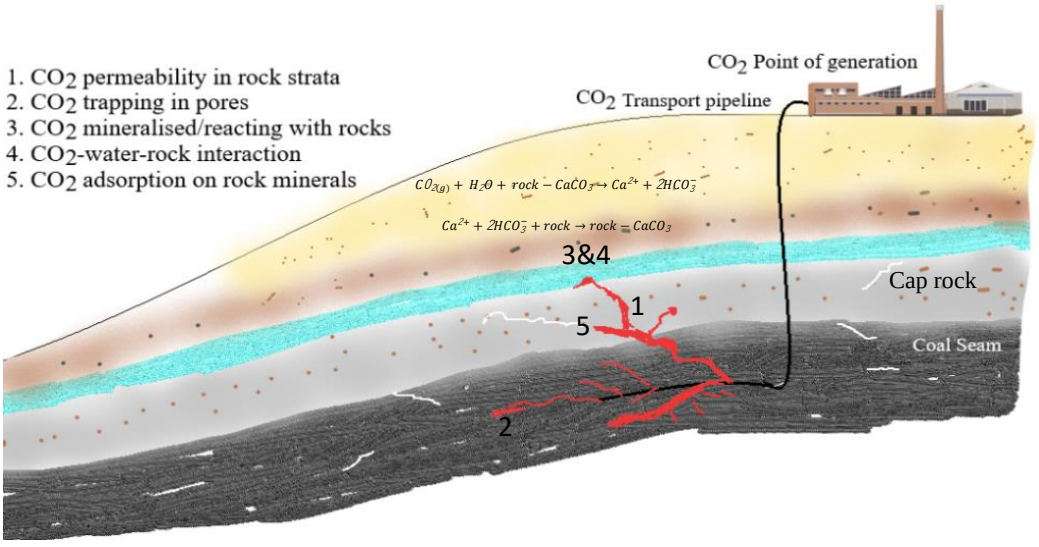

Figure 7.1. The red line represents the CO_2 movement in the coal seam and adjacent strata; (1) CO_2 permeability, (2) CO_2 trapping in pores, (3) CO_2 mineralized by reacting with rock minerals, (4) CO_2-water-rock interaction, and (5) CO_2 adsorption on rock minerals.

The caprock (also known as the seal for the CO_2 reservoir) should have a low permeability to prevent the gas from escaping. The gas can be trapped in pores, dissolved in ground water, and mineralised through reaction with other minerals (DePaolo 2013). Along with the information of permeability and the CO_2-water-rock interaction, the adsorption behaviour of pure CO_2 in the overburden rock must be investigated to comprehend the rather complex interaction of CO_2 with rock layers surrounding the reservoir.

Sedimentary rocks are porous by nature and can be filled with CO_2 gas. Sandstone, a sedimentary rock, is primarily composed of sand size grains and quartz with minor amounts of clays (e.g., montmorillonite and kaolinite) that are commonly found in rock strata adjacent to un-mineable coal seams. The biogeological conditions (water and naturally occurring microbes/biofilm) may influence on the adsorption capacity of the rock samples (Kanihira et al. 1987; Enomoto et al. 1997; Zhang et al. 2006; McGrail et al. 2009; Botan et al. 2010; Kwak et al. 2011; Loring et al. 2011; Shao et al. 2011; Tokunaga and wan 2013).

To study the CO_2 adsorption behaviour of caprock systems, adsorption experiments were performed on (*i*) rock samples from the East Irish Sea, (*ii*) dry and wet sand, (*iii*) biofilm-loaded sand, (*iv*) MX80 bentonite, and (*v*) Speswhite kaolin. The objectives of the investigation presented in this chapter were:

1. To understand the influence of mineralogy on the CO_2 adsorption of rocks. Mineralogical identification and chemical composition of caprocks were performed using X-ray diffraction and X-ray fluorescence analyses (section 7.2).
2. To examine the CO_2 adsorption isotherms of East Irish Sea rock samples, dry sand, wet sand, biofilm-loaded sand, MX80 bentonite and Speswhite kaolin samples (section 7.3). In case of biofilm-loaded sand, the influence of *Bacillus mojavensis* (a native bacterium found in rock systems in coalfields) on the CO_2 adsorption was studied.
3. To explore the interaction mechanism between CO_2 and rock and clay minerals. The experimental results of CO_2 adsorption on East Irish Sea rock samples, and samples of sand, MX80 bentonite and Speswhite kaolin

were fitted with the theoretical isotherm and kinetic models to describe the interaction mechanism between CO_2 and rock and clay minerals (sections 7.4 and 7.5).

7.2 Mineralogical identification and chemical composition of rock samples

The X-ray diffraction (XRD) patterns of East Irish Sea rock samples collected from different depths are displayed in Figure 7.2. The X-ray diffraction patterns clearly show that the rock samples are primarily composed of quartz (SiO_2, primary peaks $2\Theta = 26.64°$, 20.86° and 50.13°), ankerite (dolomite with iron substitution, Ca $(Mg_{0.67}Fe_{0.3})$ $(CO_3)_2$, primary peak $2\Theta = 30.81°$) and showed peaks attributes for halite (primary peaks at $2\Theta = 31.69°$, 45.45°), kaolinite (major peak at $2\Theta = 12.28°$) and orthoclase (major peak at $2\Theta = 25.65°$).

The chemical composition of the rock samples obtained from an x-ray fluorescence spectrometer is shown in Table 7.1. The compositions of major oxides (SiO_2, Al_2O_3, CaO, FeO, K_2O, and TiO_2) confirm the mineralogical identification of the rock samples by XRD. Quartz (SiO_2 = 50%-89% SiO_2) is the predominant constituent of the rock samples, followed by iron (1.3% to 6.6%) and calcium (3.4%-25%) containing minerals (Table 7.1).

Clearly, the overburden would contain a range of minerals, particularly carbonate minerals (Table 7.1; Figure 7.2), which are ubiquitous in sedimentary rocks and react more rapidly than silicates. Ankerite (which contains Fe) is the most common carbonate mineral after calcite, dolomite, and siderite. CO_2-laden groundwater can dissolve iron and calcium-containing minerals such as ankerite (Doner and Lynn 1989).

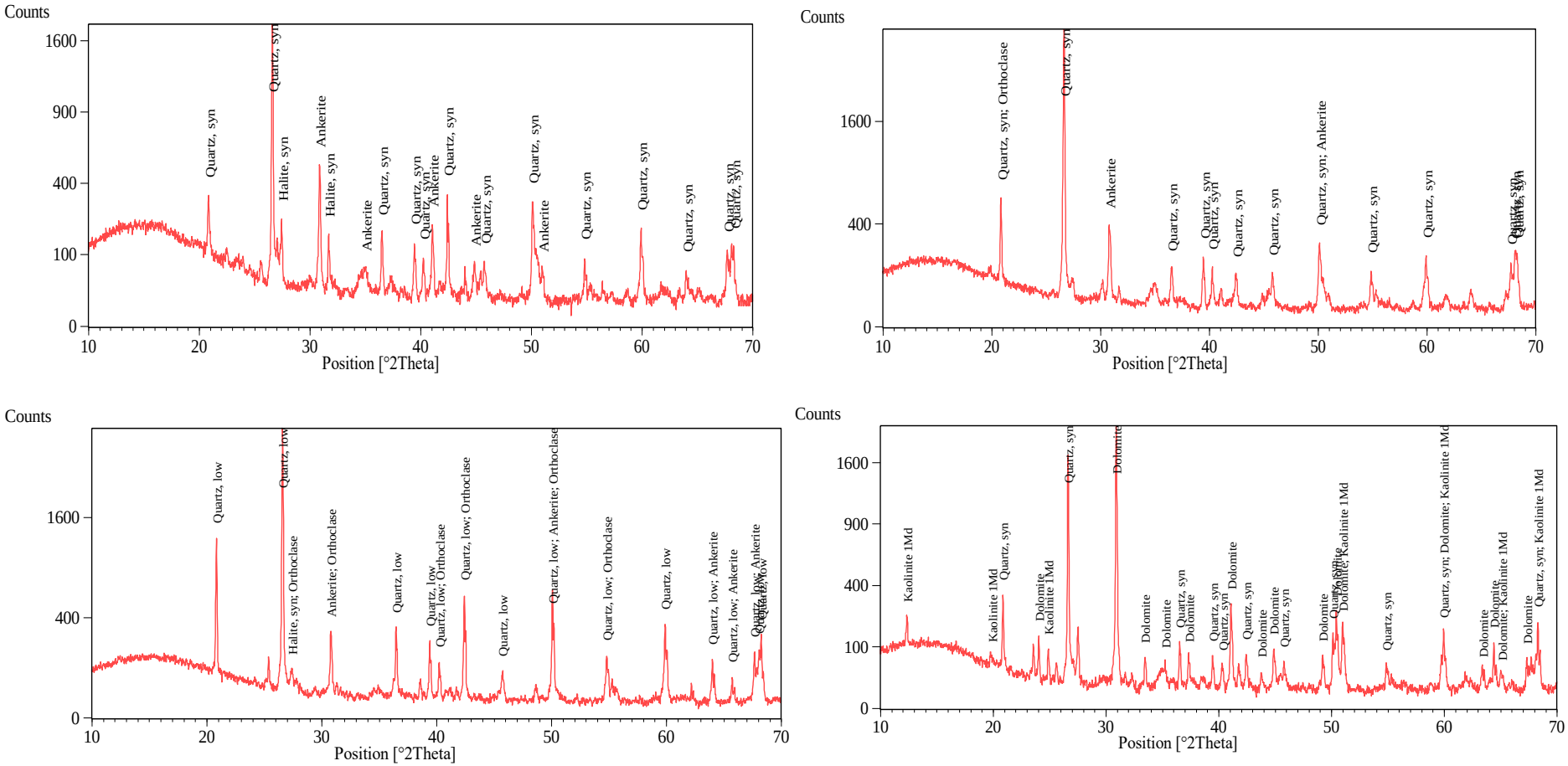

Figure 7.2. X-ray diffraction patterns of X-ray diffraction (XRD) patterns of powdered East Irish Sea rock samples (depth of the samples indicated): (a) SSK69021; 4064 m to 4065 m,(b) SSK69020; 3770 m to 3770.97 m, (c) SSK69016; 8379 m to 8379.57 m, and (d) SSK69019; 3204 m to 3205 m.

Table 7.1. Chemical composition of the rock samples (values are within ± 5% error).

Rock sample core number (depth in m)/% composition	SiO_2%	Al_2O_3 %	CaO %	FeO%	K_2O%	TiO_2%	% mass
SSK69021 (4064 to 4065 m)	63.26	1.17	20.25	4.92	9.05	1.33	99.98
SSK69010 (6971 to 6972 m)	60.41	1.35	24.68	6.20	6.06	2.22	100.92
SSK69016 (6499 to 6500 m)	80.73	0.42	9.54	1.18	1.67	0.34	93.87
SSK69020 (3770 to 3770.97 m)	71.29	1.16	6.16	1.95	4.54	0.29	85.40
SSK69009 (3515.74 to 3516.27 m)	50.44	1.30	16.77	3.08	5.53	0.38	77.50
SSK69007 (9992.4 to 9992.94 m)	55.96	2.78	3.44	4.46	6.00	0.77	73.41
SSK69022 (4069 to 4069.65 m)	78.97	0.48	14.78	2.12	3.49	0.52	100.36
SSK69006	56.62	2.34	3.70	6.03	5.03	0.71	74.43
SSK69023 (6499 to 6500 m)	65.50	0.96	13.45	6.62	2.05	0.18	88.75
SSK69019 (3204 to 3205 m)	46.48	ND	19.40	3.86	2.48	0.19	72.41
SSK69018 (3201 to 3202 m)	84.84	0.65	9.52	2.51	3.12	0.25	100.89
SSK69025, 6971 to 6972	87.93	0.24	3.80	1.33	2.96	0.11	96.38
SSK69017 (8382 m to 8383 m)	83.87	0.39	4.12	1.82	1.85	0.27	92.32
SSK69016 (8379 m to 8379.57 m)	80.96	1.30	2.78	4.11	3.93	0.43	93.51

7.3 CO_2 adsorption on rocks, sand and clays

To obtain a greater understanding of the CO_2 adsorption characteristics of the mineral composition of caprocks, adsorption tests were conducted on selected clays such as MX80 bentonite (a sodium montmorillonite) and Speswhite kaolin (a kaolinite), as well as sand (dry, wet, and biofilm-loaded sand), and the two representative rock samples from the East Irish Sea. The experimental results of CO_2 adsorption tests on East Irish Sea Rock samples, sand, and clays samples are presented in this section. Sections 7.3.1, 7.3.2, and 7.3.3 present the CO_2 adsorption isotherms of the rock samples, sands, and clays, respectively.

7.3.1 CO_2 adsorption isotherms of East Irish rock samples

The East Irish Sea rock samples SSK69021 (CaO = 20.25% and FeO = 4.9%) and SSK69016 (CaO = 9.54% and FeO = 1.18%) were chosen for adsorption experiments due to their differences in calcium and iron content (Table 7.1).

The CO_2 adsorption isotherm pattern of the East Irish rock samples is depicted in Figure 7.3. The rock sample (core number SSK69021) had a low adsorption capacity of 0.1 mol of CO_2/kg of rock up to an equilibrium pressure of 2 MPa and which increased to 0.9 mol of CO_2/kg of rock at an equilibrium pressure of 3.5 MPa (Figure 7.3 a). The results of the adsorption capacity determination are correlated with the calcium and iron contents of the representative samples. The rock sample (core no. SS69016) had a lower calcium and iron content than core no. SSK 69021 (0.9 mol of CO_2/kg of rock), resulting in a lower adsorption capacity of 0.028 mol of CO_2/kg of rock (Figure 7.3 b). When the pressure was increased, a clear Langmuir type isotherm pattern was observed (Figure 7.3 b). Previous experiments in the subcritical range of CO_2 showed 0.07 mol CO_2/kg sandstone at 1 MPa equilibrium pressure and 0.48 mol CO_2/kg sandstone at 2 MPa equilibrium pressure (Tajnik et al. 2012), with the adsorption isotherm fitting very well to the Langmuir-type (monolayer) model (Jedli et al. 2016). Fakher and Imqam (2020) found that shale rocks could adsorb 0.38 mol of CO_2/kg of rock using a volumetric adsorption setup very similar to the one used in this study.

The capacity of sandstone rock samples to adsorb CO_2 varied with depth, clay content, mineral composition, water content, and biofilm content (Botan et al. 2010; McGrail et al. 2009; Kwak et al. 2011; Loring et al. 2011; Shao et al. 2011; Tokunaga and Wan 2013; Kanihira et al. 1987; Enomoto et al. 1997; Zhang et al. 2006). Separate adsorption experiments were conducted on sand (dry, wet, and biofilm loaded), MX80 bentonite and Speswhite kaolin samples to understand the adsorption behaviour of each mineral in the sandstone, and the results are discussed in the following sections.

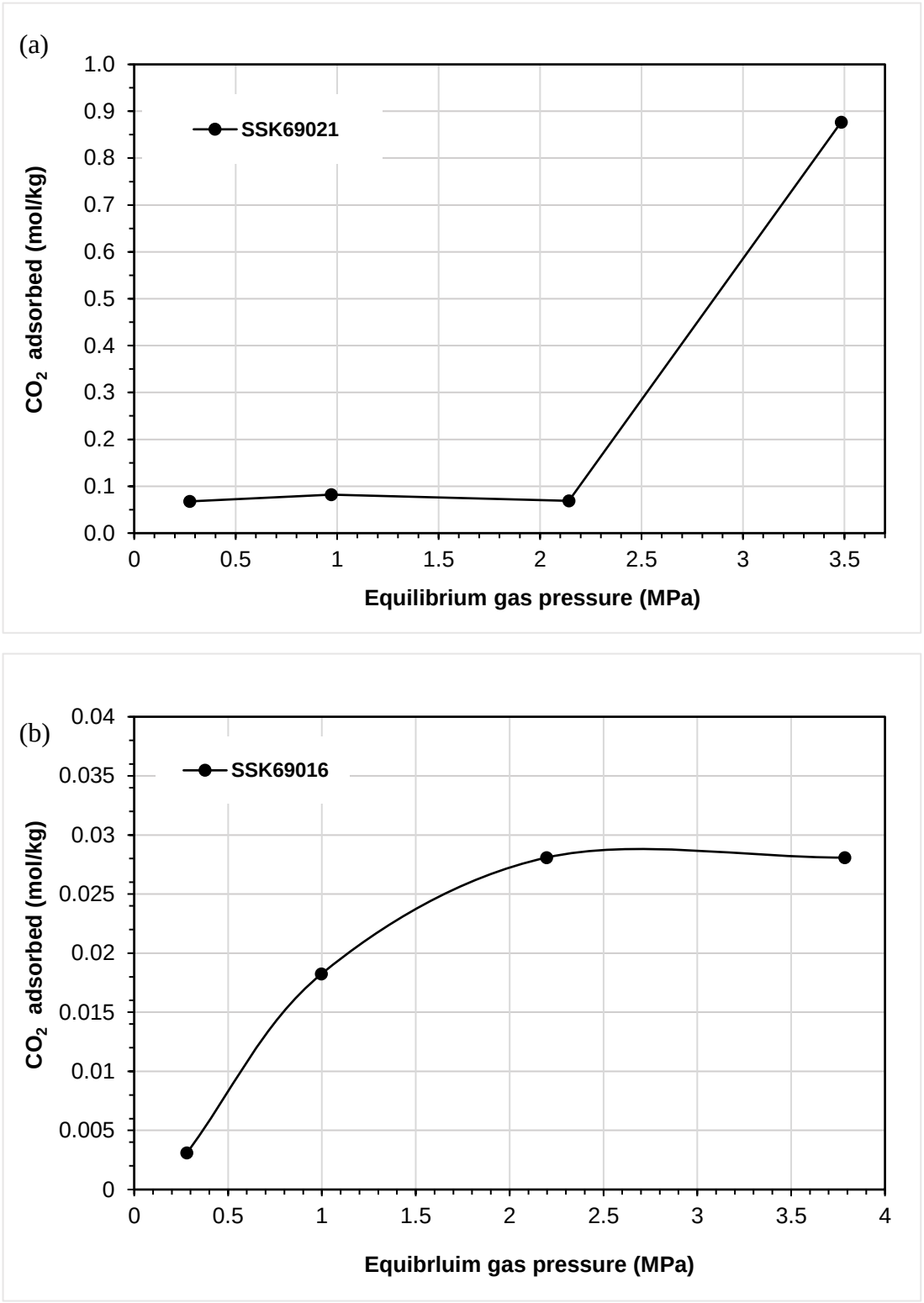

Figure 7.3 Adsorption isotherm patterns of East Irish Sea rock samples (depth of the samples indicated): (a) SSK69021; 4064 m to 4065 m and (b) SSK69016; 8379 m to 8379.57 m.

7.3.2 CO_2 adsorption isotherms of dry sand, wet sand, and sand loaded with *Bacillus mojavensis*

Bacillus mojavensis microbes are native to sandstone rock strata and could affect the interaction of CO_2 with caprock (Mitchell et al. 2004; Mitchell et al. 2008; Peet 2015). The *Bacillus* type strain grows well in the CO_2-water-rock environment. The biofilms formed by *Bacillus mojavensis* are resilient to high-pressure CO_2 and can enhance the solubility trapping, mineralization of CO_2 through ureolysis, and $CaCO_3$ precipitation. CO_2 gas adsorption tests were performed on *Bacillus mojavensis* loaded sand samples and compared to the dry and wet sand samples. Biofilm loading methods have been discussed in Chapter 3 (section 3.2.4).

Figure 7.4 (a) to (d) shows the CO_2 adsorption and desorption isotherm patterns of dry sand, sand with water, sand with Broth E and sand with bacteria, respectively. Dry sand showed a slightly reduced adsorption capacity (0.16 mol/kg) at a maximum equilibrium pressure of 3.5 MPa (Figure 7.4 a) than wet samples. Wet sand had a maximum adsorption capacity of about 0.2 mol of CO_2/kg (Figure 7.4 b).

A control adsorption test was performed using Broth.E-loaded sand that had been used to grow *Bacillus mojavensis* bacteria. The adsorption-desorption pattern observed in the control experiments is represented in Figure 7.4 (c). At higher pressures, a substantial rise in adsorption was observed followed by complete desorption. This behaviour indicates that Broth.E held the CO_2 gas molecules weakly and instantly released them. This Broth.E experiment lasted 21 days (approximately three weeks) in order to observe the impact of Broth.E on biomineralization. The complete reversibility of CO_2 from the sand sample that had Broth.E in it shows that Broth.E had no effect on CO_2 adsorption behaviour observed in *Bacillus mojavensis* loaded sample.

The maximum adsorption capacity of biofilm-loaded sand samples was 0.21 mol /kg (Figure 7.4 d). In comparison, the adsorption capacities of wet and biofilm-loaded sand samples were comparable (Figure 7.4 b and d). Wet sand had a maximum adsorption capacity of about 0.2 mol of CO_2/kg whereas biofilm loaded sample showed an adsorption capacity of 0.21 mol CO_2/kg. whereas the dry sand showed lower capacity of 0.16 mol/kg. The dry sand reached equilibrium around 2 MPa in the

isotherm patterns shown in Figure 7.4 (a), whereas the wet sand and biofilm-loaded sand showed a linear increase with pressure increase up to 3.5 MPa and 4 MPa equilibrium pressures, respectively.

Interestingly, the desorption pattern for *Bacillus mojavensis*-loaded sand demonstrated no discernible CO_2 gas desorption upon decreasing equilibrium pressure (Figure 7.4 d). on other hand, it displayed an increasing amount of CO_2 adsorbed. This behaviour demonstrates definitively that a significant portion of the 0.21 mol/kg biofilm-loaded sand may have been mineralized, and that mineralization occurs regardless of pressure. The adsorption-desorption experiment lasted 12 days in total and yielded an adsorption capacity of 0.4 mol of CO_2 per kg of biofilm-coated sand specimen (Figure 7.4 d). A similar pattern was observed for sand with water (Figure 7.4 b) showed adsorption rather than desorption during the pressure step down desorption stages, indicating that water/biofilms may enhance solubility trapping of CO_2 (Mitchell et al. 2004).

7.3.2.1 Mechanism of CO_2 adsorption on sand

The likely mechanisms of CO_2 adsorption on dry, wet, and biofilm-loaded samples are illustrated in Figure 7.5. While dry sand contains a limited number of activated sites within the quartz nanopores, wet sand retains the CO_2 at the water activated hydrophilic sites in the quartz and fills the nanopores with increased density (Figure 7.5 a) (Sun et al. 2016). Apart from the intricate mechanism by which CO_2 is retained on rock samples, microbes also induce CO_2 solubility trapping and biomineralisation (precipitate as calcium carbonate mineral; Figures 7.5 (b) and (c).

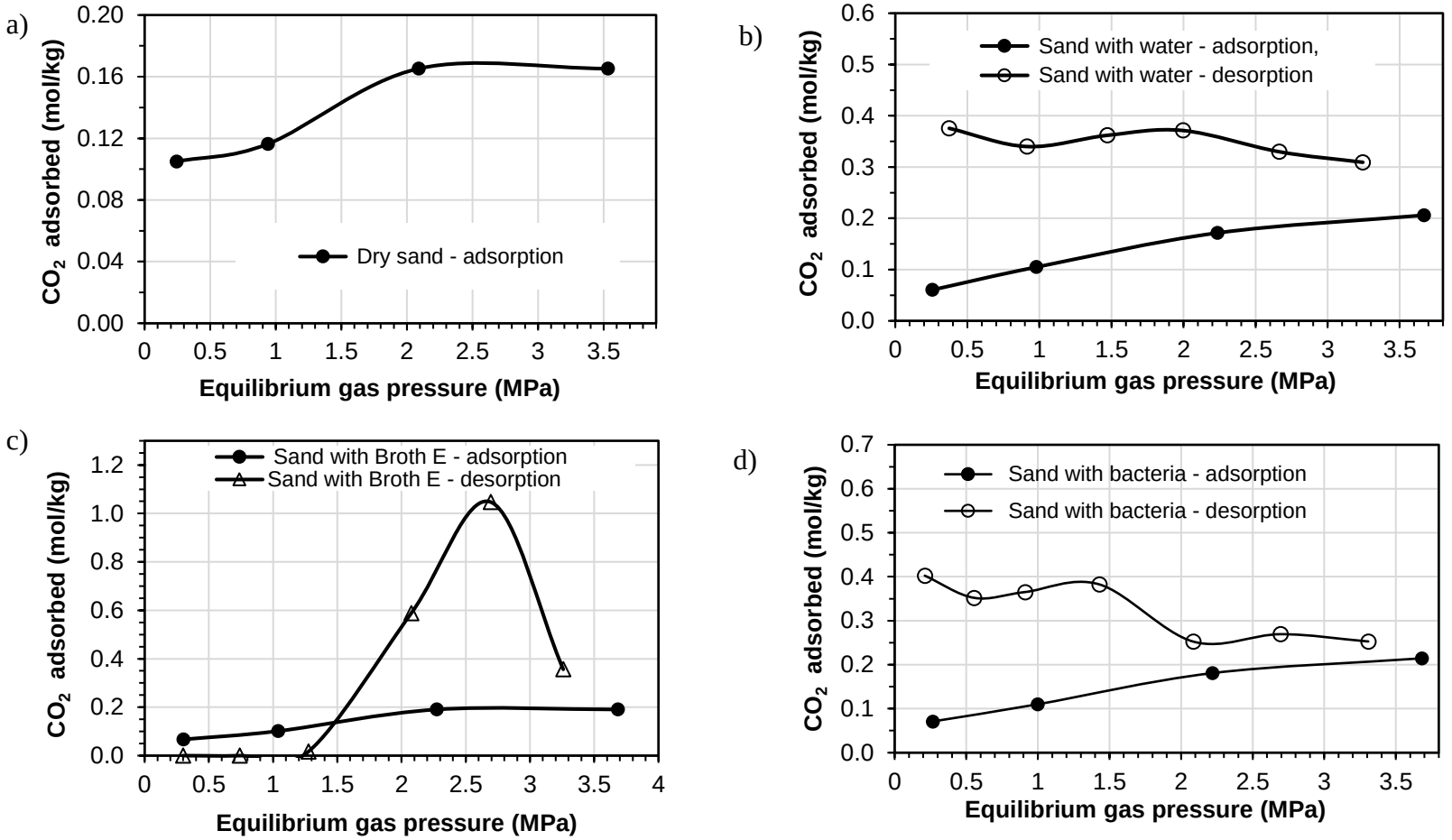

Figure 7.4. (a) Adsorption isotherm of Bacillus dry sand, (b) adsorption-desorption isotherms of sand with water (c) adsorption isotherm of control experiment with Broth.E and (d) adsorption-desorption isotherms of Bascillus mojavensis loaded sand*. (There was no desorption of CO_2 from wet and bacteria loaded sand which signifies the possible biomineralization of CO_2).*

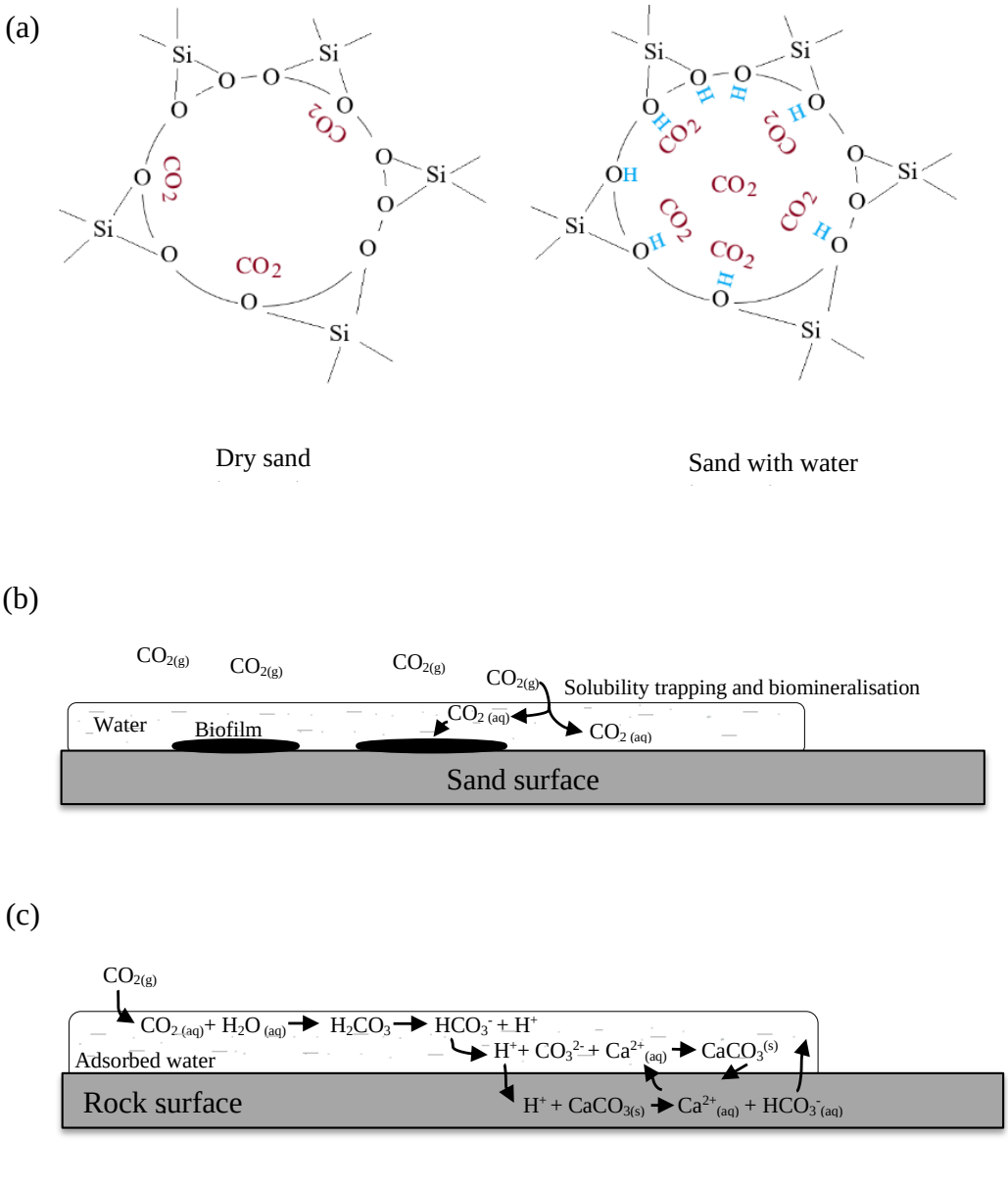

Figure 7.5. CO_2 adsorption mechanisms on dry, wet and Bacillus mojavensis loaded sand: (a) Dry sand nanopores, limited adsorption sites and interaction of CO_2 with the hydrophilic sites and densely adsorbed as single phase, (b) Biofilm induced CO_2 solubility and, (c) Dissolved CO_2 undergo mineralisation.

7.3.3 CO_2 adsorption on MX80 bentonite and Speswhite kaolin

Clay minerals are the primary constituents of the rocks, and their adsorption properties play an important role in the overburden (caprock) system of the coal seam CO_2 storage reservoir. Montmorillonite and kaolinite are clay minerals that are usually found in natural rock systems and have CO_2 adsorption properties. Many factors in clay minerals such as interlayer exchangeable cations, saturation state, the charge on the clay surface, interlayer distance affect the CO_2 adsorption capacity (Jin and Firoozabadi 2013; Lin et al. 2013; Zhang 2016; Volzone and Ortiga 2004; Rutherford et al. 1997).

Kaolinite is a 1:1 phyllosilicate clay mineral composed of a silica tetrahedral sheet bonded to an octahedral sheet. Montmorillonite is a smectite family expansive 2:1 layered silicate mineral with two tetrahedral sheets and one octahedral sheet forming the 2:1 layer (White and Dixon 2002; Reid-Soukup and Ulery 2002). The adsorption mechanism is characteristic of the individual clay minerals. The adsorption mechanism differs depending on the clay mineral. Monty Carlo simulations revealed that CO_2 molecules could be adsorbed on bentonite with cation exchange and on kaolinite micropores without cation exchange (Hu 2019).

Figure 7.6 shows the CO_2 adsorption isotherm pattern of MX80 bentonite and Speswhite kaolin. At an equilibrium pressure of 3.59 MPa, MX80 bentonite has a maximum CO_2 adsorption capacity of 0.56 mol/kg (Figure 7.6 a). Jeon et al. (2014) reported a comparable adsorption capacity of about 0.6 mol of CO_2/kg of bentonite at an equilibrium pressure of 3.5 MPa. Previous studies reported an adsorption capacity ranging from 0.16 to 0.25 mol of CO_2/kg of Na-bentonite at equilibrium pressures (3.5 MPa) (Volzone 2006).

Speswhite kaolin exhibited a maximum adsorption capacity of 0.19 mol of CO_2/kg of kaolinite at an equilibrium pressure range of 3.51 MPa (Figure 7.6). Volzone (2006) reported that the kaolinite mineral's maximum adsorption capacity was approximately 0.15 mol CO_2/kg of kaolinite, while Chen and Lu (2015) reported that Georgia kaolinite's maximum adsorption capacity was 0.3 mol CO_2/kg of kaolinite. The reported values were comparable to the current study's adsorption capacity value.

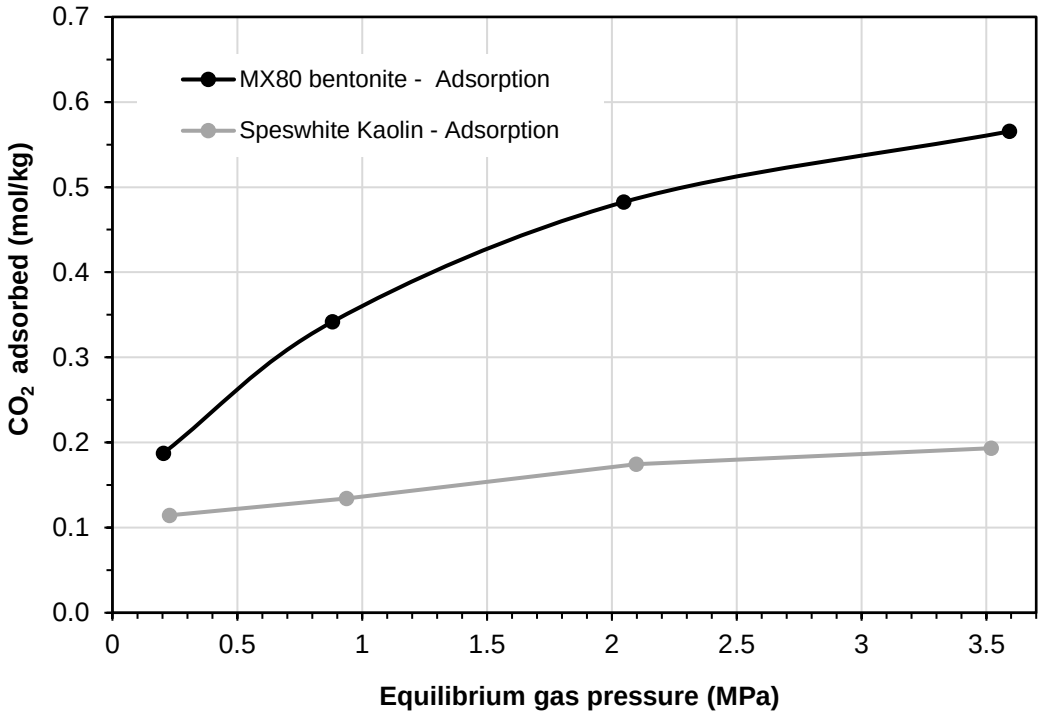

Figure 7.6. CO_2 adsorption isotherm patterns of MX80 bentonite and Speswhite kaolin.

Figure 7.7 showed CO_2 adsorption mechanism on bentonite MX80 (a) and Speswhite kaolin (b). The CO_2 molecular diameter is smaller than the interlayer spacing of bentonite and can penetrate the interlayer space (Okolo et al. 2019). Previous studies have shown CO_2 molecules can penetrate the interlayer spacing of swelling clays (bentonite) and expand the basal spacing (Loring et al. 2012; Ilton et al. 2012; Schaef 2012). However, non-polar fluids such as CO_2 cannot simply replace the cations and expel the interlayer water but diffuse into the water to reach the interlayer space of the expanding clay minerals such as bentonite (Figure 7.7 a). The CO_2 adsorption mechanism on kaolinite was ascribed to CO_2 molecules adsorbing on the intragranular porosity and was characterised as physical sorption (Chen and Lu 2015; Hu 2019) (Figure 7.7 b)

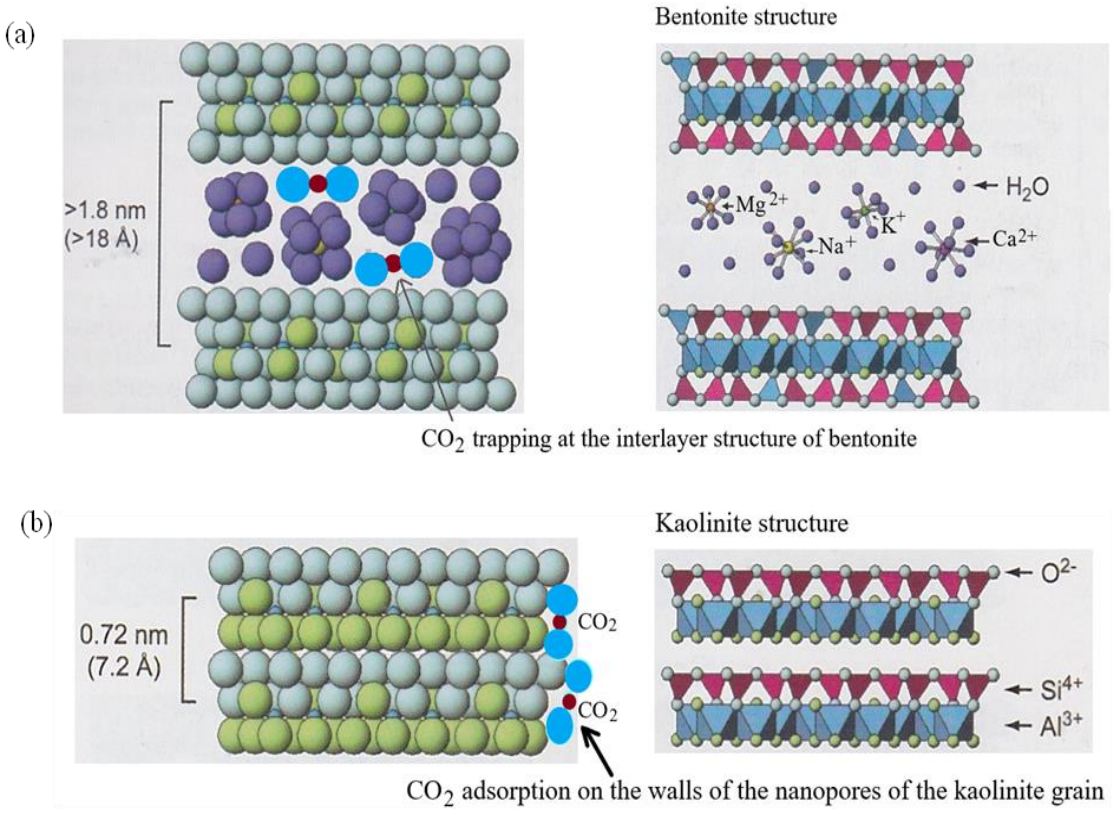

Figure 7.7. CO_2 adsorption mechanisms on (a) bentonite MX80 and, (b) speswhite kaolin.

7.4 Adsorption pressure decay curves

To better understand the kinetics and mechanism of CO_2 adsorption on miner al materials, pressure versus time curves were plotted. This section presents pressure drop curves obtained from adsorption experiments performed on dry sand, wet sand, sand with biofilm/bacteria (*Bacillus mojavensis*), and the control (Broth.E).

The dry sand showed no pressure drop over the course of the low-pressure adsorption stages (Figure 7.8 a; 0.5 MPa injection pressure) indicating there was no CO_2 adsorption on dry sand. For all other samples, a pressure drop rate of 0.01MPa/h was observed. Wet sand, sand with biofilm, and sand with *Broth.E* all reached equilibrium within 2 hours.

At intermediate pressure range (Figure 7.8 b; 1.5 MPa injection pressure), the time to reach equilibrium decreased as pressure dropped from 1 MPa to 0.98 MPa in 1 h for wet sand, 1.02 MPa to 1 MPa in 1 h for sand with biofilm, and 1.06 MPa to 1.04 MPa in 1 h for the Broth. E. At this stage (1.5 MPa injection pressure), the dry sand sample showed a noticeable drop in pressure (Figure 7.8 b) as the CO_2 molecules slowly diffused into the quartz structure's nanopores.

The time to reach equilibrium increased as the pressure range increased (Figure 7.8 c; injection pressures of 3 MPa). It took 3 hours to determine the equilibrium pressure values for all samples except Broth E. The *Broth.E* specimen showed a significant upward trend (Figure 7.8 c), indicating that significant desorption is taking place, as described in section 7.3.1 (Figure 7.4 b). The *Broth.E* was used as a control, and the pressure versus time observations confirmed the spontaneous reversibility of the CO_2 gas during the adsorption experiment. At injection pressure range of 4.5 MPa the equilibrium was attained within 1 hour (Figure 7.8 d).

Figure 7.9 portrays the pressure vs. time curves obtained for MX80 bentonite and Speswhite kaolin samples during CO_2 adsorption experiments. Both clays showed minimal pressure drop at lower experimental pressures (Figures 7.9 a and b). At injection pressures of 1 MPa, the MX80 bentonite sample began to show pressure reduction, indicating CO_2 permeation into the interlayer space, whereas the Speswhite kaolin clay shows no sign of CO_2 adsorption (Figures 7.9 a and b). However, at pressures greater than 2 MPa, the pressure drop curves observed in Speswhite kaolin minerals showed evidence of CO_2 adsorption (Figures 7.9 c and d). This implies that CO_2 gas pressure plays a key role in CO_2 adsorption on clay, exemplifying two distinct mechanisms of adsorption related to the physical structure of the clays as discussed in section 7.3.3.

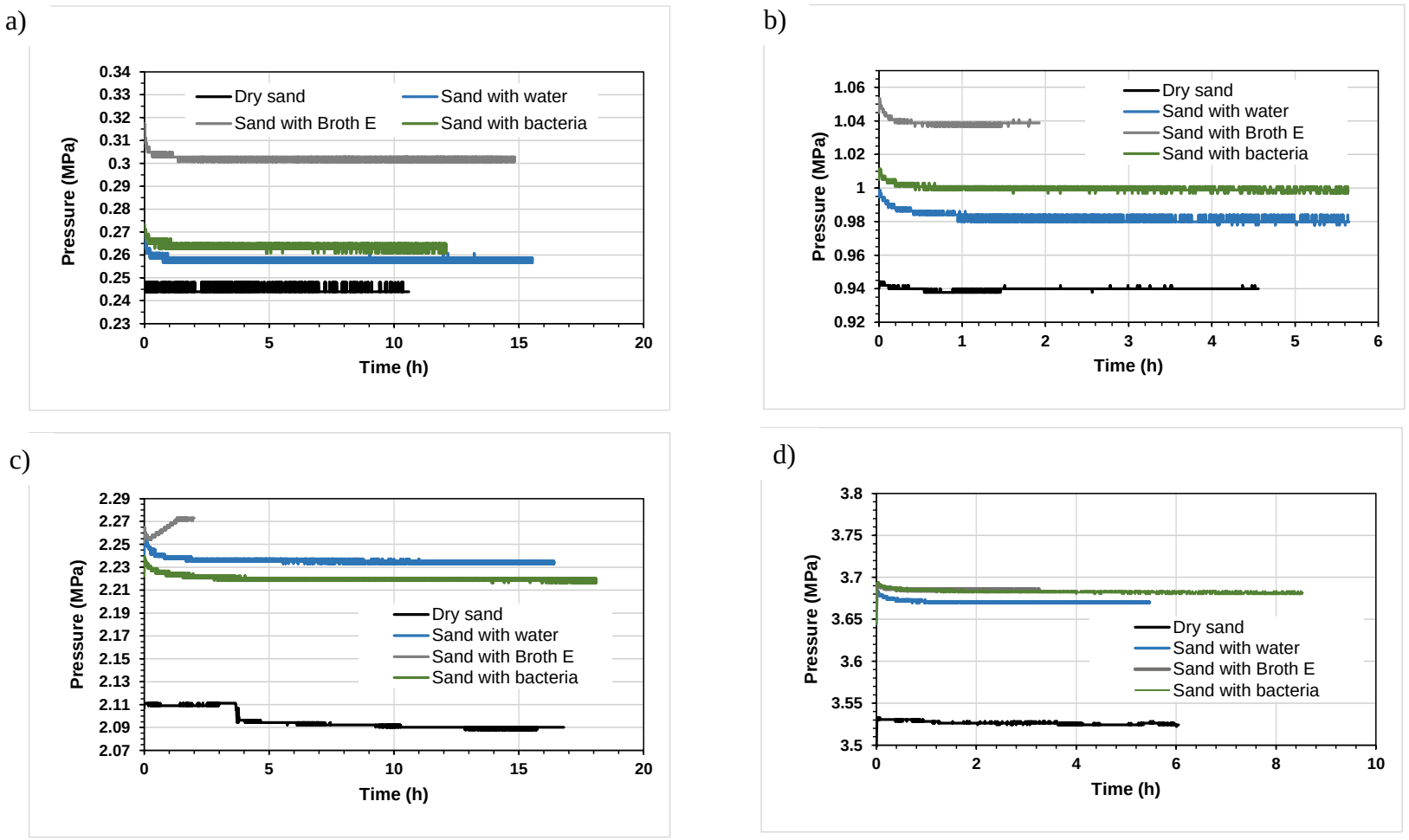

Figure 7.8. Pressure decay curves (adsorption) of dry, wet, biofilm and Broth E loaded samples at 298.15 K at injection pressures a) 0.5 MPa, b)1.5 MPa, C)3 MPa and d)4.5 MPa.

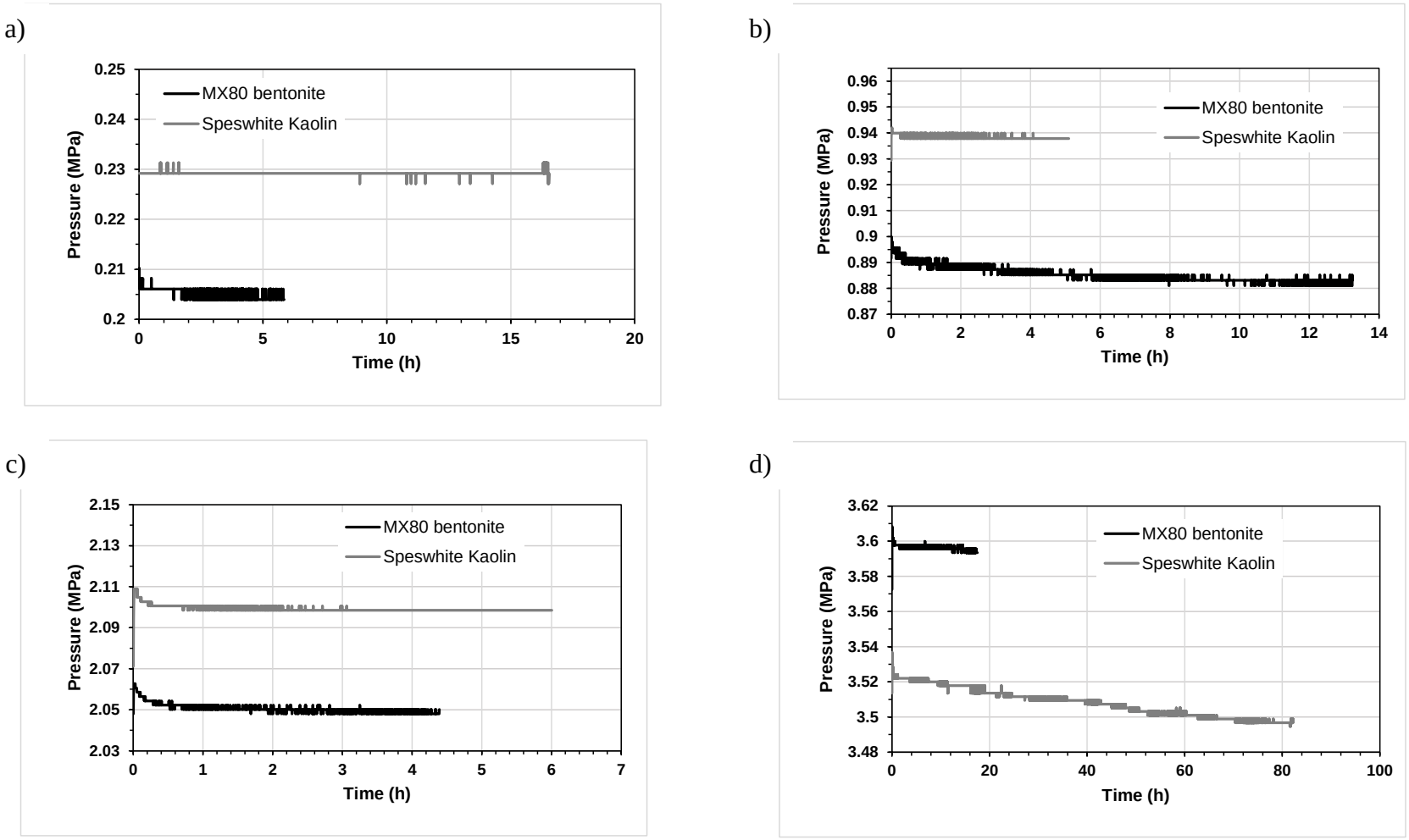

Figure 7.9. Pressure decay curves (adsorption) of MX80 bentonite and Speswhite kaolinat 298.15 K at injection pressures a)0.5 MPa, b)1.5 MPA, C)3 MPa and d)4.5 MPa.

7.5 Evaluation of CO_2 adsorption on rocks and clays using the Langmuir model

The Langmuir model was used to fit equilibrium CO_2 adsorption data obtained with dry sand, wet sand, sand with biofilm, MX80 bentonite and Speswhite kaolin (Langmuir, 1916, 1917, 1918). The mathematical expression of the model and the significance of data fitting are covered in Chapters 2 (section 2.5.1) and 3 (section 3.4). Figures 7.10 (a) to (c) depict the experimental data fitted to the Langmuir model for dry sand, wet sand and sand with biofilm, respectively. The experimental data for dry sand agrees very well with the model, indicating that the sand has a limited number of available sites for CO_2 gas molecules and that the sites are saturated at around 2 MPa equilibrium pressure. Wet sand and *Bacillus mojavensis*-loaded sand, on the other hand, deviated from the model and increased linearly, indicating that more than one adsorption mechanism influences CO_2 adsorption on biofilm-loaded sand.

The maximum Langmuir adsorption capacities of the sand samples were approximately 7.37 g of CO_2/ kg of dry sand, 10.08 g of CO_2/ kg of wet sand, and 10.08 g of CO_2/ kg of *Bacillus mojavensis* loaded sand. The half-loading pressures (*b*) were about 5.39 $\times 10^{-6}$ Pa^{-1} for dry sand, 1.14 $\times 10^{-6}$ Pa^{-1} for dry sand, 9.69 $\times 10^{-7}$ Pa^{-1} for dry sand (Table 7.2).

Zhang et al. (2018) reported the CO_2 adsorption on quartz crystals following the Langmuir type adsorption, and molecular simulations by Carchini et al. (2020) showed that the CO_2 is physically adsorbed on the quartz surface. In a simulation study (Yang et al. 2022), the energy of adsorption on the sand was given as 20.92 kJ/mol, which is comparable to the adsorption energy calculated in the current study (29.8 kJ/mol for the dry sand: Table 7.2).

Figures 7.6 represent the Langmuir adsorption isotherm model compared with experimental isotherms for MX80 bentonite and Speswhite kaolin. The experimental data of MX80 bentonite and Speswhite kaolin fit the Langmuir model very well (Figure 7.11). The maximum Langmuir adsorption capacity of MX80 bentonite was about 28.62 g/kg, and the Langmuir parameter b (half-loading pressure) was approximately 1.5 × 10^{-6} pa^{-1} (Table 7.2). For a half-loading pressure of 4.53 × 10^{-6} pa^{-1}, the Langmuir maximum adsorption capacity of the Speswhite kaolinite was

approximately 8.64 g/kg of kaolinite (Table 7.2). The adsorption energy of MX80 bentonite was -23.31 kJ/mol and that of Speswhite kaolinite was -29.02 kJ/mol (Table 7.2).

Table 7.2. Langmuir parameters and energy of adsorption obtained for dry, wet, Bacillus mojavensis loaded sand, MX80 bentonite and Speswhite kaolin.

Sample description	Half-loading parameter b (pa^{-1})	Maximum adsorption capacity, m_∞, g of CO_2/kg of coal	ΔH_{ad} kJ/mol	ΔG^0_{ad} (kJ/mol)
Dry sand	5.39×10^{-6}	7.37	-29.84	-30.07
Sand with water	1.14×10^{-6}	10.08	-25.21	-33.93
Sand with *Bacillus mojavensis*	9.67×10^{-7}	10.08	-24.81	-34.32
MX80 bentonite	1.5×10^{-6}	28.62	-23.31	-33.24
Speswhite kaolin	4.53×10^{-6}	8.64	-29.02	-34.02

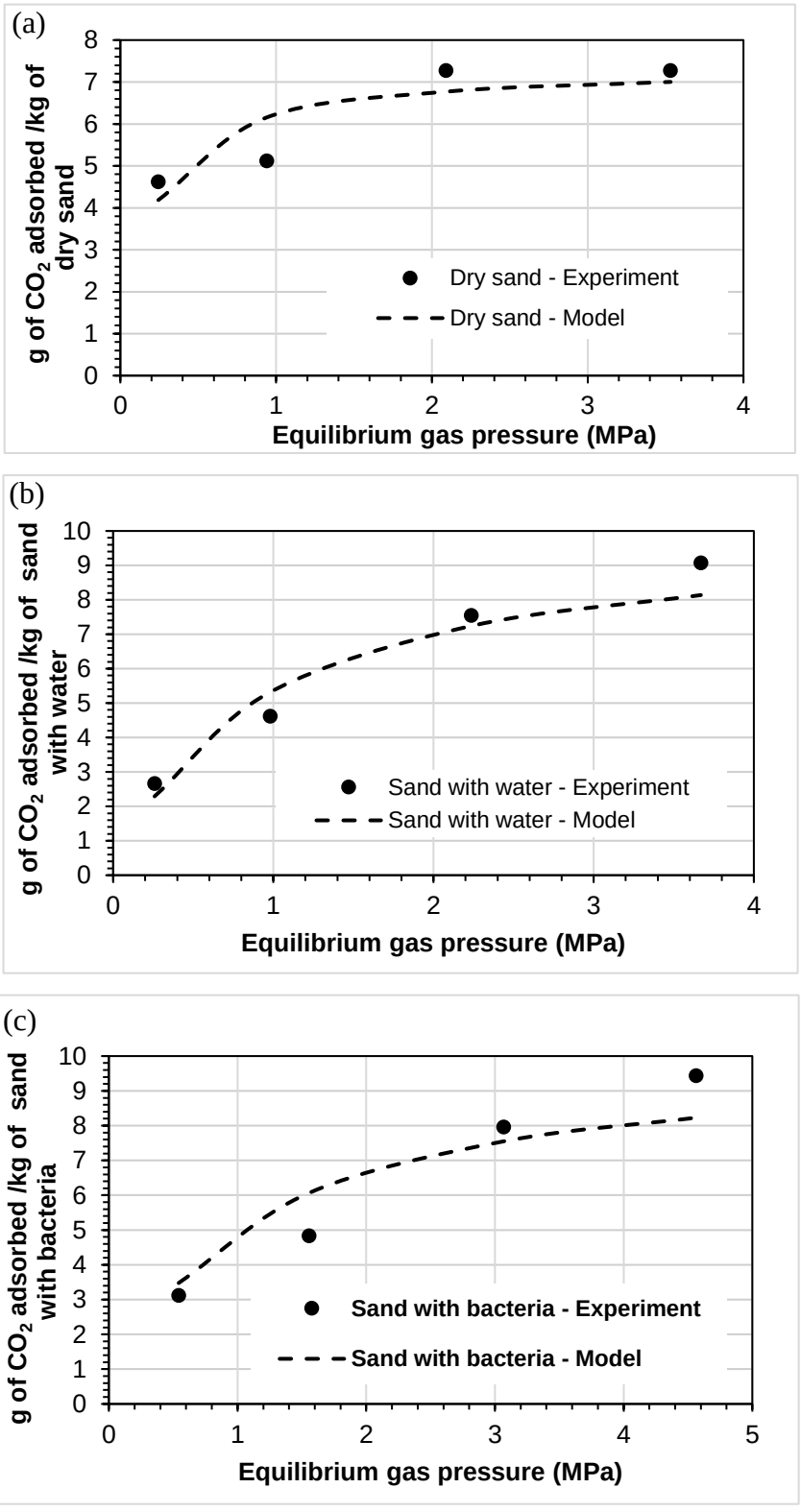

Figure 7.10. Langmuir adsorption isotherm model compared with experimental isotherms observed in (a) dry sand, (b) sand with water and (c) Bacillus mojavensis loaded sand.

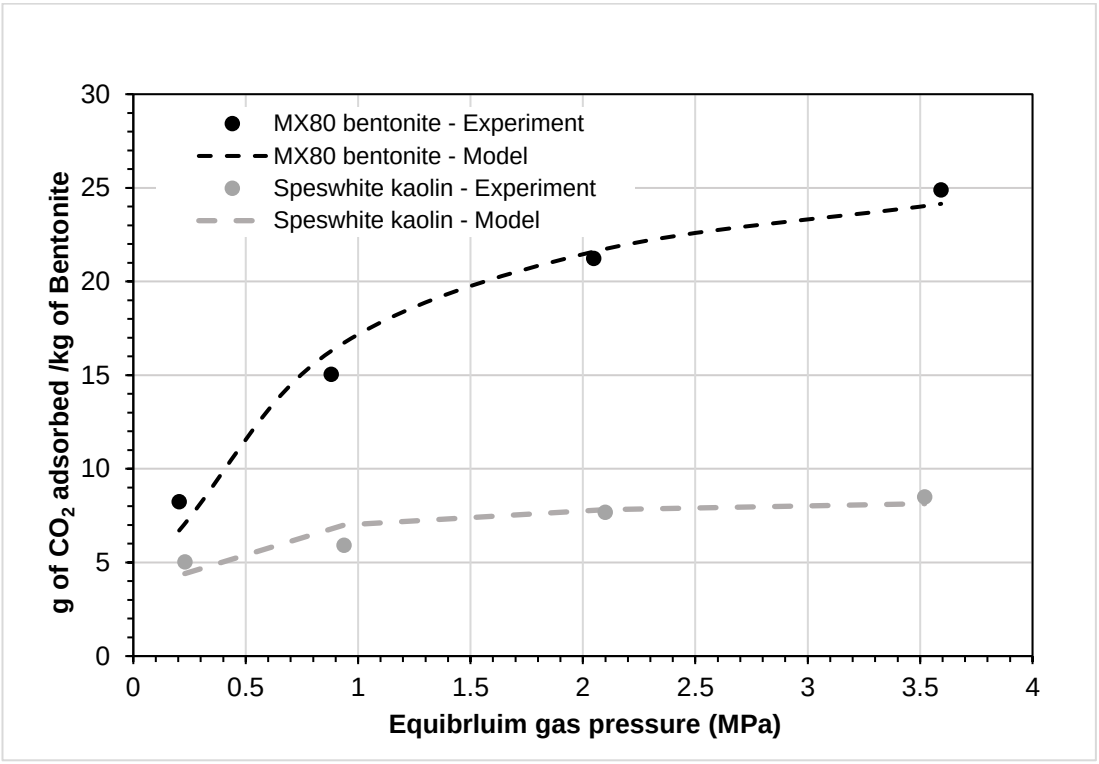

Figure 7.11. Langmuir adsorption isotherm model compared with experimental isotherms observed in MX80 bentonite and Speswhite kaolin samples.

7.6 Kinetics modelling of CO_2 adsorption on sand and clay

The data obtained from the time vs pressure drop curves were converted to time vs amount of CO_2 adsorbed (using perfect gas law) in order to comprehend the adsorption rate determining step. Experimentally determined equilibrium amounts of adsorbed CO_2 (q_e) over time (h) is compared to the values predicted by pseudo first order (PFO) and pseudo second order (PSO) models and presented in Figures 7.12 (a) to (f). Nonlinear regression analysis was used to fit the data. Table 7.3 summarises the PSO and PFO rate constants and the corresponding equilibrium amount of CO_2 adsorbed. The coefficient of determination (R^2) and standard error of the estimate values indicate the best-fitting model. The greater the R^2 value and the smaller the standard error of estimation, the more accurate the model fits.

With dry sand, MX80 bentonite and Speswhite kaolin, the rate of CO_2 adsorption was restricted by the available sites (physical adsorption) and was pressure dependent. The available sites were the rate limiting factor, as the PFO kinetics rate

law assumes that the rate of adsorption is proportional to the available sites (Loganathan et al. 2014). For dry sand, MX80 bentonite and Speswhite kaolin, the PFO model fit better than the PSO model, implying that physical sorption on available sites is the rate-determining step (Figure 7.12 a, e, and f). This was clearly demonstrated in the preceding section by the pressure versus time curves.

For the sand with *Bacillus mojavensis* and wet sand, the rate of CO_2 adsorption was controlled by the concentration of CO_2 and time of the reaction. Understandably, as discussed in section 7.3.2, the adsorption of the CO_2 was influenced by biomineralization reaction. PSO model was better fitted for the sand with water and biofilm loaded (Figure 7.12 b and d; Table 7.3) as PSO model assumes that chemical or surface interaction is the rate determining step of the adsorption process. The control experiment with Broth.E fit better with PSO because the weak surface interaction was the most likely rate determining step (Figure 7.12 c).

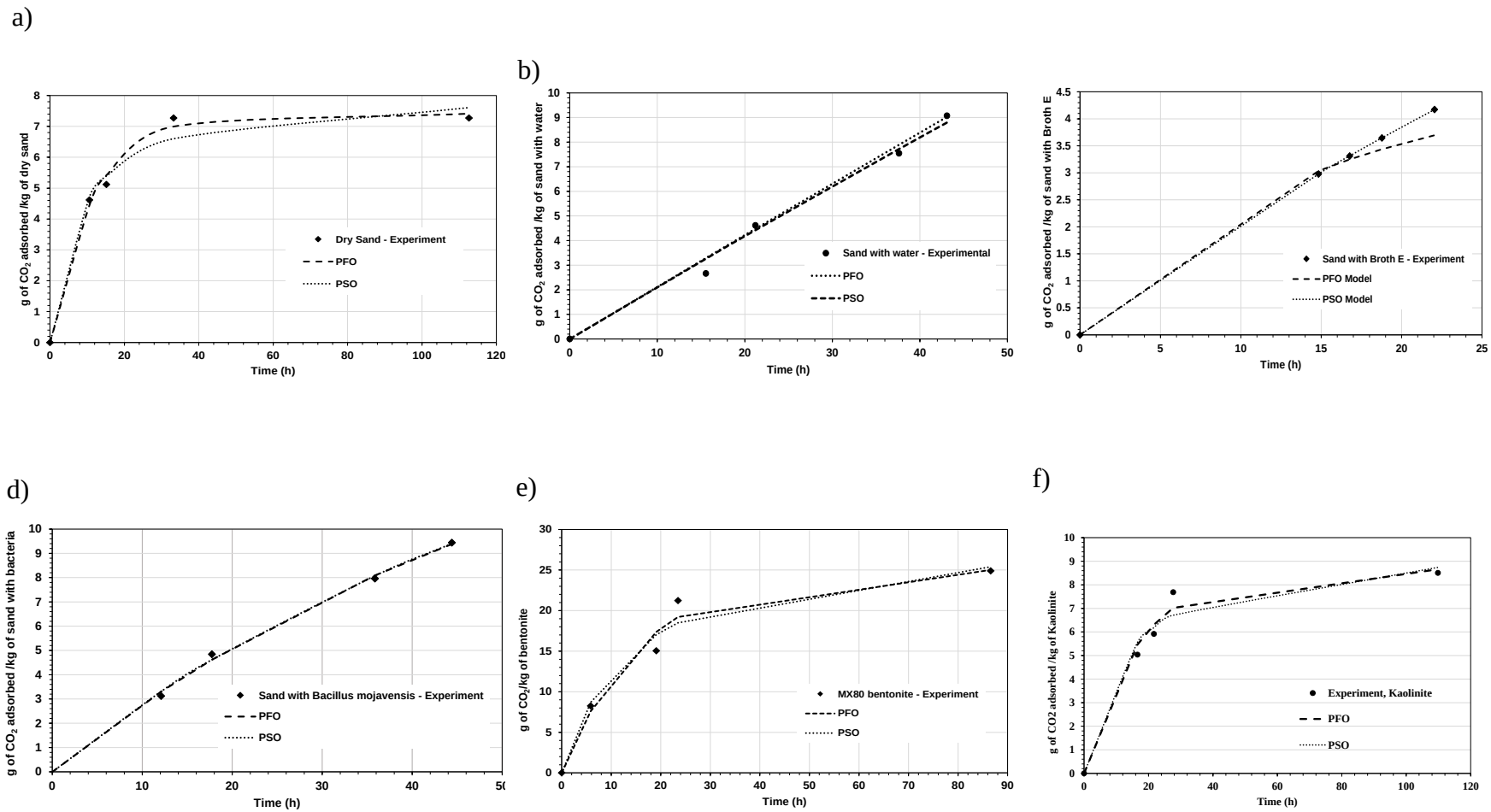

Figure 7.12. CO_2 adsorption PFO and PFO kinetics models compared with experiments of (a)Dry sand (b) Sand with water, (c) Sand with Broth.E (control experiment), (d) Bacillus mojavensis loaded sand, (e) Bentonite MX80 (f) Speswhite Kaolinite.

Table 7.3. PFO and PSO model parameters obtained for dry sand, wet sand, Broth.E loaded sand (control experiment) Bio-film loaded sand) Bentonite MX80 and Speswhite Kaolinite.

Sample description	Pseudo-first-order parameters			Pseudo-second-order kinetics parameters		
	q_e, equilibrium concentration, g of CO_2/kg of coal	Rate constant, k (h^{-1})	Correlation Coefficient R^2 and (standard error of estimate)	q_e, equilibrium concentration , g of CO_2/kg of coal	Rate constant K_2 (kg g^{-1} h^{-1})	Correlation Coefficient R^2 and (standard error of estimate)
Dry Sand	7.41	0.086	0.96 (0.23)	8.13	0.016	0.89 (0.4)
Sand with water	287	7 x 10^{-4}	0.99 (0.37)	158.96	0.33	0.99 (0.35)
Sand with Broth E	4.7	0.07	0.96 (0.71)	23.78	0.0004	0.35 (0.64)
Sand with Bacillus mojavensis	70.55	0.017	0.99 (0.15)	30.15	0.0003	0.99 (0.15)
MX80 bentonite	25.13	0.06	0.94 (0.23)	29.49	0.002	0.93 (0.4)
Speswhite kaolin	8.67	0.06	0.98 (0.27)	9.73	0.008	0.82 (0.35)

7.7 Concluding remarks

The results of CO_2 adsorption experiments on rock samples from the East Irish Sea, dry and wet sand, biofilm-loaded sand, MX80 bentonite, and Speswhite kaolin at a maximum equilibrium pressure of 3.6 MPa were presented in this chapter. The adsorption isotherm patterns were presented and discussed. The experimental results were evaluated by existing adsorption isotherm (Langmuir) and kinetic models (PFO and PSO). The adsorption of CO_2 on rock, sand and clay samples occurs through various phenomena that are influenced by the biogeological conditions. The adsorption experiment results provided important information for understanding the adsorption behaviour of rock minerals.

1. It was observed that the rock samples exhibited a lower adsorption capacity (0.028 to 0.9 mol of CO_2/kg of rock) than the coal samples (1.1 to 1.9 mol of CO_2/kg of coal) at similar equilibrium pressures of 3.6 MPa. The CO_2 adsorption capacity of the East Irish Sea rock sample with higher calcium and iron minerals was higher than the rock sample with lower calcium and iron minerals indicating the calcium and iron mineral content influences the CO_2 adsorption capacity. The following are the key findings from the investigations undertaken.
2. The adsorption capacity of wet and *Bacillus mojavensis*-loaded sand samples was greater than that of dry sand. The increased adsorption capacity was attributed to biofilm-enhanced CO_2 gas solubility/mineralization and CO_2 interaction with the hydrophilic sites of the quartz nanopores.
3. The adsorbed CO_2 on *Bacillus mojavensis*-loaded sand specimens was irreversible, indicating that biomineralization was likely. The increased CO_2 adsorption observed in the desorption experiments with wet and biofilm loaded sand confirms the potentiality of a chemical reaction (biomineralization).
4. Between the clays, the MX80 bentonite showed higher adsorption capacity (0.56 mol of CO_2/kg) than Speswhite kaolin (0.19 mol of CO_2/kg) at equilibrium pressures of 3.6 MPa. Comparing to the adsorption capacities of dry and wet sand samples (0.21 mol of CO_2/kg) with clay samples, the bentonite clay showed much higher adsorption capacity. However, the

kaolinite sample showed comparable adsorption capacity with the sand samples indicating the similar adsorption mechanisms occurs in sand and kaolinite samples (adsorption into the nanopores).

5. The experimental equilibrium adsorption data of sand, kaolinite, and bentonite samples agreed well with the Langmuir model. The energy of adsorption for all minerals ranged from 23 kJ/mol to 29 kJ/mol, owing to physical adsorption of the gas was the predominant mechanism.
6. The kinetic results show that the PSO model best fits the experimental results for sand with biofilm and sand with water, because the rate-limiting factor was surface interaction or CO_2 mineralisation. The PFO model fit the experimental data of the dry sand and clay minerals very well, implying that physical adsorption on available sites on the dry sand and clay minerals was the rate-limiting factor.

Chapter 8

Conclusions

8.1 Introduction

In the context of CO_2 sequestration in shallow level coal seams, the research works presented in this thesis aimed to improve fundamental understanding of gas/liquid adsorption CO_2 on coal and rock. The materials investigated were two different ranks of coal (anthracite coal (9ft AB and 18ft AB) and bituminous coal (Big Pit)) a sedimentary rock (East Irish Sea) a sand (dry, wet and *Bacillus mojavensis* (bacteria) loaded sand) and two clays (MX80 bentonite and Speswhite kaolin).

Manometric CO_2 adsorption and desorption laboratory experiments on coal samples were conducted to determine the adsorption capacity of intact (small blocks and 50 mm diameter core samples with undisturbed fabric) and powdered (< 250 μm) samples under isothermal conditions (298.15 K) and at varying pressures (< 6.1 MPa and near-critical pressure range of 6.1 MPa to 6.4 MPa). The laboratory adsorption-desorption experiments were conducted on samples of dry and water-saturated powdered and intact coal samples to gain a better understanding of how the fabric of coal and the presence of moisture affect the adsorption capacity.

The effect of the coexistence of liquid and vapour CO_2 on the adsorption characteristics was studied by considering the subcritical injection pressures and near critical injection pressures, which enabled understanding the thermodynamic behaviour of CO_2 in coal at a temperature of 298.15 K. Water retention tests on coal samples were performed for a large range of suction. Experimental investigations were carried out to determine alkaline mineral dissolution from coal by pH buffering. A scanning electron microscope was employed to identify the native bacteria on the natural coal sample and biofilm loaded coal.

The CO_2 adsorption process on coal samples was evaluated by fitting the data into existing adsorption isotherms (Langmuir and BET), kinetic (PFO, PSO, and Bangham pore diffusion) models and characteristic curves based on potential theory of adsorption and adsorbed phase density.

The caprock system adjacent to the coal seams may comprise sandstone, which in turn may contain rocks and clays of various mineralogy. To explore the adsorption capacity of the constituents of caprock systems, manometric CO_2 adsorption and desorption laboratory experiments on the rock samples from the East Irish Sea, sand (both in dry and wet conditions), a sample of biofilm (*Bacillus mojavensis*) loaded sand, and the clays were conducted to determine the adsorption capacity under isothermal conditions (298.15 K) and at varying equilibrium pressures up to 3.4 MPa.

8.2 Conclusions from the experimental results and theoretical evaluations

The research questions listed in Chapter 1, section 1.4 posed by reviewing the current understanding of CO_2 adsorption on coal and cap rock in the context of CO_2 sequestration in un-mineable coal seams were answered by the results of this study. The key findings from the study are listed below

1. Comparing the powdered samples of bituminous and anthracite, the bituminous coal showed lower CO_2 adsorption capacity than the anthracite coal. The CO_2 adsorption capacity of intact samples, on the other hand, showed an opposite trend. The intact bituminous coal sample had a higher adsorption capacity than the 18ft AB intact anthracite sample and less than the 9ft AB anthracite. The powdered anthracitic samples showed higher adsorption capacity than that of intact samples due to the increased surface area which exposes the polarising sites of anthracite coal. However, the intact bituminous coal showed a higher adsorption capacity than the powdered sample. An increased adsorption capacity of the intact sample of bituminous coal was linked to the high-density adsorption induced by channel-like pores, microfracture and higher swelling behaviour than anthracite coal (Pone et al. 2009; Zhao et al. 2014). Pulverising the sample destroys the microfracture network that is specific to bituminous coals (Xu et al. 2015; Tan et al. 2018; Lu et al. 2020). The

results observed in this study demonstrated the effect of the sample fabric of anthracite and bituminous coal samples on the CO_2 adsorption capacity.

2. The hysteresis observed in the adsorption-desorption isotherms and the pressure versus time curves signified that the CO_2 gas molecules trapped in the coal structure during the adsorption were not fully released due to the ink-bottle effect (where the pore entrance is blocked during the desorption).

3. At near critical pressure ranges (6.1 MPa and 6.4 MPa), the intact and powdered samples of anthracite coal showed a significant difference in the CO_2 adsorption isotherm shapes. The intact specimen showed a BET type upward trend, indicating the formation of a high dense adsorbed phase CO_2 in the microfracture volume of the intact sample. The powdered sample, on the other hand, showed the Langmuir monolayer type, demonstrated the effect of adsorption on the exposed higher surface area and nanopores (<2 nm) with a lower adsorbed phase density, which was identified by a large gap in the hysteresis (Wang et al. 2014; Wang et al. 2016; Ren et al. 2022).

4. The chilled-mirror dew-point technique was found to be suitable for establishing water retention curves of coal for a large range of suction and the van Genuchten model parameters for anthracite and bituminous coals were found to be different.

5. The wet powdered anthracite sample showed a lesser adsorption capacity than that of the dry sample, which was in agreement with the reported literature (Goodman et al. 2007). However, the adsorption capacities of wet intact anthracite coals were found to be greater than those of dry intact coal samples, implying that the sample fabric and presence of water could influence the mechanism of CO_2 adsorption on coal.

6. At equilibrium pressures of 6.4 MPa to 2 MPa, the powdered sample of wet anthracite coal showed a reversible desorption pattern, indicating the CO_2 molecules were weakly adsorbed. While at lower pressures, a hysteresis was observed similar to dry samples. These findings show that at lower pressures (2 MPa), CO_2 molecules have to compete with water molecules, and as the pressure increases, CO_2 molecules

enter into the pores and replace the water present and occupy the water activated sites (Day et al. 2008b).

7. The fact that the calcium mineral dissolved from the coal after equilibrating with water at different pH values showed that the presence of water causes the mineral to dissolve and may affect how CO_2 adsorb on coal.

8. *Bacillus mojavensis,* a coal seam native species resistant to high pressure CO_2, was identified in an intact anthracite sample, and the SEM images of the coal with laboratory-grown bacteria showed that the *Bacillus mojavensis* grows well on coal.

9. The experimental data obtained for wet (intact and powder) and dry (intact and powder) anthracite samples up to the near critical pressure range (<6.1 MPa) revealed that the Langmuir model fits the experimental data better. At near critical pressure, the BET model better fits the intact anthracite, indicating that CO_2 adsorption on the intact sample is driven by liquid-like condensation CO_2 on the coal surfaces (external and pore surfaces). The presence of nanopores and nano fractures identified in the intact samples (SEM images) substantiates the hypothesis that higher density CO_2 adsorption occurs in the intact samples than in the powdered samples.

10. The energy of adsorption calculated in this study was attributed to physical adsorption. The specific surface area calculated using the BET isotherm model of CO_2 adsorption reflected the effect of the sample fabric on the CO_2 adsorption by showing a higher microporous surface area for intact samples than for powdered samples of bituminous coal. For anthracitic coal, the intact sample showed a lower surface area than the powdered samples.

11. The experimental data fitted in to PFO, PSO, and Bangham pore diffusion kinetic models showed that pore diffusion and surface interaction mechanisms are the rate-determining steps in CO_2-coal adsorption processes.

12. The East Irish Sea rock samples had much lower CO_2 adsorption capacity than the coal samples. The rock sample with a higher amount of calcium and iron exhibited a higher adsorption capacity.

13. The CO_2 adsorption capacity of wet and *Bacillus mojavensis*-loaded sand samples was greater than that of dry sand. The adsorbed CO_2 on the *Bacillus mojavensis*-loaded sand sample was irreversible, emphasising that biomineralization occurs during the adsorption process. This was further substantiated by the increasing CO_2 adsorption trend observed during the desorption experiments with wet and biofilm loaded sand.

14. Among the two clay samples, the bentonite exhibited a higher adsorption capacity than the kaolinite, indicating the CO_2 can access the interlayer space of the bentonite. The kaolinite exhibited a comparable adsorption capacity to the dry sand sample, indicating the similar adsorption mechanism occurs (adsorption in silica nanopores).

15. The Langmuir model better fitted the CO_2 adsorption experimental data obtained for the sand, bentonite and kaolinite samples. The PFO kinetic model better fitted with the experimental results obtained for the dry sand and clays, indicating the physical adsorption on the available sites was the rate determining step. On the other hand, the PSO model better fitted the experimental results of sand with biofilm and sand with water, indicating the rate-limiting factor was the surface interaction (wet sand) or CO_2 biomineralisation (biofilm loaded sand).

Overall, the experimental results greatly contributed to current knowledge and sparked valid future research ideas inspired by the experimental observations, which are outlined as future research in the following section.

8.3 Suggestions for further research

The experimental investigations of the present work have revealed that more research is required to make CO_2 sequestration in un-mineable coal seams a viable option. Many experimental methods and hypotheses identified during the current study are left to future research due to time constraints.

The capacity of adsorption of intact and powdered samples varied with coal rank. As a consequence, larger intact samples of varying coal ranks would provide insights into the influence of coal physical and chemical properties on adsorption characteristics. The adsorption cell of the current study can hold samples up to 7 cm

long and 5 cm diameter, however much larger samples can be studied in larger size core holders to study the CO_2 adsorption capacity under confining pressures as well as the permeability. Experimentation can be used in future research to test this hypothesis.

Another intriguing question is whether it is possible to inject CO_2 into shallow level coal seams and study the spontaneity of CO_2 adsorption-desorption at lower experimental pressures. Subcritical injection can be used for shallow level injection, which is less expensive than supercritical injection in deeper seams. This intriguing fact should be investigated further in the future.

The current study attempted to grow bacteria (*Bacillus mojavensis*) on coal to better understand the role of the biofilm in CO_2 adsorption on coal. Due to experimental facility limitations and time constraints, biofilm loaded coal samples were not experimentally characterised for their adsorption capacity, but biofilm loaded sand was. The adsorption capacity results of biofilm-loaded sand and the SEM images of biofilm-loaded coal sample presented in Chapter 5 provided a starting point for this perspective and warrant further investigation. Future research in this area could focus on injecting large amounts of biomass into coal seams to improve the irreversible chemisorption of CO_2 on coal.

Bituminous coal is most abundant coal rank globally, therefore more tests under the field conditions listed above is required.

References

Abunowara, M. et al. 2020. Experimental measurements of carbon dioxide, methane and nitrogen high-pressure adsorption properties onto Malaysian coals under various conditions. *Energy* 210. doi: 10.1016/j.energy.2020.118575.

Abunowara, M., Bustam, M.A., Sufian, S. and Eldemerdash, U. 2016. Description of Carbon Dioxide Adsorption and Desorption onto Malaysian Coals under Subcritical Condition. *Procedia Engineering* 148, pp. 600–608. doi: 10.1016/J.PROENG.2016.06.521.

Allardice, D.J., Clemow, L.M., Favas, G., Jackson, W.R., Marshall, M. and Sakurovs, R. 2003. The characterisation of different forms of water in low rank coals and some hydrothermally dried products. *Fuel* 82(6), pp. 661–667. doi: 10.1016/S0016-2361(02)00339-3.

Allardice, D.J. and Evans, D.G. 1971. The-brown coal/water system: Part 2. Water sorption isotherms on bed-moist Yallourn brown coal. *Fuel* 50(3), pp. 236–253. doi: 10.1016/0016-2361(71)90014-7.

Arri, L.E., Yee, D., Morgan, W.D. and Jeansonne, M.W. 1992. Modeling Coalbed Methane Production With Binary Gas Sorption. doi: 10.2118/24363-MS.

ASTM Standards. 1999. ASTM D388-99. Standard Classification of Coals by Rank. West Conshohocken. PA: ASTM International.

ASTM Standards. 2007. ASTM D1412-07. Standard Test Method for Equilibrium Moisture of Coal at 96 to 97 Percent Relative Humidity and 30°C. PA: ASTM International.

ASTM Standards. 2012. ASTM D2013. Standard practice of preparing coal samples for analysis. Vol.05.06. West Conshohocken. PA: ASTM International.

ASTM Standards. 2014. ASTM D7012. Standard Test Methods for Compressive Strength and Elastic Moduli of Intact Rock Core Specimens under Varying States of Stress and Temperatures. Vol. 04.09. West Conshohocken. PA: ASTM International.

ASTM Standards. 2015. ASTM D3302/D3302M. Standard Test Method for Total Moisture in Coal. Vol. 05.06. West Conshohocken. PA: ASTM International.

ASTM Standards. 2015. ASTM D388. Standard Classification of Coals by Rank. Vol. 05.06. West Conshohocken. PA: ASTM International.

ASTM Standards. 2016. ASTM D6836-16. Standard Test Methods for Determination of the Soil Water Characteristic Curve for Desorption Using Hanging Column, Pressure Extractor, Chilled Mirror Hygrometer, or Centrifuge. PA: ASTM International.

ASTM Standards. 2019. ASTM D3302/D3302M–19. Standard Test Method for Total Moisture in Coal. PA: ASTM International.

Atkins, P., Paula, J. and Keeler, J., 2017. Atkins' physical chemistry. 11th ed. Oxford: Oxford University Press, p.825.

Azizian, S. and Eris, S. 2021. Adsorption isotherms and kinetics. *Interface Science and Technology* 33, pp. 445–509. Available at: https://doi.org/10.1016/B978-0-12-818805-7.00011-4 [Accessed: 4 Jan 2022].

Azizian, S., Eris, S. and Wilson, L.D. 2018. Re-evaluation of the century-old Langmuir isotherm for modeling adsorption phenomena in solution. *Chemical Physics* 513, pp. 99–104. Available at: https://doi.org/10.1016/j.chemphys.2018.06.022.

Bachu, S. 2010. Screening and selection criteria, and characterisation techniques for the geological sequestration of carbon dioxide (CO_2). *Developments and Innovation in Carbon Dioxide (Co* 2, pp. 27–56. doi: 10.1533/9781845699581.1.27.

Bangham, D.H. and Burt, F.P. 1924. The behaviour of gases in contact with glass surfaces. *Proceedings of the Royal Society of London. Series A, Containing Papers of a Mathematical and Physical Character* 105(732), pp. 481–488. Available at: https://royalsocietypublishing.org/doi/abs/10.1098/rspa.1924.0032.

Bangham, D.H. and Burt, F.P. 2002. SORPTION OF AMMONIA AND CARBON DIOXIDE BY GLASS. *The Journal of Physical Chemistry* 29:2, pp. 113–129. Available at: https://pubs.acs.org/sharingguidelines.

Bangham, D.H. and Sever, W. 1925. XCIII. An experimental investigation of the dynamical equation of the process of gas-sorption . *The London, Edinburgh, and Dublin Philosophical Magazine and Journal of Science* 49(293), pp. 935–944. Available at: https://www.tandfonline.com/doi/abs/10.1080/14786442508634671.

Baran, P., Jodlowski, G.S. and Zarebska, K. 2016. Sorption of CO_2 in lignites from Polish coal mines: measurements and thermodynamic analysis. *Adsorption* 22(4–6), pp. 839–846. Available at: https://link.springer.com/article/10.1007/s10450-016-9789-6.

Bhagat, C., Dudhagara, P. and Tank, S. 2018. Trends, application and future prospectives of microbial carbonic anhydrase mediated carbonation process for CCUS. *Journal of applied microbiology* 124(2), pp. 316–335. Available at: https://pubmed.ncbi.nlm.nih.gov/28921830/.

Botan, A., Rotenberg, B., Marry, V., Turq, P. and Noetinger, B. 2010. Carbon Dioxide in Montmorillonite Clay Hydrates: Thermodynamics, Structure, and Transport from Molecular Simulation CORE View metadata, citation and similar papers at core. *Journal of Physical Chemistry C* (35), p. 14962. Available at: https://hal.archives-ouvertes.fr/hal-00531724.

British Standards Institution. 1990. BS 1377-2:1990. Methods of test for soils for civil engineering purposes. Classification tests. Milton Keynes: BSI.

British Standards Institution. 1996. BS 1016-106.1.1:1996. Methods for analysis and testing of coal and coke. Ultimate analysis of coal and coke. Determination of carbon and hydrogen content, high temperature combustion method. Milton Keynes: BSI.

British Standards Institution. 1996. BS 1016-106.4.2:1996. Methods for analysis and testing of coal and coke. Ultimate analysis of coal and coke. Determination of total sulphur content, high temperature combustion method. Milton Keynes: BSI.

British Standards Institution. 1998. BS 1016-104.3:1998. Methods for analysis and testing of coal and coke. Proximate analysis, determination of volatile matter content. Milton Keynes: BSI.

British Standards Institution. 1998. BS 1016-104.4:1998. Methods for analysis and testing of coal and coke. Proximate analysis, determination of ash. Milton Keynes: BSI.

British Standards Institution. 1999. BS 1016-104.1:1999. Methods for analysing and testing of coal and coke. Proximate analysis, determination of moisture content of the general analysis tests sample. Milton Keynes: BSI.

Brunauer, S., Emmett, P.H. and Teller, E. 1938. Adsorption of Gases in Multimolecular Layers. *Journal of the American Chemical Society* 60(2), pp. 309–319. doi: 10.1021/ja01269a023.

Busch, A. and Gensterblum, Y. 2011. CBM and CO_2-ECBM related sorption processes in coal: A review. *International Journal of Coal Geology* 87(2), pp. 49–71. Available at: http://dx.doi.org/10.1016/j.coal.2011.04.011.

Busch, A., Gensterblum, Y. and Krooss, B.M. 2003. Methane and CO_2 sorption and desorption measurements on dry Argonne premium coals: Pure components and mixtures. *International Journal of Coal Geology* . doi: 10.1016/S0166-5162(03)00113-7.

Butt, H.-J., Graf, K. and Kappl, M. 2004a. Adsorption. *Physics and Chemistry of Interfaces* , pp. 177–205. Available at: https://onlinelibrary.wiley.com/doi/full/10.1002/3527602313.ch9.

Butt, H.-J., Graf, K. and Kappl, M. 2004b. Surface Forces. *Physics and Chemistry of Interfaces* , pp. 80–117. Available at: https://onlinelibrary.wiley.com/doi/full/10.1002/3527602313.ch6.

Byrer, C.W., Guthrie, H.D. 2000. Unminable coals in eastern U.S. basins: potential reservoirs for sequestering carbon dioxide. Pro- ceedings, 25th International Technical Conference on Coal Uti- lization and Fuel Systems, Clearwater, FL, 141–151.

Castro-Alonso, M.J., Montañez-Hernandez, L.E., Sanchez-Muñoz, M.A., Macias Franco, M.R., Narayanasamy, R. and Balagurusamy, N. 2019. Microbially induced calcium carbonate precipitation (MICP) and its potential in bioconcrete: Microbiological and molecular concepts. *Frontiers in Materials* 6, p. 126. doi: 10.3389/FMATS.2019.00126/BIBTEX.

Charrière, D. and Behra, P. 2010. Water sorption on coals. *Journal of Colloid and Interface Science* 344(2), pp. 460–467. Available at: http://dx.doi.org/10.1016/j.jcis.2009.11.064.

Chen, M., Masum, S. and Thomas, H. 2021. Modeling Non-isothermal Transport Behavior of Real Gas in Deformable Coal Matrix. *Energy and Fuels* 35(2), pp. 1605–1619. doi: 10.1021/acs.energyfuels.0c03728.

Chen, Y.H. and Lu, D.L. 2015. CO_2 capture by kaolinite and its adsorption mechanism. *Applied Clay Science* 104, pp. 221–228. doi: 10.1016/J.CLAY.2014.11.036.

Chialvo, A.A., Vlcek, L. and Cole, D.R. 2012. Aqueous CO_2 solutions at silica surfaces and within nanopore environments. Insights from isobaric-isothermal molecular dynamics. *Journal of Physical Chemistry C* 116(26), pp. 13904–13916. Available at: https://pubs.acs.org/doi/abs/10.1021/jp3001948.

Clarkson, C.R. and Bustin, R.M. 1999. Effect of pore structure and gas pressure upon the transport properties of coal: a laboratory and modeling study. 2. Adsorption rate modeling. *Fuel* 78(11), pp. 1345–1362. doi: 10.1016/S0016-2361(99)00056-3.

Clarkson, C.R. and Bustin, R.M. 2000. Binary gas adsorption/desorption isotherms: Effect of moisture and coal composition upon carbon dioxide selectivity over methane. *International Journal of Coal Geology* . doi: 10.1016/S0166-5162(99)00032-4.

Cole, D.R., Chialvo, A.A., Rother, G., Vlcek, L. and Cummings, P.T. 2010. Supercritical fluid behavior at nanoscale interfaces: Implications for CO_2 sequestration in geologic formations. *https://doi.org/10.1080/14786430903559458* 90(17–18), pp. 2339–2363. Available at: https://www.tandfonline.com/doi/abs/10.1080/14786430903559458.

Cui, X., Bustin, A.M.M. and Bustin, R.M. 2009. Measurements of gas permeability and diffusivity of tight reservoir rocks: Different approaches and their applications. *Geofluids* 9(3), pp. 208–223. doi: 10.1111/j.1468-8123.2009.00244.x.

Cui, X., Bustin, R.M. and Dipple, G. 2004. Selective transport of CO_2, CH_4, and N_2 in coals: Insights from modeling of experimental gas adsorption data. *Fuel* 83(3), pp. 293–303. doi: 10.1016/J.FUEL.2003.09.001.

Czapliński, A. and Hołda, S. 1982. Changes in mechanical properties of coal due to sorption of carbon dioxide vapour. *Fuel* 61(12), pp. 1281–1282. doi: 10.1016/0016-2361(82)90035-7.

Dąbrowski, A. 2001. Adsorption - From theory to practice. *Advances in Colloid and Interface Science* 93(1–3), pp. 135–224. doi: 10.1016/S0001-8686(00)00082-8.

DAVIDSON, R.M. 1982. Molecular Structure of Coal. *Coal Science* , pp. 83–160.

doi: 10.1016/B978-0-12-150701-5.50009-7.

Day, S., Fry, R. and Sakurovs, R. 2008a. Swelling of Australian coals in supercritical CO_2. *International Journal of Coal Geology* 74(1), pp. 41–52. doi: 10.1016/J.COAL.2007.09.006.

Day, S., Sakurovs, R. and Weir, S. 2008b. Supercritical gas sorption on moist coals. International Journal of Coal Geology 74(3–4), pp. 203–214. doi: 10.1016/j.coal.2008.01.003.

De Boer J. 1958. The structure and properties of porous materials. London: Butterworths.

Decagon Devices. 2010. Commercial publications, operator's manual for WP4C Dew Point PotentiaMeter. Pullman. Available at: www.decagon.com.

Deng, H., Fitts, J.P. and Peters, C.A. 2016. Quantifying fracture geometry with X-ray tomography: Technique of Iterative Local Thresholding (TILT) for 3D image segmentation. *Computational Geosciences 2016 20:1* 20(1), pp. 231–244. Available at: https://link.springer.com/article/10.1007/s10596-016-9560-9.

Depaolo, D.J. and Cole, D.R. 2013. Geochemistry of Geologic Carbon Sequestration: An Overview. *Reviews in Mineralogy & Geochemistry* 77, pp. 1–14. Available at: http://dx.doi.org/10.2138/rmg.2013.77.1 [Accessed: 12 March 2019].

DIN method. 2001. DIN 51913:2001. Testing of carbon materials — Determination of density by gas pycnometer (volumetric) using helium as the measuring gas — Solid materials prepared by Arbeitsausschuß NMP 281. Test Methods for Carbon and Graphite.

Doner, H.E. and Lynn, W.C. 2018. Carbonate, Halide, Sulfate, and Sulfide Minerals. *Minerals in Soil Environments* , pp. 279–330. Available at: https://onlinelibrary.wiley.com/doi/full/10.2136/sssabookser1.2ed.c6.

Dupraz, C., Reid, R.P., Braissant, O., Decho, A.W., Norman, R.S. and Visscher, P.T. 2009. Processes of carbonate precipitation in modern microbial mats. *Earth-Science Reviews* 96(3), pp. 141–162. doi: 10.1016/J.EARSCIREV.2008.10.005.

Dutta, P., Harpalani, S. and Prusty, B. 2008. Modeling of CO_2 sorption on coal. *Fuel* 87(10–11), pp. 2023–2036. doi: 10.1016/J.FUEL.2007.12.015.

Elliott, J. and Lira, C. 2012. Introductory chemical engineering thermodynamics. Upper Saddle River, NJ: Prentice Hall.

Engel, T. and Reid, P. (Philip J.. 2019. *Thermodynamics, statistical thermodynamics, and kinetics*. Fourth edi. New York: Pearson.

Enomoto, A., Nakamura, K., Nagai, K., Hashimoto, T. and Hakoda, M. 1997. Inactivation of Food Microorganisms by High-pressure Carbon Dioxide Treatment with or without Explosive Decompression. *Bioscience, Biotechnology, and Biochemistry* 61(7), pp. 1133–1137. Available at: https://academic.oup.com/bbb/article/61/7/1133/5947318.

EPA. 2014. Emission Factors for Greenhouse Gas Inventories. Environmental Protection Agency.

Espinoza, D.N., Vandamme, M., Pereira, J.M., Dangla, P. and Vidal-Gilbert, S. 2014. Measurement and modeling of adsorptive-poromechanical properties of bituminous coal cores exposed to CO_2: Adsorption, swelling strains, swelling stresses and impact on fracture permeability. *International Journal of Coal Geology* 134–135, pp. 80–95. doi: 10.1016/J.COAL.2014.09.010.

Faisal Alshalif, A., Irwan, J.M., Othman, N., Zamer, M.M. and Anneza, L.H. 2017. Carbon Dioxide (CO_2) Sequestration In Bio-Concrete, An Overview. *MATEC Web of Conferences* 103, p. 05016. Available at: https://www.matec-conferences.org/articles/matecconf/abs/2017/17/matecconf_iscee2017_05016/matecconf_iscee2017_05016.html.

Fakher, S. and Imqam, A. 2020. High pressure-high temperature carbon dioxide adsorption to shale rocks using a volumetric method. *International Journal of Greenhouse Gas Control* 95. Available at: https://doi.org/10.1016/j.ijggc.2020.102998.

Ferrari, A., Favero, V., Marschall, P. and Laloui, L. 2014. Experimental analysis of the water retention behaviour of shales. *International Journal of Rock Mechanics and Mining Sciences* 72, pp. 61–70. doi: 10.1016/j.ijrmms.2014.08.011.

Fitzgerald, J.E., Pan, Z., Sudibandriyo, M., Robinson, R.L., Gasem, K.A.M. and Reeves, S. 2005. Adsorption of methane, nitrogen, carbon dioxide and their mixtures

on wet Tiffany coal. *Fuel* . doi: 10.1016/j.fuel.2005.05.002.

Fleurbaey M., S. Kartha, S. Bolwig, Y. L. Chee, Y. Chen, E. Corbera, F. Lecocq, W. Lutz, M. S. Muylaert, R. B. Norgaard, C. Okereke, and A. D. Sagar. 2014. ustainable development and Equity. In: Climate Change 2014: Mitigation of Climate Change. Contribution of Working Group III to the Fifth Assessment Report of the Intergovernmental Panel on Climate Change [Edenhofer, O., R. Pichs-Madruga, Y. Sokona, E. Farahani, S.Kadner, K. Seyboth, A. Adler, I. Baum, S. Brunner, P. Eickemeier, B. Kriemann, J. Savolainen, S. Schlömer, C.von Stechow, T. Zwickel and J.C. Minx (eds.)]. Cambridge University Press, Cambridge, United Kingdom and New York, NY, USA.

Fredlund, D. et al. 2012. Unsaturated soil mechanics in engineering practice. Hoboken (N.J.): John Wiley & Sons.

Freundlich, Herbert. 1909. Kapillarchemie. eine Darstellung der Chemie der Kolloide und verwandter Gebiete. Akademische Verlagsgesellschaft.

Gensterblum, Y. et al. 2009. European inter-laboratory comparison of high pressure CO_2 sorption isotherms. I: Activated carbon. *Carbon* . doi: 10.1016/j.carbon.2009.06.046.

Gensterblum, Y. et al. 2010. European inter-laboratory comparison of high pressure CO_2 sorption isotherms II: Natural coals. *International Journal of Coal Geology* . doi: 10.1016/j.coal.2010.08.013.

Gensterblum, Y., Busch, A. and Krooss, B.M. 2014. Molecular concept and experimental evidence of competitive adsorption of H_2O, CO_2 and CH_4 on organic material. *Fuel* 115, pp. 581–588. Available at: https://researchportal.hw.ac.uk/en/publications/molecular-concept-and-experimental-evidence-of-competitive-adsorp.

George, S. and Barakat, M.A. 2001. The change in effective stress associated with shrinkage from gas deportation in coal. *International Journal of Coal Geology* 45(2–3), pp. 105–113. doi: 10.1016/S0166-5162(00)00026-4.

Geyer, L.L. et al. 2015. State of the Art: Iterative CT Reconstruction Techniques. *Radiology* 276(2), pp. 339–357. Available at:

https://pubmed.ncbi.nlm.nih.gov/26203706/.

Gmehling, J., Kleiber, M., Kolbe, B., & Rarey, J. (2019). Chemical Thermodynamics for Process Simulation. 2nd ed. Wiley -VCH.

Goodman, A.L. et al. 2004. An inter-laboratory comparison of CO_2 isotherms measured on argonne premium coal samples. *Energy and Fuels* . doi: 10.1021/ef034104h.

Goodman, A.L. et al. 2007. Inter-laboratory comparison II: CO_2 isotherms measured on moisture-equilibrated Argonne premium coals at 55 °C and up to 15 MPa. *International Journal of Coal Geology* 72(3–4), pp. 153–164. doi: 10.1016/j.coal.2007.01.005.

Goodman, A.L., Favors, R.N. and Larsen, J.W. 2006. Argonne coal structure rearrangement caused by sorption of CO_2. *Energy and Fuels* 20(6), pp. 2537–2543. doi: 10.1021/ef060188t.

Great Britain. Department for Business, Energy & Industrial Strategy. 2021. Net Zero Strategy: Build Back Greener. Available at https://www.gov.uk/government/uploads/system/uploads/attachment_data/file/32225/11-515-bigger-better-business-helping-small-firms.pdf

Gruszkiewicz, M.S., Naney, M.T., Blencoe, J.G., Cole, D.R., Pashin, J.C. and Carroll, R.E. 2009. Adsorption kinetics of CO_2, CH_4, and their equimolar mixture on coal from the Black Warrior Basin, West-Central Alabama. *International Journal of Coal Geology* 77(1–2), pp. 23–33. Available at: https://linkinghub.elsevier.com/retrieve/pii/S0166516208001821 [Accessed: 19 August 2019].

Gruszkiewicz, M.S., Rother, G., Wesolowski, D.J., Cole, D.R. and Wallacher, D. 2012. Direct measurements of pore fluid density by vibrating tube densimetry. *Langmuir : the ACS journal of surfaces and colloids* 28(11), pp. 5070–5078. Available at: https://pubmed.ncbi.nlm.nih.gov/22369098/ [Accessed: 5 May 2022].

Gu, B., Schmitt, J., Chen, Z., Liang, L. and McCarthy, J.F. 1994. Adsorption and Desorption of Natural Organic Matter on Iron Oxide: Mechanisms and Models. *Environmental Science and Technology* 28(1), pp. 38–46. Available at:

https://pubs.acs.org/doi/abs/10.1021/es00050a007.

Guan, C., Liu, S., Li, C., Wang, Y. and Zhao, Y. 2018. The temperature effect on the methane and CO2 adsorption capacities of Illinois coal. Fuel 211, pp. 241–250. doi: 10.1016/j.fuel.2017.09.046.

Guo, H., Cheng, Y., Wang, L., Lu, S. and Jin, K. 2015. Experimental study on the effect of moisture on low-rank coal adsorption characteristics. Journal of Natural Gas Science and Engineering 24, pp. 245–251.

Guo, J., Zhai, Z., Wang, L., Wang, Z., Wu, J., Zhang, B. and Zhang, J. 2017. Dynamic and thermodynamic mechanisms of TFA adsorption by particulate matter. *Environmental Pollution* 225, pp. 175–183. Available at: http://dx.doi.org/10.1016/j.envpol.2017.03.049.

Hadi Mosleh, M., Turner, M., Sedighi, M. and Vardon, P.J. 2018. Carbon dioxide flow and interactions in a high rank coal: Permeability evolution and reversibility of reactive processes. *International Journal of Greenhouse Gas Control* 70, pp. 57–67. doi: 10.1016/j.ijggc.2018.01.002.

Hall, F.E., Chunhe, Z., Gasem, K.A.M., Robinson, R.L. and Dan, Y. 1994. Adsorption of Pure Methane, Nitrogen, and Carbon Dioxide and Their Binary Mixtures on Wet Fruitland Coal. *All Days* . Available at: https://onepetro.org/SPEERM/proceedings/94ERM/All-94ERM/Charleston, West Virginia/56832.

Hamza, A., Hussein, I.A., Al-Marri, M.J., Mahmoud, M. and Shawabkeh, R. 2021. Impact of clays on CO_2 adsorption and enhanced gas recovery in sandstone reservoirs. *International Journal of Greenhouse Gas Control* 106. doi: 10.1016/J.IJGGC.2021.103286.

Hannah Ritchie and Max Roser .2020.CO_2 and Greenhouse Gas Emissions. Published online at OurWorldInData.org.

Harpalani, S. and Chen, G. 1995. Estimation of changes in fracture porosity of coal with gas emission. *Fuel* 74(10), pp. 1491–1498. doi: 10.1016/0016-2361(95)00106-F.

Harpalani, S., Prusty, B.K. and Dutta, P. 2006. Methane/CO_2 sorption modeling for coalbed methane production and CO_2 sequestration. *Energy and Fuels* 20(4), pp.

1591–1599. doi: 10.1021/EF050434L.

Hou, X., Liu, S., Zhu, Y. and Yang, Y. 2020. Experimental and theoretical investigation on sorption kinetics and hysteresis of nitrogen, methane, and carbon dioxide in coals. Fuel 268 y(February), p. 117349. Available at: https://doi.org/10.1016/j.fuel.2020.117349.

Hu, A., Zhang, Y., Xiong, P., Yang, Y. and Liu, Z. 2020. Kinetic characteristics and modeling comparison of methane adsorption on gas shale. *Energy Sources, Part A: Recovery, Utilization and Environmental Effects* 00(00), pp. 1–15. Available at: https://doi.org/10.1080/15567036.2020.1849461.

Hu, X., Deng, H., Lu, C., Tian, Y. and Jin, Z. 2019. Characterization of CO_2/CH_4 Competitive Adsorption in Various Clay Minerals in Relation to Shale Gas Recovery from Molecular Simulation. *Energy and Fuels* 33(9), pp. 8202–8214. Available at: https://pubs.acs.org/doi/abs/10.1021/acs.energyfuels.9b01610.

Humayun, R. and Tomasko, D.L. 2000. High-resolution adsorption isotherms of supercritical carbon dioxide on activated carbon. *AIChE Journal* 46(10), pp. 2065–2075. Available at: https://onlinelibrary.wiley.com/doi/10.1002/aic.690461017 [Accessed: 2 August 2019].

Hwang, J. and Pini, R. 2019. Supercritical CO2 and CH4 Uptake by Illite-Smectite Clay Minerals. *Environmental Science and Technology* 53(19), pp. 11588–11596. Available at: https://pubs.acs.org/doi/full/10.1021/acs.est.9b03638 [Accessed: 5 May 2022].

Ilton, E.S., Schaef, H.T., Qafoku, O., Rosso, K.M. and Felmy, A.R. 2012. In situ X-ray diffraction study of Na+ saturated montmorillonite exposed to variably wet super critical CO_2. *Environmental Science and Technology* 46(7), pp. 4241–4248. Available at: https://pubs.acs.org/doi/abs/10.1021/es300234v.

IPCC. 2005. IPCC special report on carbon dioxide capture and storage, B. Metz, O. Davidson, H.C. de Coninck, M. Loos, L.A. Meyer (Eds.), Working Group III of the Intergovernmental Panel on Climate Change, Cambridge University Press, Cambridge, UK

IPCC. 2014. Climate Change 2014: Synthesis Report. Contribution of Working Groups I, II and III to the Fifth Assessment Report of the Intergovernmental Panel on Climate Change [Core Writing Team, R.K. Pachauri and L.A. Meyer (eds.)]. IPCC, Geneva, Switzerland, 151 pp.

IPCC. 2018. Global Warming of 1.5°C.An IPCC Special Report on the impacts of global warming of 1.5°C above pre-industrial levels and related global greenhouse gas emission pathways, in the context of strengthening the global response to the threat of climate change, sustainable development, and efforts to eradicate poverty.

Jedli, H., Jbara, A., Hedfi, H., Bouzgarrou, S. and Slimi, K. 2017. Carbon dioxide adsorption isotherm study on various cap rocks in a batch reactor for CO_2 sequestration processes. *Applied Clay Science* 136, pp. 199–207. Available at: http://dx.doi.org/10.1016/j.clay.2016.11.022

Jeon, P.R., Choi, J., Yun, T.S. and Lee, C.H. 2014. Sorption equilibrium and kinetics of CO_2 on clay minerals from subcritical to supercritical conditions: CO_2 sequestration at nanoscale interfaces. *Chemical Engineering Journal* 255, pp. 705–715. doi: 10.1016/J.CEJ.2014.06.090.

Jin, Z. and Firoozabadi, A. 2013. Methane and carbon dioxide adsorption in clay-like slit pores by Monte Carlo simulations. *Fluid Phase Equilibria* 360, pp. 456–465. doi: 10.1016/J.FLUID.2013.09.047.

Jones, E.J.P. et al. 2008. Bioassay for estimating the biogenic methane-generating potential of coal samples. *International Journal of Coal Geology* 76(1–2), pp. 138–150. doi: 10.1016/J.COAL.2008.05.011.

Kadioğlu, Y. and Varamaz, M. 2003. The effect of moisture content and air-drying on spontaneous combustion characteristics of two Turkish lignites. *Fuel* 82(13), pp. 1685–1693. doi: 10.1016/S0016-2361(02)00402-7.

Kaji, R., Muranaka, Y., Otsuka, K. and Hishinuma, Y. 1986. Water absorption by coals: effects of pore structure and surface oxygen. *Fuel* 65(2), pp. 288–291. doi: 10.1016/0016-2361(86)90023-2.

Kamihira, M., Taniguchi, M. and Kobayashi, T. 1987. Sterilization of microorganisms with supercritical carbon dioxide. *Agricultural and Biological Chemistry* 51(2), pp.

407–412. doi: 10.1080/00021369.1987.10868053.

Kaszuba, J., Yardley, B. and Muriel Andreani, leedsacuk 2013. Experimental Perspectives of Mineral Dissolution and Precipitation due to Carbon Dioxide-Water-Rock Interactions. *Reviews in Mineralogy & Geochemistry* 77, pp. 153–188. Available at: http://dx.doi.org/10.2138/rmg.2013.77.5 [Accessed: 15 March 2019].

Kelemen, S.R. and Kwiatek, L.M. 2009. Physical properties of selected block Argonne Premium bituminous coal related to CO_2, CH_4, and N_2 adsorption. International Journal of Coal Geology 77(1–2), pp. 2–9. doi: 10.1016/J.COAL.2008.05.020.

Keller, J.U. and Staudt, R. 2005. Gas adsorption equilibria: Experimental methods and adsorptive isotherms. *Gas Adsorption Equilibria: Experimental Methods and Adsorptive Isotherms* , pp. 1–422. Available at: http://ebooks.kluweronline.comhttp//www.springeronline.com.

Kerisit, S., Weare, J.H. and Felmy, A.R. 2012. Structure and Dynamics of Forsterite-scCO_2/H_2O Interfaces as a Function of Water Content. *Geochimica et Cosmochimica Acta* 84, pp. 137–151. doi: 10.1016/J.GCA.2012.01.038.

Kim, J., Lin, L.C., Swisher, J.A., Haranczyk, M. and Smit, B. 2012. Predicting large CO_2 adsorption in aluminosilicate zeolites for postcombustion carbon dioxide capture. *Journal of the American Chemical Society* 134(46), pp. 18940–18943. Available at: https://pubs.acs.org/doi/abs/10.1021/ja309818u.

Kolstad,I., Wiig, A. 2015. Education and entrepreneurial success. Small Business Economy 44. PP 783-796.

KROOSS, B., BUSCH, A. and GENSTERBLUM, Y. 2005. CO_2 and CH_4 sorption kinetics on coalAn experimental and modeling approach. In: *Greenhouse Gas Control Technologies 7*. Elsevier, pp. 2243–2246. Available at: https://linkinghub.elsevier.com/retrieve/pii/B9780080447049503104 [Accessed: 19 August 2019].

Krooss, B.M., Van Bergen, F., Gensterblum, Y., Siemons, N., Pagnier, H.J.M. and David, P. 2002. High-pressure methane and carbon dioxide adsorption on dry and moisture-equilibrated Pennsylvanian coals. *International Journal of Coal Geology* . doi: 10.1016/S0166-5162(02)00078-2.

Kuuskraa, V.A., Wicks, D.E. and Thurber, J.L. 1992. Geologic and Reservoir Mechanisms Controlling Gas Recovery From the Antrim Shale. The SPE Annual Technical Conference and Exhibition. October 1992. Washington: D.C. Available at: doi: 10.2118/24883-ms.

Kwak, J.H. et al. 2011. The role of H2O in the carbonation of forsterite in supercritical CO_2. *International Journal of Greenhouse Gas Control* 5(4), pp. 1081–1092. doi: 10.1016/J.IJGGC.2011.05.013.

Kyle, C.P., Adam, J.E.F., Hernandez, H.H., Britto, V., Boreham, C., Ajo-Franklin, J.B. and Thompson, J.R. 2015. Microbial growth under supercritical CO_2. *Applied and Environmental Microbiology* 81(8), pp. 2881–2892. Available at: http://dx.doi.org/10.1128.

Lafortune, S. et al. 2014. An experimental approach to adsorption of $CO_2 + CH_4$ gas mixtures onto coal (European RFCS CARBOLAB research project). In: *Energy Procedia*. Elsevier Ltd, pp. 5870–5878. doi: 10.1016/j.egypro.2014.11.620.

Langmuir, I. 1915. Chemical reactions at low pressures. *Journal of the American Chemical Society* 37(5), pp. 1139–1167. Available at: https://pubs.acs.org/doi/abs/10.1021/ja02170a017.

Langmuir, I. 1916. The constitution and fundamental properties of solids and liquids. Part I. Solids. *Journal of the American Chemical Society* 38(11), pp. 2221–2295. Available at: https://pubs.acs.org/doi/abs/10.1021/ja02268a002.

Langmuir, I. 1917. The constitution and fundamental properties of solids and liquids. II. Liquids. *Journal of the American Chemical Society* 39(9), pp. 1848–1906. Available at: https://pubs.acs.org/doi/abs/10.1021/ja02254a006.

Langmuir, I. 1918. The adsorption of gases on plane surfaces of glass, mica and platinum. *Journal of the American Chemical Society* 40(9), pp. 1361–1403. Available at: https://pubs.acs.org/doi/abs/10.1021/ja02242a004.

Laubach, S.E., Marrett, R.A., Olson, J.E. and Scott, A.R. 1998. *Characteristics and origins of coal cleat: A review*. Available at: https://ac.els-cdn.com/S0166516297000128/1-s2.0-S0166516297000128-main.pdf?_tid=9348759a-01cf-4b59-8ae9-

a0361cd73daf&acdnat=1551268846_cb6692eb92290d37905c4784cf45312c [Accessed: 27 February 2019].

Lavalleur, H.J. and Colwell, F.S. 2013. Microbial characterization of basalt formation waters targeted for geological carbon sequestration. *FEMS Microbiology Ecology* 85(1), pp. 62–73. Available at: https://academic.oup.com/femsec/article/85/1/62/573693.

Lee, H.H., Kim, H.J., Shi, Y., Keffer, D. and Lee, C.H. 2013. Competitive adsorption of CO_2/CH_4 mixture on dry and wet coal from subcritical to supercritical conditions. *Chemical Engineering Journal* 230, pp. 93–101. doi: 10.1016/j.cej.2013.06.036.

Li, D., Liu, Q., Weniger, P., Gensterblum, Y., Busch, A. and Krooss, B.M. 2010. High-pressure sorption isotherms and sorption kinetics of CH_4 and CO_2 on coals. *Fuel* 89(3), pp. 569–580. doi: 10.1016/j.fuel.2009.06.008.

Liu, D., Yuan, P., Liu, H., Li, T., Tan, D., Yuan, W. and He, H. 2013. High-pressure adsorption of methane on montmorillonite, kaolinite and illite. *Applied Clay Science* 85(1), pp. 25–30. doi: 10.1016/J.CLAY.2013.09.009.

Liu, H., Mou, J. and Cheng, Y. 2015. Impact of pore structure on gas adsorption and diffusion dynamics for long-flame coal. *Journal of Natural Gas Science and Engineering* 22, pp. 203–213. Available at: http://dx.doi.org/10.1016/j.jngse.2014.11.030 [Accessed: 5 May 2022].

Liu, S., Sang, S., Wang, T., Du, Y., Jia, J. and Fang, H. 2018. The effects of CO_2 on organic groups in bituminous coal and high-rank coal via Fourier transform infrared spectroscopy: *https://doi.org/10.1177/0144598718764752* 36(6), pp. 1566–1592. Available at: https://journals.sagepub.com/doi/10.1177/0144598718764752.

Liu, Y. and Shen, L. 2008. From Langmuir kinetics to first- and second-order rate equations for adsorption. *Langmuir* 24(20), pp. 11625–11630. Available at: https://pubs.acs.org/doi/full/10.1021/la801839b.

Loganathan, S., Tikmani, M., Edubilli, S., Mishra, A. and Ghoshal, A.K. 2014. CO_2 adsorption kinetics on mesoporous silica under wide range of pressure and temperature. *Chemical Engineering Journal* C(256), pp. 1–8. Available at: https://www.infona.pl//resource/bwmeta1.element.elsevier-5a746ec6-70a8-3c4e-

a7e4-616753369083.

Loring, J.S. et al. 2011. In situ infrared spectroscopic study of forsterite carbonation in wet supercritical CO_2. *Environmental Science and Technology* 45(14), pp. 6204–6210. Available at: https://pubs.acs.org/sharingguidelines.

Loring, J.S. et al. 2012. In situ molecular spectroscopic evidence for CO_2 intercalation into montmorillonite in supercritical carbon dioxide. *Langmuir* 28(18), pp. 7125–7128. Available at: https://pubs.acs.org/doi/full/10.1021/la301136w.

Lu, X., Armstrong, R.T. and Mostaghimi, P. 2020. Analysis of gas diffusivity in coal using micro-computed tomography. Fuel 261, p. 116384.

Mahajan, O.P. and Walker, P.L. 1971. Water adsorption on coals. *Fuel* 50(3), pp. 308–317. doi: 10.1016/0016-2361(71)90019-6.

Majewska Z, Majewski S., Ziętek J, Ceglarska-Stefańska G. 2010. Volumetric strain induced in medium-rank coal by sorption of carbon dioxide, methane and their mixture. Chapter 4. Carbon Sequestration: Methods, Modeling and Impacts. Edited by Elke Hoch and Siegbert Crunwald. New York: Nova Publishers.

Malani, A. and Ayappa, K.G. 2009. Adsorption Isotherms of Water on Mica: Redistribution and Film Growth. *Journal of Physical Chemistry B* 113(4), pp. 1058–1067. Available at: https://pubs.acs.org/doi/abs/10.1021/jp805730p.

Marcott, S.A., Shakun, J.D., Clark, P.U. and Mix, A.C. 2013. A reconstruction of regional and global temperature for the past 11,300 years. Science 339(6124), pp. 1198–1201. Available at: http://www.sciencemag.org/content/339/6124/1198.full.html.

Masoudian, M.S. 2016. Multiphysics of carbon dioxide sequestration in coalbeds: A review with a focus on geomechanical characteristics of coal. *Journal of Rock Mechanics and Geotechnical Engineering* 8(1), pp. 93–112. doi: 10.1016/J.JRMGE.2015.08.002.

Masoudian, M.S., Airey, D.W. and El-Zein, A. 2014. Experimental investigations on the effect of CO_2 on mechanics of coal. *International Journal of Coal Geology* 128–129, pp. 12–23. doi: 10.1016/J.COAL.2014.04.001.

Massarotto, P., Golding, S.D., Bae, J.S., Iyer, R. and Rudolph, V. 2010. Changes in

reservoir properties from injection of supercritical CO_2 into coal seams - A laboratory study. *International Journal of Coal Geology* 82(3–4), pp. 269–279. doi: 10.1016/J.COAL.2009.11.002.

Mastalerz, M., Gluskoter, H. and Rupp, J. 2004. Carbon dioxide and methane sorption in high volatile bituminous coals from Indiana, USA. *International Journal of Coal Geology* 60(1), pp. 43–55. Available at: https://linkinghub.elsevier.com/retrieve/pii/S0166516204000916 [Accessed: 19 August 2019].

Mathews, J.P., Campbell, Q.P., Xu, H. and Halleck, P. 2017. A review of the application of X-ray computed tomography to the study of coal. *Fuel* 209, pp. 10–24. Available at: https://pennstate.pure.elsevier.com/en/publications/a-review-of-the-application-of-x-ray-computed-tomography-to-the-s [Accessed: 5 May 2022].

Mavor, M.J., Gunter, W.D., Robinson, J.R., Law, D.H.-S. and Gale, J. 2002. Testing for CO2 Sequestration and Enhanced Methane Production from Coal. All Days . Available at: https://onepetro.org/SPEGTS/proceedings/02GTS/All-02GTS/Calgary, Alberta, Canada/135573

McGrail, B.P., Schaef, H.T., Glezakou, V.A., Dang, L.X. and Owen, A.T. 2009. Water reactivity in the liquid and supercritical CO_2 phase: Has half the story been neglected? *Energy Procedia* 1(1), pp. 3415–3419. doi: 10.1016/J.EGYPRO.2009.02.131.

Melnichenko, Y.B., Mayama, H., Cheng, G. and Blach, T. 2010. Monitoring phase behavior of sub- and supercritical CO_2 confined in porous fractal silica with 85% porosity. *Langmuir : the ACS journal of surfaces and colloids* 26(9), pp. 6374–6379. Available at: https://pubmed.ncbi.nlm.nih.gov/20043698/ [Accessed: 6 May 2022].

Meng, M., Qiu, Z., Zhong, R., Liu, Z., Liu, Y. and Chen, P. 2019. Adsorption characteristics of supercritical CO_2 /CH_4 on different types of coal and a machine learning approach. *Chemical Engineering Journal* , pp. 847–864. doi: 10.1016/j.cej.2019.03.008.

Mitchell, A.C., Phillips, A.J., Hamilton, M.A., Gerlach, R., Hollis, W.K., Kaszuba, J.P. and Cunningham, A.B. 2008. Resilience of planktonic and biofilm cultures to supercritical CO_2. *The Journal of Supercritical Fluids* 47(2), pp. 318–325. Available at: https://linkinghub.elsevier.com/retrieve/pii/S0896844608002040.

Mitchell, A.C., Phillips, A.J., Hiebert, R., Gerlach, R., Spangler, L.H. and Cunningham, A.B. 2009. Biofilm enhanced geologic sequestration of supercritical CO_2. *International Journal of Greenhouse Gas Control* 3(1), pp. 90–99. doi: 10.1016/j.ijggc.2008.05.002.

Mitra, A., Harpalani, S. and Liu, S. 2012. Laboratory measurement and modeling of coal permeability with continued methane production: Part 1 - Laboratory results. Fuel 94, pp. 110–116. doi: 10.1016/J.FUEL.2011.10.052.

Miura, K., Mae, K., Li, W., Kusakawa, T., Morozumi, F. and Kumano, A. 2001. Estimation of Hydrogen Bond Distribution in Coal through the Analysis of OH Stretching Bands in Diffuse Reflectance Infrared Spectrum Measured by in-Situ Technique. *Energy and Fuels* 15(3), pp. 599–610. Available at: https://pubs.acs.org/doi/abs/10.1021/ef0001787

Montoya, A., Mondragón, F. and Truong, T.N. 2003. CO_2 adsorption on carbonaceous surfaces: A combined experimental and theoretical study. *Carbon* 41(1), pp. 29–39. doi: 10.1016/S0008-6223(02)00249-X.

Morozova, D., Wandrey, M., Alawi, M., Zimmer, M., Vieth, A., Zettlitzer, M. and Würdemann, H. 2010. Monitoring of the microbial community composition in saline aquifers during CO_2 storage by fluorescence in situ hybridisation. *International Journal of Greenhouse Gas Control* 4(6), pp. 981–989. doi: 10.1016/J.IJGGC.2009.11.014.

Mosleh, M.H. 2014. An Experimental Investigation of Flow and Reaction Processes during Gas Storage and Displacement in Coal. PhD Thesis, Cardiff University.

Mukherjee, M. and Misra, S. 2018. A review of experimental research on Enhanced Coal Bed Methane (ECBM) recovery via CO_2 sequestration. *Earth-Science Reviews* . doi: 10.1016/j.earscirev.2018.02.018.

Mukherjee, M., Misra, S., Gupta, A. 2021. Control of pore-size distribution on CO2 adsorption volume and kinetics in Gondwana coals: Implications for shallow-depth CO2 sequestration potential. Journal of Natural Gas Science and Engineering, Volume 89, 103901, ISSN 1875-5100, https://doi.org/10.1016/j.jngse.2021.103901

Murata, S., Hosokawa, M., Kidena, K. and Nomura, M. 2000. Analysis of oxygen-

functional groups in brown coals. *Fuel processing technology* 67(3), pp. 231–243. doi: 10.1016/S0378-3820(00)00102-8.

Myers, A.L. and Monson, P.A. 2014. Physical adsorption of gases: The case for absolute adsorption as the basis for thermodynamic analysis. *Adsorption* 20(4), pp. 591–622. doi: 10.1007/s10450-014-9604-1.

Nie, B., Wang, K., Gao, Q. and Cao, M. 2021. Pore Distribution and Variation Rules of the Coal Sample with CO_2 Adsorption at Different Pressures Based on Small-Angle X-ray Scattering. *Energy and Fuels* 35(3), pp. 2243–2252. Available at: https://pubs.acs.org/doi/abs/10.1021/acs.energyfuels.0c04033.

Nishino, J. 2001. Adsorption of water vapor and carbon dioxide at carboxylic functional groups on the surface of coal. *Fuel* 80(5), pp. 757–764. Available at: www.elsevier.com/locate/fuel

Njikam, E. and Schiewer, S. 2012. Optimization and kinetic modeling of cadmium desorption from citrus peels: A process for biosorbent regeneration. *Journal of Hazardous Materials* 213–214, pp. 242–248. doi: 10.1016/J.JHAZMAT.2012.01.084.

NOAA. 2022. Global Monitoring Laboratory - Carbon Cycle Greenhouse Gases. [online] Available at: <https://gml.noaa.gov/ccgg/about.html> [Accessed 3 March 2022].

NOAA 2022. National Centers for Environmental information, Climate at a Glance: Global Time Series. published May 2022, retrieved on May 21, 2022 from https://www.ncdc.noaa.gov/cag/

Nodzeński, A. 1998. Sorption (CMI, co and desorption of gases *) on hard coal and active carbon at elevated pressures. *Fuel* 77(11), pp. 1243–1246. doi: 10.1016/S0016-2361(98)00022-2.

Ogunsola, O.I. 1993. Thermal upgrading effect on oxygen distribution in lignite. *Fuel Processing Technology* 34(1), pp. 73–81. doi: 10.1016/0378-3820(93)90062-9.

Okolo, G.N., Everson, R.C., Neomagus, H.W.J.P., Sakurovs, R., Grigore, M. and Bunt, J.R. 2019. Dataset on the carbon dioxide, methane and nitrogen high-pressure sorption properties of South African bituminous coals. *Data in Brief* 25, p. 104248. doi: 10.1016/J.DIB.2019.104248.

Otsu, N. 1979. THRESHOLD SELECTION METHOD FROM GRAY-LEVEL HISTOGRAMS. *IEEE Trans Syst Man Cybern* SMC-9(1), pp. 62–66. doi: 10.1109/TSMC.1979.4310076.

Ottiger, S., Pini, R., Storti, G. and Mazzotti, M. 2008. Competitive adsorption equilibria of CO_2 and CH4 on a dry coal. *Adsorption* 14(4–5), pp. 539–556. doi: 10.1007/s10450-008-9114-0.

Ozdemir, E., Morsi, B.I. and Schroeder, K. 2003. Importance of volume effects to adsorption isotherms of carbon dioxide on coals. *Langmuir* 19(23), pp. 9764–9773. Available at: https://pubs.acs.org/doi/full/10.1021/la0258648.

Ozdemir, E., Morsi, B.I. and Schroeder, K. 2004. CO_2 adsorption capacity of argonne premium coals. *Fuel* 83(7–8), pp. 1085–1094. Available at: https://linkinghub.elsevier.com/retrieve/pii/S001623610300396X [Accessed: 19 August 2019].

Ozdemir, E. and Schroeder, K. 2009. Effect of Moisture on Adsorption Isotherms and Adsorption Capacities of CO_2 on Coals. *Energy & Fuels* 23(5), pp. 2821–2831. Available at: https://pubs.acs.org/doi/10.1021/ef801126a [Accessed: 21 August 2019].

Pan, Z., Connell, L.D., Camilleri, M. and Connelly, L. 2010. Effects of matrix moisture on gas diffusion and flow in coal. *Fuel* 89(11), pp. 3207–3217. doi: 10.1016/J.FUEL.2010.05.038.

Perera, M.S.A. and Ranjith, P.G. 2012. Carbon dioxide sequestration effects on coal's hydro-mechanical properties: A review. International Journal of Energy Research 36(10), pp. 1015–1031. doi: 10.1002/ER.2921.

Perry, S., Perry, R.H., Green, D.W. and Maloney, J.O. 2000. *Perry's chemical engineers' handbook*. doi: 10.5860/choice.38-0966.

Pirzada, M.A., Zoorabadi, M., Lamei, H., Canbulat, I. and Roshan, H. 2018. CO_2 sorption induced damage in coals in unconfined and confined stress states : A micrometer to core scale investigation. *International Journal of Coal Geology* 198(September), pp. 167–176. Available at: https://doi.org/10.1016/j.coal.2018.09.009.

Plazinski, W., Dziuba, J. and Rudzinski, W. 2013. Modeling of sorption kinetics: The pseudo-second order equation and the sorbate intraparticle diffusivity. *Adsorption* 19(5), pp. 1055–1064. Available at: https://link.springer.com/article/10.1007/s10450-013-9529-0.

Pohl R. W. 1954. Experimentalphysik. Vol. 1. Berlin: Mechanik, Akustik, Wärmelehre Springer.

Polanyi, M. 1932. Section III.—Theories of the adsorption of gases. A general survey and some additional remarks. Introductory paper to section III. *Transactions of the Faraday Society* 28(0), pp. 316–333. Available at: https://pubs.rsc.org/en/content/articlehtml/1932/tf/tf9322800316.

Pone, J.D.N., Halleck, P.M. and Mathews, J.P. 2009. Sorption capacity and sorption kinetic measurements of CO_2 and CH_4 in confined and unconfined bituminous coal. *Energy and Fuels* 23(9), pp. 4688–4695. doi: 10.1021/ef9003158.

Prasetyo, L., Tan, S. (Johnathan), Xu, H., Loi, Q.K., Do, D.D. and Nicholson, D. 2020. Fundamentals of gas separation in nanoporous materials. *Nanoporous Materials for Molecule Separation and Conversion* , pp. 143–168. doi: 10.1016/B978-0-12-818487-5.00005-4.

Puri, R., Evanoff, J.C. and Brugler, M.L. 1991. Measurement of Coal Cleat Porosity and Relative Permeability Characteristics, SPE Gas Technology Symposium. Houston, Texas. SPE 21491.

Qi, N. and LeVan, M.D. 2005. Adsorption equilibrium modeling for water on activated carbons. *Carbon* 43(11), pp. 2258–2263. doi: 10.1016/J.CARBON.2005.03.040.

Le Quéré, C. et al. 2015. Global Carbon Budget 2015. *Earth System Science Data* 7(2), pp. 349–396. doi: 10.5194/ESSD-7-349-2015.

Rahaman, A., Grassian, V.H. and Margulis, C.J. 2008. Dynamics of water adsorption onto a calcite surface as a function of relative humidity. *Journal of Physical Chemistry C* 112(6), pp. 2109–2115. doi: 10.1021/JP077594D.

Ramandi, H.L., Mostaghimi, P., Armstrong, R.T., Saadatfar, M. and Pinczewski, W.V. 2016. Porosity and permeability characterization of coal: A micro-computed

tomography study. International Journal of Coal Geology 154–155, pp. 57–68. doi: 10.1016/j.coal.2015.10.001.

Y.V.C. Rao. 1997. Chemical Engineering Thermodynamics. Universities Press (India).

Reid-Soukup, D.A. and Ulery, A.L. 2018. Smectites. *Soil Mineralogy with Environmental Applications* 7, pp. 467–499. Available at: https://onlinelibrary.wiley.com/doi/full/10.2136/sssabookser7.c15.

Ren, J., Weng, H., Li, B., Chen, F., Liu, J. and Song, Z. 2022. The Influence Mechanism of Pore Structure of Tectonically Deformed Coal on the Adsorption and Desorption Hysteresis. Frontiers in Earth Science 10, p. 91. doi: 10.3389/feart.2022.841353.

Reznik, A.A., Singh, P.K. and Foley, W.L. 1984. Analysis Of The Effect Of CO_2 Injection On The Recovery Of In-Situ Methane From Bituminous Coal: An Experimental Simulation. *Society of Petroleum Engineers journal* 24(5), pp. 521–528. doi: 10.2118/10822-PA.

Roberts, M.S., Nakamura, L.K. and Cohan, F.M. 1994. Bacillus mojavensis sp. nov., distinguishable from Bacillus subtilis by sexual isolation, divergence in DNA sequence, and differences in fatty acid composition. *International Journal of Systematic Bacteriology* 44(2), pp. 256–264. Available at: https://pubmed.ncbi.nlm.nih.gov/8186089/.

ROCCS 2020. Establishing a Research Observatory to unlock European Coal seams for Carbon dioxide Storage (ROCCS). Available at: https://www.roccsproject.com/. [Accessed: 10 November 2021].

Rother, G., Krukowski, E.G., Wallacher, D., Grimm, N., Bodnar, R.J. and Cole, D.R. 2012. Pore size effects on the sorption of supercritical CO_2 in mesoporous CPG-10 silica. *Journal of Physical Chemistry C* 116(1), pp. 917–922. Available at: https://pubs.acs.org/doi/abs/10.1021/jp209341q.

Rouquerol, F., Rouquerol, J. and Sing, K. 1999. Introduction. *Adsorption by Powders and Porous Solids* , pp. 1–26. doi: 10.1016/B978-012598920-6/50002-6.

Rouquerol F, Rouquerol J, Sing K,. 2014. Chapter 1 - Introduction, Editor(s): Françoise Rouquerol, Jean Rouquerol, Kenneth Sing, Françoise Rouquerol, Jean Rouquerol, Kenneth Sing. Adsorption by Powders and Porous Solids, Academic Press. Pages 1-24.

Rutherford, D.W., Chiou, C.T. and Eberl, D.D. 1997. Effects of exchanged cation on the microporosity of montmorillonite. *Clays and Clay Minerals* 45(4), pp. 534–543. Available at: https://researchoutput.ncku.edu.tw/en/publications/effects-of-exchanged-cation-on-the-microporosity-of-montmorilloni.

Ruthven, D. M. 1984. Principles of adsorption and adsorption processes. New York: Wiley & Sons.

Sadasivam, S., Thomas, H.R., Zagorščak, R., Davies, T. and Price, N. 2019. Baseline geochemical study of the Aberpergwm mining site in the South Wales Coalfield. *Journal of Geochemical Exploration* 202, pp. 100–112. doi: 10.1016/j.gexplo.2019.03.006.

Saghafi, A., Faiz, M. and Roberts, D. 2007. CO_2 storage and gas diffusivity properties of coals from Sydney Basin, Australia. International Journal of Coal Geology 70(1–3), pp. 240–254. doi: 10.1016/J.COAL.2006.03.006.

Saif, T., Lin, Q., Butcher, A.R., Bijeljic, B. and Blunt, M.J. 2017. Multi-scale multi-dimensional microstructure imaging of oil shale pyrolysis using X-ray micro-tomography, automated ultra-high resolution SEM, MAPS Mineralogy and FIB-SEM. *Applied Energy* 202, pp. 628–647. doi: 10.1016/J.APENERGY.2017.05.039.

Sakurovs, R., Day, S., Weir, S. and Duffy, G. 2007. Application of a modified Dubinin - Radushkevich equation to adsorption of gases by coals under supercritical conditions. *Energy and Fuels* 21(2), pp. 992–997. doi: 10.1021/ef0600614.

Salame, I.I. and Bandosz, T.J. 1999. Experimental Study of Water Adsorption on Activated Carbons. *Langmuir* 15(2), pp. 587–593. Available at: https://pubs.acs.org/doi/full/10.1021/la980492h.

Schaef, H.T., Glezakou, V.-A., Owen, A.T., Ramprasad, S., Martin, P.F. and Mcgrail, B.P. 2013. Surface Condensation of CO 2 onto Kaolinite. Available at: https://pubs.acs.org/sharingguidelines.

Schaef, H.T., Ilton, E.S., Qafoku, O., Martin, P.F., Felmy, A.R. and Rosso, K.M. 2012. In situ XRD study of Ca_2+ saturated montmorillonite (STX-1) exposed to anhydrous and wet supercritical carbon dioxide. *International Journal of Greenhouse Gas Control* 6, pp. 220–229. doi: 10.1016/j.ijggc.2011.11.001.

Shao, H., Ray, J.R. and Jun, Y.-S. 2011. Effects of Salinity and the Extent of Water on Supercritical CO_2-Induced Phlogopite Dissolution and Secondary Mineral Formation. *Environ. Sci. Technol* 45, pp. 1737–1743. Available at: https://pubs.acs.org/sharingguidelines [Accessed: 5 May 2022].

Shi, F., Wei, Z., Zhang, D. and Huang, G. 2020. Isotherms and kinetics of deformation of coal during carbon dioxide sequestration and their relationship to sorption. International Journal of Coal Geology 231(September), p. 103606. Available at: https://doi.org/10.1016/j.coal.2020.103606.

Siemons, N. and Busch, A. 2007. Measurement and interpretation of supercritical CO_2 sorption on various coals. *International Journal of Coal Geology* 69(4), pp. 229–242. doi: 10.1016/j.coal.2006.06.004.

De Silva, P.N.K. and Ranjith, P.G. 2014. Understanding and application of CO_2 adsorption capacity estimation models for coal types. *Fuel* 121, pp. 250–259. Available at: http://dx.doi.org/10.1016/j.fuel.2013.11.051 [Accessed: 5 May 2022].

De Silva, P.N.K., Ranjith, P.G. and Choi, S.K. 2012. A study of methodologies for CO_2 storage capacity estimation of coal. *Fuel* 91(1), pp. 1–15. doi: 10.1016/J.FUEL.2011.07.010.

Sing, K.S.W., Everett, D.H., Haul, R.A.W., Moscou, L., Pierotti, R.A., Rouquerol, J. and Siemieniewska, T. 1985. Reporting Physisorption Data for Gas/Solid Systems with Special Reference to the Determination of Surface Area and Porosity. *Pure and Applied Chemistry* 57(4), pp. 603–619. Available at: https://www.degruyter.com/document/doi/10.1351/pac198557040603/html?lang=en.

Sips, R. 1948. On the structure of a catalyst surface. *The Journal of Chemical Physics* 16(5), pp. 490–495. Available at: https://aip.scitation.org/doi/abs/10.1063/1.1746922.

Smirnov, V.G. et al. 2018. The formation of carbon dioxide hydrate from water sorbed by coals. *Fuel* 228(February), pp. 123–131. Available at:

https://doi.org/10.1016/j.fuel.2018.04.131.

Smith, J. M., & Van, N. H. C. 2004. Introduction to chemical engineering thermodynamics. New York: McGraw-Hill.

Span, R. and Wagner, W. 1996. A new equation of state for carbon dioxide covering the fluid region from the triple-point temperature to 1100 K at pressures up to 800 MPa. *Journal of Physical and Chemical Reference Data* . doi: 10.1063/1.555991.

Speight, James G. 2017. Lange's Handbook of Chemistry. 17th ed. New York: McGraw-Hill Education. pp.296-299.

Stach, E., Chandra, D., Taylor, G.H., Teichmuller, R., M, T. and Mackowsky, M. 1982. Stach's Textbook Coal Petrology Stach. Available at: https://books.google.com/books/about/Stach_s_Textbook_of_Coal_Petrology.html?id=5cb3AAAAIAAJ [Accessed: 6 May 2022].

Staib, G., Sakurovs, R. and Gray, E.M.A. 2014. Dispersive diffusion of gases in coals. Part I: Model development. *Fuel* 143, pp. 612–619. Available at: http://dx.doi.org/10.1016/j.fuel.2014.11.086.

Stevenson, M.D., Pinczewski, W. V., Somers, M.L. and Bagio, S.E. 1991. Adsorption/Desorption of Multicomponent Gas Mixtures at In-Seam Conditions. *Society of Petroleum Engineers - SPE Asia-Pacific Conference, APC 1991* , pp. 741–756. doi: 10.2118/23026-MS.

Strąpoć, D., Mastalerz, M., Schimmelmann, A., Eble, C. eds. 2005. Biogenic and thermogenic coalbed gas in the Illinois Basin: insight from compound-specific carbon isotopic ratios. In: Proceedings of the 22nd International Meeting on Organic Geochemistry, Seville, Spain, September 12–16, 2005, vol. 1, pp. 113–114.

Sudibandriyo, M., Pan, Z., Fitzgerald, J.E., Robinson, R.L. and Gasem, K.A.M. 2003. Adsorption of methane, nitrogen, carbon dioxide, and their binary mixtures on dry activated carbon at 318.2 K and pressures up to 13.6 MPa. *Langmuir* . doi: 10.1021/la020976k.

Švábová, M., Weishauptová, Z. and Přibyl, O. 2011. Water vapour adsorption on coal. *Fuel* 90(5), pp. 1892–1899. doi: 10.1016/j.fuel.2011.01.005.

Švábová, M., Weishauptová, Z. and Přibyl, O. 2012. The effect of moisture on the

sorption process of CO_2 on coal. *Fuel* 92(1), pp. 187–196. doi: 10.1016/J.FUEL.2011.08.030.

Swan, E. and Urquhart, A.R. 1927. Adsorption Equations. *The Journal of Physical Chemistry* 31(2). 2002. pp. 251–276. Available at: https://pubs.acs.org/doi/abs/10.1021/j150272a008.

Tan, Y., Pan, Z., Liu, J., Kang, J., Zhou, F., Connell, L. D. and Yang, Y. 2018. Experimental study of impact of anisotropy and heterogeneity on gas flow in coal. Part I: Diffusion and adsorption. Fuel 232:444-453.

The Global Status of CCS 2018. Australia: Global CCS Institute. Available at: https://www.globalccsinstitute.com/wp-content/uploads/2020/10/Global-Status-of-CCS-Report-2018_FINAL.pdf [Accessed: 1 January 2022].

Thermophysical Properties of Fluid Systems. 2021. Available at: https://webbook.nist.gov/chemistry/fluid/.

Thimons, E.D. and Kissell, F.N. 1973. Diffusion of methane through coal. *Fuel* 52(4), pp. 274–280. doi: 10.1016/0016-2361(73)90057-4.

Thomas, L. 2013. Coal Geology. Second Edition. Wiley-Blackwell. A Clarkson vailable at: doi: 10.1002/9781118385685.

Thommes, M., Kaneko, K., Neimark, A. V., Olivier, J.P., Rodriguez-Reinoso, F., Rouquerol, J. and Sing, K.S.W. 2015. Physisorption of gases, with special reference to the evaluation of surface area and pore size distribution (IUPAC Technical Report). *Pure and Applied Chemistry* 87(9–10), pp. 1051–1069. Available at: https://www.degruyter.com/document/doi/10.1515/pac-2014-1117/html.

Tien, C. 2019. Adsorption Equilibrium Relationships, Isotherm Expressions, Their Determinations, and Predictions. *Introduction to Adsorption* , pp. 23–85. Available at: https://doi.org/10.1016/B978-0-12-816446-4.00003-8.

Tokunaga, T.K. and Wan, J. 2013. Capillary Pressure and Mineral Wettability Influences on Reservoir CO_2 Capacity. *Reviews in Mineralogy & Geochemistry* 77, pp. 481–503. Available at: http://dx.doi.org/10.2138/rmg.2013.77.14 [Accessed: 15 March 2019].

Tóth, J. 2002. Adsorption: theory, modelling, and analysis Surfactant. New York: Marcel Dekker, pp.971-983.

UN Climate Change Conference (COP26) at the SEC – Glasgow 2021. 2022. COP26 Goals - UN Climate Change Conference (COP26) at the SEC – Glasgow 2021. [online] Available at: <https://ukcop26.org/cop26-goals/.

United Nations Environment Programme .2019. Emissions Gap Report 2019. UNEP. available at: https://wedocs.unep.org/bitstream/handle/20.500.11822/30797/EGR2019.pdf?sequence=1&isAllowed=y.

Nairobi. Vangkilde-Pedersen, T. et al. 2009. Assessing European capacity for geological storage of carbon dioxide–the EU GeoCapacity project. *Energy Procedia* 1(1), pp. 2663–2670. doi: 10.1016/J.EGYPRO.2009.02.034.

Volzone, C. 2007. Retention of pollutant gases: Comparison between clay minerals and their modified products. *Applied Clay Science* 36(1–3), pp. 191–196. doi: 10.1016/J.CLAY.2006.06.013.

Volzone, C. and Ortiga, J. 2004. Influence of the exchangeable cations of montmorillonite on gas adsorptions. *Process Safety and Environmental Protection* 82(2 B), pp. 170–174. doi: 10.1205/095758204322972807.

Wang, G. Da, Ren, T.X., Qi, Q.X., Wang, K. and Zhang, L. 2016. Mechanism of adsorption-desorption hysteresis and its influence on deep CBM recovery. Meitan Xuebao/Journal of the China Coal Society 41(1), pp. 49–56.

Wang, K., Wang, G., Ren, T. and Cheng, Y. 2014. Methane and CO2 sorption hysteresis on coal: A critical review. International Journal of Coal Geology 132, pp. 60–80.

Wang, L., Chen, E. tao, Liu, S., Cheng, Y. ping, Cheng, L. biao, Chen, M. yi and Guo, H. jun 2017. Experimental study on the effect of inherent moisture on hard coal adsorption–desorption characteristics. Adsorption 23(5), pp. 723–742. Available at: https://link.springer.com/article/10.1007/s10450-017-9889-y.

Wang, L., Zhang, M. and Redfern, S.A.T. 2003. Infrared Study of CO_2 Incorporation into Pyrophyllite [Al2Si4O10(OH)$_2$] during Dehydroxylation. *Clays and Clay Minerals 2003 51:4* 51(4), pp. 439–444. Available at: https://link.springer.com/article/10.1346/CCMN.2003.0510410 [Accessed: 6 May

2022].

Wang, S., Elsworth, D. and Liu, J. 2011. Permeability evolution in fractured coal: The roles of fracture geometry and water-content. *International Journal of Coal Geology* 87(1), pp. 13–25. doi: 10.1016/j.coal.2011.04.009.

Wang, Z., Hu, P. and Ge, Q. 2020. Gas Surface Interaction and Surface Reactions. *Springer Handbooks* , pp. 905–928. Available at: https://link.springer.com/chapter/10.1007/978-3-030-46906-1_27.

WANG, Z. tang, FU, Z. kun, ZHANG, B. an, WANG, G. xiong, RUDOLPH, V. and HUO, L. wen 2009. Adsorption and desorption on coals for CO_2 sequestration. *Mining Science and Technology* 19(1), pp. 8–13. doi: 10.1016/S1674-5264(09)60002-8.

Wensink, E.J.W., Hoffmann, A.C., Apol, M.E.F. and Berendsen, H.J.C. 2000. Properties of adsorbed water layers and the effect of adsorbed layers on interparticle forces by liquid bridging. *Langmuir* 16(19), pp. 7392–7400. Available at: https://pubs.acs.org/doi/full/10.1021/la000009e

White, C.M. et al. 2005. Sequestration of Carbon Dioxide in Coal with Enhanced Coalbed Methane Recovery s A Review †. *Enery & Fuels* 19(3)

White, G.N. and Dixon, J.B. 2018. Kaolin–Serpentine Minerals. *Soil Mineralogy with Environmental Applications* 7, pp. 389–414. Available at: https://onlinelibrary.wiley.com/doi/full/10.2136/sssabookser7.c12.

Wildenborg, T. and Lokhorst, A. 2005. Introduction on CO2 Geological Storage - Classification of Storage Options; Introduction on CO2 Geological Storage - Classification of Storage Options. 60(3), pp. 513–515. Available at: https://hal.archives-ouvertes.fr/hal-02017223.

H. Xu, D. Tang, J. Zhao, S. Li, S. Tao. 2015. A new laboratory method for accurate measurement of the methane diffusion coefficient and its influencing factors in the coal matrix**.** Fuel 158. pp. 239-247.

Yang, K., Lu, X., Lin, Y. and Neimark, A. V. 2011. Effects of CO_2 adsorption on coal deformation during geological sequestration. *Journal of Geophysical Research: Solid Earth* 116(8). doi: 10.1029/2010JB008002.

Yang, N. and Yang, X. 2011. Molecular simulation of swelling and structure for Na-Wyoming montmorillonite in supercritical CO_2. *http://dx.doi.org/10.1080/08927022.2010.547939* 37(13), pp. 1063–1070. Available at: https://www.tandfonline.com/doi/abs/10.1080/08927022.2010.547939.

Yang, R.T. 1987. Adsorbents and Adsorption Isotherms. *Gas Separation by Adsorption Processes* , pp. 9–48. doi: 10.1016/B978-0-409-90004-0.50005-2.

Yee, D., Seidle, J.P. and Hanson, W.B. 1993. Gas Sorption on Coal and Measurement of Gas Content. *Hydrocarbons from Coal* . doi: 10.1306/ST38577C9.

Zagorščak, R. 2017. An Investigation of Coupled Processes in Coal in Response to High Pressure Gas Injection. PhD Thesis, Cardiff University.

Zagorščak, R. and Thomas, H.R. 2019. High-Pressure CO_2 Excess Sorption Measurements on Powdered and Core Samples of High-Rank Coals from Different Depths and Locations of the South Wales Coalfield. *Energy & Fuels* 33(7), pp. 6515–6526. Available at: https://pubs.acs.org/doi/abs/10.1021/acs.energyfuels.9b00381.

Zhang, J., Clennell, M.B., Liu, K., Pervukhina, M., Chen, G. and Dewhurst, D.N. 2016. Methane and Carbon Dioxide Adsorption on Illite. Available at: https://pubs.acs.org/sharingguidelines.

Zhang, J., Davis, T.A., Matthews, M.A., Drews, M.J., LaBerge, M. and An, Y.H. 2006. Sterilization using high-pressure carbon dioxide. *Journal of Supercritical Fluids* 38(3), pp. 354–372. doi: 10.1016/j.supflu.2005.05.005.

Zhang, Q.B. and Zhao, J. 2013. Determination of mechanical properties and full-field strain measurements of rock material under dynamic loads. *International Journal of Rock Mechanics and Mining Sciences* 60, pp. 423–439. doi: 10.1016/j.ijrmms.2013.01.005.

Zhang, Y. et al. 2018. Nanoscale rock mechanical property changes in heterogeneous coal after water adsorption. *Fuel* 218, pp. 23–32. Available at: https://doi.org/10.1016/j.fuel.2018.01.006 [Accessed: 5 May 2022].

Zhao, J., Xu, H., Tang, D., Mathews, J.P., Li, S. and Tao, S. 2016. A comparative evaluation of coal specific surface area by CO_2 and N_2 adsorption and its influence on CH_4 adsorption capacity at different pore sizes. *Fuel* 183, pp. 420–431. doi:

10.1016/j.fuel.2016.06.076.

Zhou, J., Liu, M., Xian, X., Jiang, Y., Liu, Q. and Wang, X. 2019a. Measurements and modelling of CH4 and CO_2 adsorption behaviors on shales: Implication for CO_2 enhanced shale gas recovery. *Fuel* 251, pp. 293–306. Available at: https://doi.org/10.1016/j.fuel.2019.04.041.

Zhou, L., Feng, Q., Chen, Z. and Liu, J. 2012. Modeling and Upscaling of Binary Gas Coal Interactions in CO_2 Enhanced Coalbed Methane Recovery. *Procedia Environmental Sciences* 12, pp. 926–939. doi: 10.1016/j.proenv.2012.01.368.

Zhou, W., Wang, H., Zhang, Z., Chen, H. and Liu, X. 2019b. Molecular simulation of CO_2/CH_4/H_2O competitive adsorption and diffusion in brown coal. *RSC Advances* 9(6), pp. 3004–3011. Available at: https://pubs.rsc.org/en/content/articlehtml/2019/ra/c8ra10243k.

Zhuravlev, Y.N. and Porokhnov, A.N. 2019. Computer simulation of coal organic mass structure and its sorption properties. *International Journal of Coal Science and Technology* 6(3), pp. 438–444. Available at: https://link.springer.com/article/10.1007/s40789-019-0256-3.

Zutshi, A. and Harpalani, S. 2004. Matrix swelling with CO_2 injection in a CBM reservoir and its impact on permeability of coal. *International Coalbed Methane Symposium, University of Alabama, Tuscaloosa, Alabama* , pp. 12–14.